5-2004

Structural Studies of Superacidic Systems Using Neutron and High Energy X-ray Diffraction

Syliva Ellen McLain

To the Graduate Council:

I am submitting herewith a dissertation written by Syliva Ellen McLain entitled "Structural Studies of Superacidic Systems Using Neutron and High Energy X-ray Diffraction." I have examined the final electronic copy of this dissertation for form and content and recommend that it be accepted in partial fulfillment of the requirements for the degree of Doctor of Philosophy, with a major in Chemistry.

John F. C. Turner, Major Professor

We have read this dissertation and recommend its acceptance:

Chris Benamore, L. J. Magid

Accepted for the Council:

Carolyn R. Hodges

Vice Provost and Dean of the Graduate School

(Original signatures are on file with official student records.)

To the Graduate Council:

I am submitting herewith a dissertation written by Sylvia Ellen McLain entitled "Structural studies of superacidic systems using neutron and high energy X-ray diffraction." I have examined the final paper copy of this dissertation for form and content and recommend that it be accepted in partial fulfillment of the requirements for the degree of Doctor of Philosophy, with a major in Chemistry.

John F. C. Turner, Major Professor

We have read this dissertation and

recommend its acceptance:

Acceptance for the Council:

Vice Chancellor and Dean of

Graduate Studies

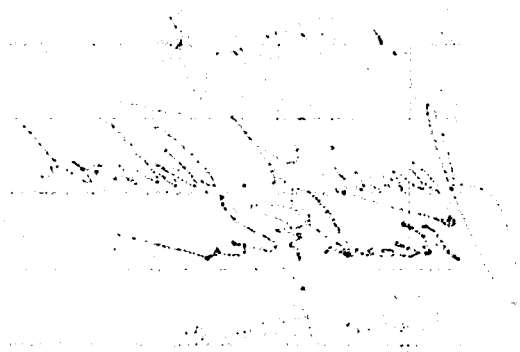

STRUCTURAL STUDIES OF SUPERACIDIC SYSTEMS USING NEUTRON AND HIGH ENERGY X-RAY DIFFRACTION

A Dissertation
Presented for the
Doctor of Philosophy Degree
The University of Tennessee, Knoxville

Sylvia Ellen McLain
May 2004

DEDICATION

This body of work is dedicated in memory of my father, Dr. Howard A. McLain (1936-2000), whom I hope would have been very proud.

ACKNOWLEDGEMENTS

First and foremost I would like to thank Dr. J. F. C. Turner and Dr. C. J. Benmore for their excellent supervision and infinite patience, and equally for teaching me everything I know about neutrons. I would like to thank Argonne National Lab, in particular Dr. Ray Teller, for the generous funding of my graduate research and education. I would also like to thank Dr. G. K. Schweitzer for giving me that first chance and Dr. S. D. Gilman for encouraging me to return to graduate school. I would like to thank Dr. T. Barnes for reading all of my flailing physics sections, the very careful editing and for always being excited about everything we did.

I would like to thank Tim Free for the hours of beautiful and amazing machine work, without which none of my research could have ever happened. Thanks to Tim as well for all the extra help, going above and beyond the call of duty, thereby saving me from more than a few almost catastrophic situations. Thanks to Arthur Pratt for providing the glassware I needed, always at the last minute, and for all of the patience in helping me fix my glass-blown messes and to Bill Gurley for helping me sort out all of those perplexing computer problems, even when they were not really there. Thanks to Prof. A.K. Soper for the use of a SANDALS monitor file.

Thanks to Dr. F. M. Schell for all of the encouraging words and support and to Dr. Charmaine Mamantov for all of the encouragement, being the best role model a woman in science can have and for taking me to much needed symphony concerts. Thanks to Marissa for letting me sleep on her floor in Oxford thereby saving me from the ISIS user housing and for being that someone to go to the pub with after all of those experiments. Thanks to Thomas Proffen for all of the .cif files, the hours of discussions about diffraction physics, editing things at the last minute and to Yvonne, Lukas and Klara for feeding me, entertaining me and letting me use their spare bedroom during my trips to Los Alamos.

I would like to thank all of the folks in the Turner Group for the slack they cut me while I was traveling or forgot to turn on the stills for the 4th day in a row. In particular I would like to thank Cara for being my companion through all of those long hours of writing and analysis and providing me with someone to laugh with.

Thanks to Joan, who not only worked amazingly hard to push this research forward but made me laugh and listened to me complain and fret as only the truest of friends can. Thanks to my friend Flora who read all of this, voluntarily, and kindly asked me to make complete sentences.

Thanks to Claire and Michael for taking care of me, feeding me, reminding me that I had mail and most importantly providing me with a "pause" button whenever I needed to forget about work. Thanks explicitly to Claire for being my dearest most supportive friend and all of the stuff that necessarily entails. Thanks to my brother, David for all of the funny phone conversations. And finally I would like to thank my mother, Verna McLain and her husband Herman, for understanding, amongst other things, when I had to go to work.

ABSTRACT

The structure of two superacids in the liquid phase, hydrogen fluoride and fluorosulfuric acid, have been determined by neutron and high energy X-ray diffraction in this study. In addition the structure of a molecular Lewis acid, BF_3, has been determined for the liquid state as well as the supercritical state. Experiments were also performed on solutions of the hydronium ion in fluorosulfuric acid by neutron and X-ray diffraction as well as by Raman spectroscopy.

In addition this thesis presents the design and construction of sample cells for neutron and X-ray scattering experiments and the design and construction of a high vacuum/fluorine line capable of handling hydrogen fluoride as well as other fluorine containing species.

TABLE OF CONTENTS

LIST OF TABLES Page

LIST OF TABLES Page

LIST OF FIGURES Page

LIST OF FIGURES, CONTINUED Page

NOMENCLATURE

Units

Å	angstrom, 1 Å=1 x 10^{-10} m
barns	1 x 10^{-28} m^2
fm	femtometer, 1 fm=1 x 10^{-15} m
h	Planck constant, 6.626 x 10^{-34} Js
k_B	Boltzmann's constant, 1.381 x 10^{23} JK^{-1}
mm	millimeter
m_N	mass of neutron , 1.67495 x 10^{-27} kg
meV	millielectron volts
MeV	megaelectron volts
Q	Scattering vector, $Q = k' - k$

Abbreviations

ANL	Argonne National Laboratory
APS	Advanced Photon Source
CCSD	Cambridge Crystallographic Structural Database
GLAD	Glass, Liquids and Amorphous Materials Diffractometer
IPNS	Intense Pulsed Neutron Source
RMC	Reverse Monte Carlo modeling
SANDALS	Small Angle Neutron Diffractometer for Amorphous and Liquid Samples
TOF	Time of flight

CHAPTER 1: INTRODUCTION TO NEUTRON AND HIGH ENERGY X-RAY SCATTERING AND THE CHEMISTRY OF SUPERACIDS.

This chapter is divided into two parts. The first part summarizes diffraction theory, the interaction of neutrons and X-rays with matter and the application of these sources to condensed matter. The second part gives a brief introduction to the structural aspects of superacids. More detailed introductions about each superacid studied are provided in the appropriate chapter.

All neutron data presented in this thesis were measured on the **G**lass **L**iquids and **A**morphous **D**iffractometer (GLAD) at the **I**ntense **P**ulsed **N**eutron **S**ource (IPNS) at **A**rgonne **N**ational **L**aboratory (ANL), Argonne, Illinois; high energy X-ray diffraction data were collected at the 11-IDC beam line at **B**asic **E**nergy **S**ciences **S**ynchrotron **R**adiation **C**enter (BESSRC) at the **A**dvanced **P**hoton **S**ource (APS), also located at ANL.[1-3]

Part A of this work is referenced sparingly but details that are not explicitly mentioned in the text can be readily found in the literature.[4-15]

PART A: NEUTRON AND HIGH ENERGY X-RAY SCATTERING

1.1 DESCRIPTION OF THE NEUTRON

Evidence for the existence of a neutron was announced by Chadwick in 1932.[16,17] Prior to this discovery, Bothe had shown that when beryllium was bombarded by α-particles, it emitted a radiation of "great penetrating power".[18] Webster had also reported the observation of particles with energies of approximately 7 MeV, more energetic than any known α-ray. He interpreted this as high speed corpuscles containing a proton and an electron.[19] Chadwick repeated the experiment on beryllium and showed that similar particles were ejected from helium, lithium, carbon, nitrogen and argon. Chadwick noted in these experiments that the particles ejected from the different nuclei, assuming the conservation of energy and momentum, could be explained by the existence of a neutron, an uncharged particle with a mass similar to that of a proton.

The neutron is a fermion (spin ½) and a constituent of atomic nuclei. It obeys the wave-particle duality relationship given by de Broglie

$$\lambda = \frac{h}{p} \tag{1.1}$$

where λ is the wavelength of the neutron, h is Planck's constant and p is the momentum of the neutron,

$$p = m_N \mathrm{v} \tag{1.2}$$

where m_N, the mass of the neutron, is 1.674 x 10^{-27} kg and v is its velocity.

The kinetic energy, E_k of a non-relativistic neutron is given by

$$E_k = \frac{1}{2} m_N \mathrm{v}^2 = \frac{h^2}{2 m_N \lambda^2} \tag{1.3}$$

Table 1.1 shows a list of conversion factors between neutron wavelength, velocity and the kinetic energy of the system, determined from the relations in equations 1.1, 1.2, and 1.3.

Neutrons and the production of neutrons have found several uses in the modern world - nuclear energy applications among others - and with the advent of these energy sources, thermal or 'slow' neutrons have become an increasingly powerful tool for probing the structure and dynamics of condensed matter.

1.2 NEUTRON PRODUCTION

Neutrons can be produced by several methods, but most commonly are produced either from a nuclear reactor source, such as the **H**igh **F**lux **I**sotope **R**eactor (HIFR) at

Table 1.1: Conversion factors for neutrons

	λ /Å	v/ ms^{-2}	E /meV
wavelength,λ	1	2197.8	45.447
velocity, v	3956	1	5.2 x 10^{-6}
Energy, E	9.045	437.4	1

Oak Ridge National Laboratory, or at a spallation source such as IPNS. Accelerator sources are sometimes used to produce neutrons either by using a synchrotron to create photoneutrons, or by a beam of deuterium or tritium atoms. Nuclear reactors produce neutrons through a neutron-induced nuclear fission process which releases fast neutrons giving rise to a chain reaction and the production of high energy neutrons (~200MeV). Spallation sources produce neutrons through the interaction of an accelerated proton beam with a heavy metal target, such as ^{238}U or Ta. The work presented here is concerned with the application of spallation-produced neutrons.

1.2.1 SPALLATION SOURCES

Spallation generation of neutrons relies on the collision of a beam of energetic protons with nuclei that have a high atomic number. The production of neutrons by spallation occurs by two processes. First, when a nucleus is struck by a proton, the collision releases "weakly" bound neutrons immediately. Secondly, neutrons are released by an evaporation process, in which the previously excited nuclei release neutrons as they transition into lower energy levels. Approximately 15-20 neutrons are produced per incident proton.

1.2.2 REACTOR SOURCES

Nuclear reactors produce neutrons through a process knows as neutron-induced nuclear fission. In the process a nuclei, typically ^{235}U, ^{238}U, ^{232}Pu or ^{232}Th, captures a neutron and subsequently splits, or fissions, into two daughter nuclei, releasing at least two high-energy neutrons and a large amount of kinetic energy, typically 200 MeV for each fission. By sustaining a controlled chain-reaction, it is possible to produce neutrons with energies much higher than for a spallation source. As is the case with spallation produced neutrons, reactor neutrons must be slowed down or moderated in order to be useful to most condensed matter applications.

1.3 SLOW NEUTRON MODERATION

Moderators are used to produce "thermal neutrons" which have sufficiently low energies and therefore long wavelengths, to be useful as probes for the structural and dynamical properties of materials. Neutrons are moderated to different temperatures to provide the appropriate velocities for different experimental techniques. Moderators reduce the energy, and therefore lengthen the wavelength and lower the velocity of the produced neutrons, through collisions between the incident neutrons and the nuclei present in the moderator. In the case of thermal neutrons, the moderator source is typically held between 30 K and 350 K, and normally contains either D_2O or methane. Hydrogenated substances are most often used as moderator materials, as hydrogen has a large absorbance cross-section which is essential for the energy exchange process. Conventionally, thermal neutrons are defined as those with a mean velocity of 2200 ms^{-1}.

In addition to the temperature and composition of the moderator, the thickness plays an important role in the spectrum of moderated neutrons. When the moderator is sufficient in thickness, the neutron flux can be described by a Maxwellian distribution which is given by

$$\Phi(\mathrm{v}) \propto \mathrm{v}^3 \exp\left(\frac{-\frac{1}{2} m_N \mathrm{v}^2}{k_B T}\right) \tag{1.4}$$

where $\Phi(\mathrm{v})\mathrm{dv}$ is the number of neutrons through unit area per second, k_B is Boltzmann's constant and T is the temperature of the moderator. The mean velocity is given by

$$\mathrm{v} = \left(\frac{3k_B T}{m_N}\right)^{\frac{1}{2}} \tag{1.5}$$

where probability conservation implies

$$\int_0^\infty n(\mathrm{v})\mathrm{dv} = 1. \tag{1.6}$$

where $n(\mathrm{v})$ is the number of neutrons at a velocity, v.

The Maxwellian velocity distribution can be expressed as an energy or wavelength distribution, using

$$n(\mathrm{v})\mathrm{d}\mathrm{v} = n(\lambda)\mathrm{d}\lambda = n(E)\mathrm{d}E\,. \tag{1.7}$$

GLAD is equipped with a methane moderator at a temperature of 30 K, which produces a distribution of thermalized neutrons with a peak maximum at ~2.95 Å, corresponding to a velocity of ~745 m/s. The distribution of wavelengths for the flux on GLAD is shown in figure 1.1, for the empty instrument for 40,000 pulses. The moderator on GLAD is not sufficiently thick to produce a perfect Maxwellian distribution, but instead shows a high-energy "tail" at shorter wavelengths.

Spallation-produced neutrons are under-moderated in order to maintain a pulsed spectrum, which allows for the use of time-of-flight (TOF) techniques. This would not be practical with a thicker moderator.

For a comparison with the spectrum produced by the moderator on GLAD, an incident neutron spectrum from the SANDALS instrument at the ISIS facility is shown in figure 1.2, for a single pulse. In this case, the moderating material is liquid methane held at a temperature of 110 K. A higher temperature moderator produces higher

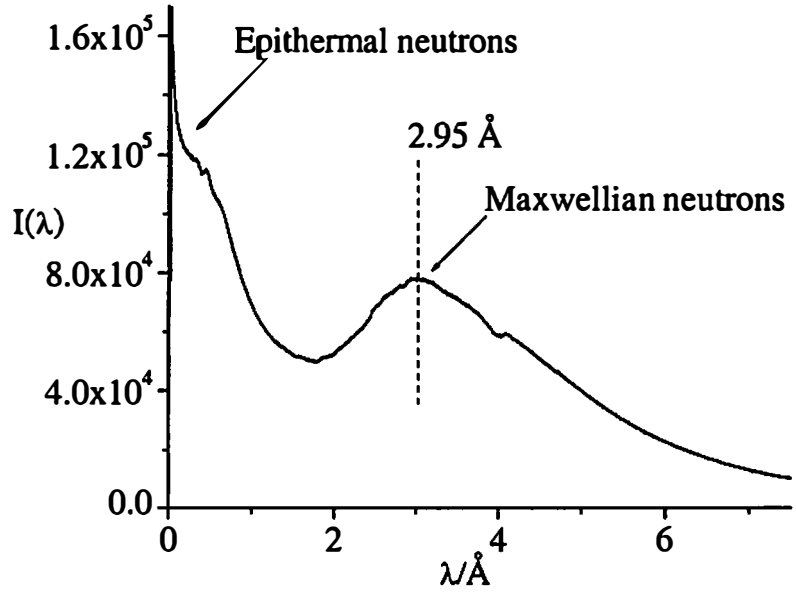

Figure 1.1: Incident neutron spectrum on GLAD.

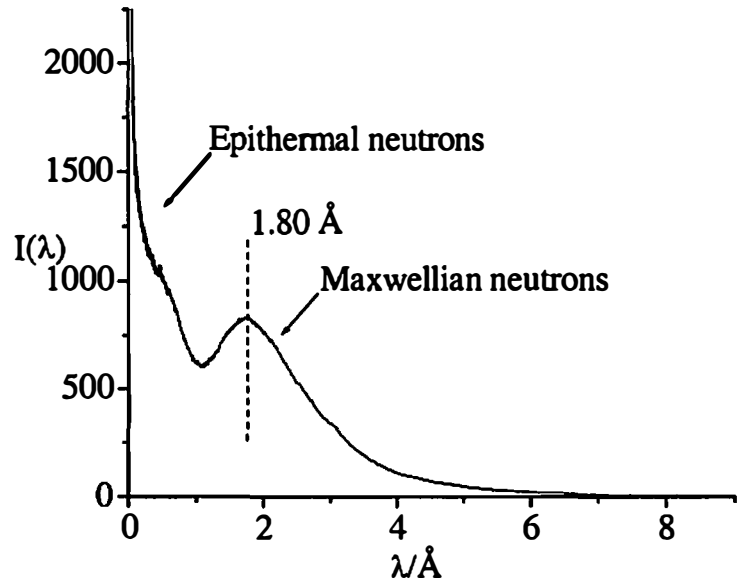

Figure 1.2: Incident neutron spectrum on SANDALS.

energy neutrons, where in this case the moderator produces conventional thermal neutrons, $\lambda \approx 1.81$ Å and $v = 2200\ ms^{-1}$. It should be noted that the stability provided by the solid methane moderator on GLAD is advantageous for applications to condensed matter. The liquid methane moderator as seen on SANDALS, though it produces higher energy neutrons, does not have the same stability as its solid counterpart. The details of this are beyond the scope of this discussion but are given in the literature.[20-28]

There are several crucial reasons for the utility of thermal neutrons probes of condensed matter. First, thermal neutrons have wavelengths that are comparable to typical interatomic distances, allowing the details of the atomic structure of condensed matter systems to be directly probed. In addition, the energies of slow neutrons are comparable to the energies of most excitations, including magnetic excitations, in condensed matter, allowing the dynamics of most systems to be directly probed.

1.4 NEUTRON DETECTION

Neutron detectors are designed to measure the flux of neutrons produced in a scattering experiment. Detector responses are governed by the energy spectra of the

incident neutrons - some detectors are most efficient for slow neutron detection, while others are more sensitive to fast (non-moderated) neutrons. Slow neutron detectors are normally proportional detectors, such as ^{3}He on GLAD, fission counters or scintillators. ^{3}He detectors consist of cylindrical tubes filled with pressurized (~2.5 bar) helium, in which neutrons are detected through a p,n reaction with thermal neutrons, that is

$$^3\mathrm{He} + n^0 \longrightarrow {}^3\mathrm{H} + p^+ \tag{1.8}$$

As the proton possesses a positive charge, it can act as a charge carrier in order to electronically record the scattering of the neutron from a sample.

The GLAD instrument is described in more detail in section 1.10.1.

1.5 NEUTRON SCATTERING CROSS-SECTIONS

The probability of an interaction between a specific nucleus and a neutron is defined in terms of the cross-section, σ (barns), which describes the effective scattering target area for a reaction between nucleus, X and an incident neutron. Each element has a different associated neutron scattering cross-section for the each of the neutron-nucleus reactions that can occur. These can be summed together to give a total cross-section, and can be written as

$$\sigma_{total} = \sigma_{scatt} + \sigma_{cap} \tag{1.9}$$

where σ_{scatt} is the scattering cross-section and σ_{cap} is the neutron capture cross-section. Because neutron capture leads to a compound nucleus by absorption of the neutron, this is usually termed the absorption cross-section, σ_{abs}.

1.6 SCATTERING THEORY

Neutrons are scattered by fixed nuclei either due to a direct strong interaction between the incident neutron and the nuclei present in the sample, or through and electromagnetic dipole-dipole interaction between the magnetic moments of the neutron

and the sample. Conversely, X-ray scattering occurs electromagnetically through an interaction between the incident X-ray and the electrons in the sample.

In any scattering experiment, the incident wavefunction can be approximated as a one-dimensional plane wave,

$$\Psi(r) = \exp(ik \cdot r) \tag{1.10}$$

where k is the momentum vector of the incident particles and r is the position vector. After scattering from a fixed nucleus, the outgoing wavefunction can be approximated by

$$\Psi'(r) = c\ \exp(ik' \cdot r) \tag{1.11}$$

where c is a complex constant scattering amplitude that depends on the incident probe as well as the composition of the sample from which the scattering occurs, k' is the momentum vector of the scattered wave and r is again the position vector. In thermal neutron diffraction, the scattered waves are approximated by a three dimensional S-wave as the scattered waves are isotropic.

1.6.1 INELASTIC AND ELASTIC SCATTERING

Scattering can be classified as inelastic, where energy is transferred to or from the probe to the sample, or elastic, where there is no energy transfer in the system. Elastic scattering or diffraction gives structural information about a scattering system or sample, whereas inelastic scattering yields dynamical information about a system.

Inelastic neutron scattering occurs when the incident neutron excites a normal mode in the material being probed, leading to the emission of a scattered neutron with a different energy than the incident neutron energy. Inelastic photon scattering (Raman scattering) also occurs by normal mode excitation. In elastic scattering, the kinetic energy of the collision is conserved and in the case of a fixed nucleus no energy is exchanged between the incident probe and the sample.

In terms of the relationship between the incident wavevector, k and the scattered wavevector, k', in elastic scattering there is no change in magnitude between

k and k' but there is a change in the direction of k'. Conversely, in inelastic scattering there is an exchange of energy as well as a change in the magnitude and direction of the wavevector.

Figure 1.3 shows a graphical representation of this scattering process as a scattering triangle.

In general the transferred wavevector is given by

$$Q = (k' - k) \tag{1.12}$$

where Q is defined as the scattering vector and $\hbar Q$ is the momentum transfer. When $k = k'$ the scattering is elastic and when $k \neq k'$ the scattering is inelastic.

From figure 1.3, the magnitude of k and k', Q and the scattering angle, θ, are related by

$$\sin\theta = \frac{Q/2}{k} \tag{1.13}$$

which implies through equation 1.1

$$|Q| = 4\pi \sin\theta/\lambda \tag{1.14}$$

where λ is the wavelength of the scattered neutron.

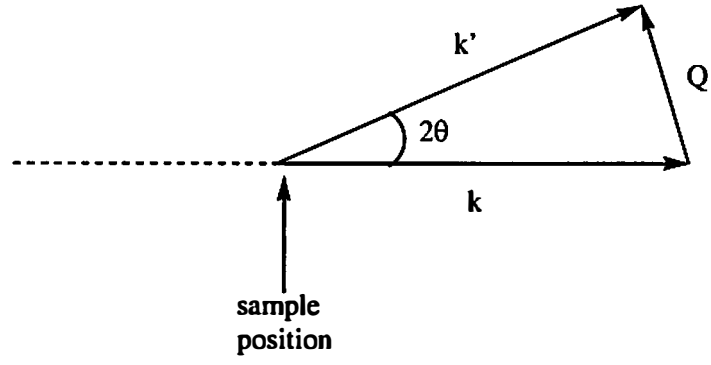

Figure 1.3: Geometrical relationship between the incident wavevector, k and the scattered wavevector, k'.

1.6.2 DIFFRACTION

Diffraction measured using any probe is the interference between the elastically scattered waves from each atom. In a diffraction experiment the scattering intensity observed is a function of momentum transfer, which has the general form

$$I(Q) = \sum_{i,j} f_i f_j \exp\left(iQ \cdot \vec{r}_{ij}\right) \qquad (1.15)$$

where f_i and f_j are the scattering factor for atoms i and j, respectively. As stated above, the scattering that arises from X-rays or neutrons occurs by distinctly different scattering mechanisms.

X-ray scattering is an electromagnetic process where photons which scatter directly from the electron charge density of the atoms being studied. Because heavier atoms have higher electron densities, they give rise to a greater intensity in an X-ray diffraction pattern. The scattering intensity observed in an X-ray scattering experiment depends upon the product of, the atomic form factors, $f(Q)$, as well as the concentration of each atom present in the sample. $f(Q)$ a function of Q, and at $Q = 0\,\text{Å}^{-1}$, $f(Q=0)$ is equal to the atomic number, Z, of the element being probed.[29] The strong Q dependence of X-ray scattering arises from the fact that the size of the scattering target for most elements is typically ~1 Å and at the X-ray energies most often employed the wavelength is ~1 Å and with high energy X-rays is ~0.1 Å. This ensures that the wavelength of the incident X-ray beam is comparable to the same length scale as the target itself, leading to an angular dependency to the scattered wave or $f(Q)$.

The scattering intensity observed in a neutron diffraction experiment is a function of the concentration of atoms in the sample and the bound coherent scattering length, b, of each atom present in the sample.[30,31] In contrast to X-rays, the intensity of the scattering from a single nucleus is constant over all values of Q. This is also due to the incident wavelength-target size relationship. The size of the nucleus is similar to the range of the strong nuclear force. The nuclear boundary is where the attractive strong

nuclear force and the repulsive (Coulombic) force are approximately equal. As a consequence of the strength of the nuclear force, the size of the nucleus and the scattering length of the isotope are generally comparable in magnitude. Given that the radius of the nucleus is a few femtometers or fermis, the range of the nuclear force is extremely small compared to the length scale of the atomic separations in condensed matter, which is a few Å.

Thermal neutrons, like X-rays, have wavelengths of ~1Å and as the length scale of the scattering is $\sim 10^{15}$m. This neutron-nucleus size relationship implies that the nuclei are essentially point sources, which results in no angular dependence of the scattered wave.

Scattering cross-sections, σ and scattering lengths, b are related by

$$\sigma = 4\pi b^2 \qquad (1.16)$$

b , like σ, is different for each different nucleus and therefore must be measured independently for each isotope. Coherent scattering lengths do not follow any simple patterns with respect to the Periodic Table and are different for isotopomers. Neutrons are strongly scattered by light elements such as hydrogen and deuterium, which are virtually transparent to X-rays, and the isotopic dependence of b plays a fundamental role in neutron scattering, as isotopic substitution can yield structural information that cannot be as easily obtained in an X-ray experiment (anomalous X-ray scattering being the exception). Figure 1.4 shows the differing values of b across the

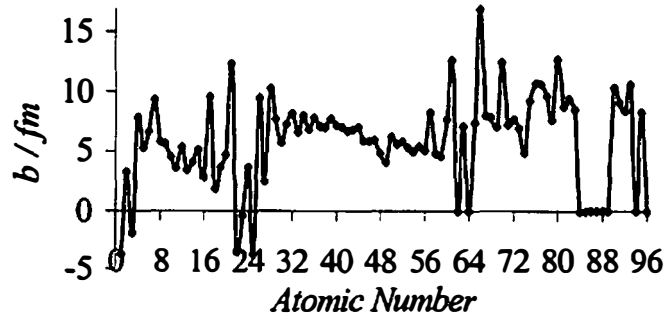

Figure 1.4: Bound coherent scattering lengths of the first 96 elements in the periodic table.

periodic table and a comparison between neutron scattering intensities and X-ray intensities is shown in figure 1.5.

The length scale of the scattering nuclei is evidently negligible in comparison to the length scale of the separation between the scattering sources in space. This allows the effective scattering potential for the sample to be written as a simple dimensionless intensity factor, the bound coherent scattering length, *b*, together with a mathematical description of the density of these points in space, the Dirac delta function. In this approximation the neutron scattering potential for the sample can be written as

$$V(r) = V_{Fermi}(r) = \sum_i \mathrm{b}_i \delta(r - r_i) \qquad (1.17)$$

where V_{Fermi} is known as the Fermi pseudo-potential and is written for the sample, b_i is the *bound* scattering length (so called because it relates to a fixed nucleus as is the case in condensed matter) of atom *i*, $(r - r_i)$ is the distance between from the neutron to the ith nucleus in the sample and $\delta(r - r_i)$ is a Dirac delta function, which prescribes a scattering event.

It is also noteworthy that long-range forces such as the interaction between the neutron spin and the nuclear spin do not significantly depend on the size of the scatterer as the forces are long-range and the spin interaction has no obvious angular

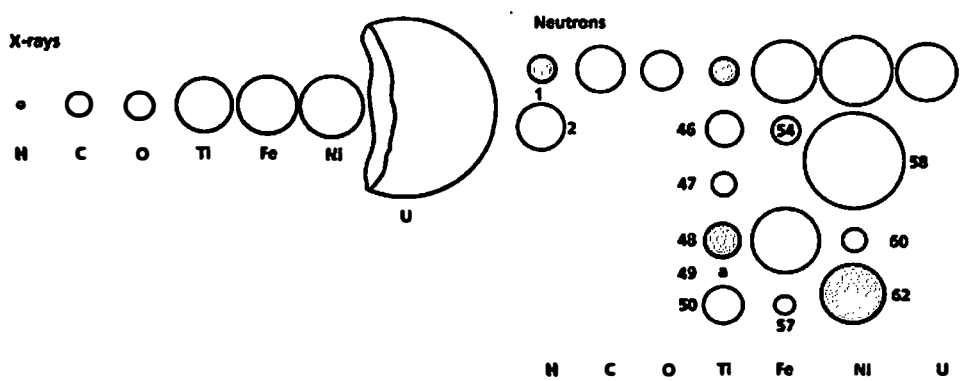

Figure 1.5: X-ray scattering intensities compared with neutron scattering intensities. The blue shading represents a negative neutron scattering wavelength the numbers are the atomic masses of the elements.

dependency. Given that most materials are diamagnetic and their thermally accessible nuclear spin states have energies comparable to their ground states, then the spin states of the nuclei in question can treated as a spin average. This nuclear spin average is implicitly included in the scattering lengths, where most elements are in an averaged spin state.

1.6.3 BRAGG VS. NON-BRAGG DIFFRACTION

Crystalline systems are defined by long-range order and periodicity. Because the atomic positions an ideal crystal are fixed, measurement over all values of Q give a diffraction pattern which is non-zero only at certain Q values, which are identical with a vector in reciprocal space that exists within the sample.

In a single crystal, the allowed Q values are defined by a vector in reciprocal space, which can be indexed by h,k,l values; these values correspond to the space between atomic planes in the crystal lattice. This is known as Bragg scattering and was first observed by Bragg and von Laue.[32-34] Bragg's law is specified by the constraint

$$n\lambda = 2d_{h,k,l}\left(\frac{Q/2}{k}\right) = 2d_{h,k,l}\sin\theta \qquad (1.18)$$

where λ is the wavelength of the incident probe, $d_{h,k,l}$ is the spacing between lattice planes and the angle θ is defined in figure 1.2.

A polycrystalline powder, like a single crystal, satisfies the Bragg condition, however all the absolute directions of the individual h,k,l values are lost as crystalline powders contain an isotropic distribution of many small single crystals. Polycrystalline powders give rise to Bragg peaks in the diffraction pattern, where the intensity of the Bragg peaks are proportional to the number of reflections with identical $|\bar{h},\bar{k},\bar{l}|$, as the random orientation of the crystals in a powder gives degenerate h,k,l values.

Both powder diffraction and single crystal diffraction contain information not only about the average periodic structure of the powder but also contain information

about the local structure of the system. However, in many cases diffraction from single crystals or powders are analyzed only in terms of understanding the average structure of the system in question without any assessment of the local structure. A notable exception to this rule is the **P**air **D**istrubtion **F**unction (PDF) technique, which is used increasingly to study the local structure present in polycrystalline powders.[5,6,35-43] Local structural information arises, in addition to the scattering observed from the Bragg peaks, from the diffuse scatter, which appears as long, broad oscillations in the diffraction pattern. Diffuse scatter is not always observable in a powder diffraction pattern as it usually has much less intensity than the Bragg scatter.

Diffuse scatter contains only information about the local structure of the system and is sometimes referred to as elastic non-Bragg scattering. Liquids and amorphous systems have no long-range order and therefore no periodicity or lattice and the Bragg formulation is inapplicable. In a liquid diffraction experiment, only diffuse scattering is present and as such only information concerning the local structure and intermediate range order is possible by diffraction. Liquid diffraction is discussed in more detail in section 1.9.

1.7 Neutron Scattering Measurements

Neutron scattering experiments typically measure the intensity of the scattering as a function of energy and solid angle, through the double differential scattering cross-section. This is defined by

$$\frac{d^2\sigma}{d\Omega dE} = \frac{\left(\begin{array}{l}\text{neutrons scattered per unit time into the} \\ \text{solid angle } d\Omega \text{ with energy between E and E}'\end{array}\right)}{\Phi d\Omega dE} \qquad (1.19)$$

where Φ is the flux of the incident neutron beam, E is the energy of the scattered neutrons and Ω is the solid angle where the neutrons are detected.

Van Hove derived a general expression for the intensity of neutrons scattered from a multi-component system in terms of an intermediate scattering function $I(Q,\omega)$,

where ω is the energy transfer between the initial energy, E_0, of the incident neutron and the final energy, E_f, of the scattered neutron, and $\omega = E_f - E_0$. This is defined by

$$I(Q,\omega) = \frac{d^2\sigma}{d\Omega d\omega} = \frac{k'}{k}\frac{1}{h}\sum_{ij} b_i b_j \int_{-\infty}^{\infty} \left\langle \exp(-iQ\cdot\bar{r}_j(0))\exp(iQ\cdot\bar{r}_i(t))\right\rangle \exp(-i\omega t)dt \tag{1.20}$$

where t represents the time component, b_i and b_j are the bound scattering lengths of nuclei i and j, respectively, and the sum is over pairs of nuclei and the nucleus i is at position r_i at time t and the jth nucleus is at position r_j at $t = 0$. The brackets $\langle ... \rangle$ denotes a thermal average over all states of the system.

Although $I(Q,\omega)$ is expressed in terms of quantum mechanical operators, it may be conveniently expressed in terms of a single plane wave using the identity

$$\sum_{ij} b_i b_j \exp(-iQ\cdot\bar{r}_j(0))\exp(iQ\cdot\bar{r}_i(t)) = \sum_{ij} b_i b_j \int_{-\infty}^{\infty} \delta(r - [(r_j(0)) - r_i(t)])\exp(-iQ\cdot r)dt \tag{1.21}$$

where the delta function represents the distance between r_i and r_j.

1.7.1 TIME DEPENDENT PAIR CORRELATION FUNCTION AND TOTAL SCATTERING FUNCTION

$G(r,t)$, the time-dependent total pair correlation function describes the correlation between a particle at position r' at time t' and a particle at a position $r'+r$ at time $t'+t$ averaged over all r'. $G(r,t)$ is a Fourier transform of the total scattering function $S(Q,\omega)$. $S(Q,\omega)$ and subsequently $G(r,t)$ can be derived directly from equation 1.20 as

$$\frac{1}{N}\frac{d^2\sigma}{d\Omega d\omega} = \frac{k'}{k}\sum_{i,j=1,i\neq j}^{n} \bar{b}_i \bar{b}_j S_{ij}^{d}(Q,\omega) + \frac{k'}{k}\sum_{i=1}^{n} \bar{b}_i^2 S_i^{s}(Q,\omega) \tag{1.22}$$

where N is the number of atoms in a scattering system which contains n different chemical species, $S_{ij}^{d}(Q,\omega)$ is the distinct total scattering function and $S_i^s(Q,\omega)$ is the self-scattering total scattering function. $S(Q,\omega)$ is related to $G(r,t)$ by

$$S(Q,\omega)=\frac{N}{2\pi}\int\exp[i(Q\cdot\bar{r}-\omega t)]G(r,t)\mathrm{d}r\mathrm{d}t \qquad (1.23)$$

and

$$G(r,t)=\frac{1}{N(2\pi)^3}\int\exp[i(\omega t-Q\cdot\bar{r})]S(Q,\omega)\mathrm{d}Q\mathrm{d}\omega \qquad (1.24)$$

in the limit of $N\longrightarrow\infty$, $G(r,t)$ is equal to the number density, ρ.

1.7.2 COHERENT AND INCOHERENT SCATTERING

As is seen in equation 1.20, the intensity observed in a neutron scattering experiment depends on the scattering length, but even in a scattering system that is composed of only one element, the scattering lengths are usually not all identical. The scattering length not only varies from one element to another, but also depends on nuclear spin and the presence of isotopes. This may be addressed by separating the mean elemental scattering length b can be subdivided where f_i is the frequency of finding each distinct isotope or spin state. The conservation of probability implies

$$\sum_i f_i = 1 \qquad (1.25)$$

and the average scattering length for a single component system is

$$\bar{b} = \sum_i f_i b_i \qquad (1.26)$$

The average value of b^2 is

$$\bar{b}^2 = \sum_i f_i b_i^2 \qquad (1.27)$$

Since there is no correlation between the values of b for each nucleus, the probability of finding a specific value of b_i is f_i.

When a system has a large number of nuclei present, it can be assumed that the there is no correlation between b_i values on different nuclei, so that the measured intensity is given by the average scattering length exhibited by any element. For a single element system, equation 1.22 becomes

$$\frac{\mathrm{d}^2\sigma}{\mathrm{d}\Omega\mathrm{d}\omega} = \frac{k'}{k}\sum_{jj'}\bar{b}_{j'}\bar{b}_j \int_{-\infty}^{\infty}\langle j', j\rangle \exp(-i\omega t)\mathrm{d}t \tag{1.28}$$

where $\langle j', j\rangle = \left\langle \exp\left(-iQ\cdot\vec{r}_j(0)\right)\exp\left(iQ\cdot\vec{r}_i(t)\right)\right\rangle$.

There are only two possibilities in this one component system namely, $\bar{b}_{j'}\bar{b}_j = (\bar{b})^2$ when $j' \neq j$ and $\bar{b}_{j'}\bar{b}_j = \bar{b}^2$ when $j' = j$.

This allows equation 1.28 to be divided into two parts

$$\frac{\mathrm{d}^2\sigma}{\mathrm{d}\Omega\mathrm{d}\omega} = \frac{k'}{k}\sum_{jj'}(\bar{b})^2 \int_{-\infty}^{\infty}\langle j', j\rangle \exp(-i\omega t)\mathrm{d}t + \frac{k'}{k}\sum_{jj'}\left(\bar{b}^2 - (\bar{b})^2\right)\int_{-\infty}^{\infty}\langle j', j\rangle \exp(-i\omega t)\mathrm{d}t \tag{1.29}$$

The first term is known as the coherent scattering cross-section and the second is the incoherent scattering cross-section.

$$\frac{\mathrm{d}^2\sigma}{\mathrm{d}\Omega\mathrm{d}\omega} = \left(\frac{\mathrm{d}^2\sigma}{\mathrm{d}\Omega\mathrm{d}\omega}\right)_{\mathrm{coh}} + \left(\frac{\mathrm{d}^2\sigma}{\mathrm{d}\Omega\mathrm{d}\omega}\right)_{\mathrm{incoh}} \tag{1.30}$$

Coherent scattering describes the scattered waves produced by the interference of scattering from different nuclei. Incoherent scattering, in contrast, gives rise to scattered waves from different nuclei that do not interfere with each other. In terms of the total scattering function $S(Q,\omega)$, equation 1.29 can be written as

$$\frac{1}{N}\frac{\mathrm{d}^2\sigma}{\mathrm{d}\Omega\mathrm{d}\omega} = \frac{k'}{k}\sum_{i,j=1}^{n}\bar{b}_i\bar{b}_j S_{ij}(Q,\omega) + \frac{k'}{k}\sum_{i=1}^{n}\left(\bar{b}_i^2 - (\bar{b})^2\right)S_i^s(Q,\omega) \tag{1.31}$$

where the first term on the right hand side of the equation defines the coherent scattering function and the second term on the right hand side of the equation defines the incoherent scattering function. What it noteworthy about equation 1.31 is that the distinct scattering term in this equation is the summation is taken over all pairs that all

atoms, i and j atoms and that in this case i can equal j. In this formula, it is clear that the scattering between distinct atoms of the same type give rise to intensity in the interference function.

1.7.3 STATIC APPROXIMATION

In a diffraction experiment, $S(Q)$, the static structure factor, is the quantity sought as its Fourier transformation gives rise to the time independent pair correlation function, $G(r,0) = G(r)$. $G(r)$ yields only structural information about the sample being probed as $S(Q)$ is confined to the elastic coherent scattering that arises from the sample.

Time invariance in the pair correlation function is important when regarding interference terms or distinct terms in order to provide accurate atomic distances, as it provides the time averaged structure of the material in question. All diffraction probes give rise to scattered waves and the interference between scattered waves at different atomic positions provides structural information about the scattering system, which is often interpreted assuming fixed atomic positions. In order for the static approximation to be valid, it must be assumed that the scattered waves travel at sufficient velocities so that the atomic motion can be neglected

In the case of conventional X-rays ($\lambda \approx 1$ Å), the static approximation is a clearly justified assumption. Scattered X-rays travel at the speed of light (~2.998 x 10^8 ms^{-1}) and typical interatomic distances are several angstroms. Therefore, the time for the scattered waves to interact locally is approximately 10^{-18} seconds. In most condensed matter systems the relaxation time from an excited state is approximately 10^{-12}s to 10^{-13}s, which is much larger than the characteristic X-ray scattering time.

In thermal neutron diffraction by thermal neutrons the velocity of the diffracted waves is ~10^3 ms^{-1}, giving an interaction time scale of approximately 10^{-13} s. Here the static approximation is not justified in general.

In neutron diffraction, the differential scattering cross-section, which gives a system whose scattering is solely dependent on Q, is performed by integrating the double differential cross-section over all values of ω to give the differential scattering cross-section per solid angle

$$\frac{d\sigma}{d\Omega} = \int \frac{d^2\sigma}{d\Omega d\omega} d\omega \tag{1.32}$$

The differential scattering cross section is related to the total static structure factor $S(Q)$ by

$$\begin{aligned} \frac{1}{N}\frac{d\sigma}{d\Omega} &= \frac{1}{N}\int \frac{d^2\sigma}{d\Omega d\omega} d\omega = \frac{k'}{k}\sum_{i,j=1}^{n} \bar{b}_i \bar{b}_j S_{ij}(Q) + \frac{k'}{k}\sum_{i=1}^{n}\left(\bar{b}_i^2 - \left(\bar{b}\right)^2\right) S_i^s(Q) \\ &= \left(\frac{d\sigma}{d\Omega}\right)_{distinct} + \left(\frac{d\sigma}{d\Omega}\right)_{self} \end{aligned} \tag{1.33}$$

where distinct refers to coherent scattering and self is incoherent scattering.

1.7.4 PARTIAL STRUCTURE FACTORS AND PAIR CORRELATION FUNCTIONS

From equation 1.33, the incoherent scattering term or the self-scattering term, $S_i^s(Q)$ is equivalent to the proportion of nuclei, i, and their respective intensities in the scattering system that is $S_i^s(Q) = c_i \bar{b}_i^2$. $S_{ij}(Q)$, the coherent term can be defined as

$$S_{ij}(Q) = \sum_{i,j=1}^{n} c_i c_j \bar{b}_i \bar{b}_j \left(A_{ij}(Q) - 1\right) \tag{1.34}$$

where $A_{ij}(Q)$ are the Faber-Ziman partial structure factors.[44] Thus equation 1.33 becomes

$$\frac{1}{N}\frac{d\sigma}{d\Omega} = \sum_{i,j=1}^{n} c_i c_j \bar{b}_i \bar{b}_j \left(A_{ij}(Q) - 1\right) + \sum_{i=1}^{n} c_i \bar{b}_i^2 \tag{1.35}$$

In all the above equations $S_{ij}(Q)$ refers to the total static structure factor. It is convenient to redefine $S_{ij}(Q)$ as the interference term or distinct term, $F(Q)$ and $A_{ij}(Q)$ as $S_{\alpha\beta}(Q)$ as is shown in the following equation

$$F(Q) = \sum_{\alpha,\beta} c_\alpha c_\beta b_\alpha b_\beta \left(S_{\alpha\beta}(Q) - 1\right) \tag{1.36}$$

In this equation i, j is replaced by α, β, respectively in order to avoid confusion with the original $S_{ij}(Q)$. $F(Q)$, the intermediate scattering function is related to the total structure factor by

$$S^{total}(Q) = \frac{F(Q)}{\sum_{\alpha,\beta} c_\alpha c_\beta b_\alpha b_\beta} = \frac{1}{\sum_{\alpha,\beta} c_\alpha c_\beta b_\alpha b_\beta} \sum_{\alpha\beta} c_\alpha c_\beta b_\alpha b_\beta \left(S_{\alpha\beta}(Q) - 1\right) \tag{1.37}$$

where $S^{total}(Q)$ is the total static structure factor and $S_{\alpha\beta}(Q)$ are the Faber-Ziman partial structure factors.

Just as $S(Q,\omega)$ is related to $G(r,t)$ by direct Fourier transformation, the total static structure factor, $S^{total}(Q)$ and the time independent total pair correlation function, $G^{total}(r)$, are related by the following equations

$$S^{total}(Q) = 1 + \frac{4\pi\rho}{Q} \int r\left[G^{total}(r) - 1\right] \sin(Qr) dr \tag{1.38}$$

and

$$G^{total}(r) = 1 + \frac{4\pi}{(2\pi)^3 \rho r} \int Q\left[S^{total}(Q) - 1\right] \sin(Qr) dQ \tag{1.39}$$

where ρ is the number density (atoms/Å^{-3}) of the scattering system or sample.

By virtue of the Fourier transformation, the total radial distribution function can be described as the sum of partial radial distribution functions weighted appropriately as an analogous equation to equation 1.36 as

$$G^{total}(r) = \frac{1}{\sum_{\alpha,\beta} c_\alpha c_\beta b_\alpha b_\beta} \sum_{\alpha,\beta} c_\alpha c_\beta b_\alpha b_\beta \left(g_{\alpha\beta}(r) - 1\right) \qquad (1.40)$$

The partial structure factors and partial pair correlation functions are also related to each other by direct Fourier transformation.

1.8 HIGH ENERGY X-RAY SCATTERING

High energy X-rays, produced from synchrotron sources, yield diffraction measurements analogous to the neutron diffraction measurements. Conventional X-rays, where $\lambda \cong 0.7$ Å are limited in the depth which they can penetrate and as such are not useful for determining the structure of polymers or liquids. High energy X-rays on the other hand, have enough energy to easily penetrate yielding measurements analogous to neutron scattering data. High energy X-rays $, \lambda = 0.1$ Å ($E_{incident} \approx 100$ keV), provide adequate penetration of X-rays through both the sample and container in transmission geometry. Additionally, the static approximation applies in X-ray diffraction (section 1.5.3).[45] In a high-energy X-ray experiment, the differential scattering cross-section can be written as

$$\frac{d\sigma}{d\Omega} = \frac{d\sigma}{d\Omega}_{Compton} + \frac{d\sigma}{d\Omega}_{self} + \frac{d\sigma}{d\Omega}_{distinct} = C_X(Q) + \sum_\alpha c_\alpha f_\alpha^2(Q) + I_X(Q) \qquad (1.41)$$

where c_α and c_β are the concentration species α and β, respectively and $f_\alpha(Q)$ is the atomic form factor for species α. $C_X(Q)$ is the Compton scattering function which like the atomic form factor is dependent on Q. Compton scattering is incoherent X-ray scattering, that is, there is no phase relationship between scattered waves in the case of Compton scattering.

The X-ray total structure factor or the pseudo-nuclear function, $S_X(Q)$ can be obtained from the differential scattering cross-section as

$$S_X(Q) = \frac{\left[I_X(Q) - C_X(Q) - \sum c_\alpha f_\alpha^2(Q) \right]}{\sum_{\alpha,\beta} c_\alpha c_\beta f_\alpha(Q) f_\beta(Q)} \qquad (1.42)$$

The X-ray total structure factor can also be written in terms of the Faber-Ziman partial structure factors as

$$S_X(Q) = \frac{1}{\sum_{\alpha,\beta} c_\alpha c_\beta f_\alpha(Q) f_\beta(Q)} \sum_{\alpha,\beta} c_\alpha f_\alpha(Q) c_\beta f_\beta(Q) (S_{\alpha\beta}(Q) - 1) \qquad (1.43)$$

1.9 SCATTERING FROM LIQUIDS

The liquid state is the most complex phase of matter. Densities of liquids are comparable to densities of the solids, implying that the forces between particles in the liquid are of the same magnitude as those forces present in the solid. However, there is no simplification due to the presence of a lattice and no satisfactory analytic theory of the liquid state exists.[8,46-57] Although liquids have no intrinsic long range order however, atoms and molecules in a liquid possess local structure and are subject to attractive and repulsive forces. Liquids are an example of a many body problem, where even if the interaction between particles is known the exact structure is impossible to exactly predict.

1.9.1 NEUTRON DIFFRACTION FROM LIQUIDS

In a neutron diffraction experiment, because of inelasticity, multiple scattering and attenuation, all instruments measure only an approximate $S(Q)$ and as such all of these effects must be correct for in order to accurately obtain the static $S(Q)$ for the system being studied. In liquid diffraction, the inelasticity effect is exacerbated by the fact that liquids possess a large number of low energy translational and rotational modes which are excited by virtue of the neutron scattering process leading to a large number

of inelastic scattering events. In these systems inelasticity is the most prominent effect that must be corrected for to obtain a good approximation to the static $S(Q)$.

Inelasticity effects, experimentally, cause neutrons to either arrive earlier or later to the detector than they would have if the scattering was purely elastic. In the absence of multiple scattering and attenuation, the measured structure factor, $S_M(Q)$ is related to $S(Q)$ by the following equation.

$$S_M(Q,\theta) = S(Q) + P(Q,\theta) \tag{1.44}$$

where $P(Q,\theta)$ is the inelasticity or Placzek correction and is a function of the momentum transfer Q as well as the angle θ at which the neutrons are detected. Practically the Placzek correction is the difference between the static approximation, $S(Q)$ and the measured differential scattering cross-section. In order to determine $P(Q,\theta)$ exactly, $S(Q)$ must be accurately known and as is obviously the case in diffraction experiments this is not possible or the experiment would be merely superfluous. Moreover, inelasticity effects are present in both the distinct and self-scattering components of the measured differential scattering cross-section and using equation 1.36 can be written as

$$\frac{1}{N}\frac{d\sigma}{d\Omega} = \sum_{i,j=1}^{n} c_i c_j \bar{b}_i \bar{b}_j \left[\left(A_{ij}(Q) - 1\right) + P_{ij}(Q,\theta)\right] + \sum_{i=1}^{n} c_i \bar{b}_i^2 \left[1 + P_i(Q,\theta)\right] \tag{1.45}$$

and as such the Placzek correction must be applied to both distinct and self-scattering terms in order to obtain an accurate $S(Q)$ or as in the case in equation 1.45, accurate partial structure factors. In the case of the interference term, it is normally not possible to evaluate the inelasticity effects which are expected to be small.[14,58,59]

For neutron diffraction experiments on liquids containing light atoms such as hydrogen or deuterium, as is the case with much of the data presented in this thesis, there are further difficulties due to the presence of hydrogen, either stoichiometrically or, as an impurity.

The scattering cross-section that arises from a neutron diffraction experiment is simply the integral of the differential scattering cross-section at a particular wavelength summed over all angles of detection as is shown in equation 1.32. In the static approximation, and after the employment of the Placzek correction, the scattering intensity measured should be exactly proportional to the concentrations of the atoms present in the samples and the bound coherent scattering lengths of these atoms. In reality, the measured intensity deviates from the values for the bound coherent scattering lengths and is different depending on the angle of detection and the wavelength in question. For many systems this is calculable but with light atoms, in particularly hydrogen, this is difficult to calculate.

The differential scattering cross-section measured for samples containing hydrogen and deuterium "fall' or drop off in intensity at higher values of Q, the shape of which is dependent on the nature of the sample itself, the energy of the neutron probe and whether or not the neutrons are TOF neutrons or monochromatic neutrons. In these cases, the differential cross-section measured for a deuterium or a hydrogen containing sample, the effective value for b is somewhere between the bound coherent scattering length and the unbound or "free" coherent scattering length and the value of b deviates from the bound scattering length to the largest degree with high energy neutrons. At high energies the actual coherent scattering length observed can be approximated by

$$b_{effective} = \left(\frac{M}{M+1}\right)^2 b \qquad (1.46)$$

where M is the mass of the nucleus and for hydrogen the bound coherent scattering length observed is approximately 25% of that calculated and for deuterium 44%, indicating a large fall in the differential scattering cross-section observed. An example of this is shown in figure 1.6 for $0.9FSO_3H{:}0.1H_2O$ and $0.9FSO_3D{:}0.1D_2O$ for two different detector banks on GLAD. This light atom effect, in addition to the inelasticity effects, must be corrected for in a deuterated or hydrogenated sample in order to obtain $S(Q)$.

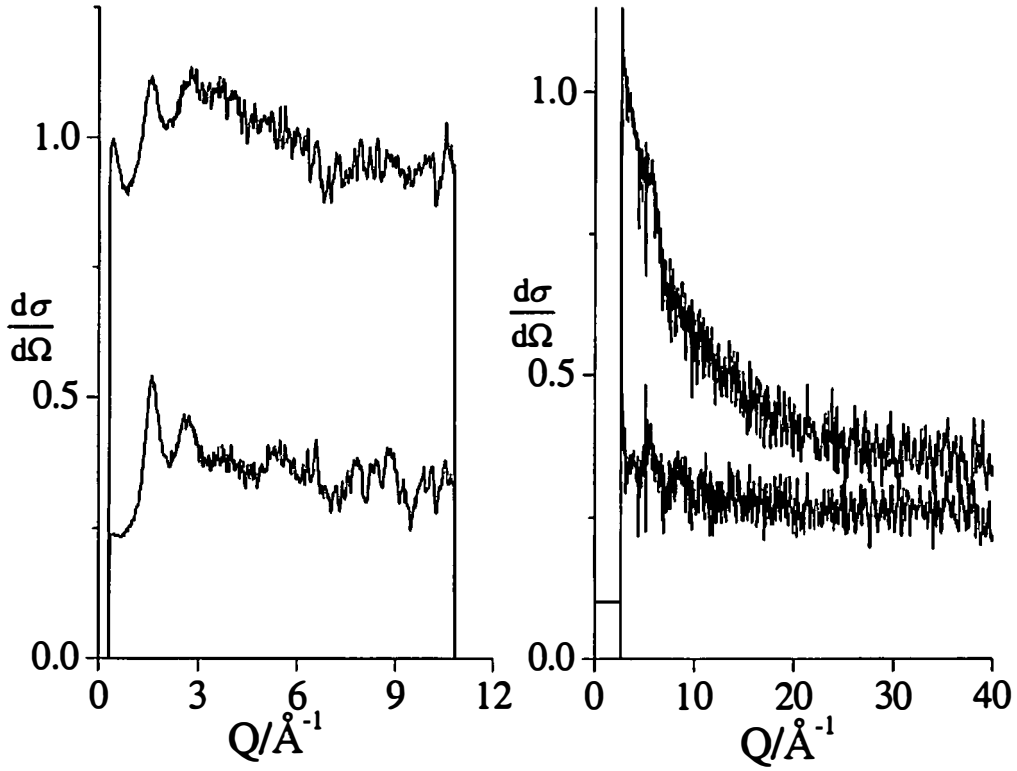

Figure 1.6: Differential scattering cross-section for $0.9FSO_3D:0.1D_2O$(bottom) and $0.9FSO_3H:0.1H_2O$(top). The left graph shows both data sets measured in the first detector bank on GLAD and the right graphs shows both data sets in the nineteenth detector bank on GLAD. $0.9FSO_3H:0.1H_2O$ data is scaled by 0.1 in right graph for clarity.

1.10 INSTRUMENTATION FOR LIQUID DIFFRACTION MEASUREMENTS USING NEUTRONS

To accurately measure a diffraction pattern for a liquid, a sufficient range in Q is needed as the scatter is confined to diffuse scatter which have long broad oscillations in reciprocal space. $S(Q)$, measured over a long range of Q, leads to better resolution in real space and a more accurate Fourier transformation. Reactor instruments typically only measure to approximately $Q = 16\ \text{Å}^{-1}$ whereas spallation source instruments extend over larger ranges of Q.

Most TOF liquid diffractometers are equipped with many detector banks at different scattering angles around the sample position. GLAD is typical of this type of instrument and a schematic of GLAD is shown in figure 1.7. GLAD has 19 detector banks covering angles from 125° to -47° where the detector angle corresponds to 2θ. As $Q \propto \sin\theta/\lambda$ the lower angle detectors measure lower values in Q, corresponding to lower energy, longer wavelength neutrons. Each detector bank covers a different range in Q and must be summed together in order to give a single diffraction pattern for the sample measured. Figure 1.8 shows the differential scattering cross section files measured for SiO_2 for each of the 19 detector banks on GLAD.

1.11 PRACTICAL NEUTRON DIFFRACTION DATA ANALYSIS

For each diffraction experiment, in addition to the measured samples, data is measured for the empty container and appropriate sample environment equipment, the empty instrument and a vanadium rod or plate, depending on the geometry of the sample container. For each of these, the raw data is in the form of a number of diffraction patterns, one for each detector, consisting of counts as a function of time of flight. In order to first obtain the differential scattering cross-section, the following steps must be taken[14,58,60]:

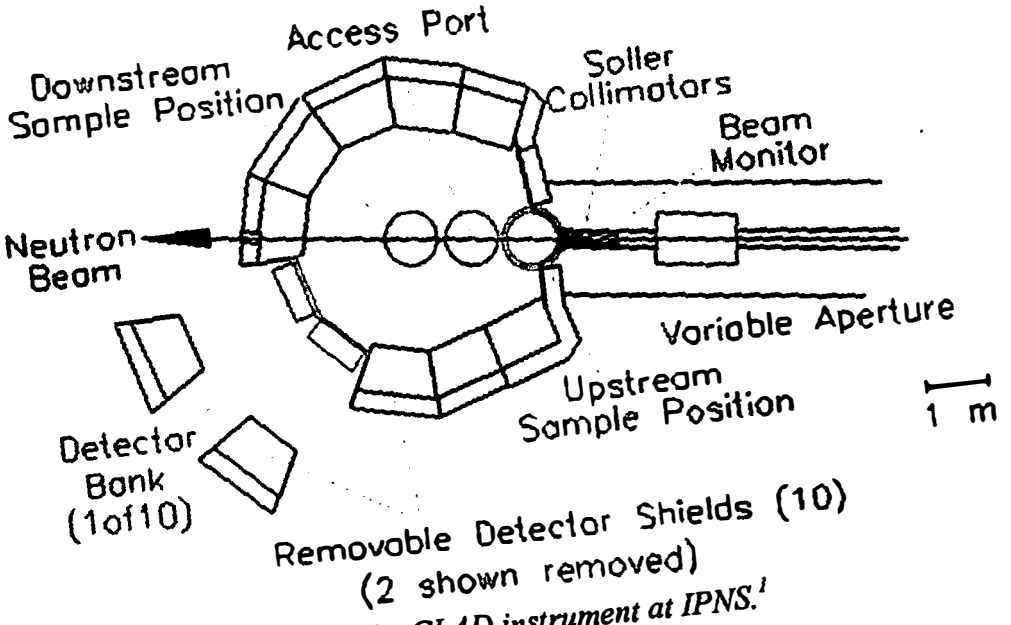

Figure 1.7: Schematic of the GLAD instrument at IPNS.[1]

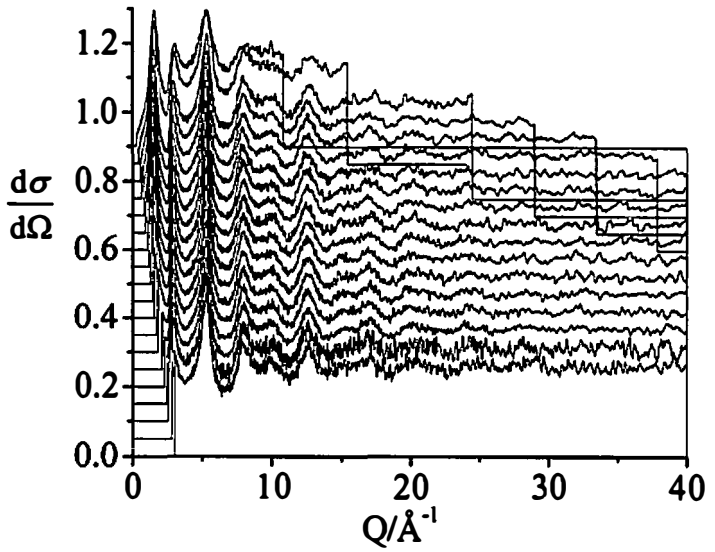

Figure 1.8: Differential scattering cross section files for SiO_2 measured on GLAD. Each detector bank is offset by 0.5 in $d\sigma/d\Omega$ with detector bank 1 at the top of the scale.

1. For each data set data from equivalent detectors are summed and then normalized to the beam monitor count from the instrument. In addition, corrections are made to account for the detector efficiency of the instrument.

2. Each sample and vanadium spectrum is corrected for background and container scattering and attenuation.

3. The vanadium spectra are corrected for multiple scattering and used to put the sample spectra on an absolute scale.

4. The sample spectra are corrected for multiple scattering and absorbance.

5. The inelasticity and self-scattering corrections are applied to the sample spectra expressed as a function of Q and when hydrogen or deuterium are present the sample spectra are corrected for these effects.

6. The different spectra from the different detector banks are combined, producing an experimental $F(Q)$ and thereby the associated pair correlation function in real space through Fourier transformation.

Multiple scattering arises when a neutron interacts with more than one nucleus to produce additional scattering that cannot be correlated to distinct atom positions. The amount of multiple scattering that occurs in the diffraction pattern is dependent upon the nature of the sample. Absorption is also dependent on the elements in the sample while attenuation is dependent on the elements present in the sample as well as those in the sample container. It has been found that while the multiple scattering and absorption effects have a significant Q-dependence, the attenuation coefficient is usually relatively constant with momentum transfer at high energies.[61]

Neutron diffractometers, such as GLAD, are calibrated with a vanadium standard, of an analogous geometry to the sample container, in order to put the measured sample spectra on an absolute scale. Vanadium is used because it has a large incoherent cross-section $(\sigma_V = 5.08 \text{ barns})$ in addition to a very small bound coherent scattering length $(b_V = -0.3824 \text{ fm})$. As incoherent scattering has no angular dependence, the scattering from pure vanadium allows for an accurate calibration of the instrument. Vanadium is used for this purpose as the density is well known and the scattering per atom can be calculated. Attenuation, absorption and multiple scattering can be calculated to a high degree of accuracy and are done so in standard analysis procedures.[14,60] In addition normalization *via* the vanadium calibration standard is achieved directly in the analysis procedures. Multiple scattering and attenuation corrections have been described in detail by Soper and are described in more detail in chapter 6.[62,63]

After steps 1-4 are complete, the differential scattering cross-section is obtained. At this stage in the analysis, it is necessary to complete the self-scattering corrections as well as the Placzek correction and in the case of hydrogen or deuterium containing

samples, a light atom correction in order to obtain the static structure factor, $S(Q)$. The self-scattering as well as the Placzek correction to the self-scattering for many samples with heavier atoms can be directly calculated and is proportional to the scattering cross-section of the sample measured. In the case of light atoms, this cannot be calculated but rather must be obtained empirically.

1.11.1 PLACZEK CORRECTION

In 1952, Placzek showed that for heavy nuclei, the inelasticity correction for a neutron diffraction experiment has a form that is dependent only on the mass of the nucleus, the temperature and the incident neutron energy.[59] Most importantly Placzek showed that at neutron energies higher than the energy states of the sample itself that the inelasticity effects for the interference term are negligible.

Because thermal neutrons have energies that are on the same order of magnitude as dynamical energies in condensed matter, the Placzek correction to the self scattering must be applied as is the case with liquids. There have been several attempts at to modify this procedure for TOF neutrons which usually either involve a power series expansion to express the correction in terms of the moments of $S(Q,\omega)$ where the first few moments are known.[8,14,58,64,65]

The Placzek correction is much larger with low energy neutrons, at high temperatures and with light elements. For most heavy atom systems this correction is easily calculated by standard analysis procedures; however, with samples that contain hydrogen and deuterium, this is not the case.

The light atom effect, which appears in hydrogen and to a lesser extent in deuterium, contributes to the inelasticity observed in the measured differential cross-section data (figure 1.6). For this reason, the Placzek correction for the self-scattering in light atom containing samples is obtained by fitting the differential scattering cross-section data with a Chebyshev polynomial and the subsequent subtraction to create the

interference function, $F(Q)$ for each detector bank.[66] This is shown graphically in figure 1.9 for $0.9FSO_3D:0.1D_2O$, again from two different detector banks on GLAD.

In Figure 1.9, the self-scattering inelasticity correction is estimated by a first order Chebyshev polynomial in each case. For any liquid sample containing hydrogen or deuterium this technique is used to produce the interference function for each detector bank. The banks are subsequently merged together, weighted by the vanadium calibration, to produce a single $F(Q)$ for the entire sample.

1.11.2 Errors in the measured data

Measured $S(Q)$ data using neutron diffraction contain a distribution of distances in reciprocal space which can be described by a Poisson distribution. Random error in a Poisson distribution is defined as the square root of the measured counts and can usually be estimated to be of the same order of magnitude as the scatter of the data points. For this reason no error bars are shown in the data measured in this thesis.

The relative size of systematic errors in the data are more problematic to evaluate, and arise from inaccuracies in the background, attenuation, multiple scattering and the Placzek corrections for liquid diffraction data (as well as other experimental problems). The background error for a liquid sample contained in a polycrystalline or partially crystalline material, mostly appear as sharp peaks or dips in the spectra. This arises from problems occurring from the attenuation of the beam by the sample, leading to a shift of the container Bragg peak position when the sample is present and so manifests itself as additional noise on the measured data.

The Fourier transformation of any measured $S(Q)$ to $G(r)$ contains certain error as $S(Q)$ can never be measured to infinity and there is error generated upon truncation of the data. Experimental measures of $S(Q)$ also contain error arising from the inaccuracies in the absorption, multiple scattering and Placzek calculations. Smoothly varying systematic errors results in unphysical low-r values in the real space Fourier transform.

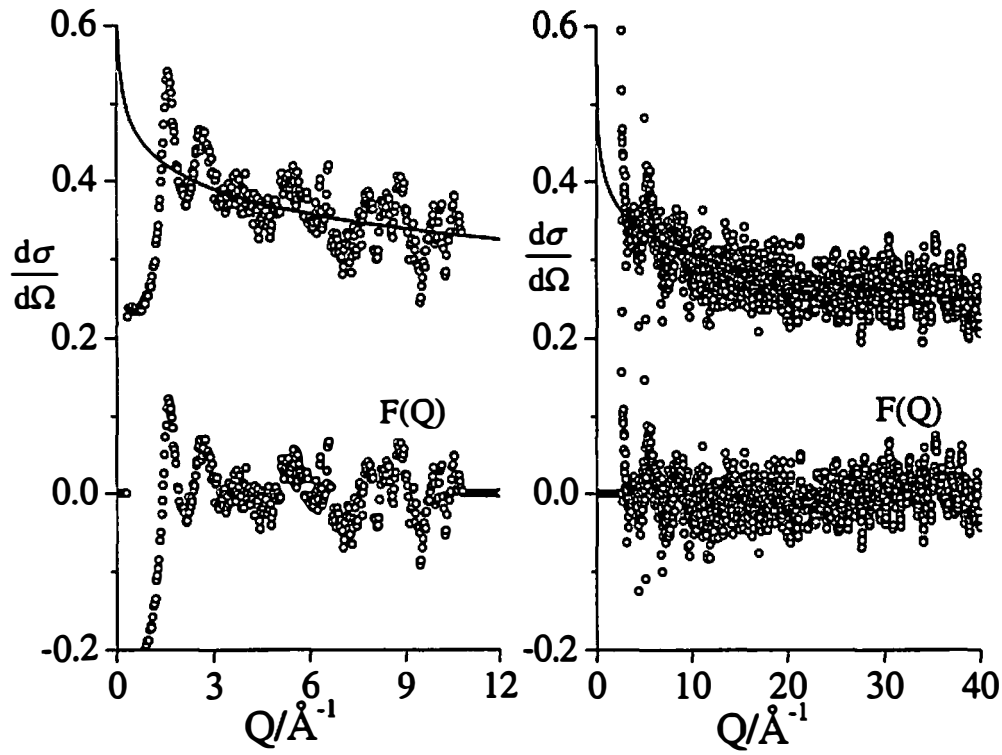

Figure 1.9: Differential scattering cross- section data for $0.9FSO_3D:0.1D_2O$ (circles), the estimated inelasticity correction (line) and the resulting interference function, $F(Q)$. The left graph is the data from detector bank 1 on GLAD and the right graph is the data from detector bank 19 on GLAD

These systematic errors together with Fourier transform artifacts decrease rapidly with increasing r, but may also appear as an additional slope in $G(r)$. In order to minimize these effects, all of the $S(Q)$ data presented in this thesis were Fourier transformed using a Lorch modification function. Error in measured neutron data and its effects to the Fourier transformation are discussed in detail in several sources.[5,6,14,58]

1.12 NEUTRON DIFFRACTION WITH ISOTOPIC SUBSTITUTION (NDIS)

A key advantage of neutron diffraction is that isotopes of the same element exhibit different bound coherent scattering lengths. This allows the extraction of partial structure factors from data measured from isostructural but isotopomeric samples. The structure of any multi-atomic system may be expressed as $\frac{1}{2}(m(m+1))$ partial structure factors, where m is the number of unique atoms in the sample. The total structure factor is the weighted sum of the partial structure factors, and in the case of a many atom system, all partial structure factors contained in one measurement. For example, FSO_3H contains 10 partial structure factors contained in $S(Q)$ for the entire sample. NDIS is a technique by which some, if not all, of the partial structure factors can be isolated and therefore analyzed. One of the most common isotopic substitutions takes advantage of the contrast in scattering lengths between hydrogen ($b_{coh}^{H} = -3.373$ fm) and deuterium ($b_{coh}^{D} = 6.671$ fm). It is possible to isolate only the partial structure factors related to hydrogen by subtraction of two data sets that only differ isotopomerically with respect to the hydrogen site. The subtracted data is termed the first order difference function. For example, in FSO_3H, the first order difference can be taken by subtracting the measured differential cross-section for FSO_3H, $\left(\frac{d\sigma}{d\Omega}\right)_H$, from the measured differential cross-section for FSO_3D, $\left(\frac{d\sigma}{d\Omega}\right)_D$ to obtain ΔS_{HX} where $X = F, S, O, H$. This subtraction eliminates the partial structure factors concerning only the heavy atom positions ΔS_{XX} where $X = F, S, O$. This technique

has been widely applied to diffraction studies of pure liquids and liquid mixtures[66-92] as well as other disordered systems.[93-101]

1.13 HIGH ENERGY X-RAY DIFFRACTION DATA ANALYSIS

The use of high energy X-rays allows for experimental access to a large momentum transfer, $\hbar Q$, range. The 11-IDC BESSRC beam line has one moveable detector that scans from 0.1 to 30 $Å^{-1}$. The incident X-ray beam on BESSRC is monochromated using Si [311] to give $E_{incident} \approx 115\,keV$.

The high energy X-ray data measured must first be corrected for detector deadtime, the radiation polarized out of the scattering plane and the geometry of the detector path in order to obtain $I_X(Q)$. At high energies absorption and multiple scattering are assumed to be negligible in the limit of a small sample size, less than ~6mm, and are therefore neglected. The intensity of the scatter is measured in counts per second. This measured quantity is shown for FSO_3H plus the borosilicate glass container in figure1.10.

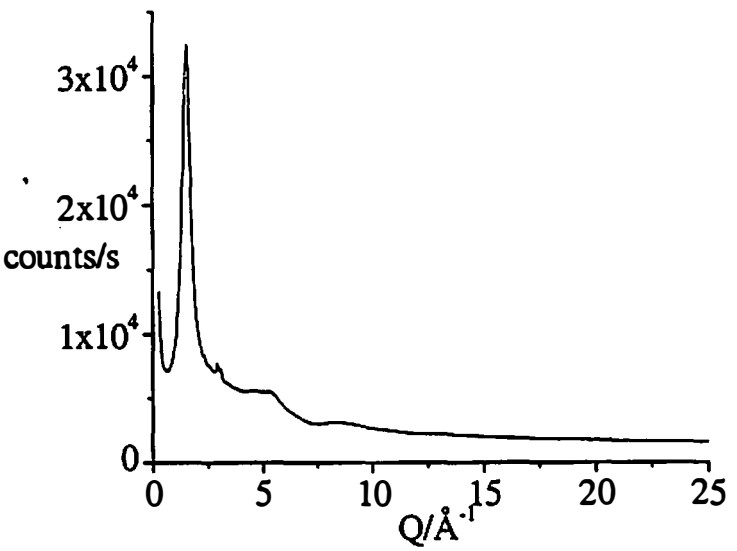

Figure 1.10: Measured intensity for FSO_3H + borosilicate glass container using high energy X-rays.

As is shown in equation 1.43, in order to obtain a pseudo-nuclear function for X-ray scattering, $S_X(Q)$, the measured $I_X(Q)$ must be corrected for Compton scattering for each element as well as being normalized to the concentration weighted form factors for each element. Q dependent form factor and Compton scattering values have been compiled for each by Hubbell *et al.*[29] $S_X(Q)$ for high energy X-ray diffraction is easily obtained with standard analysis procedures using the program ISOMER-X.[102] All of the $S_X(Q)$ data presented in this thesis show representative error bars from 15 to 20 Å^{-1}.

1.14 EXTRACTION OF PARTIAL STRUCTURE FACTORS

Much of the data presented in this thesis is a combination of neutron diffraction measurements and high energy X-ray measurements, used in concert to elicit both the hydrogen positions as well as the heavy atom positions through determination of both the nuclear and the electron distribution in the sample. By taking linear combinations of diffraction patterns, the structure factor equations can be solved explicitly isolating individual structure factors.

In the case of anhydrous hydrogen fluoride, in which there are only two atom types, it is possible to extract all of the structure factors using a combination of high energy X-ray and neutron diffraction measurements. The results of this experiment are discussed in detail in chapter 3, though here the exact subtractions are delineated as an example.

In a neutron diffraction experiment, equation 1.36 can be written for deuterium fluoride as follows

$$F_{DF}^{N}(Q) = c_D^2 b_D^2 S_{DD}(Q) + 2c_D c_F b_D b_F S_{DF}(Q) + c_F^2 b_F^2 S_{FF}(Q) \qquad (1.47)$$

and similarly equation 1.38 as

$$S_{DF}^{N}(Q) = \frac{c_D^2 b_D^2 S_{DD}(Q) + 2\ c_D c_F b_D b_F S_{DF}(Q) + c_F^2 b_F^2 S_{FF}(Q)}{\left(c_D^2 b_D^2 + 2\ c_D c_F b_D b_F + c_F^2 b_F^2\right)} \qquad (1.48)$$

where N signifies a neutron measurement. Upon substitution of the concentration of each atom and the scattering length for D and F equation 1.47 becomes:

$$F_{DF}^{N}(Q) = 0.11126\ S_{DD}(Q) + 0.18859\ S_{DF}(Q) + 0.07992\ S_{FF}(Q) \quad (1.49)$$

and equation 1.48 becomes

$$S_{DF}^{N}(Q) = 0.293\ S_{DD}(Q) + 0.497\ S_{DF}(Q) + 0.21\ S_{FF}(Q) \quad (1.50)$$

Similarly for hydrogen fluoride, equation 1.36 can be written as:

$$F_{HF}^{N}(Q) = 0.03495\ S_{HH}(Q) - 0.1057015\ S_{HF}(Q) + 0.07992\ S_{FF}(Q) \quad (1.51)$$

The first order neutron difference can be taken by subtracting the measured differential cross-section for HF from the measured differential cross-section for DF obtaining $F_{DF-HF}^{N}(Q)$, the first order difference function. This is only possible when the measured isotopomers are structurally equivalent, and exhibit no isotope effect.[91,103-106] This subtraction eliminates the partial structure factor concerning the fluorine-fluorine interaction, $S_{FF}(Q)$, giving

$$F_{DF-HF}^{N}(Q) = 0.07631\ S_{HH}(Q) + 0.29429\ S_{HF}(Q) \quad (1.52)$$

and

$$S_{DF-HF}^{N}(Q) = 0.2059\ S_{HH}(Q) + 0.7941\ S_{HF}(Q) \quad (1.53)$$

High energy X-ray diffraction measurements on both DF and HF give rise to the same intensity and upon numerical substitution for the form factors at $Q = 0$ Å^{-1} equation 1.44 can be written as Å

$$S_{HF}^{X}(Q) = 0.81 S_{FF}(Q) + 0.09 S_{HF}(Q) + 0.01 S_{HH}(Q) \quad (1.54)$$

where the predominant amount of scattering arises from $S_{FF}(Q)$ and the hydrogen-hydrogen interaction is negligible. The atomic form factor curves for the F and H are shown in figure 1.11.

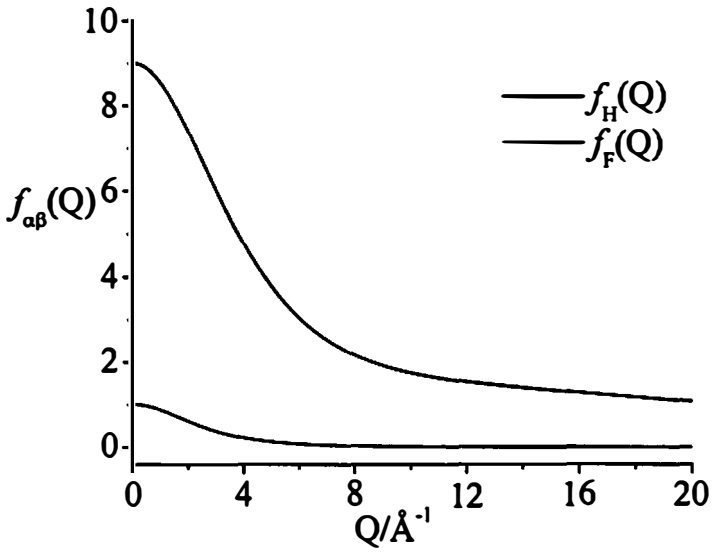

Figure 1.11: X-ray form factors for hydrogen and fluorine.

By taking linear combinations of three simultaneous equations, in this case equations 1.52, 1.54 and 1.56, it is possible to extract each individual partial structure factor and thereby the individual pair correlation functions for this two component system, allowing a complete picture of the liquid to be ascertained.

1.15 COORDINATION NUMBER ANALYSIS

In order to understand the average local structure of a liquid, integration of $g_{\alpha\beta}(r)$ gives the coordination number of atoms α around β atoms between two distances, r_1 and r_2 as

$$n_{\alpha}^{\beta}(r) = 4\pi\, c_{\beta}\rho \int_{r1}^{r2} g_{\alpha\beta}(r) r^2 dr \qquad (1.55)$$

where ρ corresponds to the atomic number density of the sample and c_{β} is the concentration of atom β.

In the case of a pair correlation function which contains only one $g_{\alpha\beta}(r)$, this is most easily obtained by a running coordination number curve. A running coordination

number is the integral over the entire $g_{\alpha\beta}(r)$ function multiplied by the constant seen in equation 1.58. An example of this is shown for the $g_{FF}(r)$ function derived from measurements on hydrogen fluoride in figure 1.12.

In the case of a pair correlation function which contains more than one partial pair correlation function, the coordination number can be obtained by

$$n_{\alpha}^{\beta}(r) = 4\pi\rho \frac{\sum_{\alpha\beta} c_{\alpha}c_{\beta}b_{\alpha}b_{\beta}}{2b_{\alpha}b_{\beta}c_{\alpha}} \int_{r1}^{r2} g_{\alpha\beta}(r)r^2 dr$$

(1.56)

The difference between equation 1.55 and 1.56 is equation 1.55 applies for a function with only contains two atoms, such as $g_{FF}(r)$. In equation 1.56, the total pair correlation function is assessed for only the coordination number with respect to one of the partial pair correlation functions and is only applicable for a peak in the total pair correlation function that corresponds to only one atom-atom correlation.

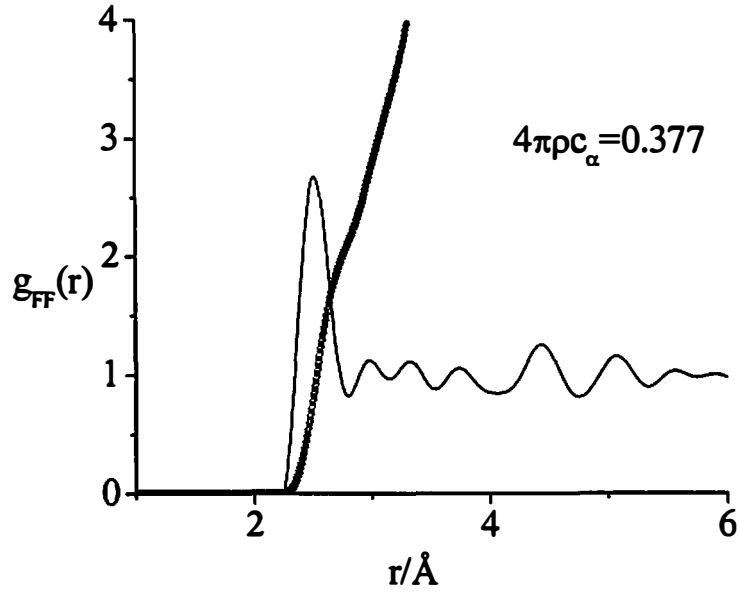

Figure 1.12: FF pair correlation function, $g_{FF}(r)$ and corresponding running coordination number curve.

In practice, the coordination number at any point in *r* is obtained either by integrating over the entire pair correlation function, as is the case with the running coordination number seen in figure 1.12, or by fitting individual peaks in the total pair correlation function with a Gaussian function on order to obtain the area. Both of these methods are used in the work presented here.

PART B: STRUCTURAL ASPECTS OF SUPERACIDS

Superacids are a class of fluids which possess extremely high acidities that far exceed those observed for the strongest aqueous acid systems. Superacids can protonate almost any known chemical bond and as such the normal range of bases are augmented in superacidic media by species such as methane, xenon, hydronium ion and first row diatomic molecules.

The term "superacid" was introduced by R. J. Gillespie to define this class of acids.[107,108] Superacids may then be classed as highly electron poor hydrogen bound systems, in contrast to 'normal' hydrogen bound systems such as water, ammonia and alcohols, which are comparatively electron rich. Sulfuric acid, H_2SO_4, fluorosulfuric acid, FSO_3H, trifluoromethylsulfuric acid, CF_3SO_3H and HF, when anhydrous, are the common molecular superacids. The strength of the acidity in these compounds can be increased by the addition of Lewis acids such as BF_3, SO_3 and MF_5 (M=Sb, Nb, or Ta). In general, superacids are regarded as those which have an acidity greater than or equal to 100% H_2SO_4.

In 1994 George Olah was awarded the Nobel Prize in Chemistry for his investigation of "superelectrophiles" such as carbocations, onium cations, nitronium cations as well as many other electron deficient species which can be formed in superacidic media.[109,110] It is the ability to protonate the C-H bond that gives these fluids their industrial and academic importance. They are used extensively for hydrocarbon management - the isomerization and cracking of petroleum products as well as the investigation of reactive and otherwise transient intermediates in organic chemistry. Although the majority of Olah's work concerns organic reactions in

superacidic media, superacids are also useful as inorganic solvents; they are able to stabilize transition metal oxidation states which are unattainable in aqueous media.[111-128]

In the known solid state structures of superacids and salts of superacids,[127-141] there is nothing to suggest the extraordinary strength of acidity that these fluids display.

The structure of these fluids is a classic example of a light-heavy atom problem, to which the complimentary nature of neutron and X-ray scattering may be applied.

Prior to this work there were very few structural studies on this class of liquids.[142,143] We therefore sought to characterized the pure fluid structures of HF, BF_3 and FSO_3H, before characterizing the structures of solutes in these fluids. This work is therefore comprised of the determination of the structure of liquid HF, BF_3 and FSO_3H, as well as the determination of the structure of the water as a solute in a FSO_3H solvent.

CHAPTER 2: THE STRUCTURE OF LIQUID FLUOROSULFURIC ACID

Part of the work reported in this chapter has been published in the *Journal of Chemical Physics*[144] and is included in its published form the appendix.

All calculations included in this chapter were performed by Dr. R. J. Hinde of the University of Tennessee.

2.1 INTRODUCTION

An overview of the structure of superacids is provided in chapter 1. Here a brief description of fluorosulfuric acid, FSO_3H, is given. Fluorosulfuric acid can be prepared from HF and SO_3 gases to give the liquid at standard temperature and pressure and its physical properties have been investigated in detail by Gillespie.[107]

Lewis and Brønsted-Lowry acid-base descriptions are not always adequate to explain the acidicity observed either in organic solvents or in anhydrous liquids. Indeed, the concept of pH becomes meaningless in some systems such as the protonation of an organic molecule in a pure superacidic solvent. For this reason, the Hammett acidity function, H_0 is used as it can give a comparison between different acidic solvents by protonation of a basic indicator.[145] The bases used are compounds which are usually non-basic in aqueous solution such as trinitrotoluene, trinitrobenzene and dicholorotrinitrobenzene to name a few. The equilibrium between a protonic acid and a base can be written as follows

$$B + H^+ \rightleftharpoons BH^+ \tag{2.1}$$

where the equilibrium constant is

$$\frac{[B][H^+]}{[BH^+]} = K_{BH+} \tag{2.2}$$

and the Hammett acidity function is defined as

$$H_0 = pK_{BH+} = -\lg \frac{[BH^+]}{[B]} \tag{2.3}$$

H_0 is equivalent to pH in aqueous solution. Table 2.1 shows the Hammett acidity functions of anhydrous superacids relative to other anhydrous acids.

Fluorosulfuric acid is the strongest of all complex molecular superacids known, with a Hammett acidity function of H_0=-15.07. The acidity of FSO_3H is increased by ten-fold on the addition of SbF_5 and SO_3-SbF_5.[107] The Hammett acidity function of FSO_3H is comparable with the molecular superacid HF, however the addition of the SbF_5 to HF gives rise to much higher acidities than seen in the SbF_5-FSO_3H system.[111]

Fluorosulfuric acid is a strongly hydrogen bound fluid which is to be expected given the electronegative nature of the ligating atoms around the central sulfur atom. Physically, it is a highly mobile liquid with a liquid range of 253.8 K, this long liquid range being attributable to the hydrogen bonded nature of the fluid. For comparison, the melting and boiling point of sulfuryl difluoride, O_2SF_2, are 137.2 K and 217.6 K respectively - a liquid range of 80.4 K. Table 2.2 lists some physical properties of FSO_3H.

The electrical conductivity of FSO_3H at 298 K is primarily attributable to autoprotolysis of pure FSO_3H

$$FSO_3H + FSO_3H \rightleftharpoons FSO_3H_2^+ + FSO_3^- \qquad (2.4)$$

In the case of the pure liquid the ionic product is $K_{FSO_3H} \cong 4x10^{-8} mol^2kg^2$ and subsequently the concentration of each ion is ~2 x 10^{-4} $molkg^{-1}$.[107] The concentration of ions in pure fluorosulfuric acid is higher than that of HF (chapter 3) but much lower

Table 2.1 Hammett acidity functions for common superacids compared with H_3PO_4 and H_2CO_3.[111]

Acid	$-H_0$	Acid	$-H_0$
FSO_3H	15.07	1:1 FSO_3H:SbF_5	17.3
HF	15.1	1:1 HF:SbF_5	20.9
CF_3SO_3H	14.33	H_3PO_4	5.0
H_2SO_4	11.9	H_2CO_3	2.2

Table 2.2 Physical properties of FSO_3H.[111]

Boiling point/K	435.7
Melting point/K	184.07
Density at 298 K/gcm^{-3}	1.743
Viscocity at 298 K/cP	1.56
Specific conductance at 298 K/ohm^{-1}cm^{-1}	1.805 x 10^{-4}

than H_2SO_4 which is heavily ionized as a pure fluid and contains a variety of ionic species. The evidence of a greater autoprotolysis constant in H_2SO_4 is also reflected in the electrical conductivity constant (1.043 x 10^{-2} ohm^{-1}cm^{-1}).

2.1.1 Gas phase and solid state structure of FSO_3H

The molecular structure for FSO_3H consists of a *pseudo*-tetrahedral sulfur atom ligated by oxo-, fluoro- and hydroxyl ligands and is shown in figure 2.1 with appropriate atomic labels. That FSO_3H is strongly associated is evident in all phases. FSO_3H is strongly dimerized at temperatures as high as 333 K in the gas phase, although measurements at 393 K yielded only monomeric species with no evidence of association.[146]

From infrared measurements on FSO_3H, Savoie proposed that two FSO_3H molecules were associated either by virtue of O-H···F bonds or by O-H···O bonds.[147] The possibility of O-H···F bonds was discounted by Chackalackal *et. al* who stated that

> "*the shift in the S-F stretch to lower frequency as the acid passes from the associated to monomeric state indicates that the fluorine atom is not directly involved in hydrogen bond formation*"[146].

The authors justify this statement by comparison with infrared spectra collected from H_2SO_4, where the shift in the O-H···O stretching frequency from dimerized H_2SO_4 to the monomeric species is increased by 60 cm^{-1}.[148] However, upon careful examination of the FSO_3H infrared data, the S-F stretch is also lowered in frequency from the gas phase to the liquid phase, as are both the asymmetric and symmetric SO_2

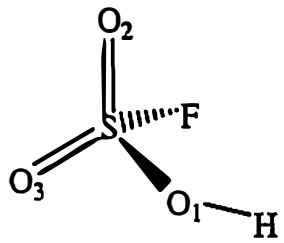

Figure 2.1: The molecular structure of FSO_3H.

stretches. In FSO_3H, the asymmetric SO_2 stretch decreases in the liquid from the monomeric gas measurements by $40cm^{-1}$. In addition the symmetric SO_2 stretch decreases by $13cm^{-1}$ and the S-F frequency decreases by $10cm^{-1}$ while the SO_2 rock and SO_2 bending frequencies remain unchanged from the liquid phase to the gas phase.

Unsurprisingly, it is evident that, in both systems, the stretching frequencies decrease from the monomeric species to the presence of more associated species. However, it is not evident from these measurements that O-H···F association in FSO_3H does not occur. A large shift in O-H···O frequency in H_2SO_4 upon association does not necessarily indicate a shift between associated and non-associated FSO_3H need be of the same magnitude. In light of the shift decrease of S-O and S-F frequencies, it cannot be discounted that hydrogen bonding by virtue of O-H···F bonding or by O-H···O bonding is equally plausible. Moreover, these spectroscopic measurements do not provide a direct structural measurement of the system in question.

The structure of fluorosulfuric acid has been determined in the solid state by X-ray diffraction[132] and is shown in figure 2.2. At 123 K, FSO_3H crystallizes in the orthorhombic space group P $2_12_12_1$ with 4 molecules in each unit cell. In this crystal structure, the heavy atoms (F, S, and O) form slightly distorted tetrahedra which are linked by O-H···O bonds to form infinite chains along the *c*-axis.

Salient bond lengths and angles from the solid state X-ray diffraction of FSO_3H as well as structures that contain the fluorosulfate anion and the bifluorosulfate anion are shown in table 2.3.[125]

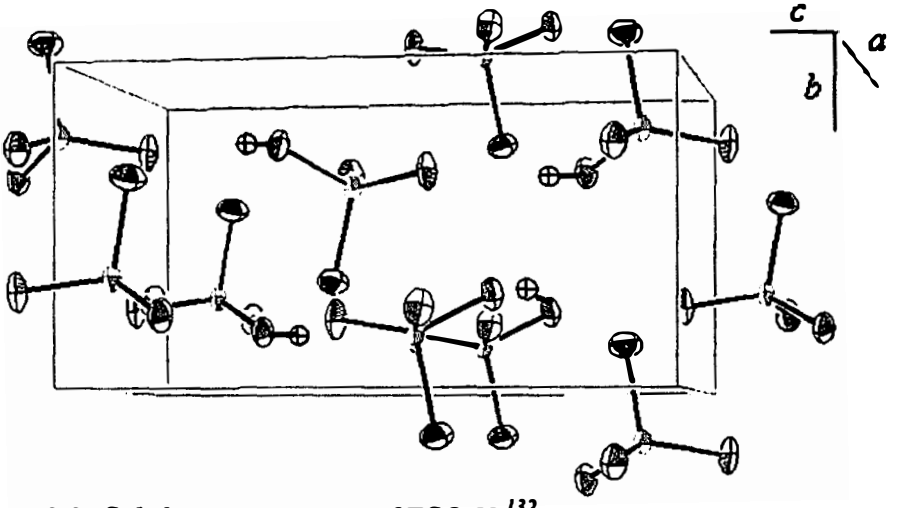

Figure 2.2: Solid state structure of FSO_3H.[132]

Table 2.3: Interatomic distance and angles for fluorosulfuric acid, fluorosulfate and bifluorosulfate.[125,132]

Distances/ Å			
	FSO_3H	$[SO_3F]^-$	$[FSO_3HO_3SF]^-$
r(S-O_1)	1.518(1)	1.458	1.471
r(S-O_2)	1.412(1)	1.437	1.406
r(S-O_3)	1.420(1)	1.436	1.399
r(S-F)	1.540(1)	1.569	1.531
r(O_1-H)	0.63(3)	-	1.210
r(H···O_3')	2.02(3)	-	-
Angles/ ^{0}			
	FSO_3H	$[SO_3F]^-$	$[FSO_3HO_3SF]^-$
O_1-S-O_3	107.2(1)	112.7	113.8
O_2-S-O_3	120.9(1)	113.6	113.0
O_1-S-O_2	113.1(1)	113.6	116.3
O_1-S-F	100.7(1)	102.3	104.8
O_2-S-F	106.6(1)	106.3	105.3
O_3-S-F	106.2(1)	107.8	101.7

It should be noted from table 2.3 that the hydroxyl O-H bond length, $r(O_1\text{-}H)$, is exceedingly short, a determination that is most likely due to the inherent insensitivity of X-ray scattering to the presence of hydrogen. This bond length is shorter than the bond distance seen in H_2 and is almost certainly non-physical. Finding a hydrogen atom in a hydrogen bond is difficult in a conventional X-ray experiment due to the asymmetric nature of the electron density associated with the hydrogen atom position. In addition, the authors measured the crystal encased in a Teflon® capillary, which gives rise to a high background (see chapter 6) which would add to the difficulty of determining an accurate hydrogen positions.

Table 2.3 also shows intra atomic distances from the fluorosulfate anion, $[FSO_3]^-$, and bifluorosulfate ion, $[FSO_3HO_3SF]^-$, as determined by X-ray crystallography where the counter ion in each case is Cs^+.[125] Again, both of these structures show a slightly distorted tetrahedron of oxygen and fluorine atoms around a central sulfur atom.

Until this work, the structure of liquid FSO_3H had not been investigated. Here, neutron and high energy X-ray experiments are presented, elucidating the structure of FSO_3H in the liquid state. In addition Raman measurements and density measurements are reported. This study provides the first direct evidence for the structure of fluorosulfuric acid in the liquid phase.

2.2. EXPERIMENTAL

2.2.1. SAMPLE HANDLING AND PREPARATION

Fluorosulfuric acid is an exceedingly aggressive material and the presence of water will slowly hydrolyze fluorosulfuric acid, liberating HF and forming H_2SO_4 causing glass storage vessels to corrode over time. However, when FSO_3H is pure, it can be easily handled in rigorously dried glassware or in Teflon apparatus. Krytox® LVP grease, a fully fluorinated vacuum grease, was used at all times and minimal contact between the vapor or liquid was ensured, especially at high temperatures, where FSO_3H attacks Krytox®. Burns from fluorosulfuric acid are excruciatingly painful but

can be treated with sodium bicarbonate solutions and prolonged irrigation with water. Face shields and heavy duty butyl rubber gloves were used at all times, in addition to usual laboratory safety measures.

All manipulations of FSO_3H and FSO_3D were carried out under an argon atmosphere or under vacuum on a Schlenk line ($p_{min} < 10^{-2}$mbar). All glassware was flame-dried under vacuum at least four times and allowed to cool under an argon atmosphere. FSO_3H (Allied Chemical Co.) was quadruply distilled under vacuum from H_2SO_4, which has a considerably higher boiling point (603 K), in a 1:1 molar mixture of the two acids. The use of excess H_2SO_4 caused FSO_3H to be impossible to distill as upon heating, oleum was formed (H_2SO_4:xSO_3) and HF was subsequently liberated from the reaction mixture. FSO_3D was prepared by the exchange with D_2SO_4 in a 1:1 molar ratio, where the two acids were stirred with a Teflon®-coated stir bar prior to distillation. The deuteration of FSO_3H has previously been described in the literature,[149] however instead of the recommended single exchange the exchange between D_2SO_4 and FSO_3H was performed four times to ensure maximum deuteration. NMR measurements and neutron analysis *vide infra* revealed that the incorporation of D for H was greater than 99.6%. NMR data were collected either using a 400 MHz Bruker Instrument or, using a 300 MHz Varian instrument. The spectrum of pure FSO_3H is shown in figure 2.3. As there is only one proton present in the system, a single peak appears at $\delta = 10.95$ ppm. In this spectrum no solvent peak is present as the spectrum was acquired only on the pure fluid without a lock solvent or an internal standard. The known literature value for FSO_3H is $\delta = 10.47$ ppm at 298 K relative to TMS.[150] The ^1H spectrum for pure FSO_3D is not shown as no peaks were present.

2.2.2 RAMAN MEASUREMENTS

The purity of FSO_3H with respect to water content was assessed by Raman spectroscopy. The Raman data are shown in figure 2.4. The spectra recorded from pure FSO_3H at 298±2 K were in good agreement with previous measurements.[151]

There are nine fundamental vibrations for the heavy atoms present in FSO_3H,

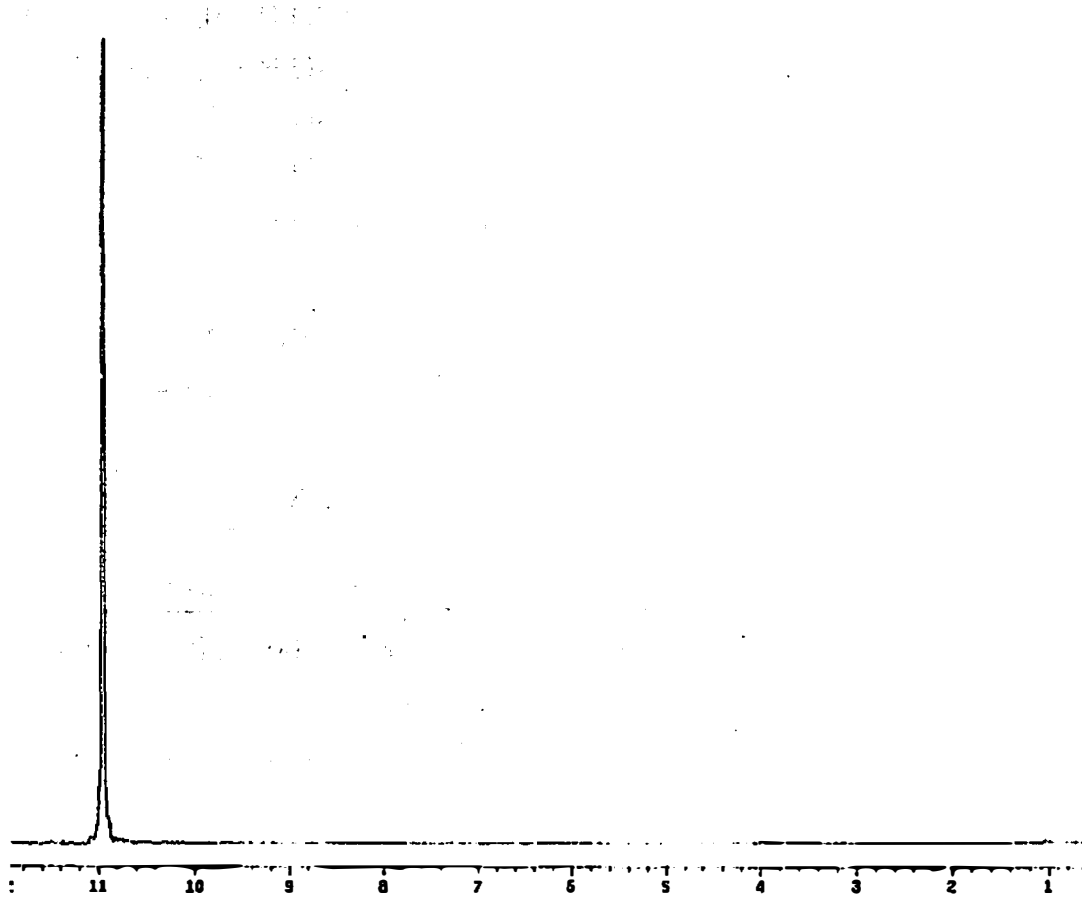

Figure 2.3: ^{1}H NMR spectrum for FSO_3H.

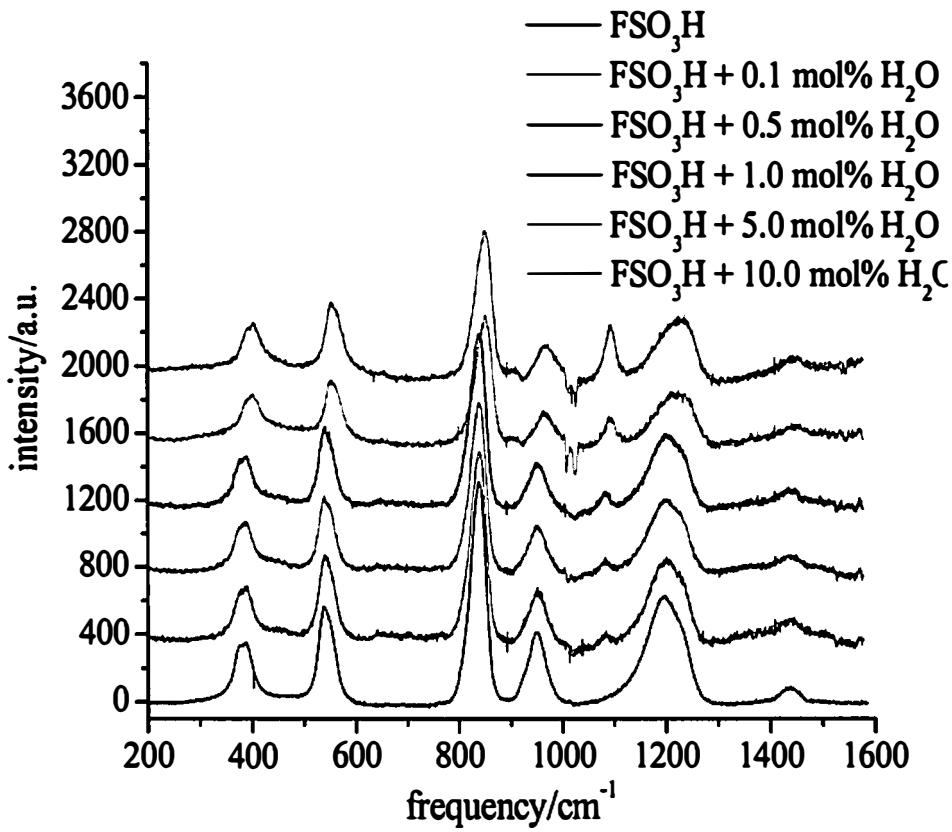

Figure 2.4: Raman spectra for FSO_3H and FSO_3H with varying amounts of H_2O added.

these are listed in table 2.4. In addition, there are three O-H vibrations present, though the O-H stretching modes, estimated to appear at ~3000 cm^{-1} were not distinguishable as FSO_3H exhibited a high fluorescent background. The peak assignments for the pure FSO_3H spectrum are shown in table 2.4.[151]

In addition to the measurement of FSO_3H, varying molar concentrations of H_2O were added to the pure fluid in order to determine the effects of known quantities of water to the Raman spectrum. Figure 2.4 also shows the Raman spectra for pure FSO_3H and FSO_3H with the addition of 0.1 mol % H_2O, 0.5 mol % H_2O, 1.0 mol % H_2O, 5.0 mol % H_2O and 10 mol % H_2O.

With the addition of 0.1 mol % H_2O, a new vibrational peak appears at 1080 cm^{-1}, and the peak intensity continues to increase at higher water concentrations as shown in figure 2.4. At the same time, the peaks corresponding to the O-H bend, the S-OH stretch, the S-F stretch and the SO_2 symmeteric and asymmetric stretches in pure FSO_3H decreased in intensity. In a solution of FSO_3H, H_2O is fully protonated, thus the decrease in the O-H bend and S-OH stretch seen in the spectra are likely due to the loss of a proton from fluorosulfuric acid. The S-F stretch and the SO_2 symmeteric and asymmetric stretches also decrease in intensity, implying that the hydrogen bonding present in pure FSO_3H has been perturbed.

Peak position/ cm^{-1}	Possible vibrational assignment
388	O-H torsion S-F wag
537	SO_2 bend SO_2 rock S-O wag
837	S-F stretch
950	S-OH stretch SO_2 sym. stretch
1196	O-H bend
1436	SO_2 asym. stretch

Table 2.4: Observed Raman frequencies and peak assignment for FSO_3H at 298±2 K.[151]

Assessment of this peak afforded a determination of the quantity of H_2O present in the neutron samples. In order to determine this, the area of the 1080 cm^{-1} peak was determined for each water containing sample. The peak area compared to the molar concentration of water is shown in figure 2.5 and extrapolation shows the mol % H_2O present in FSO_3H neutron samples to be below the detection limit of these spectra. All Raman spectra were acquired on a Dilor XY Raman spectrometer (Instruments S.A., Inc, Edison, NJ) using a 514nm Rayleigh line.

2.2.3 DENSITY MEASUREMENTS

In order to accurately determine the density of FSO_3H at low temperature, a glass pychnometer was constructed from borosilicate glass for use on a glass high vacuum line ($p_{min} < 10^{-5}$mbar). Borosilicate glass has a significant coefficient of thermal expansion and therefore must be calibrated in order to ensure accurate measurements. The pychnometer was standardized using anhydrous methanol (CH_3OH), which has a well-known density,[152] in order to extract a correction factor to account for the changes due to the pychnometer itself. This was subsequently applied to the measured density of FSO_3H to determine the actual density of FSO_3H. The

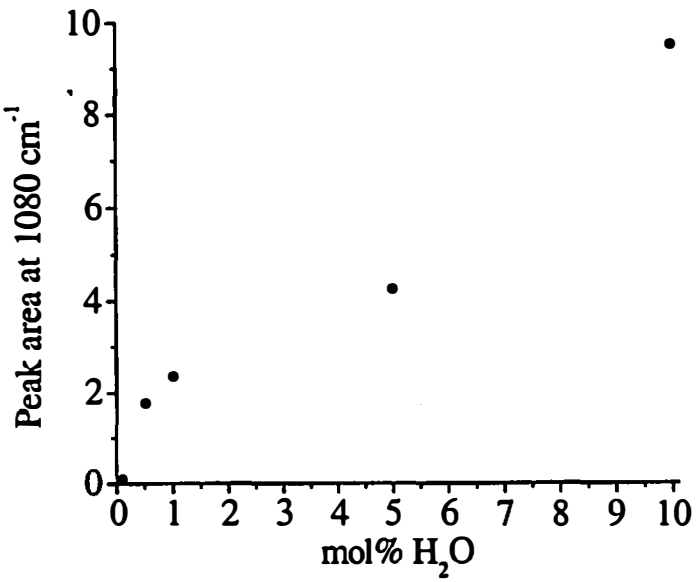

Figure 2.5: Peak area versus H_2O concentration in FSO_3H.

density of both CH_3OH and FSO_3H were measured at several different temperatures using a variety of cold slush baths.

In Figure 2.6 the raw corrected data for methanol and FSO_3H are shown. The corrected density for protio-fluorosulfuric acid yielded values of $\rho = 1.743$ gcm^3 and $\rho = 1.891$ gcm^3 at 300 K and 193 K respectively.

2.2.4 NEUTRON MEASUREMENTS

Samples for neutron diffraction were prepared by distilling FSO_3H and FSO_3D into SiO_2 tubes (0.4cm ID, 0.5cm OD). Each sample was flame-sealed under vacuum to give a sample volume of approximately 0.478 cm^3. The small sample thickness minimizes multiple scattering effects due to the large amount of incoherent scattering from hydrogen. In addition, both tubes were blown from the same cane of tube to ensure that their wall geometries were virtually identical in order to minimize systematic errors in the difference experiments. The small error between the quartz

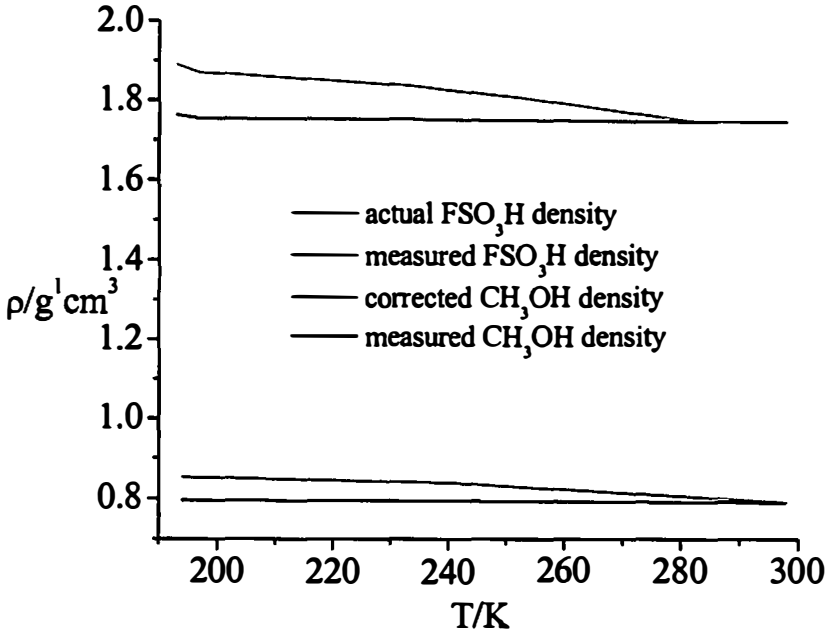

Figure 2.6: Density measurements for CH_3OH and FSO_3H.

tubes was additionally checked by comparison of the calculated intramolecular scattering contribution to the measured data. Both neutron differences agreed to within 5% to the expected intramolecular nearest neighbor atoms, *vide infra*.

Data sets were collected for both FSO_3H and FSO_3D at 300±2 K and at 193±2 K. The neutron diffraction data were corrected for container scattering, attenuation, multiple scattering and inelastic scattering using standard analysis procedures which are described in detail in chapter 1.[14] Given that isostructurality between both isotopomers is assumed for the subtraction method to be applicable, the density values for protio-fluorosulfuric acid were used for all the data corrections.

2.2.5 HIGH ENERGY X-RAY MEASUREMENTS

High energy x-ray diffraction data from FSO_3D and FSO_3H were measured at 300±2 K. These data were corrected for detector efficiency, instrumental geometrical effects, polarization, empty container scattering and subsequently normalized to the sum of the atomic form factors plus Compton scattering to yield a pseudo-nuclear structure factor.[102] The corrections for high energy X-ray diffraction measurements are described in detail in chapter 1.

X-ray experiments were performed on both of the isotopomers at the same state conditions and showed no significant isotopic quantum effect, within the limits of experimental error (~1%), supporting the use of the isotopic substitution technique in neutron diffraction in this case.

2.2.6 DFT CALCULATIONS

In order to analyze the various pair correlation functions determined in these diffraction experiments, the structure of a single fluorosulfuric acid molecule was calculated using density functional theory (DFT) calculations at the B3LYP/aug-cc-pVDZ level of theory using the Gaussian 98 package.[153] In addition the monomer was calculated by the same program at the MP2/aug-cc-pVDZ level of theory which incorporates interactions between electrons.

The distances and angles for these calculations are shown in table 2.5 with respect to the atomic positions in figure 2.1. In addition, fluorosulfuric acid dimers were also calculated using DFT at the B3LYP/aug-cc-pVDZ level of theory the results of which are discussed in detail below.

2.2.7 EXPERIMENTAL DATA

The total measured neutron structure factor for FSO_3D, $S_T^N(Q)$ at both temperatures is shown in figure 2.7. The pseudo-nuclear functions, $S_T^X(Q)$, from the high energy X-ray data for both the FSO_3H and FSO_3D data are shown in figure 2.8.

The total pair correlation function for FSO_3H, $G_T^A(r)$ where A is the radiation source used, can be written as:

$$G_T^A(r) = \sum_{\alpha,\beta} a_{\alpha\beta}^A g_T(r) = a_{HH}^A g_{HH}(r) + 2a_{HF}^A g_{HF}(r) + 2a_{HS}^A g_{HS}(r) + 2a_{HO}^A g_{HO}(r) + 2a_{SO}^A g_{SO}(r) + 2a_{SF}^A g_{SF}(r) + 2a_{OF}^A g_{OF}(r) + a_{OO}^A g_{OO}(r) + a_{FF}^A g_{FF}(r) + a_{SS}^A g_{SS}(r) \quad (2.5)$$

Table 2.5: Interatomic distance and angles for FSO_3H calculated by DFT.

Distances/ Å		
	MP/aug-cc-pVDZ	B3LYP/aug-cc-pVDZ
r(S-O_1)	1.628	1.629
r(S-O_2)	1.456	1.463
r(S-O_3)	1.465	1.455
r(S-F)	1.636	1.636
r(O_1-H)	0.977	0.974
Angles/ ^{0}		
	MP/aug-cc-pVDZ	B3LYP/aug-cc-pVDZ
S-O_1-H	106.8	107.9
O_1-S-O_3	107.2	107.4
O_2-S-O_3	125.8	125.4
O_1-S-O_2	110.3	110.2
O_1-S-F	97.6	97.8
O_2-S-F	106.6	105.9
O_3-S-F	105.7	106.6

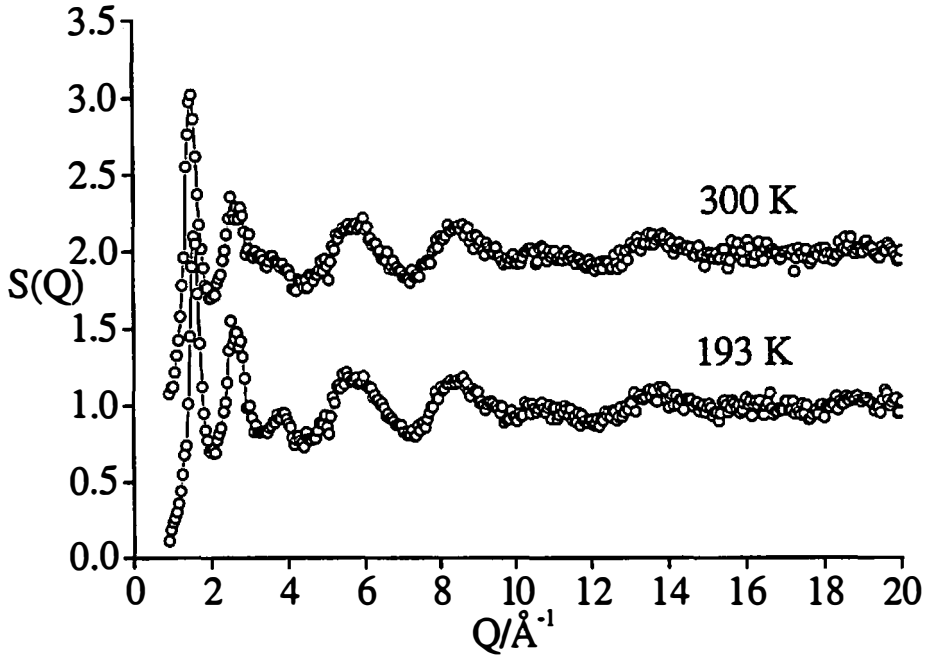

Figure 2.7: Measured total structure factor for FSO_3D using neutrons, $S_T^N(Q)+1$ at 300 K and $S_T^N(Q)$ at 193 K.

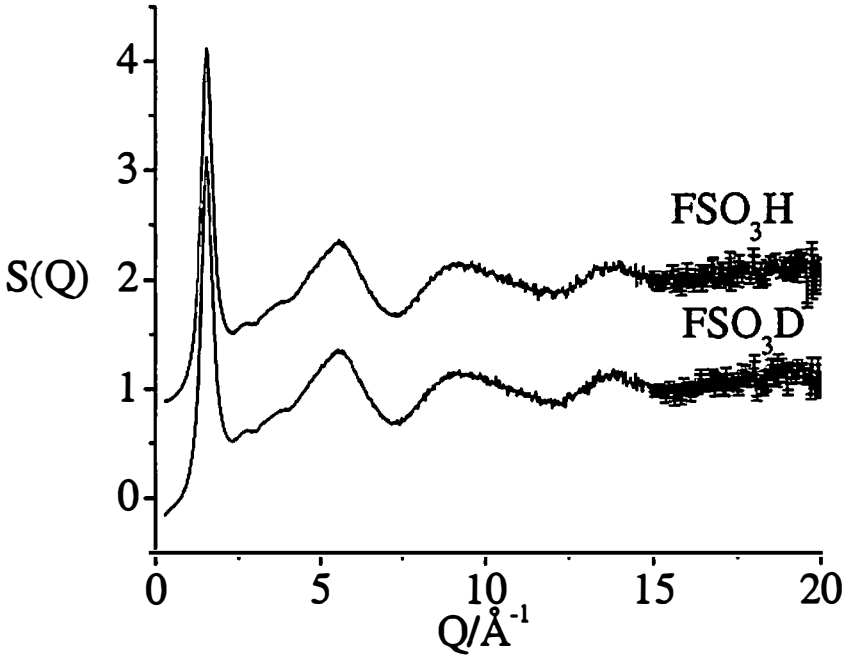

Figure 2.8: High energy X-ray total structure factor measurements for FSO_3H, $S_T^X(Q)+1$ and FSO_3D, $S_T^X(Q)$ at 300 K.

where $a_{\alpha\beta}^{A}$ is the weighting from atoms α and β for radiation source A, where N signifies a neutron measurement and X signifies a high energy X-ray measurement. These constants are listed in table 2.6 for all of the measurements obtained.

$G_T^N(r)$ and $G_T^X(r)$ are the sum of the partial pair correlation functions, although in the case of the high energy X-rays the intensity of the scatter arises mostly from the heavy atom positions.

The total pair correlation functions from the neutron data at the two temperatures measured, $G_T^N(r)$, are shown in figure 2.9.

In this figure the hydrogen distances beyond the intramolecular O-H distance are overlaid with the heavy atom distances, rendering the structure related only to the hydrogen site indistinguishable from the rest of the molecular structure. FSO_3H contains 10 partial structure factors and as such the total pair correlation function contains all intra- as well as inter-atomic positions. From table 2.4 it is clear that the high energy X-ray diffraction measurements essentially measure only the heavy atom positions and $G_T^X(r)$ in this case can be written as

$$G_T^X(r) = 0.96 g_{XX} + 0.04 g_{HX} \qquad (2.6)$$

where X=F, O or S. This formula is given for the values at Q=0 however with X-rays, as discussed in chapter 1, the form factors vary with Q which, is not easily expressed in real space. The total pair correlation function, $G_T^X(r)$, from the high energy X-ray diffraction measurements is shown in figure 2.10.

2.2.8 FIRST ORDER DIFFERENCE FUNCTION AND NULL SCATTERING FUNCTION

In order to elucidate the structure related only to the hydrogen positions, hereafter termed the [H,D] site, independent neutron diffraction measurements for isostructural and isotopomeric samples of FSO_3H and FSO_3D allowed for the first order difference function to be obtained as described in chapter 1. The first order difference function, in this case, only contains the partial structure factors with the respect to the

Table 2.6: Neutron and X-ray weighting factors for FSO_3H and FSO_3D.

	FSO_3D neutron	FSO_3H neutron	X-ray Q=0 Å^{-1}	X-ray Q=1 Å^{-1}	X-ray Q=2 Å^{-1}	X-ray Q=5 Å^{-1}	X-ray Q=10 Å^{-1}
a_{HH}^{A}	0.0123	0.0039	0.028	0.021	0.010	0.000	0.000
a_{HF}^{A}	0.0210	-0.0117	0.500	0.415	0.251	0.028	0.002
$2\,a_{HS}^{A}$	0.0106	-0.0059	0.889	0.717	0.417	0.058	0.004
$2\,a_{HO}^{A}$	0.0645	-0.0361	1.334	1.092	0.6422	0.067	0.004
$2\,a_{SO}^{A}$	0.0275	0.0275	21.334	18.462	12.929	3.965	1.259
$2\,a_{SF}^{A}$	0.0089	0.0089	8.000	7.013	5.055	1.651	0.464
$2\,a_{OF}^{A}$	0.0547	0.0547	12.000	10.679	7.793	1.903	0.456
a_{SS}^{A}	0.0023	0.0023	7.111	6.062	4.193	1.719	0.641
a_{FF}^{A}	0.0089	0.0089	2.251	2.028	1.524	0.396	0.0841
a_{OO}^{A}	0.0842	0.0842	16.000	14.058	9.963	2.286	0.618

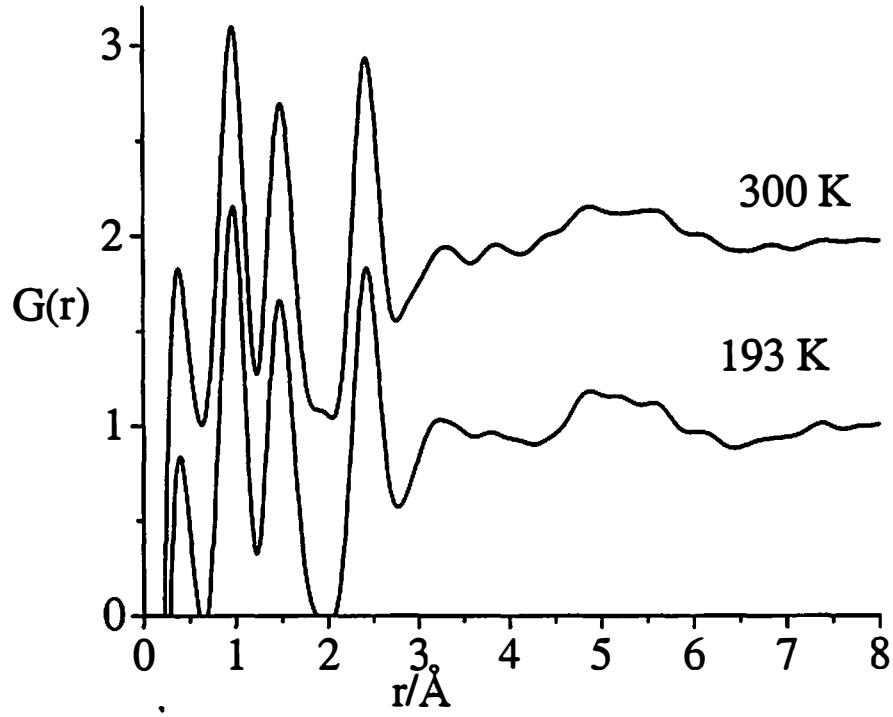

Figure 2.9: Neutron total pair correlation function for FSO_3D, $G_T^N(r)+1$ at 300 K and $G_T^N(r)$ at 193 K.

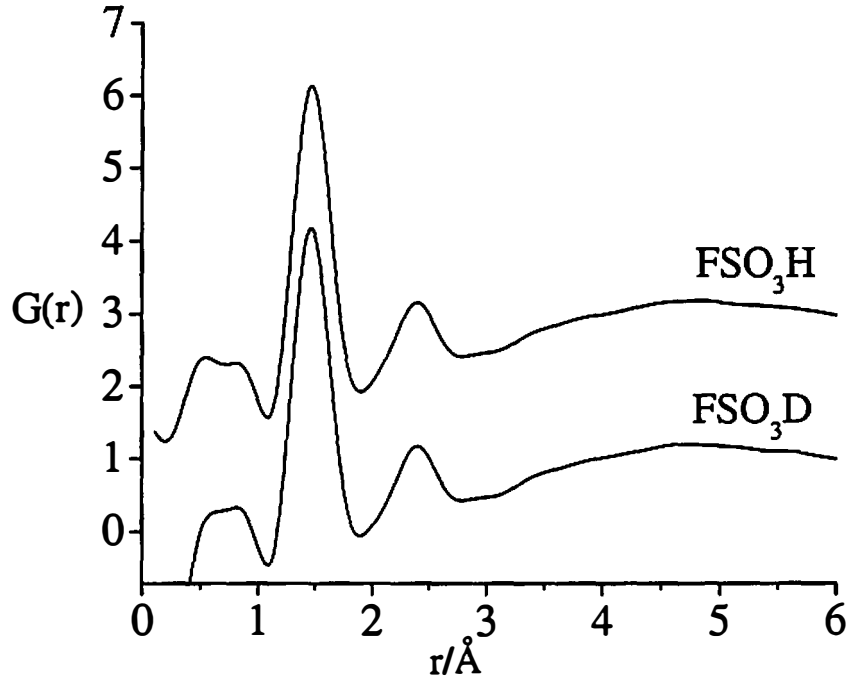

Figure 2.10: High energy X-ray total structure factor measurements for FSO_3H, $G_T^X(r)+2$ and FSO_3D, $G_T^X(r)$.

[H,D] site, namely $\Delta S_{HX}^{N}(Q)$.

The extracted $\Delta S_{HX}^{N}(Q)$ function is shown for both measured temperatures in figure 2.11. The Fourier transformation $\Delta S_{HX}^{N}(Q)$ yields the real space counterpart, $\Delta G_{HX}^{N}(r)$ which shown in figure 2.12. Explicitly, $\Delta G_{HX}^{N}(r)$ may be written as

$$\Delta G_{HX}^{N}(r) = 0.636 g_{HO}(r) + 0.207 g_{HF}(r) + 0.104 g_{HS}(r) + 0.054 g_{HH}(r) \qquad (2.7)$$

The structure factor derived from scattering for all non-hydrogen sites, $\Delta S_{XX}^{N}(Q)$, was extracted from the data by subtraction of $\Delta S_{HX}^{N}(Q)$ from the measured neutron total structure factor for FSO_3D. $\Delta S_{XX}^{N}(Q)$ is hereafter termed the null structure factor and is shown in figure 2.13. The corresponding pair correlation function, $\Delta G_{XX}^{N}(r)$, which contains only information about the heavy atom (S,O and F) positions can be written as

$$\begin{aligned}\Delta G_{XX}^{N}(r) = {} & 0.147 g_{SO}(r) + 0.048 g_{SF}(r) + 0.293 g_{FO}(r) + 0.451 g_{OO}(r) \\ & + 0.048 g_{FF}(r) + 0.012 g_{SS}(r)\end{aligned} \qquad (2.8)$$

$\Delta G_{XX}^{N}(r)$ is shown in figure 2.14 together with the high energy X-ray data for FSO_3H, with each peak labeled as to the information it contains. Both the high energy X-ray data and the null pair correlation function contain the heavy atom positions and as such both show peaks at the same positions.

2.3 Discussion

Data analysis was performed by empirically fitting the $\Delta G_{HX}^{N}(r)$ function at both temperatures with Gaussian functions in order to determine the coordination number as is described in chapter 1.[154] One of the most prominent features in $\Delta G_{HX}^{N}(r)$ (Figure 2.12) is the OH intramolecular peak at 0.98 Å, which has a coordination number of $c_{OH} = 1.11 \pm 0.1$ at 300 K and at 298 K. No reliable estimate for the O-H intramolecular distance could be obtained from the measured X-ray data, scattering associated with the hydrogen correlations only accounts for ~4% of the scattering

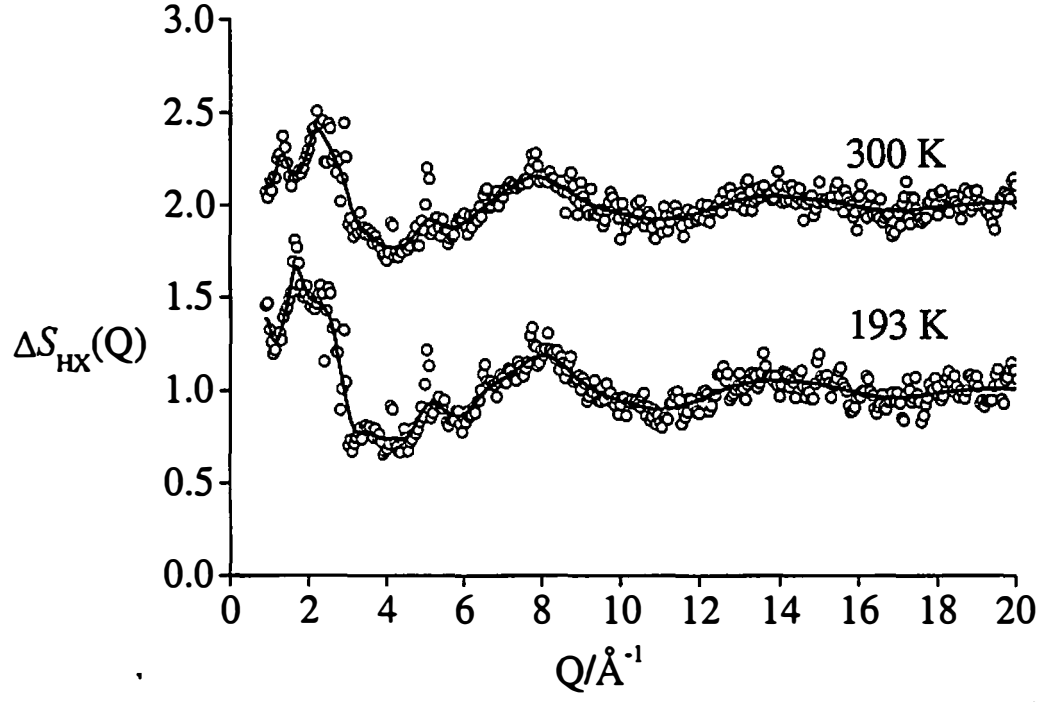

Figure 2.11: Partial structure factor for hydrogen distances in FSO_3H, $\Delta S^N_{HX}(Q)$ +1 at 300 K and $\Delta S^N_{HX}(Q)$ at 193 K. The lines represent the smoothed fit to the data.

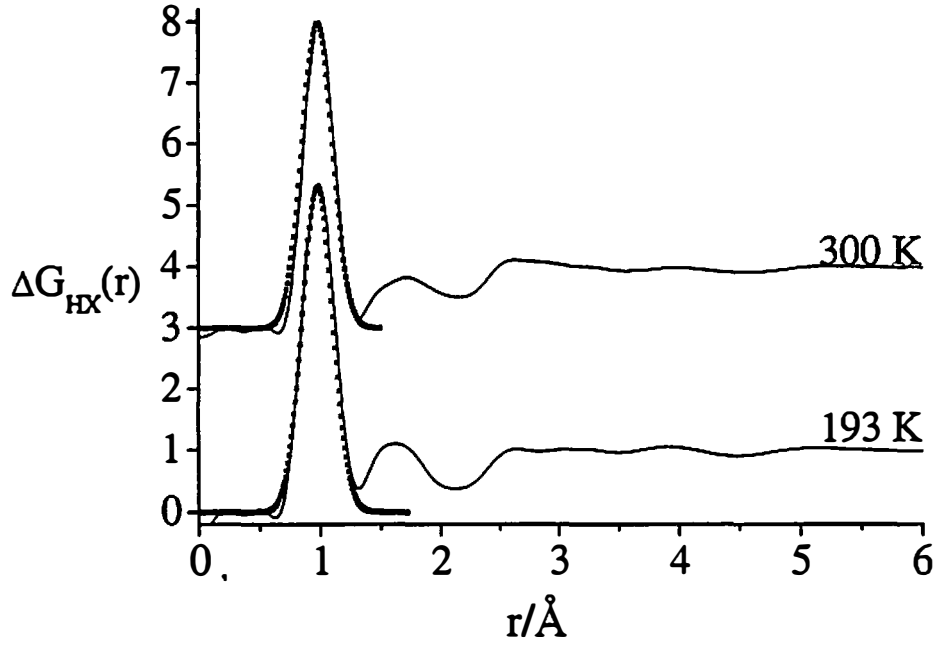

Figure 2.12: Partial pair correlation functions for the hydrogen distances in FSO_3H, $\Delta G_{HX}(r)+1$ at 300 K and $\Delta G_{HX}(r)$ at 193 K. A Gaussian fit to the first peak in r is also shown (see text).

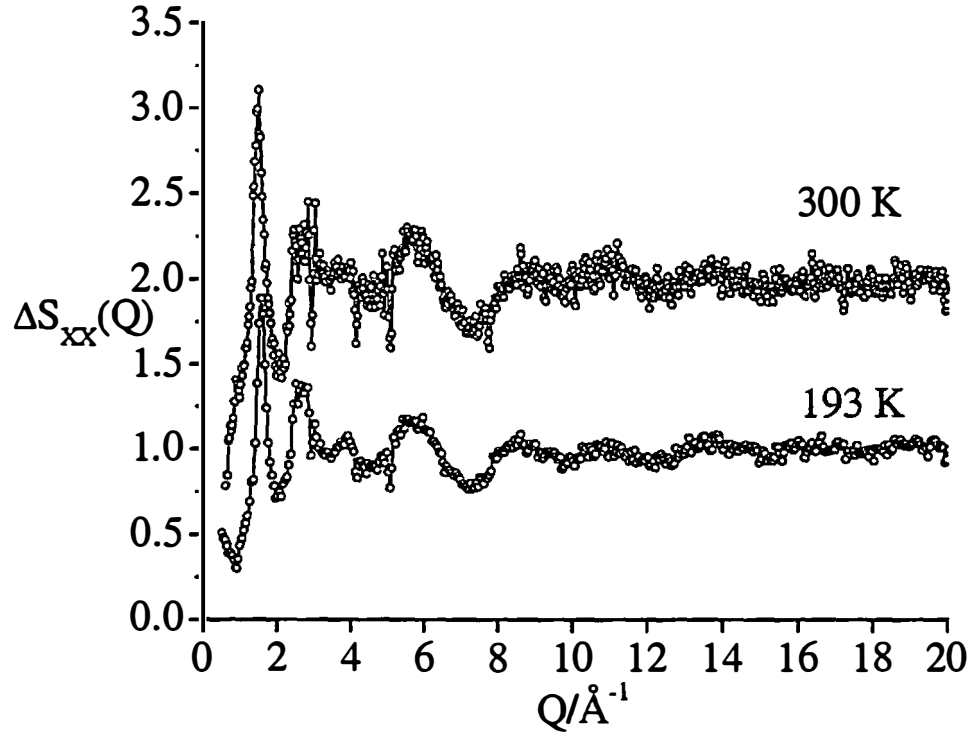

Figure 2.13: Partial structure factor for heavy atom distances in FSO_3H, $\Delta S^N_{XX}(Q)+1$ at 300 K and $\Delta S^N_{XX}(Q)$ at 193 K.

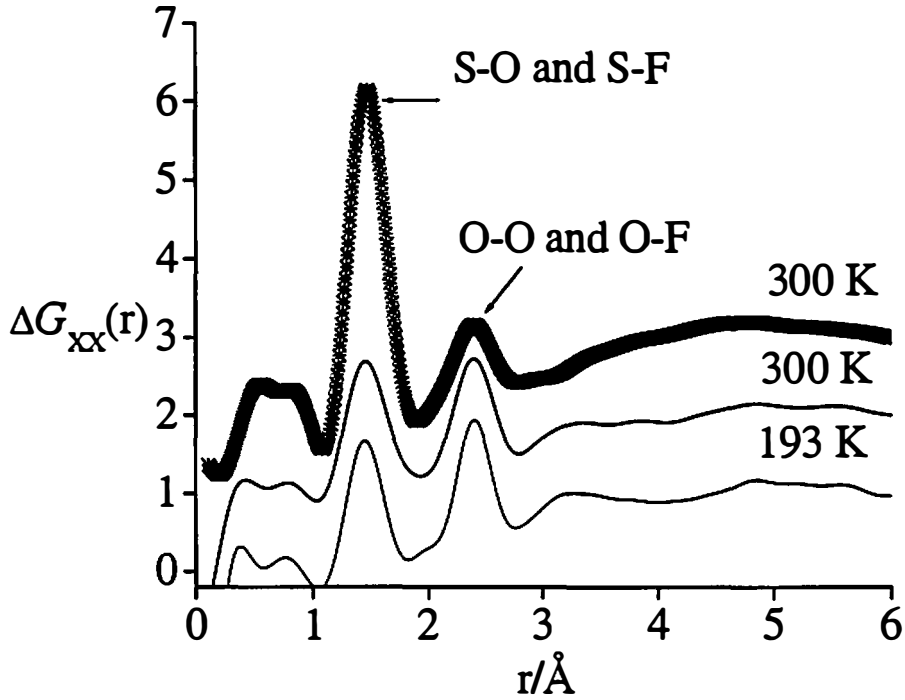

Figure 2.14: Partial pair correlation functions for the heavy atom distances in FSO_3H compared with high energy X-ray total pair correlation function. $G_T^X(r)+2$ *and* $\Delta G_{XX}^N(r)+1$ *at 300 K and* $\Delta G_{XX}^N(r)$ *at 193 K*

intensity.

The solid state values in the literature for intramolecular distances between hydrogen and the heavy atoms in FSO_3H are unreliable as the reported X-ray crystal structure shows the covalent O-H bond to be 0.63Å, which is unreasonably short.[132] On the other hand the solid state X-ray data for the bifluorosulfate anion gives an OH intramolecular distance of 1.210Å.[125] This distance is for a bridging hydrogen and is therefore much longer than would be expected for an O-H intramolecular distance. The position of the first peak in $\Delta G_{HX}^{N}(r)$ is predicted well by both DFT monomer calculations (table 2.5).

The second prominent feature in the $\Delta G_{HX}^{N}(r)$ function is a broader peak at approximately 1.6 Å in each data set which corresponds to the intermolecular hydrogen bond. The solid state X-ray data estimates this distance to be about 2.02 Å, presumably due to the exceedingly short OH intramolecular distance, where this reported distance is considerably longer than most common hydrogen bonds.

At 300 K in the liquid, the hydrogen bonding peak in $\Delta G_{HX}^{N}(r)$ is asymmetric and can be more accurately fitted as the sum of two peaks centered at 1.48 Å and 1.74 Å, showing a 1:4 area ratio with respective coordination numbers of $c_{HX} = 0.15 \pm 0.1$ and $c_{HX} = 0.61 \pm 0.1$ with respect to oxygen or fluorine, as shown in figure 2.15.

It should be noted that the coherent neutron scattering lengths of oxygen and fluorine are very similar and oxygen and fluorine cannot be distinguished in this experiment. At 193 K, where the hydrogen bond peak is sharper, the two Gaussian peaks are centered at 1.48 Å and 1.73 Å and have coordination numbers with respect to oxygen or fluorine of $c_{HX} = 0.31 \pm 0.1$ and $c_{HX} = 0.80 \pm 0.1$ with the areas showing a 1:2.6 ratio. The running coordination number plot is shown in figure 2.16. The 31% increase in hydrogen coordination, calculated from the Gaussian fits and clearly illustrated in the running coordination number plot, provides evidence of a significant increase in the hydrogen bond chain length (and/or chain branching) upon cooling the liquid. The shift to lower *r* upon cooling, and the development of more distinct

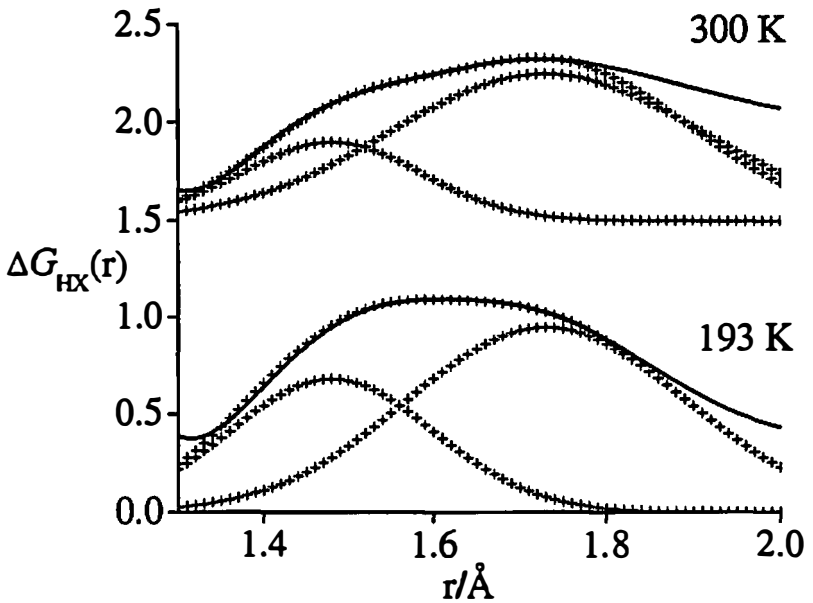

Figure 2.15: Partial pair correlation functions hydrogen bonding distances in FSO_3H. $\Delta G^{N}_{HX}(r)+1$ *at 300 K and* $\Delta G^{N}_{HX}(r)$ *at 193 K*

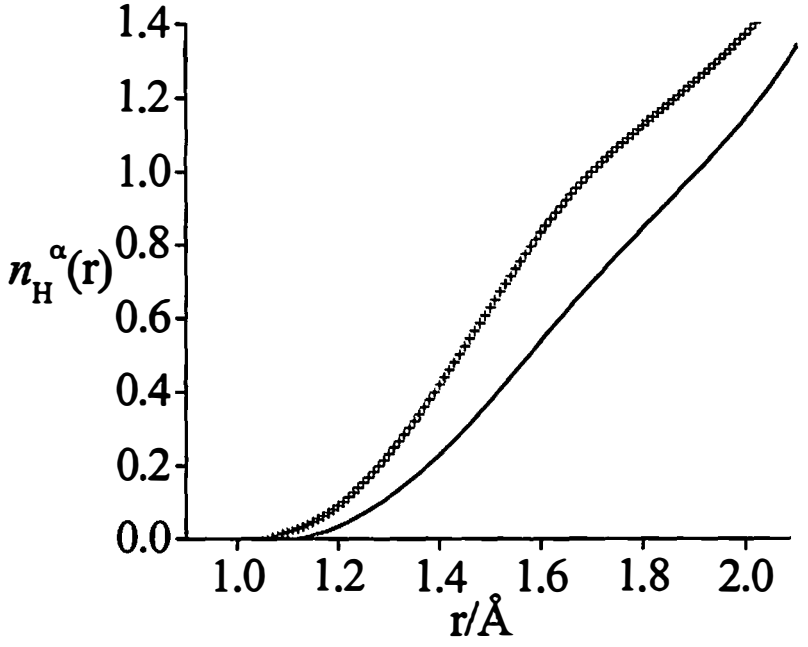

Figure 2.16: Running coordination number curve for FSO_3H first order difference function. The dotted line represents the 193 K data and the solid line represents the 300 K data.

inflection point in the running coordination number (Figure 2.16) is consistent with the presence of stronger, better defined hydrogen bonding structure at the lower temperature.

These results imply that there are two distinct hydrogen bond distances, a phenomenon that does not occur in any other hydrogen bound liquids such as water, methanol or ethanol, in which only one hydrogen bonding atom type is present.[92,152,155] This may be evidence that there are hydrogen bonds to both fluorine and oxygen in the liquid phase. The Raman data shows that the multi-site hydrogen bonding cannot be due to H_2O contamination as shown in figures 2.2 and 2.3.

Hydrogen bonding to both oxygen and fluorine atoms is also supported by B3LYP/aug-cc-pVDZ calculations performed on two sets of fluorosulfuric acid dimers, one bound by virtue of hydrogen bonding between oxygen (OO dimer) and one *via* hydrogen bonds to fluorine (FF dimer). Both dimer configurations are shown in Figure 2.17.

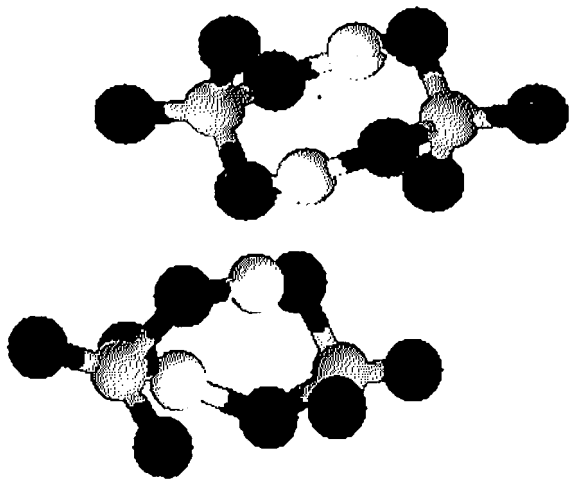

Figure 2.17: OO and FF dimer configurations from DFT calculations. The red atoms are oxygen, white atoms are hydrogen, green atoms are fluorine and the gold atoms represent sulfur.

Both cyclic dimers exist at the B3LYP/cc-pvdz level and give intermolecular hydrogen bonds of 1.65 Å in the case of the O-O dimer and 1.79 Å in the case of the F-F dimer and both give true energetic minima.[156] Both of these dimer configurations were originally proposed by Savoie as possible interpretations for infrared measurements of dimerized FSO_3H in the gas phase.[147] However, as described in section 2.1.1 there is debate about the existence of an FF dimer in the gas phase.[146]

In the reported crystal structure of FSO_3H, linear chains of molecules are bound through S-OH···O=S linkages only.[132] The other heavy atom distances in this structure include $r_{S\text{-}OH}$ = 1.518(1) Å, $r_{S=O}$ = 1.412(1) and 1.420(1) Å and $r_{S\text{-}F}$= 1.540(1)Å. These distances are not atypical, as revealed by a search of the Cambridge Crystallographic data base (CCSD), where the mean distances for these values were found to be 1.54 ± 0.04 Å (S-F) and 1.54 ± 0.05 Å (S-OH) and 1.42 Å ± 0.04 Å (S=O).[157,158] It therefore appears that, from this study in the liquid state, a different hydrogen bonding structural motif is present which is not found in the solid state but may indeed be found in the gas phase.

Because the intermolecular OH bonding peak is better fitted by two Gaussians and the distinct change in the profile of the intermolecular OH bonding peak with temperature, the presence of two possible hydrogen bonding interactions, namely O-H···F and O-H···O is a reasonable conclusion. This evidence is supported by the DFT calculations which show that dimers held together by O-H···F or O-H···O both exist, and show true energy minima. Moreover the hydrogen bonding distances from these calculations, although a different actual configuration than in the measured diffraction data, are noticeably different with the O-H···O hydrogen bond showing the shortest distance of 1.65Å.

That F···H bonding may occur in the liquid structure is not surprising given that fluorine is more electronegative than oxygen. The phase diagrams of the hydrates of the hydrohalic acids are rationalized on the exceptional strength of the hydrogen bond between H and F. The crystalline hydrates of HX (X=Br,Cl) have compositions written as $HX.nH_2O$ (n =1,2,3,4,6),[159] whereas the crystalline hydrates of HF are of the form

$H_2O.mHF$ (m =1,2,4).[160,161] Indeed, the low pK_a of aqueous HF has been attributed to the strong hydrogen bonding interaction between H and F, which leads to the formation of HF_2^- even in the presence of a large statistical excess of water. Also, the strongest hydrogen bond known is between hydrogen and fluorine in the bifluoride ion $[F\text{-}H\text{-}F]^-$, and the strongest known theoretical hydrogen bond is between formic acid and the fluoride ion $[HCO_2H\text{-}F^-]$.[162,163]

Intramolecular distances between pairs of heavy atoms were available from X-ray crystallographic studies as well as from the measured high energy X-ray data. Intramolecular contributions to $\Delta G_{xx}^{N}(r)$ and $\Delta G_{T}^{X}(r)$ were interpreted using distances derived from the X-ray crystal structure data for the fluorosulfate ion, FSO_3^- and the $[FSO_3HO_3SF]^-$ anion (table 2.1), as well as those extracted from the DFT calculations.[125,156]

Although the experimental resolution does not allow for the assignment of individual heavy atom distances, both the high energy X-ray data total pair distribution function, $\Delta G_{T}^{X}(r)$ and the derived neutron heavy atom pair correlation function, $\Delta G_{xx}^{N}(r)$ reveal two common features. First, both show an asymmetric peak with a maximum at ~ 1.47 Å. This peak corresponds to the S-O and S-F intramolecular bonds, and in $\Delta G_{xx}^{N}(r)$ shows a coordination number of $\sim c_{sx} = 4.16 \pm 0.1$ fluorine or oxygen atoms bound to sulfur (figure 2.14) at each temperature. The second peaks in both $\Delta G_{T}^{X}(r)$ and $\Delta G_{xx}^{N}(r)$ are located at ~ 2.41 Å where this peak represents the O-O and F-O distances present in the molecule. In the case of the neutron correlation function this peak gives a coordination number of $c_{xx} = 6.22 \pm 0.1$ with respect to oxygen and fluorine distances at each temperature.

It is interesting to note that at each temperature the neutron pair correlation functions show identical peak maxima with respect to the heavy atom positions (figures 2.9 and 2.14). In addition, upon examination of the high energy X-ray pair correlation function (figure 2.10) all of the heavy atom distances are also consistent. Moreover, none of the heavy atom peaks are asymmetric. All of this suggests equivalent distances

for each S-X (X=F, O) bond in the liquid phase and is inconsistent with the differing distances that appear in the solid state or the DFT calculations (tables 2.1 and 2.3).

Using the peak position from the data presented here the calculated angles between all heavy atoms in the molecule are $O\hat{S}X = 110.1^0 \pm 10^0, X = O, F$, showing a tetrahedral configuration of the molecule. These distances are in accord with the values in the literature,[125] as well as those extracted from the CCSD, specifically cited above for the directly bonded and non-bonded distances respectively. Given that the heavy atom structure of fluorosulfuric acid is essentially unchanged at the two experimental temperatures within the resolution of the experiment, the largest change in the structure of the liquid is due to the change in hydrogen bond structure. Moreover, this change in hydrogen bond structure may be due to a change in mol fraction of molecules bound by O-H···F and O-H···O, as is shown by the change in coordination number for the double Gaussian fits to the intermolecular hydrogen bond peak (figures 2.15 and 2.16).

2.4 Conclusions

The hydrogen bond peak profile in fluorosulfuric acid is asymmetric and the asymmetry varies in temperature. The temperature variation, combined with the changes in the running coordination number, imply that a multi-site hydrogen bonding motif may be present in the liquid. Although, from these measurements alone, the nature of the atoms involved in this O-H···X bond cannot be determined, due to the similarity of the scattering intensity for O and F in both high energy X-ray and neutron diffraction, the presence of O-H···F and O-H···O bonding cannot be excluded. This conclusion supported by DFT calculations, in which O-H···F bonded dimers are shown to be stable at the level of theory used in this work. In addition the heavy atom positions in liquid fluorosulfuric acid are pseudo-tetrahedral to within the accuracy of the measurements presented here, again supporting the conclusion that either O-H···F or O-H···O bonding may be present in the liquid state as fluorine and oxygen atoms are effectively indistinguishable.

CHAPTER 3: THE STRUCTURE OF LIQUID ANHYDROUS HYDROGEN FLUORIDE

Part of the work reported in this chapter has been published in *Angewandte Chemie*[164] and is included in its published form in the appendix.

All RMC calculations were performed by Ms. J. E. Siewenie of Argonne National Laboratory.

3.1. INTRODUCTION

Liquid hydrogen fluoride (HF) is an important chemical and it is widely used in the petrochemical industry, as a catalyst for hydrocarbon management, and in the glass and ceramics industries.[165,166] Academically, its superior properties as a solvent have found application in both organic and inorganic chemistry, and the superacidic properties have been exploited in both disciplines in the study of reactive intermediates and reaction mechanisms as described in chapter 1.[109,111] That these highly desirable properties are not more widely applied is largely due to the exceedingly toxic and corrosive nature of the material,[167,168] which is severe when anhydrous and only somewhat lessened in solution. Hydrofluoric acid is an exceptionally dangerous material to handle; it has a very high chemical toxicity and causes severe and highly dangerous burns in contact with human tissue, even in aqueous solution.[169,170] Anhydrous hydrogen fluoride is even more dangerous due to the high fat solubility and volatility.

HF can be prepared by several different avenues such as by treating AgF_2 with H_2 gas or by the reaction between C_6H_5COF and H_2O.[130,171] It was first prepared in its anhydrous form by Gore and others by heating KHF_2 to "redness" to liberate HF in a platinum apparatus.[172] Industrially it usually is prepared by the reaction between fluorospar (CaF_2) and concentrated H_2SO_4.[173] HF is a superacid with a Hammett acidity function, similar to that of FSO_3H, of $H_0 = -15.1$ as described in chapter 2.

HF, in comparison with the other hydrogen halides, has an anomalously high melting point (189.5 K) and boiling point (292.5 K). In addition HF has a much longer liquid range (103 K) than the other hydrogen halides which are 29.1 K, 21.5 K and 15.9

K for HCl, HBr and HI, respectively, in addition HF exhibits a high heat of vaporization that is not seen in the other hydrogen halides. This is indicative of the strong hydrogen-bonds present in hydrofluoric acid. HF is a volatile liquid at room temperature and has a very high dielectric constant, indicating that the HF molecule is not only strongly associated in the liquid state but that the dipole associated with the HF molecule is locally ordered in the bulk. That the HF bond is very polarized is not surprising given the difference in electronegativity between fluorine and hydrogen, namely $\Delta E_A = 1.78$.[174] Some of the salient physical properties for hydrofluoric acid are listed in table 3.1.[111,173,175-178]

Because the ionic species present in pure HF are complex the self-ionization equation can be written most simply as

$$HF \rightleftharpoons [H_{solv}]^+ + [F_{solv}]^+ \qquad (3.1)$$

where the ionic product is $K_{HF} \cong 5x10^{-13} mol^2kg^{-2}$ and subsequently the concentration of each ion is 7.08 x 10^{-8} $molkg^{-1}$.[179,180] The concentration of ions in HF is much lower than that of FSO_3H and H_2SO_4 (chapter 2). HF also has the lowest electrical conductivity constant and therefore less proton mobility of all the molecular superacids.

3.1.1 SOLID STATE AND GAS PHASE STRUCTURE OF HF

The hydrogen bond is the dominant feature of the structure of HF in all phases. In the gaseous phase the structure of HF is complex and has yet to be unequivocally

Table 3.1 Physical properties of HF.[111]

Boiling point/K	292.5
Melting point/K	189.6
Density at 298 K/g cm^{-3}	0.997
Viscocity at 273 K/cP	0.256
Specific conductance at 273 K/ohm cm^{-1}	~10^{-6}
Dielectric constant at 273 K/ $\varepsilon\ \varepsilon_0^{-1}$	83.6
Dipole moment/ Debye	1.961

determined. Spectroscopic measurements on HF in the vapor phase are consistent with cyclic hexamers and tetramers.[181-184] Moreover, gas phase electron diffraction data are best fit by a mixture of cyclomers, predominately hexamers, as well as monomers at 295 K and 254 K. In these measurements, the mean $F\hat{F}F$ angle was found to be 104° with the average closest F···F distance to be $r_{FF} = 2.535 \pm 0.003$ Å and the second neighbor F···F distance at $r_{FF} = 3.88 \pm 0.06$ Å.[181] In addition the H-F intramolecular distance determined from the electron diffraction data is $r_{HF} = 0.973 \pm 0.009$ Å. In this study the authors note that the fit to the radial distribution function produced by these measurements underestimated the height in the first peak, the HF intramolecular peak by 34 % in the 295 K data and by 23 % in the 254 K data which was believed to imply a longer H-F intramolecular bond that was greater than 1 Å. The results of this study also led authors to believe that there was a possibility that appreciable concentrations of "chain-type" species could exist.[181]

HF, in the solid state, is composed of unbranched, zigzag chains and crystallizes in the orthorhombic space group, $Bm2_1b$.[129,130] The structure of solid HF was first studied by Gunther in 1939, who indexed powder diffraction photographs to give a tetragonal unit cell with nearest neighbor F···F distance of $r_{FF} = 2.7$ Å.[185]

In 1954, Atoji and Lipscomb determined the structure of HF using single crystalline X-ray diffraction.[129] Initial attempts at determining this structure resulted in the determination of SiF_4 as the authors placed the sample in a glass capillary.[186] After finding suitable containment, X-ray diffraction measurements on crystalline HF at 148 K showed the solid state structure to be comprised of infinite zigzag chains with 4 fluorine atoms per unit cell. The electron density associated with the hydrogen site in this structure could not be located and as such the authors chose the space group based on a disordered model where the hydrogen positions could occupy two different positions in the unit cell. For this reason the authors assigned the orthorhombic space group Bmmb. Subsequent spectroscopic measurements on solid HF were in disagreement concerning this result where some predicted a different hydrogen bonding

structure in the solid state.[187-190] The bond distances and angles from this structure are reported in table 3.2.

A later neutron diffraction study on deuterium fluoride (DF) in the solid state showed that at 4.2 K and at 85 K DF crystallized in the orthorhombic space group $Bm2_1b$ with zigzag chains parallel to the b axis.[130] This structure is shown in figure 3.1.

The advantage of neutron diffraction in this case, as described in chapter 1, is the large bound coherent scattering length of deuterium yielding a more accurate determination of hydrogen (or deuterium) position. The distances and angles from the DF at the two temperatures are listed in table 3.2.[129,130] It is notable that the nearest neighbor F...F distance in all of the crystalline structures is essentially invariant with temperature and that the mean value of the three solid state structures, namely $r_{FF} = 2.50 \pm 0.01$ Å is only 0.03 Å shorter than the F···F distance seen in the gas phase.

3.1.2 PREVIOUS STUDIES OF LIQUID HF

The evidence from the macroscopic properties (table 3.1) and the structure in the gas phase and solid state indicates that HF is very strongly hydrogen bound. And indeed the structure of liquid of hydrogen fluoride, like the gas and the solid, has long been known to be complex.[191] Early infrared measurements on HF were thought to indicate a large proportion of polymers present in the liquid that dissociate to monomers

Table 3.2: Distances and angles for HF and DF in the solid state.[129,130]

Distances/ Å			
	DF at 4.2 K	DF at 85 K	HF at 148 K
r(H-F)	0.97	0.95	-
r(H···F)	1.53	1.56	-
r(F-F)	2.50	2.51	2.49
Angles/ ^{0}			
	DF at 4.2 K	DF at 85 K	HF at 148 K
F-H···F	180	180	-
F···F···F	116.6	116.7	120.1

upon the addition of SO_2.[191] This existence of polymers was concluded from a broad peak in the spectra at 3450 cm^{-1} for pure HF, which became sharper upon the addition of SO_2. This conclusion was supported by NMR studies which suggested that HF depolymerized upon the addition of other liquids and when pure upon an increase in temperature as evidenced by a change in chemical shift.[192] In these early studies, only the polymeric nature of HF was suggested; the exact form of these polymers, that is whether they were hexamers, tetramers or chain structures, was not ascertained.

Inelastic neutron scattering studies also predicted that HF exists in a polymeric form in the liquid state. In each of these studies a simple chain structure was predicted.[187,193,194] In later Raman and IR measurements on the liquid, Desbat *et al.* supported the chain model and stated that

> *"the most probable structure for HF at 293 K is zigzag chains with six or seven molecules"*

and that a decrease in temperature led to an increase in the number of HF molecules in the chain.[195] The chain structure model is also consistent with the high dielectric constant and its pressure dependence seen in HF.[175-177] Although all of the

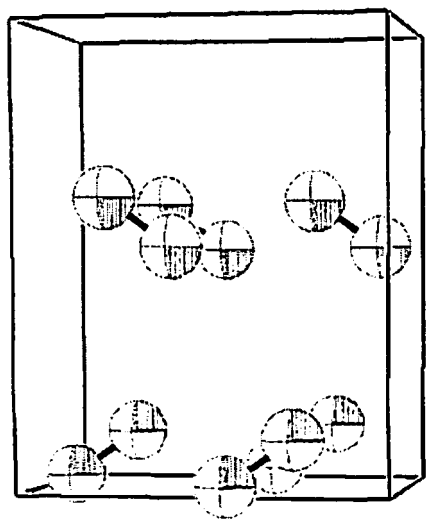

Figure 3.1: Solid state structure of DF at 85 K.[130]

measurements described above support a polymeric structure in the liquid none of these data provide any direct evidence for the structure of HF in the liquid phase.

To date, only two diffraction measurements of the liquid state have been performed on DF using neutrons that give the total structure factor of DF, $S_{DF}^{N}(Q)$. In 1985 Deraman *et al.* first measured the structure of liquid DF at 293 K.[143] More recently, Pfleiderer *et al.* extended this range to two liquid and four supercritical states.[142]

Deraman predicted the structure of HF in the liquid to be polymeric but, as t i[204-207,231]he measurements were confined to the total pair correlation function, the distinction between chains and cyclic polymers could not be ascertained.[143] In this study, cyclic hexamers in the liquid state were favored as the most likely possibility, given their presence in the gas phase, though it was concluded that a more detailed study was needed to distinguish between the two structural possibilities. In addition, the authors noted the underestimation in peak height by the electron diffraction results and thought this might be due to the presence of anomalous protons.[143,181]

In the more recent neutron diffraction study, the total pair correlation function was interpreted as being consistent with $(DF)_n$ chains under normal temperatures and pressures, which forms a very different hydrogen bonding structure as pressure and temperature increase.[142] The actual change in the structure of liquid DF upon the increase of temperature and pressure could not be determined as these changes could only be deduced from peak positions and heights in the total pair correlation functions of the recorded data.

3.1.3 THEORETICAL STUDIES ON THE STRUCTURE OF HYDROGEN FLUORIDE

HF is the simplest archetype for the strong hydrogen bond and the molecular simplicity of this molecule makes it an attractive model for strongly hydrogen bonded systems. In view of the toxic nature of liquid HF it has also been stated that the calculation of its properties is to be preferred over measurement.[196]

The microscopic structure of liquid HF has been the subject of many theoretical investigations.[196-236] Before diffraction data on liquid hydrogen fluoride were available, these simulations were based on either atom-atom (two site) potentials or three site models.[209-211,213-216] Most of these early studies predicted chain-like structures in the liquid, which in most cases the chains were of infinite length. The peak positions from the simulated peak pair correlation functions as well as the coordination numbers from some of these simulations are shown in table 3.3.[209-211,213-216]

In these simulations many of the calculated values differed significantly from the known experimental values for the gas phase dimers on which the models were based. When the results of these simulations were subsequently compared to the total structure factor data on liquid DF, many of the calculated values were found to differ from the experimental values; in particular, most failed to accurately predict H···F intermolecular bond length in the liquid.

Since the appearance of liquid diffraction data for DF, Monte Carlo (MC) and molecular dynamics (MD) simulations of the structure have been performed with a variety of different potentials,[204-207,218,221,227-231] as well as Quantum Mechanics/Molecular Mechanics (QM/MM) models.[219,220,232]

MC simulations performed by Jedlovszky and Vallauri[204-207,231] using both

Table 3.3: Peak positions and coordination numbers for early HF simulations.[209-211,213-216]

	r_{HH} /Å	r_{HF}^{inter} /Å	r_{FF} /Å
HF2	2.3	1.7	2.6
HF3	2.2	1.8	2.7
STO-3G	~2.1	1.6	2.45
6-31G	~2.7	~1.9	~2.6
	c_{HH}	c_{HF}^{inter}	c_{FF}
HF2	2	1	2
HF3	2	1	2
STO-3G	-	1.4	6.9
6-31G	-	1.8	8.8

polarizable and non-polarizable potentials on both the liquid and the supercritical fluid agree reasonably well with the HF dimer but again, do not accurately predict the measured position of the hydrogen bonding peak. In each of these MC simulations, HF is predicted to consist of hydrogen bonded chains in the liquid state.

Parrinello *et al.*[228,229] have employed *ab initio* MD to simulate the structure of liquid HF at various thermodynamic states and predict the liquid structure to consist of bent hydrogen bonding chains of varying length with very little branching at room temperature. Liem *et al.* have also employed MD to simulate the liquid using a quantum electrostatic topological potential (QCT) which is comparable to the *ab initio* MD model only with respect to the HH pair correlation function, $g_{HH}(r)$.[235]

The MD results have been recently corroborated by Muñoz-Losa *et al.* using a QM/MM model.[219] In addition Wierzchowski *et al.* have employed both *ab initio* MC as well as QM/MM to model HF at the different state points reported by Pfleiderer *et al.*[142,232,233]

In contrast to the chain structure seen in most simulations, MD simulations by Yogi predict HF to be dimerized in the liquid,[230] and a combination of MC and MD techniques led Sun *et al.* to also predict clustering in liquid HF.[218] A similar view was also suggested by Karmakar *et al.* by analogy with simulations on tert-butyl alcohol, who noted that the diffraction data on DF indicated clustering even though this was unsupported by most computer simulations at that time.[237]

The fact that most computer simulations have predicted chain structures of some description in liquid HF has led to the theoretical claim that

> *"It is well known that in liquid HF the majority of molecules exist as hydrogen bonded chains"* [208]

even though the detailed structure of the liquid has never been experimentally determined.

One point of discrepancy among all of the simulations is the shape of the FF partial pair correlation function $g_{FF}(r)$; this is discussed in more detail in section 3.3.

Some models predict a peak or a shoulder around 3.2 Å,[206,210,218,219,228] while others do not.[205,216,235] Parrinello *et al.* noted this discrepancy between simulations on liquid HF as evidence that the structural prediction is extremely sensitive to the intermolecular potentials chosen in a simulation.[228] The $g_{FF}(r)$ function appears to be the most sensitive to this phenomena, in comparing simulations, as the $g_{HF}(r)$ and $g_{HH}(r)$ functions remain similar in shape, though not peak position, between the extant computer models.

A summary of the calculated inter- and intra- molecular distances and coordination numbers, where reported, is given in table 3.4 for the computer simulation studies published after the publication of the first diffraction data on liquid DF.

3.2 EXPERIMENTAL

3.2.1 SAMPLE HANDLING AND PREPARATION

In order accurately measure the partial structure factors of HF, high purity isotopic samples of HF, DF and an $[H_{1/2}D_{1/2}]F$ mixture were prepared. HF and DF were prepared on a metal high vacuum line *via* the reaction of H_2SO_4 or D_2SO_4 with dry CaF_2 in a metal bomb under static vacuum. Samples were purified by cryogenic distillation, dried with F_2, degassed, barometrically measured and subsequently transferred into sample cells constructed from Alloy 400. The design of these cells and sample transfer line are described in detail in chapter 6. All of the samples had chemical and isotopic purities of > 99.9% with <0.1% H_2O as confirmed by the neutron measurements presented here, vapor pressure measurements and the purity of the starting materials. The purity of DF was also assessed by vapor pressure measurements at varying temperatures and were found to be in accord with reported literature values.[238,239]

3.2.2 NEUTRON MEASUREMENTS

Neutron diffraction measurements were performed on samples of DF (0.183 moles) and HF (0.0365 moles). DF was measured at 296 K, 286 K, 246 K and at 195 K

Table 3.4: Peak positions and coordination numbers for recent HF simulations.[204,218,219,228,235]

	r_{HH} /Å	r_{HF}^{inter} /Å	r_{FF} /Å
QM/MM	~2.3	1.65	2.5
ab initio MD	2.2	1.6	2.5
Non-polarizable potential MC	2.0	1.5	2.4
Polarizable potential MC	2.5	1.8	2.7
Sun	2.2	1.8	2.7
QCT	2.18	1.53	2.43
	c_{HH}	c_{HF}^{inter}	c_{FF}
QM/MM	2.24	1.00	2.24
ab initio MD	2.2	1.00	2.6
Non-polarizable potential MC	2.2	1.00	2.5
Polarizable potential MC	2.45	1.00	2.25
QCT	2.0	1.0	2.0

and HF was measured at 296 K and at 195 K, where all temperatures were recorded with an error of ± 2 K. The corresponding pressure at the temperatures measured are 1.2 bar, 0.8 bar, 0.1 bar, and ~0 bar, respectively with an error of ±0.1 bar.[184] The neutron data have been corrected for detector efficiency, empty cell scattering, attenuation and multiple scattering using standard methods as described in chapter 1.[14,66] The number density at each temperature for HF at each temperature measured is shown in table 3.5.

In order to enable an accurate background correction for each sample container separate experiments were performed on each of the Alloy 400 cells. In another set of experiments, both of the cells were measured filled with D_2O in order to obtain the correct normalization coefficients for each container and account for slight variations between the cells. The D_2O data were corrected using standard analysis techniques without removing the residual Bragg scatter. In each case, the differential cross section files were assessed to ensure that the interference function oscillated about the predicted self scattering function, indicating that normalization of the can was correct. For the D_2O in DF container, the coordination number of the O-D intramolecular peak was assessed in the total pair correlation function $G(r)$, $c_{DO} = 0.98 \pm 0.10$, to verify the volume of sample in the neutron beam. The D_2O-filled HF container was constrained to give the same level of scatter in the oscillations at high Q as the normalized D_2O in the DF container ensuring a correct normalization of the HF can. By this method a correct sample container thickness was obtained for each individual sample cell and subsequently used to normalize the HF and DF data collected.

Table 3.5: Number density of HF at measured temperatures.

T/K	ρ /atomsÅ^{-3}
296	0.0600
286	0.0600
246	0.0625
195	0.0637

The can normalization led to an unconstrained DF coordination number in the D-F intramolecular peak was $\sim c_{DF} \cong 1.0 \pm 0.1$, *vide infra*, at each temperature measured. The first order difference data matched oscillations at high Q for the DF data ensuring that normalization of the HF was correct.

3.2.3 BACKGROUND SUBTRACTION IN THE NEUTRON DATA

The primary difficulty in the corrections arises from contaminant Bragg scattering from the polycrystalline Alloy 400 cell. This was largely removed by standard analysis procedures, although careful additional empirical subtraction of the individual contaminant Bragg peaks was required to extract the underlying diffuse scatter from the samples. The subtraction was performed on 13 of the 19 detector banks available on GLAD for each of the data sets measured in the differential cross section files before the application of the Placzek correction, which is described in chapter 1.[66] In the higher angle detector banks, the contaminant Bragg scatter proved too difficult to remove with reasonable accuracy and were therefore omitted. Figure 3.2 shows the measured DF, $S_{DF}^{N}(Q)$ at 296 K before and after removal of the Alloy 400 cell background.

3.2.4 HIGH-ENERGY X-RAY MEASUREMENTS

High energy x-ray diffraction data from DF (0.161 moles), HF (0.050 moles) and $[H_{1/2}D_{1/2}]F$ (0.108 moles) and an empty Alloy 400 cell were collected at 296 K. In separate experiments DF (0.030 moles), HF (0.059 moles) and an empty Alloy 400 cell were measured at 195 K. The high energy x-ray data were corrected for detector efficiency, instrumental geometrical effects and polarization using standard analysis procedures described in chapter 1.[102]

As was the case with the neutron data, the primary difficulty in the corrections arises from contaminant Bragg scattering from the polycrystalline Alloy 400 cells. The empty container scattering was subtracted by first scaling the empty container to align

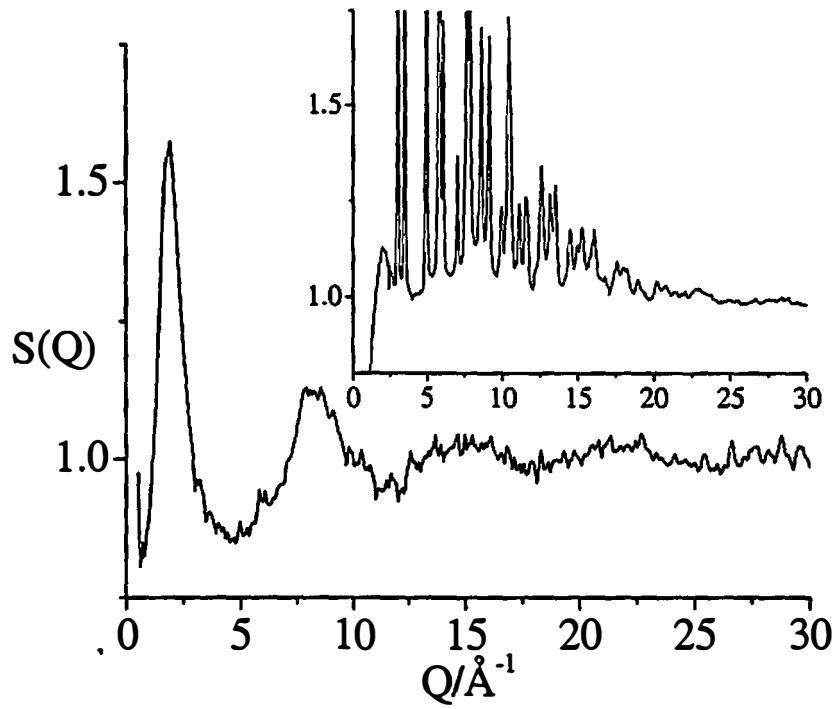

Figure 3.2: DF neutron total structure factor measurements, $S_{DF}^{N}(Q)$ after background corrections at 300 K. The insert shows $S(Q)$ for DF with the Alloy 400 background.

with the Bragg peaks measured in the container with the sample. Further empirical subtraction of the individual Bragg peaks was required in order to extract the underlying diffuse scatter from the samples. After the removal of background the x-ray data were normalized to the sum of the atomic form factors plus Compton scattering to obtain the pseudo-nuclear structure factor. Figure 3.3 shows the measured DF, $S_{DF}^{X}(Q)$ at 296 K before and after removal of the Alloy 400 cell background.

3.2.5 EXPERIMENTAL DATA

The total measured structure factor, $S_{DF}^{N}(Q)$ for DF at both temperatures is shown in figure 3.4 with the smoothed $S_{DF}^{N}(Q)$ from Deraman *et al.* as a comparison. The 286 K data has been truncated at $Q_{max} = 25$ Å^{-1} as the errors above this point only added statistical noise into the Fourier transformation of the data. At this temperature, the DF was measured for less time than the rest of the data, thereby decreasing the quality of the data.

The pseudo-nuclear functions from the high energy X-ray data, $S_{DF}^{X}(Q)$ are shown for the average of DF, HF and $[H_{1/2}D_{1/2}]F$ at 296 K and for HF at 195 K in figure 3.5.

3.2.6 PAIR DISTRIBUTION FUNCTIONS

The diffraction pattern of a sample of HF, collected with radiation source A and written as $S_T^A(Q)$ and the Fourier transformation that gives rise to the total pair correlation function $G_T^A(r)$ can be written in terms of the partial pair correlation functions as

$$G_T^A(r) = \sum_{\alpha\beta} a_{\alpha\beta}^A g_T(r) = a_{HH}^A g_{HH}(r) + a_{FF}^A g_{FF}(r) + 2a_{HF}^A g_{HF}(r) \qquad (3.2)$$

where $a_{\alpha\beta}^A$ (α, β = H,F) is the weighting of the scattering from α and β from

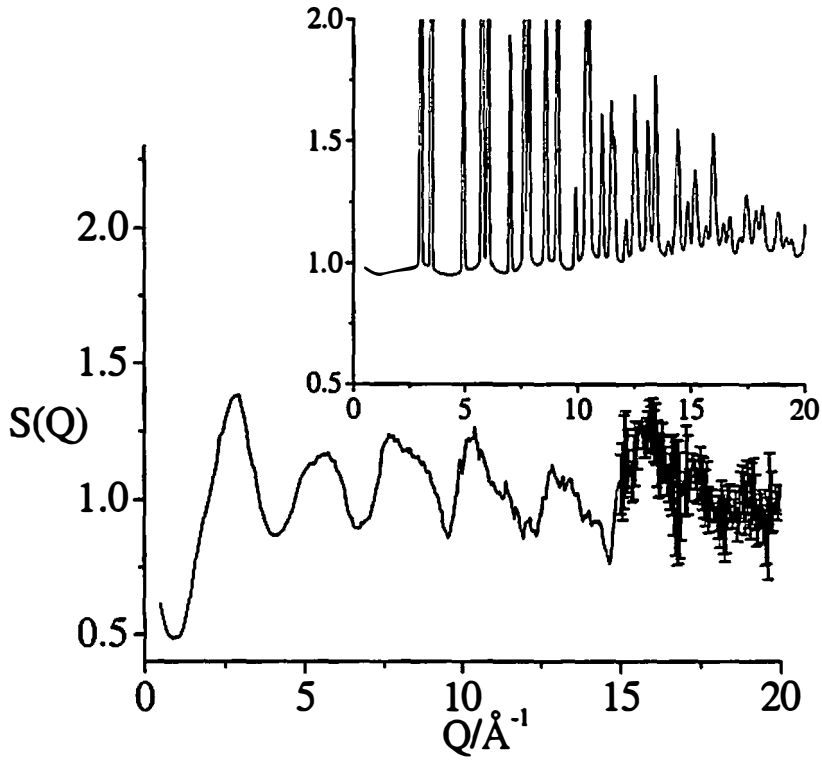

Figure 3.3: DF high energy X-ray total structure factor measurements, $S^{X}_{DF}(Q)$ after background corrections at 300 K. The insert shows $S(Q)$ for DF with the Alloy 400 background.

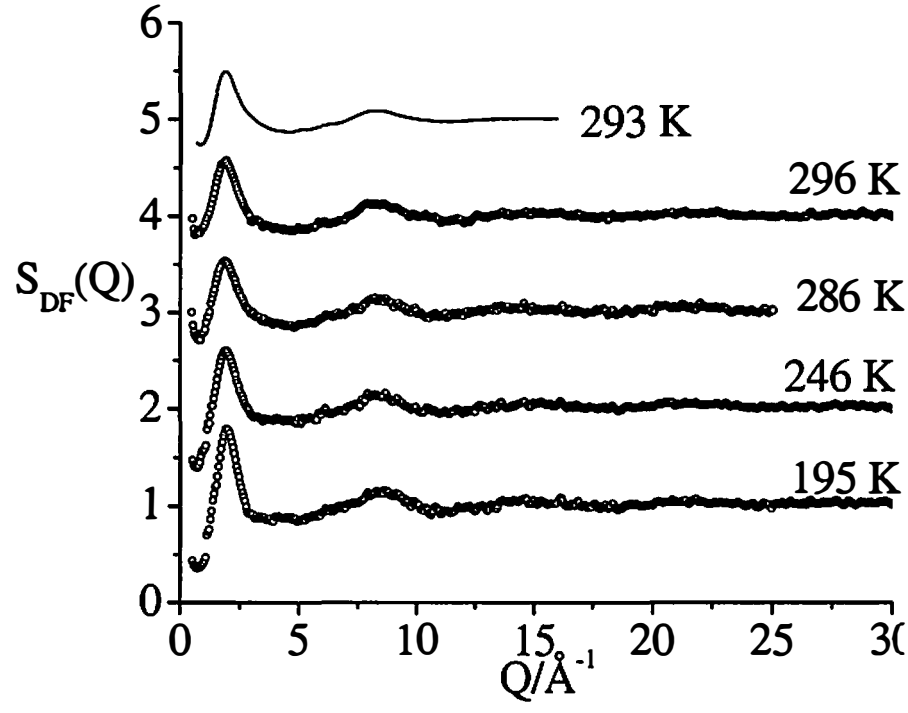

Figure 3.4: Corrected DF neutron total structure factor measurements. $S^N_{DF}(Q)+4$ at 293 K, $S^N_{DF}(Q)+3$ at 296 K, $S^N_{DF}(Q)+2$ at 286 K, $S^N_{DF}(Q)+1$ at 246 K and $S^N_{DF}(Q)$ at 195 K.

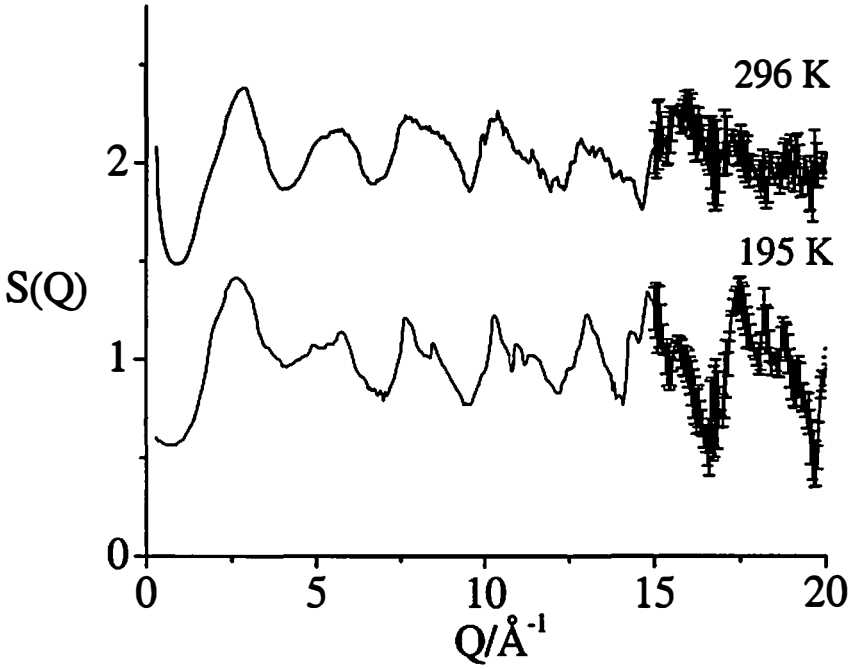

Figure 3.5: Corrected DF X-ray total structure factor measurements. $S^{X}_{DF}(Q)+1$ *at 300 K and* $S^{X}_{DF}(Q)$ *at 195 K.*

radiation source A where *N* signifies a neutron measurement and *X* signifies a high energy X-ray measurement. The weighting factors for these neutron and X-ray experiments are shown in table 3.6.

Fourier transformation of the total structure factor gives rise to the total pair correlation function, $G_{DF}^{N}(r)$ in the case of the neutron diffraction data can be explicitly written as

$$G_{DF}^{N}(r) = 0.293 g_{HH}(r) + 0.497 g_{HF}(r) + 0.210 g_{FF}(r) \qquad (3.3)$$

$G_{DF}^{N}(r)$ is shown at each of the temperatures measured in figure 3.6.

The total pair correlation function in the case of the high energy X-ray diffraction is dominated $g_{FF}(r)$ function. The total pair correlation function for the high energy X-ray measurements are shown in for the average of DF, HF and $[H_{1/2}D_{1/2}]F$ at 296 K and for HF at 195 K in figure 3.7.

For the 296 K data, X-ray experiments were performed on both of the isotopomers at the same state conditions and showed no significant isotopic quantum effect, within the limits of the experimental error (~5%), supporting the use of the isotopic substitution technique in neutron diffraction in this case.

Table 3.6: Weighting factors for DF and HF neutron experiments and X-ray experiments at Q= 0Å^{-1},1Å^{-1},2Å^{-1},5Å^{-1}, and 10Å^{-1}

	DF neutron	HF neutron	X-ray Q=0 Å^{-1}	X-ray Q=1 Å^{-1}	X-ray Q=2 Å^{-1}	X-ray Q=5 Å^{-1}	X-ray Q=10 Å^{-1}
a_{HH}^{A}	0.1113	0.0350	0.250	0.191	0.093	0.004	0.000
a_{FF}^{A}	0.0799	0.0799	20.250	18.253	13.715	3.569	0.435
$2a_{HF}^{A}$	0.1886	-0.1057	4.500	3.732	2.260	0.250	0.014

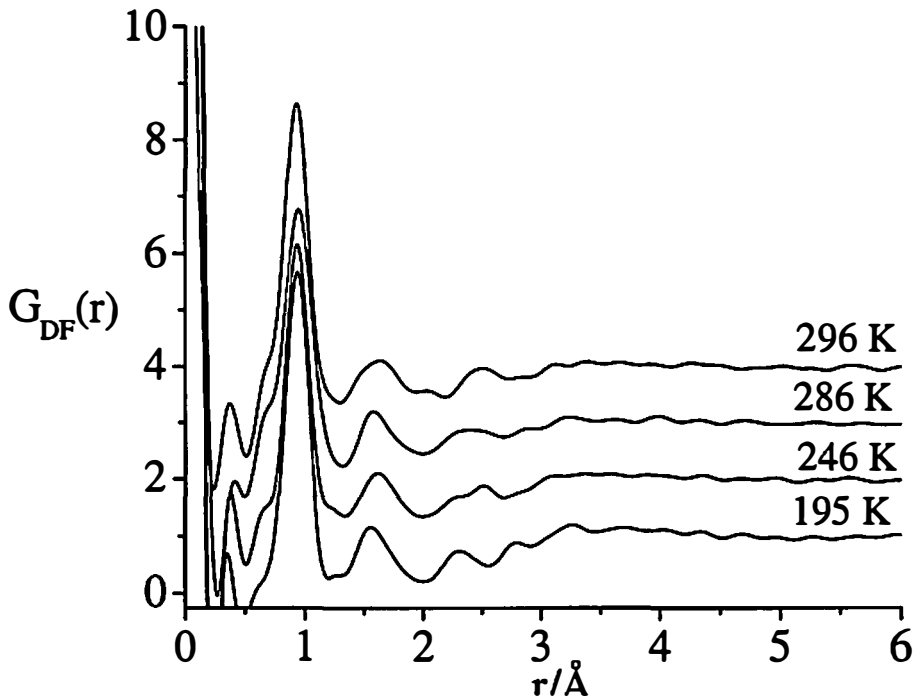

Figure 3.6: DF total pair correlation functions using neutrons. $G_{DF}^{N}(r)+$ *3 at 296 K,* $G_{DF}^{N}(r)$ +2 at *286 K,* $G_{DF}^{N}(r)$ +1 *at 246K and* $G_{DF}^{N}(r)$ *at 195 K.*

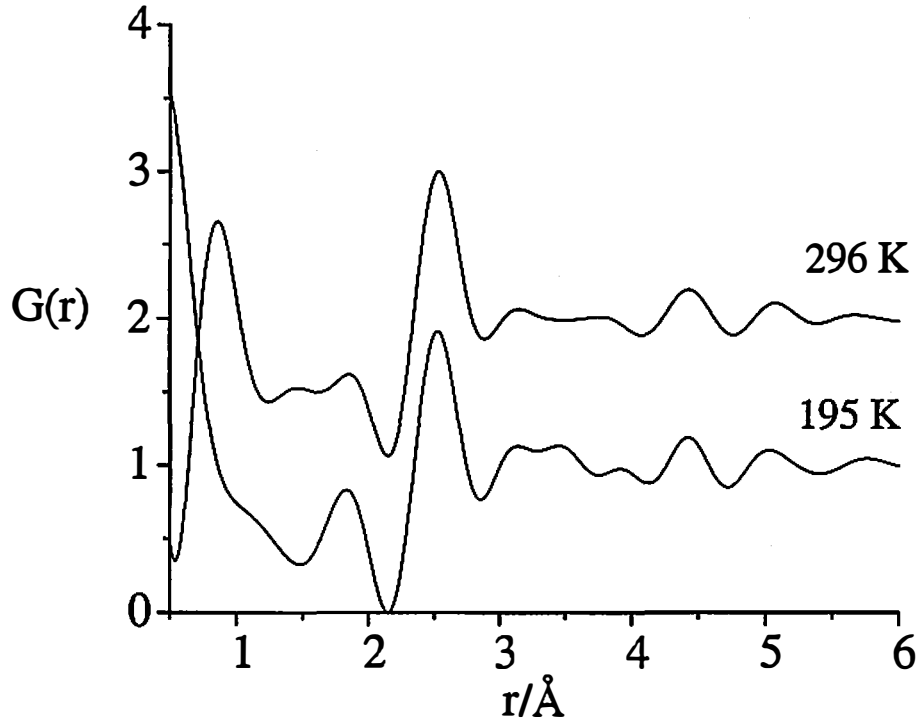

Figure 3.7: DF total pair correlation functions using X-rays. $G_{DF}^{X}(r)+1$ *at 296 K and* $G_{DF}^{X}(r)$ *at 195 K.*

3.2.6 FIRST ORDER DIFFERENCE FUNCTION

In order to elucidate the structure related only to the hydrogen positions, hereafter termed the [H,D] site, independent neutron diffraction measurements for isostructural and isotopomeric samples of HF and DF allowed the determination of the first order difference function as described in chapter 1. The first order difference function, in this case, contains only the partial structure factors with the respect to the [H,D] site, namely $\Delta S^N_{HX}(Q)$. The extracted function $\Delta S^N_{HX}(Q)$ is shown for both measured temperatures in figure 3.8.

The Fourier transformation $\Delta S^N_{HX}(Q)$ yields the real space counterpart, $\Delta G^N_{HX}(r)$ which shown in figure 3.9. As interference terms related only to the [H,D] site are. present in $\Delta S^N_{HX}(Q)$, $\Delta G^N_{HX}(r)$ shown in figure 3.9 represents only the pair correlation functions associated with the [H,D] sites where

$$\Delta G^N_{HF}(r) = 0.206 g_{HH}(r) + 0.794 g_{HF}(r) \tag{3.5}$$

3.2.7 EXTRACTION OF THE PARTIAL STRUCTURE FACTORS

By using complimentary information provided by both types of radiation, and by performing measurements on three isotopic samples with identical structures, it is possible to extract all of the partial structure factors for a two component system. Here the partial structure factors for HF, $S_{HH}(Q)$, $S_{HF}(Q)$ and $S_{FF}(Q)$, were extracted by taking linear combinations of the diffraction patterns from both radiation sources. The details of this procedure are presented in Chapter 1.

As is shown in table 3.6 and equation 3.4, the high energy X-ray diffraction measurements are dominated by $S_{FF}(Q)$ and the isotopic substitution neutron diffraction measurements provide an accurate determination of the hydrogen interactions. The extracted partial structure factors at 296 K are shown in figure 3.10 and the corresponding pair correlation functions, $g_{HH}(r)$, $g_{FF}(r)$ and $g_{HF}(r)$ are shown in figure 3.11. It should be noted that $S_{HH}(Q)$ and $S_{FF}(Q)$ were truncated at

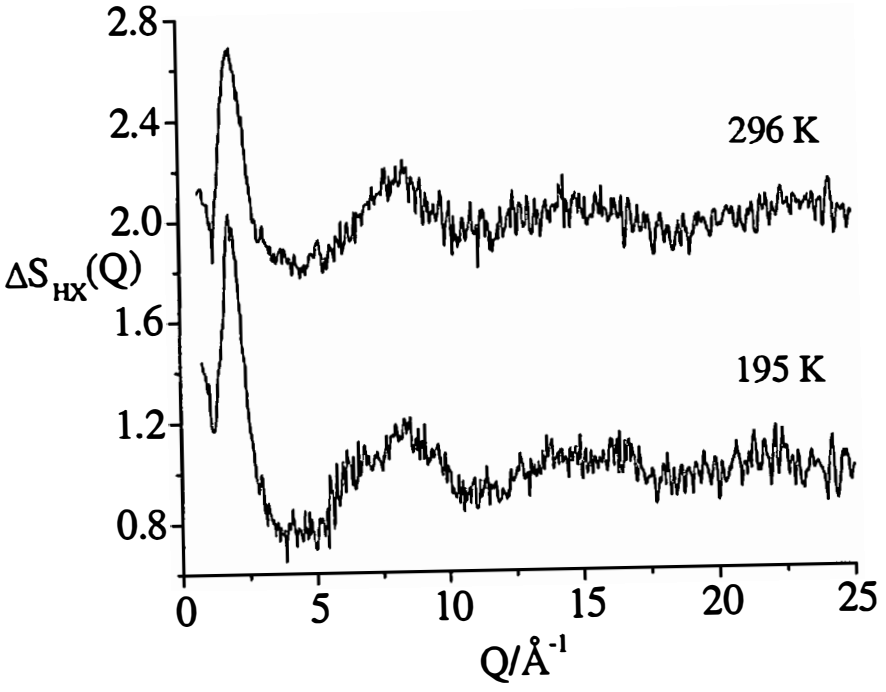

Figure 3.8: Partial structure factor for hydrogen distances in HF. $\Delta S^{N}_{HX}(Q)$ *+1 at 296 K and* $\Delta S^{N}_{HX}(Q)$ *at 195 K*

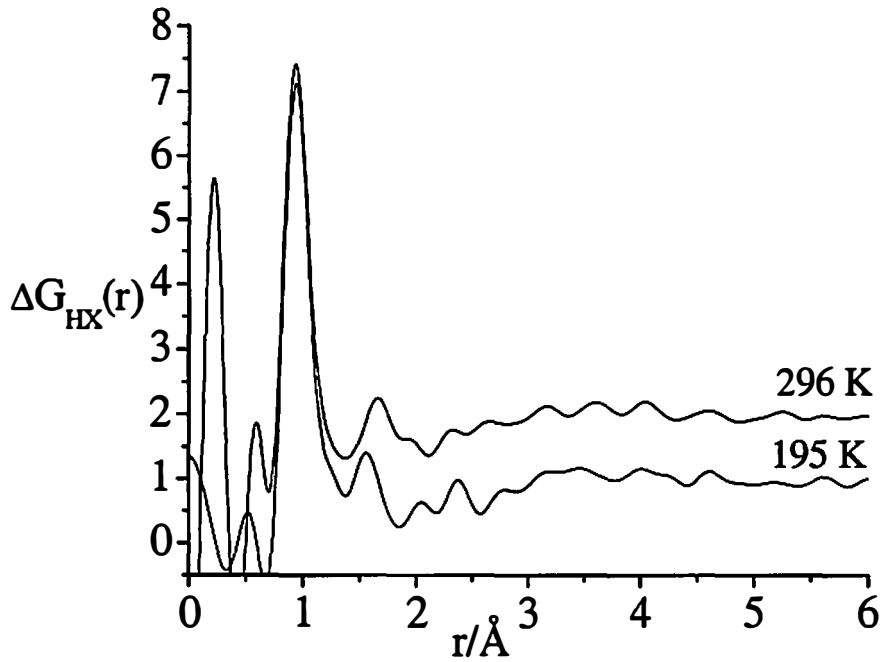

Figure 3.9: Partial pair correlation functions for the hydrogen distances in HF. $\Delta G^{N}_{HX}(r)+1$ *at 296 K and* $\Delta G^{N}_{HX}(r)$ *at 195 K*

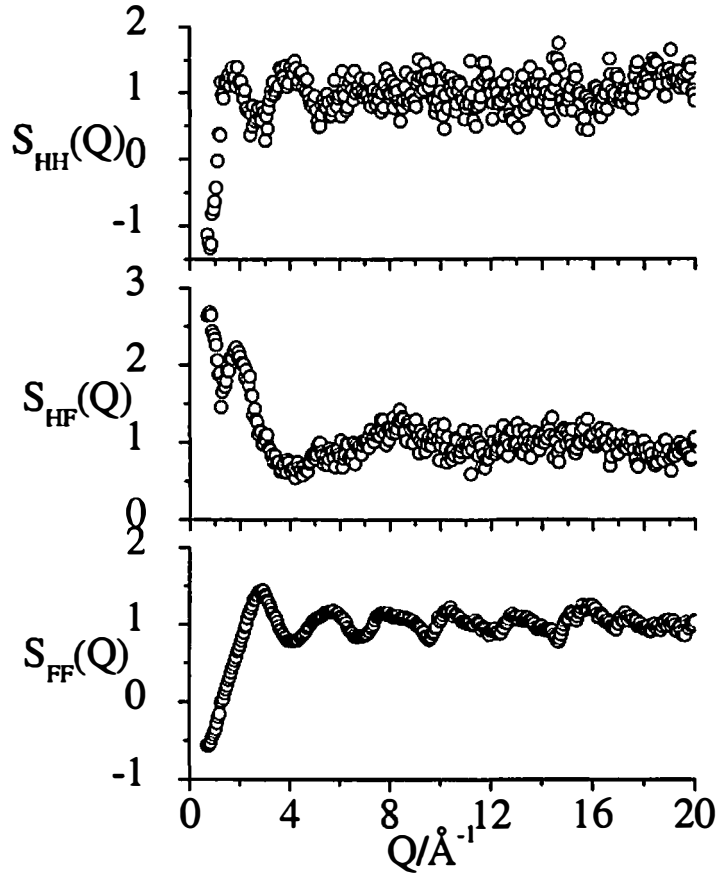

Figure 3.10: Partial structure factors for HF, $S_{HH}(Q)$, $S_{HF}(Q)$ and $S_{FF}(Q)$ at 296 K.

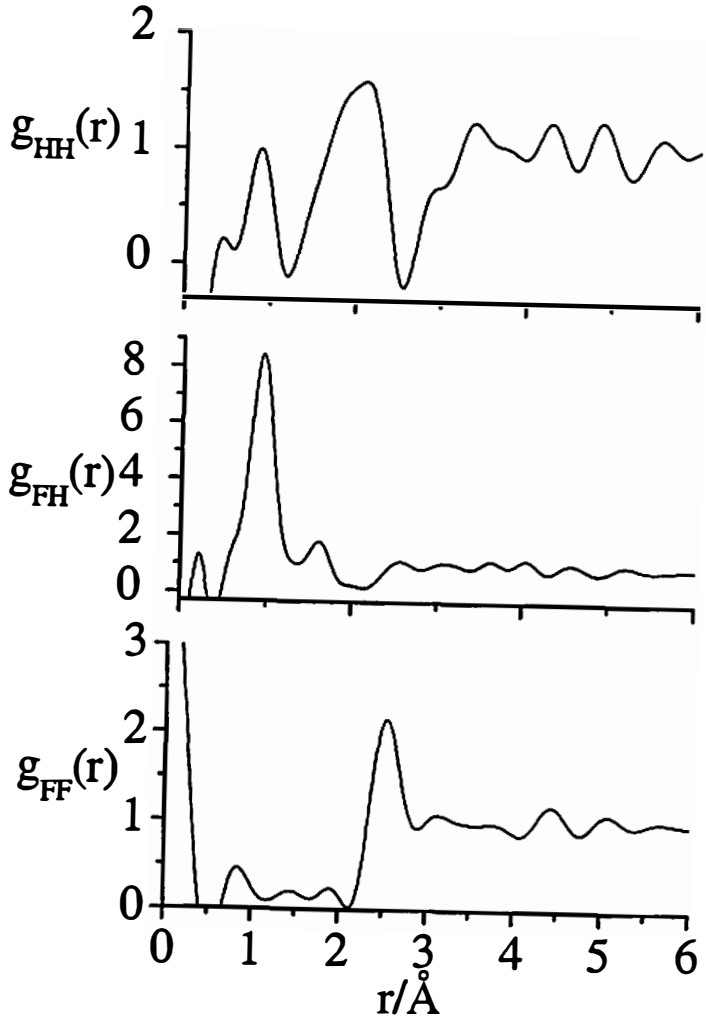

Figure 3.11: Partial pair correlation functions for HF, $g_{HH}(r)$, $g_{HF}(r)$ and $g_{FF}(r)$ at 296 K

$Q_{max} = 15$ Å^{-1} to obtain the $g_{HH}(r)$ and $g_{FF}(r)$ curves given in this work. The Fourier transformation of both $S_{HH}(Q)$ and $S_{FF}(Q)$ at $Q_{max} = 20$ Å^{-1} yielded the same coordination numbers within the experimental error as is shown below. The Fourier transform at the larger Q_{max} was consistent with the Fourier transformation at the $Q_{max} = 15$ Å^{-1} but contained a larger number of statistical error.

In order to ensure that the extraction of the partial structure factors was consistent with the measured data, $S_{HH}(Q)$, $S_{HF}(Q)$ and $S_{FF}(Q)$ were summed to reconstruct $S^N_{DF}(Q)$. The comparison with the $S^N_{DF}(Q)$ and is shown in figure 3.12. In addition, these reconstructed partials were subsequently Fourier transformed and compared with $G^N_{DF}(r)$ and is shown in figure 3.13.

3.2.8 Reverse Monte Carlo (RMC) analysis

In order to provide a model for the collected data, **R**everse **M**onte **C**arlo (RMC) fits were obtained for the extracted partial structure factor data.[240-245] RMC modeling has been widely used to provide structural fits for scattering data to aid in the interpretation in the case of disordered systems.[241,246-253]

RMC generates a possible configuration that is consistent with the data,[241,244,245] and this model is often assumed to be the most disordered structure that is consistent with the data.[254] There is debate about the precise physical meaning of an RMC model, given that when such a molecular configuration is used to calculate thermodynamic properties, the energies that are calculated are often high.

However, if the assertion that the structure of the RMC model is one of the most disordered consistent with the data is correct, then structure evolved in the RMC model must be required in order to fit the observed data. It should be stressed that RMC gives one or more possible configurations and that these configurations are not unique.[255]

The RMC simulation was performed simultaneously on the three measured partial structure factors at 296 K in a cubic box containing 5000 H atoms and 5000 F

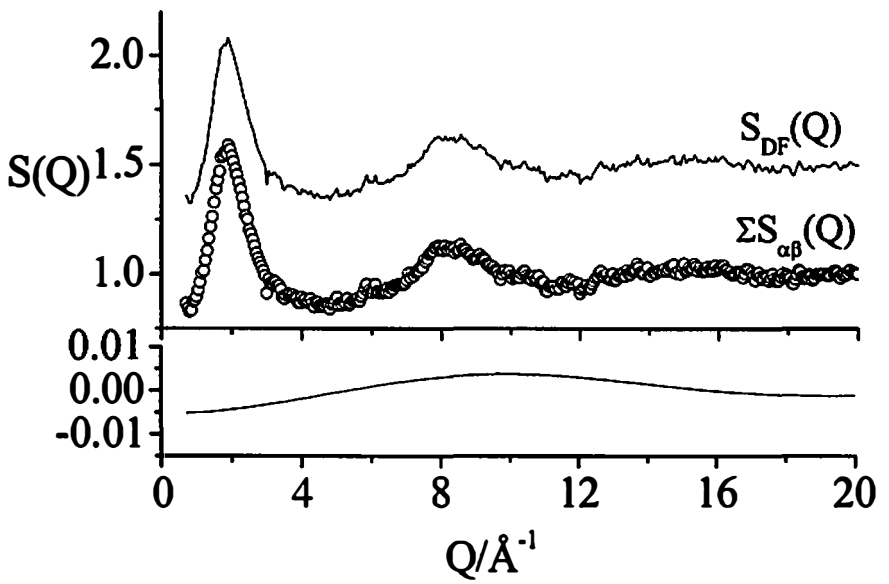

Figure 3.12: Reconstruction of partial structure factors compared with $S_{DF}^{N}(Q)$ *at 296 K.* $\sum S_{\alpha\beta}(Q)$ $(\alpha,\beta = \mathrm{H,F})$, $S_{DF}^{N}(Q)$ *+0.5 and the red line shows the difference.*

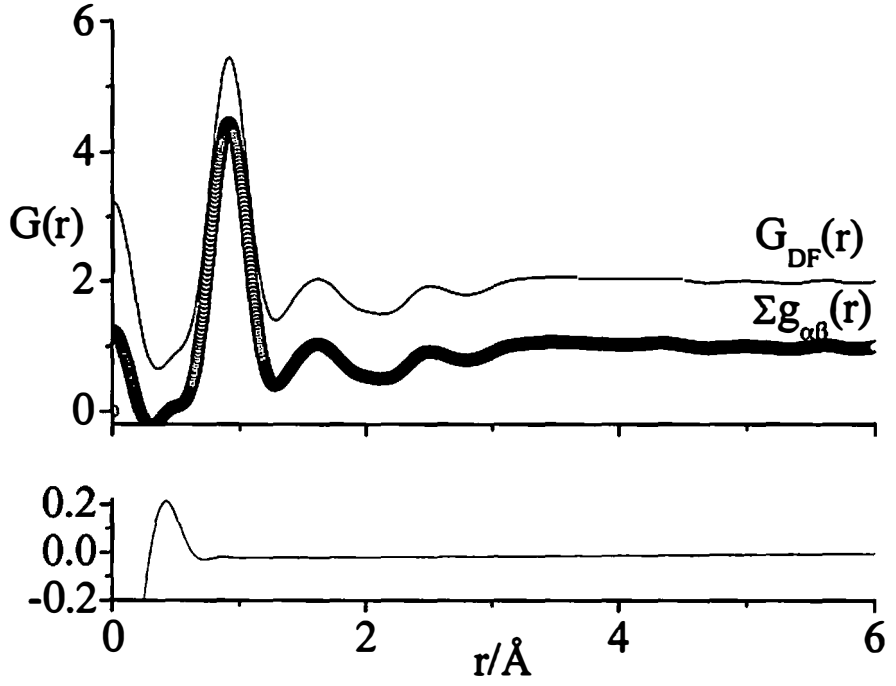

Figure 3.13 Reconstruction of partial pair distribution functions $G_{DF}^{N}(r)$ *at 296 K.* $\sum g_{\alpha\beta}(r)$ $(\alpha,\beta = \mathrm{H,F})$, $G_{DF}^{N}(r)$ *+1 and the red line shows the difference.*

atoms with each atom constrained to form half of an HF molecule. The second constrained imposed on the RMC simulation was that the average coordination number and peak position of the first peak in real space had to agree with the value obtained from a direct Fourier transform of the measured partial structure factor data to within the experimental error quoted below. The RMC fits in comparison to the experimentally extracted partial structure factors at 296 K are shown in figure 3.14.

The corresponding RMC generated radial distribution functions are compared with the experimentally extracted pair correlation functions in figure 3.15; the sum of the partial structure factors derived from RMC compared with the total structure factor measured for DF at 296 K $S_{DF}^{N}(Q)$ is shown in figure 3.16.

The agreement between the RMC generated partial structure factors and the data derived partial structure factors is good except at low Q. This is due to the Placzek correction employed by the method discussed in chapter 1. For spallation sources the Placzek is manifested by a steep rise at low Q plus a gradual slope declining towards higher Q values.[14,256] For this reason, the data is most difficult to accurately correct for inelasticity effects in this region.

3.3 DISCUSSION

3.3.1 TOTAL PAIR CORRELATION FUNCTIONS AND FIRST ORDER DIFFERENCE FUNCTIONS

3.3.1.1 INTRAMOLECULAR STRUCTURE

At each temperature measured the HF intra molecular bonding peak in $G_{DF}^{N}(r)$ (Figure 3.6) is centered at $r_{HF} \approx 0.93 \pm 0.02$ Å, indicating that the HF intra-molecular structure is largely invariant with temperature, and in agreement with the previously determined distances in liquid DF, which are 0.93 Å and 0.925 Å respectively.[142,143] It should be noted however that in each of the previous measurements the authors believed this to be an underestimation, based on comparisons with electron diffraction of gaseous HF

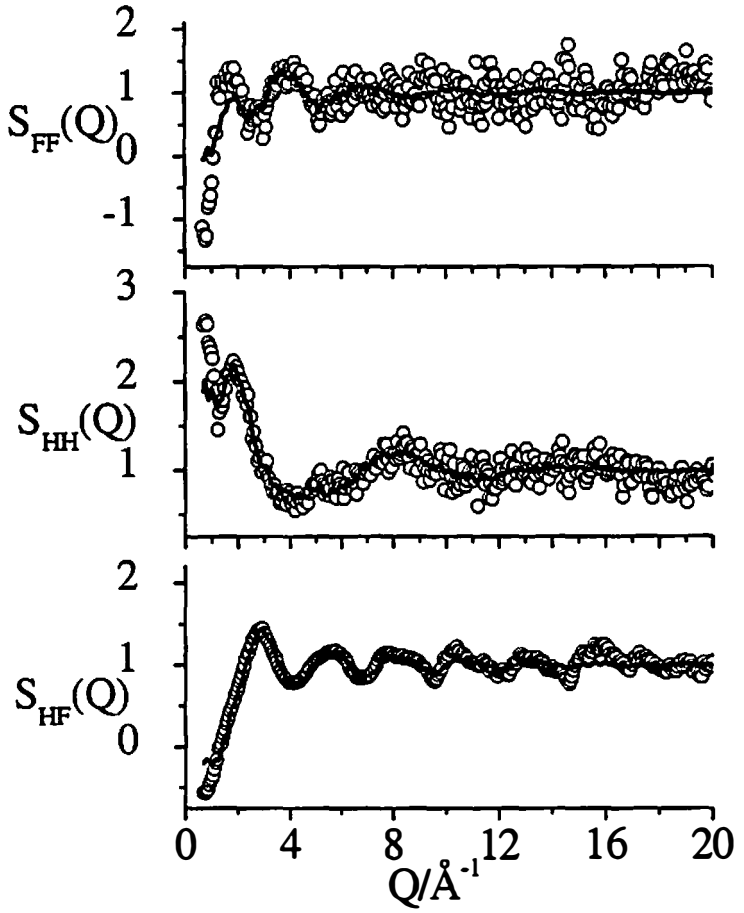

Figure 3.14: RMC fit (solid line) to the partial structure factors extracted from the data (circles) at 296 K.

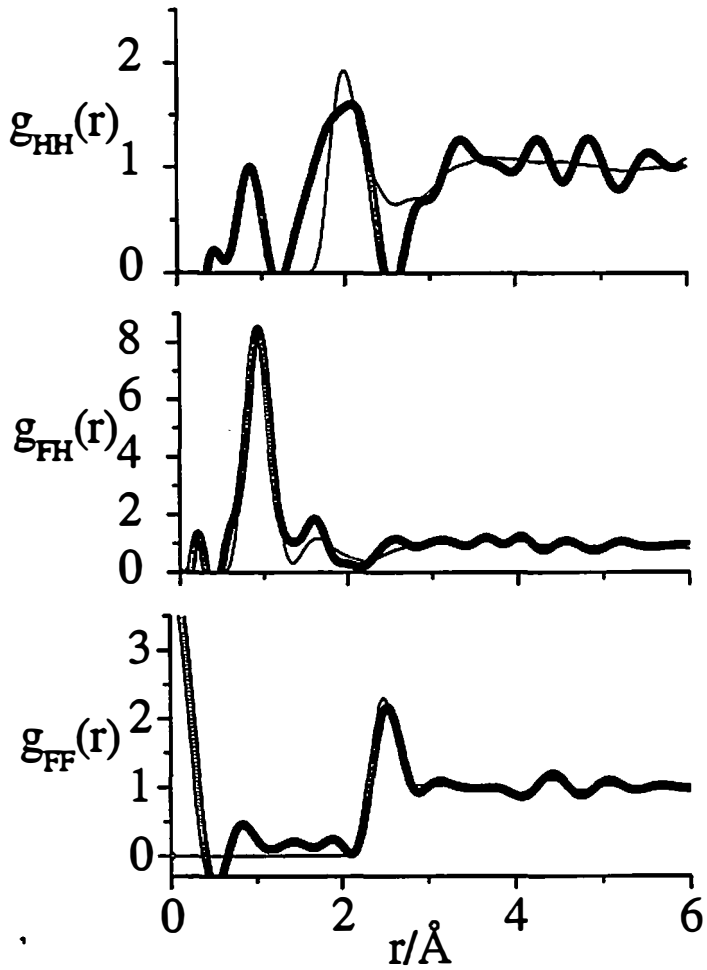

Figure 3.15: RMC fit (solid line) to the partial pair correlation functions (circles) at 296 K.

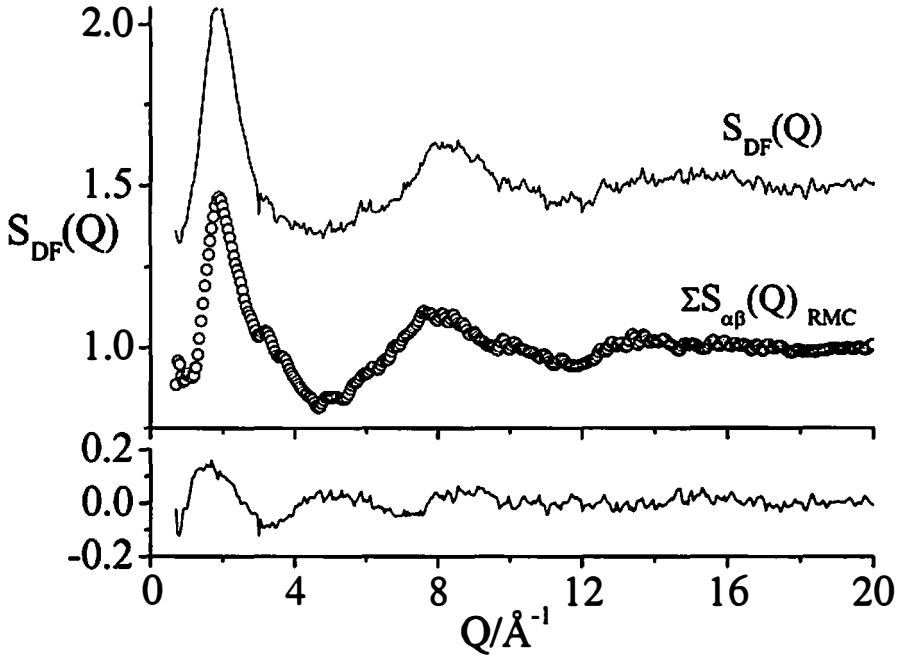

Figure 3.16: Reconstruction of RMC generated partial structure factors compared with $S^{N}_{DF}(Q)$ *at 296 K.* $\sum S_{\alpha\beta}(Q)_{RMC}$ $(\alpha,\beta = \mathrm{H,F})$, $S^{N}_{DF}(Q)$ *+0.5 and the red line shows the difference.*

which gives $r_{HF} = 0.973$ Å,[181] and the solid state structure of DF, which gives $r_{HF} = 0.95$ Å at 85 K.[130] In the 293 K liquid structure, the authors applied a furthermodification to their data to produce an HF intramolecular bond of 0.95 Å.[143] Pfleiderer *et al.* did not modify their intramolecular bond length to adjust the data. However, they did note that the intramolecular bond in HF decreased with increasing temperature.[142] It is of interest that the solid state structure of DF, determined by neutron diffraction, was initially determined to have an intramolecular bond length of $r_{HF} = 0.95$ Å at 4.3 K and $r_{HF} = 0.93$ Å at 85 K. These distances were revaluated to shift each bond length by 0.02 Å.[130]

The coordination numbers with respect to the number of fluorine atoms around deuterium atoms in the first peak in $G^{N}_{DF}(r)$ was assessed at each temperature measured. The coordination numbers are listed in table 3.7 along with the r_{min} value for each intramolecular peak and the peak maximum at each temperature recorded.

The coordination number of the first peak in $\Delta G_{HX}(r)$ with respect to fluorine around hydrogen is $c_{HF} = 0.78 \pm 0.10$ at 296 K and $c_{HF} = 1.03 \pm 0.10$ at 195 K, for peak maxima at $r_{HF} = 0.943 \pm 0.03$ Å and $r_{HF} = 0.939 \pm 0.03$ Å, respectively (figure 3.9). The coordination number at 296 K is lower than expected, however this is well within the experimental error due to the difficulty of the Placzek correction for HF. As an HF sample contains 50 atom % hydrogen, the inelasticity effects are greatly enhanced in this system. The inelasticity correction for HF on GLAD is not analytically

Table 3.7: Coordination number for intramolecular DF peak in $G^{N}_{DF}(r)$.

T/K	First peak position/ Å	c^{intra}_{DF}	r_{min}/Å
296	0.928±0.030	1.05±0.10	1.28
286	0.947±0.030	1.03±0.10	1.31
246	0.929±0.030	0.99±0.10	1.32
195	0.940±0.030	0.99±0.10	1.20

soluble practically at this time but, is merely estimated by virtue of the method described in chapter 1. For this reason, the first order difference data were verified by oscillations at high Q which corresponded to the same level of scatter seen in the DF data. In addition, as noted in chapter 1 the inelasticity effects vary with temperature, with higher temperatures showing a larger inelasticity effect.

3.3.1.2 INTERMOLECULAR STRUCTURE

In contrast to the intramolecular structure, the intermolecular structure, as seen in $G_{DF}^{N}(r)$ and $\Delta G_{HX}^{N}(r)$, is clearly different at each measured temperature. In figures 3.6 and 3.7, the second clear peak at all temperatures can be attributed largely to the HF intermolecular structure. From the total structure factor neutron measurement (figure 3.6), this peak becomes sharper as the temperature decreases and shifts significantly from $r_{HF} = 1.64 \pm 0.05$ Å at 296 K to $r_{HF} = 1.56 \pm 0.02$ Å at 195 K which is identical to the hydrogen bond distance in the solid state structure of HF at 85 K ($r_{HF} = 1.56 \pm 0.03$ Å).[129,130] The shift to lower r with a decrease in temperature is indicative of a more tightly bound hydrogen bond at lower temperatures. This is also reflected at 246 K (figure 3.6) where the second peak is more well-defined than at the highest temperature measured and shows a maximum at $r_{HF} = 1.61 \pm 0.02$Å. It should be noted however that this hydrogen bonding peak in the total structure factor contains significant contribution from the $g_{HH}(r)$ function and cannot merely be described as hydrogen bonding distance as is described in more detail below.

At 296 K $G_{DF}^{N}(r)$ shows a third peak centered at 2.51 ± 0.05Å which can be attributed in part to the $g_{FF}(r)$ function (described below). This peak may also imply a longer HF bonding distance. As the temperature decreases to 195 K this peak shifts to 2.34 ± 0.05Å, suggesting a closer contact between neighboring HF molecules. This peak in the low temperature data is almost certainly attributable to an additional HF interaction as the total pair correlation function for the HF measurement using high energy X-rays at 195 K (figure 3.7) shows a clear peak at ~2.5Å which can be attributed

to the FF distance. At the intermediate temperature this peak in $G_{DF}^{N}(r)$ becomes much less well defined and the peak shape indicates there are two peak maxima contained within this peak, one at ~2.3Å and one at ~2.5Å.

The assignment of this peak in the total pair correlation functions as an HF interaction is corroborated by both $\Delta G_{HX}(r)$ functions (figure 3.9). In $\Delta G_{HX}(r)$ this peak also appears at both temperatures measured and can be attributed to an additional HF distance as ~80% of the scattering intensity arises from the $g_{HF}(r)$ partial pair correlation function (equation 3.5). In the 296 K data this feature is located at ~2.5Å. and at 195 K the $\Delta G_{HX}(r)$ function shows a peak at $r_{HX} = 2.37 \pm 0.10$ Å.

3.3.2 PARTIAL PAIR CORRELATION FUNCTIONS

The peak maxima, coordination numbers and corresponding r_{min} values are listed for each partial pair correlation function, $g_{HH}(r)$, $g_{HH}(r)$ and $g_{FF}(r)$ at 296 K, for both the direct Fourier transformation of the data and the RMC fit to the data are listed in table 3.8. The coordination numbers have been determined using the running

Table 3.8: Peak maxima, coordination numbers and r_{min} value for HF pair correlation functions, $g_{HF}(r)$, $g_{HH}(r)$ and $g_{FF}(r)$.

	Peak position/Å	r_{min}/Å	CN
$g_{HF}(r)$	0.93±0.03	1.32	1.06±0.10
$g_{HF}(r)$ RMC	0.93		1.01
$g_{HF}(r)$	1.60±0.05	2.22	1.85±0.10
$g_{HF}(r)$ RMC	1.64		1.82
$g_{HH}(r)$*	2.07±0.12	2.47	1.71±0.10
$g_{HH}(r)$ RMC	1.99		1.64
$g_{FF}(r)$*	2.51±0.10	2.79	2.11±0.10
$g_{FF}(r)$ RMC	2.48		2.21

* *Fourier transformed from Q_{max}=15*

coordination number method described in chapter 1.

The intermolecular peak position in $g_{HF}(r)$ is a relatively short distance is indicative of a very strong hydrogen bond. Moreover, the average intermolecular hydrogen-fluorine coordination number is consistent with the presence of hydrogen bonded chains which are short and therefore not infinite. This result is in agreement with Raman and infrared spectroscopy studies which have been interpreted using a model with chains of six or seven HF molecules.[195] This can be described mathematically as

$$c_{HF}^{inter} = \frac{n-1}{n} = 0.85 \therefore n = 6.67 \tag{3.5}$$

where n is the number of molecules in the chain. The first peak in $g_{HH}(r)$ has a coordination number, which is also indicative of short chains in the liquid which are on the average 6 to 7 molecules long. This can be shown again mathematically by

$$c_{HH} = \frac{2(n-1)}{n} = 1.71 \therefore n = 6.90 \tag{3.6}$$

where n is the number of molecules in the chain. It should be noted that the errors in these chain length calculations are quite large given the ~20% error in the coordination number assignments as is shown in table 3.8.

The first peak in $g_{HH}(r)$ extends into the region at lower r and overlaps with the intermolecular hydrogen bond in $G_{DF}^{N}(r)$. This phenomenon has also been noted in the simulation literature, though at a different thermodynamic state point of the liquid.[229] The accurate separation of the overlapping peaks in $g_{HH}(r)$ and $g_{HF}(r)$ as well as the extraction of the $g_{FF}(r)$ function, is essential in understanding the complete structure of the liquid.

The first peak in $g_{FF}(r)$ occurs at $r_{FF} = 2.51 \pm 0.03$ Å in the 296 K. At 195 K, $G_{DF}^{X}(r)$ the first sharp peak corresponding to the FF distance is $r_{FF} = 2.53 \pm 0.05$ Å (Figure 3.7). As was seen in the intramolecular structure, the structure with respect to the F···F distance is virtually the same at each temperature measured. It is notable that

this invariance in the F···F distance is seen in all phases of HF-with an average F···F distance in the crystalline structures of $r_{FF} = 2.50 \pm 0.01$ Å and the F···F distance in the gas phase of $r_{FF} = 2.535 \pm 0.005$ Å. In addition, $g_{FF}(r)$ shows several peaks occurring beyond the first peak as does $G_{DF}^{X}(r)$ at 195 K. This indicates a large number of longer intermolecular F···F contacts in the liquid at both temperatures measured.

The separation of the partial pair correlation functions is essential to comparing the simulations on liquid HF. The partial pair correlation functions obtained by Fourier transformation of the data are compared to *ab initio* MD simulations, the Muñoz-Losa QM/MM model as well as polarizable and non-polarizable pair potential models in figures 3.17, 3.18 and 3.19 for $g_{FF}(r)$, $g_{HF}(r)$ and $g_{HH}(r)$, respectively.[204-206,219,228]

In figure 3.18, the first peak in $g_{HF}(r)$ was removed from the data derived pair correlation function to show only the intermolecular structure. This was accomplished by fitting this peak with an appropriate Gaussian function and then subtracting this function from the real space data.

From figure 3.19, the best fits to the $g_{HH}(r)$ function are from the MC simulation using a non-polarizable potential, the QCT model and *ab initio* MD simulations.[205,228,235] It should be noted however that $g_{HH}(r)$ derived from the data is the least accurate of the pair correlation functions obtained and that all of the models are within the experimental error reported in table 3.8 with the exception of the polarizable potential MC simulation which gives a distance of $r_{HH} = 2.5$ Å.[204-206,219,228]

Figure 3.18, only shows the intermolecular portion of the pair correlation function with the QCT model and *ab initio* MD simulations showing the best fit to the data.[228,235] The *ab initio* MD simulations show the same peak position and shape as the measured data but does not predict any features beyond the hydrogen bonding peak. The QCT model has a distinct feature at ~3Å which may correspond to the longer H···F distance seen in the data.

As mentioned above, the shape of the $g_{FF}(r)$ function shown in figures 3.17 is important in distinguishing the accuracy of the different models. The first peak in

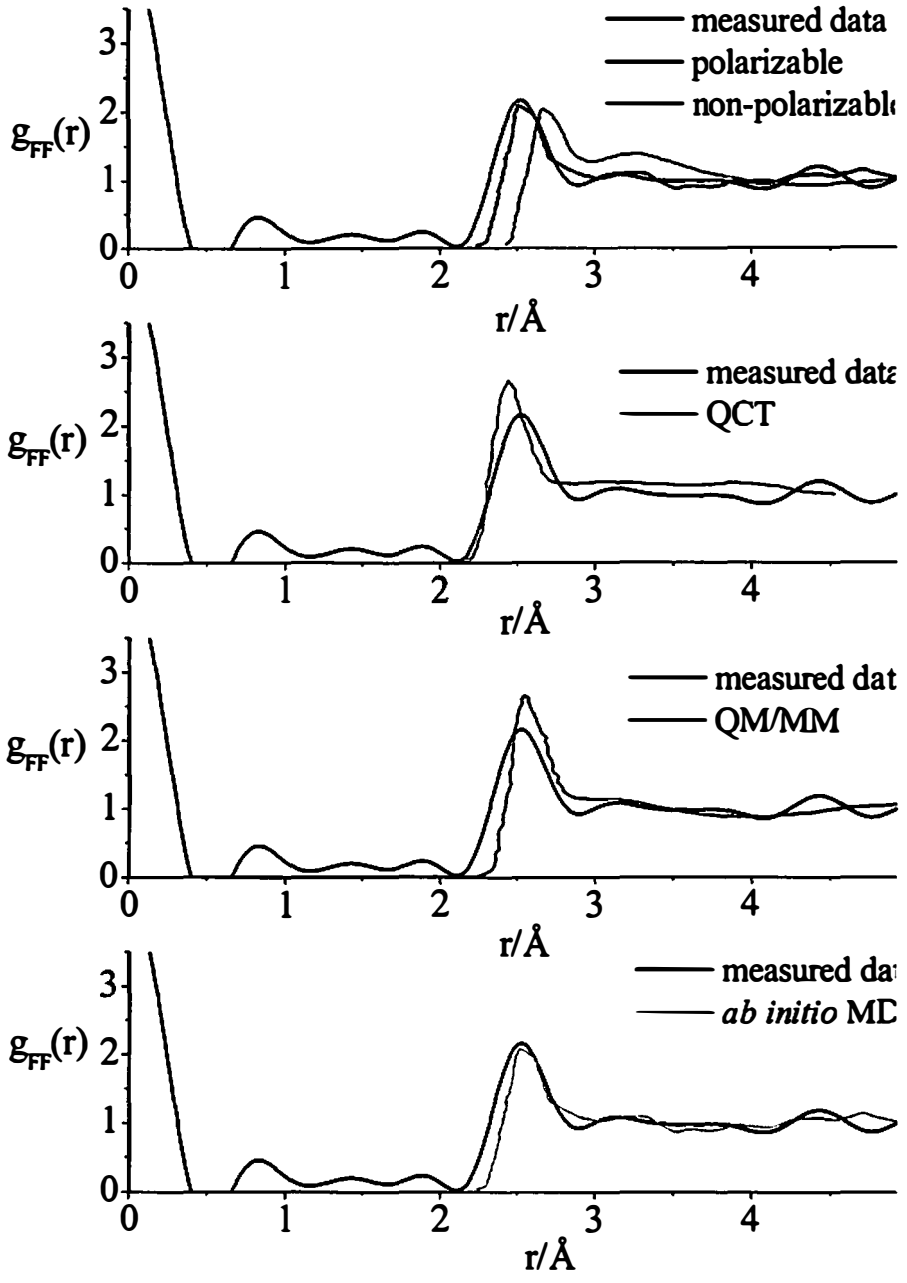

Figure 3.17: Data derived $g_{FF}(r)$ function compared with current simulations.

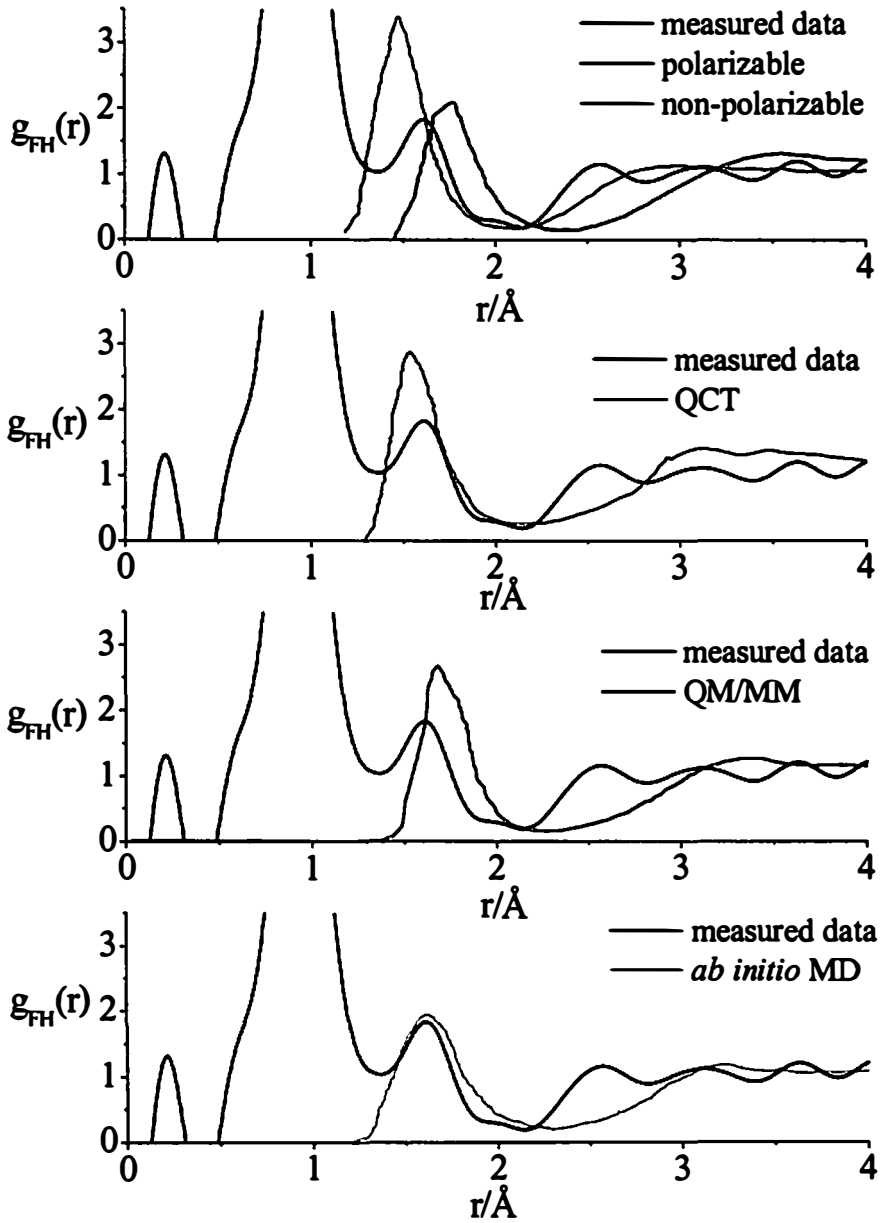

Figure 3.18: Data derived $g_{FH}(r)$ function compared with current simulations.

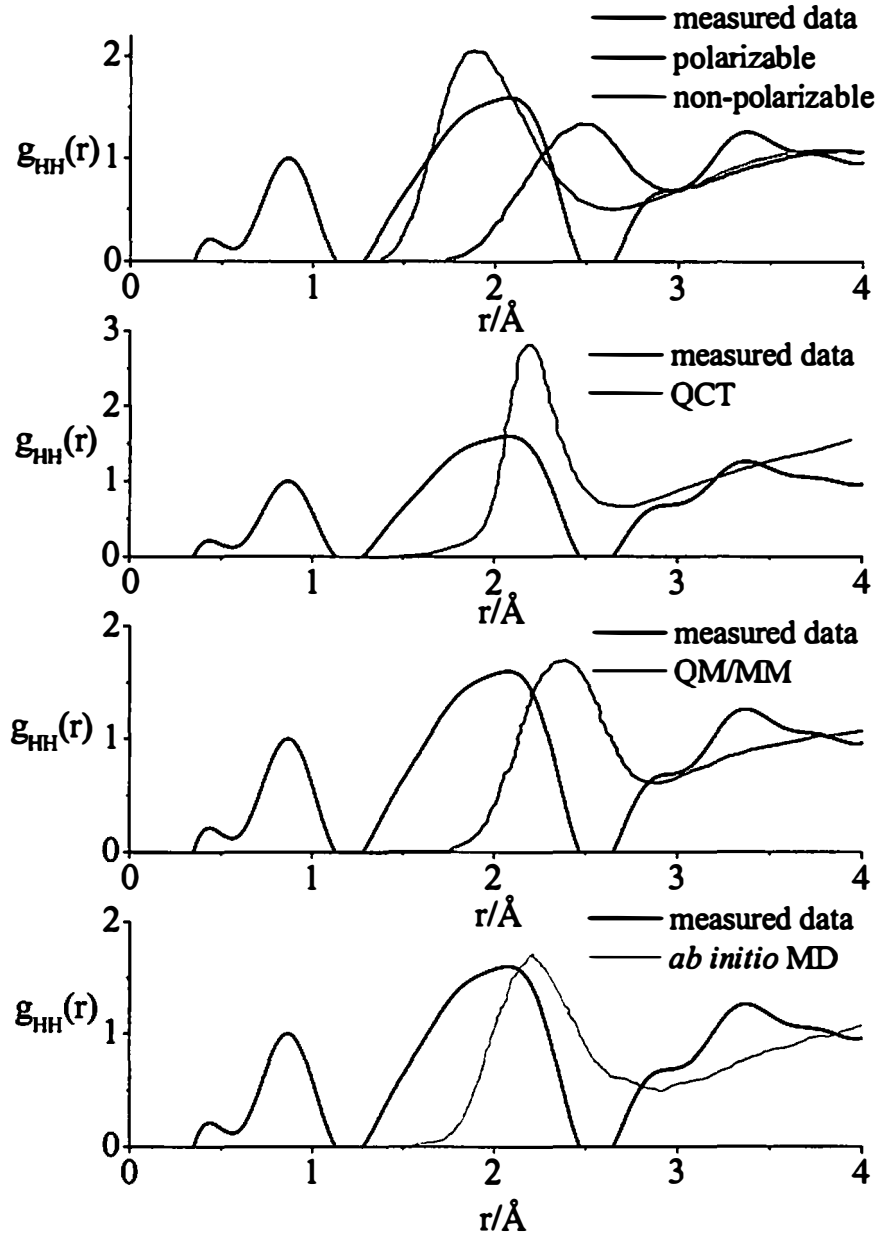

Figure 3.19: Data derived $g_{HH}(r)$ function compared with current simulations.

$g_{FF}(r)$ occurs at $r_{FF} = 2.51 \pm 0.03$Å is in close agreement with *ab initio* MD simulations and most models predict this distance with reasonable accuracy.[204,206,209,213-216,219,228,235]

Moreover, in figure 3.17 the data derived pair correlation function shown several peaks occurring beyond the first peak in $g_{FF}(r)$. A second F···F distance was first noted by Klein *et al.* in an early pair potential simulation at ~3.3Å.[209] This was discounted later by the same authors who found the first F···F distance to be at 2.7Å ,which was thought to be strong evidence for the existence of dimers.[210]

A "shoulder" in $g_{FF}(r)$ was also found in the *ab initio* MD simulations, where the authors noted that this feature was noisy due to their short simulation time and could possibly be resolved into two peaks, one at 2.9 Å and one at 3.3 Å.[228] This peak is additionally seen in the QM/MM simulation and in the MC simulation using a polarizable potential.[204,206]

This feature indicates strong interchain interactions which are similar to those seen in solid HF and DF where second nearest F···F neighbor is $r_{FF} = 3.2$ Å.[129,130]

3.3.4 CHAIN CONFORMATION AND ANGLE ANALYSIS

Taking the peak maxima from the extracted pair correlation functions as the basis for intermolecular angular calculations is instructive. The average H···F-H angle gives an indication of the linearity of the chains and was calculated by the bond lengths *via*

$$(r_{HH})^2 = (r_{HF}^{\text{intra}})^2 + (r_{HF}^{\text{inter}})^2 - 2(r_{HF}^{\text{intra}})(r_{HF}^{\text{intra}})\cos\theta \qquad (3.7)$$

where $\theta = H\hat{F}H$.

At 296 K using the peak maxima from the partial pair correlation functions, $g_{HF}(r)$ and $g_{HH}(r)$ this angle was found to be $H\hat{F}H = 106 \pm 10^0$ indicative of bent angles. The corresponding value from the RMC fit to the data is $H\hat{F}H_{\text{RMC}} = 100^0$.

The polarizable pair potential model predicts this value most accurately at $H\hat{F}H = 107^0$, although the bond lengths in this model vary from the present work.[204,206]

The average F···H-F angle defines the degree of orientation between different molecules in the chain and is calculated in the same matter as equation 3.7 that is

$$(r_{FF})^2 = (r_{HF}^{\text{intra}})^2 + (r_{HF}^{\text{inter}})^2 - 2(r_{HF}^{\text{intra}})(r_{HF}^{\text{intra}})\cos\theta \qquad (3.8)$$

where $\theta = F\hat{H}F$.

At 296 K this value was calculated as $F\hat{H}F = 165 \pm 10^0$. The corresponding value from the RMC fit to the data is $F\hat{H}F_{\text{RMC}} = 156°$. The most accurate corresponding simulation value, from the ab initio MD calculations is in perfect agreement with the RMC fit to the data.[228] Both non-polarizable and polarizable pair potential models predict this angle as $F\hat{H}F = 180^0$.[204-206]

The degree of chain branching that occurs in the liquid also varies widely between the different models, ranging from 0%[210] to 20% branching.[216] A snapshot of the RMC simulation shown in figure 3.20 indicates that short, winding, unbranched, hydrogen bonded chains dominate the liquid state.

Integration of $g_{HF}^{RMC}(r)$ to $r_{\text{min}} = 2.15$ Å, reveals only 8% of the molecules form branched chains, this compares to values of 3.5% predicted by the ab initio simulation[228] and 7% predicted by the polarizable potential model.[204,206]

3.4 CONCLUSIONS

Despite the inherent difficulty of sample confinement, handling and extraction of the diffuse scattering signal, we have presented the first experimental description of the structure of hydrogen fluoride at the partial structure factor level. Liquid hydrogen fluoride at the temperature and pressure of this measurement is consistent with the presence of short, bent, strongly hydrogen-bonded chains, with strong interchain interactions and very little branching. Despite the strength of the hydrogen bond in the

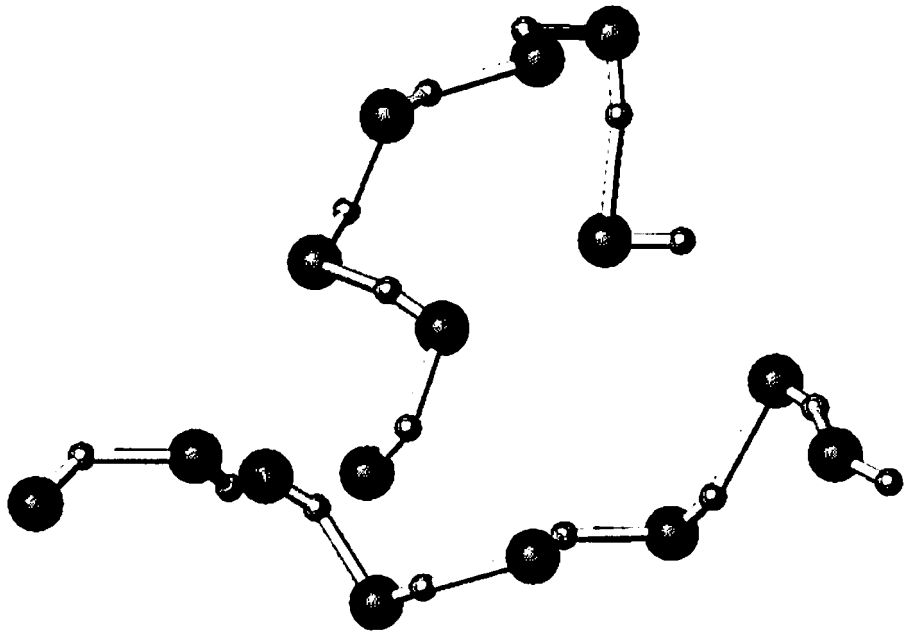

Figure 3.20: Two representative molecular groups taken from the RMC simulation show winding hydrogen bonded chains dominate the liquid structure.

liquid, the chains appear to be truncated at a length of around an average of 7 molecules per chain.

CHAPTER 4: THE STRUCTURE OF LIQUID AND SUPERCRITICAL BORON TRIFLUORIDE

Part of the work reported in this chapter has been published in the *Journal of Chemical Physics* [257] and is included in its published form in the appendix.

All Reverse Monte Carlo simulations and the subsequent triplet extractions were performed by Ms. J. E. Siewenie of Argonne National Laboratory. All molecular orbital calculations were performed by Dr. J. F. C. Turner of the University of Tennessee

4.1 INTRODUCTION

Whereas the structural chemistry of the first row elements from carbon onwards in increasing atomic number is comparatively simple in terms of the bonding types present, it has been stated that boron displays the widest variation in bonding types and structural motifs in the periodic table.[173] The reason for this wide range of bonding motifs is due to the electronic configuration of boron, namely $2s^2 2p^1$. The fact that there are fewer electrons than energetically available orbitals ensures that neutral boron compounds are automatically electron deficient in the sense that the completion of the octet can only be obtained through the employment of multi-center multi-electron bonding.

The boron halides are archetypes for electron deficient molecules. The σ-framework of the halides are composed of 2-center 2-electron bonds, accounting for the 6 bonding electrons.

The boron trihalides are prototypical Lewis acids and have wide application as catalysts in industry and academic chemical research. They are common catalysts in Friedel-Crafts alkylation reactions as well as in other Lewis acid-catalyzed reactions.[258,259] The simplicity of the molecular structure of boron trifluoride, together with the small size of the component atoms, has ensured that BF_3 has been widely studied as an archetype for Lewis acidity.

4.1.1 STRUCTURAL CHEMISTRY OF BX_3 IN THE GAS PHASE AND SOLID STATE

The molecular structure of BF_3, determined by electron diffraction in the gas phase[260-262] and confirmed by spectroscopic studies[260,262-265] consists of a rigorously trigonal planar structure of D_{3h} symmetry with three fluorine atoms ligating the central boron atom, as shown in figure 4.1. The boron-fluorine distance determined in these studies is r_{BF} = 1.3133 Å, together with a fluorine-fluorine distance of r_{FF} = 2.2747 Å. BCl_3, BBr_3 and BI_3 also adopt D_{3h} symmetry in the gas phase and only differ from BF_3 in the B-X bond length.[266] There is no notable difference between BF_3 and the rest of the BX_3 series.

The solid-state structures of the heavier congeners of the BX_3 group namely, BCl_3, BBr_3 and BI_3, all crystallize in the hexagonal space group $P6_3/m$ and adopt a layered packing motif with few intermolecular interactions.[267-270] These structures are shown in figure 4.2. Moreover, solid BCl_3, BBr_3 and BI_3 all have similar infra-red spectra that are in accordance with the group theoretical predictions.[266,271] Infra-red spectra of solid BF_3 are different, as the spectrum of the solid shows the presence of the υ_1 breathing mode, which is forbidden for a purely D_{3h} molecule.[271-273] This result allowed the prediction of B-F···B bonds in solid BF_3 prior to the X-ray structural determination as well as the prediction that BF_3 would crystallize in a lower symmetry space group with more molecules per unit cell than the other boron trihalides.[271,273,274]

The published structures of boron trifluoride in the solid state are complex and all show intermolecular interactions that are not present in the other BX_3 solid state

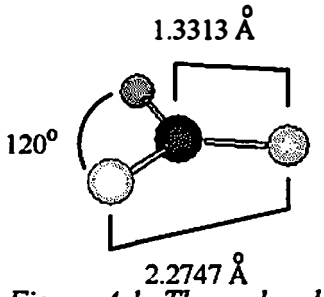

Figure 4.1: The molecular structure of BF_3 in the gas phase.[266]

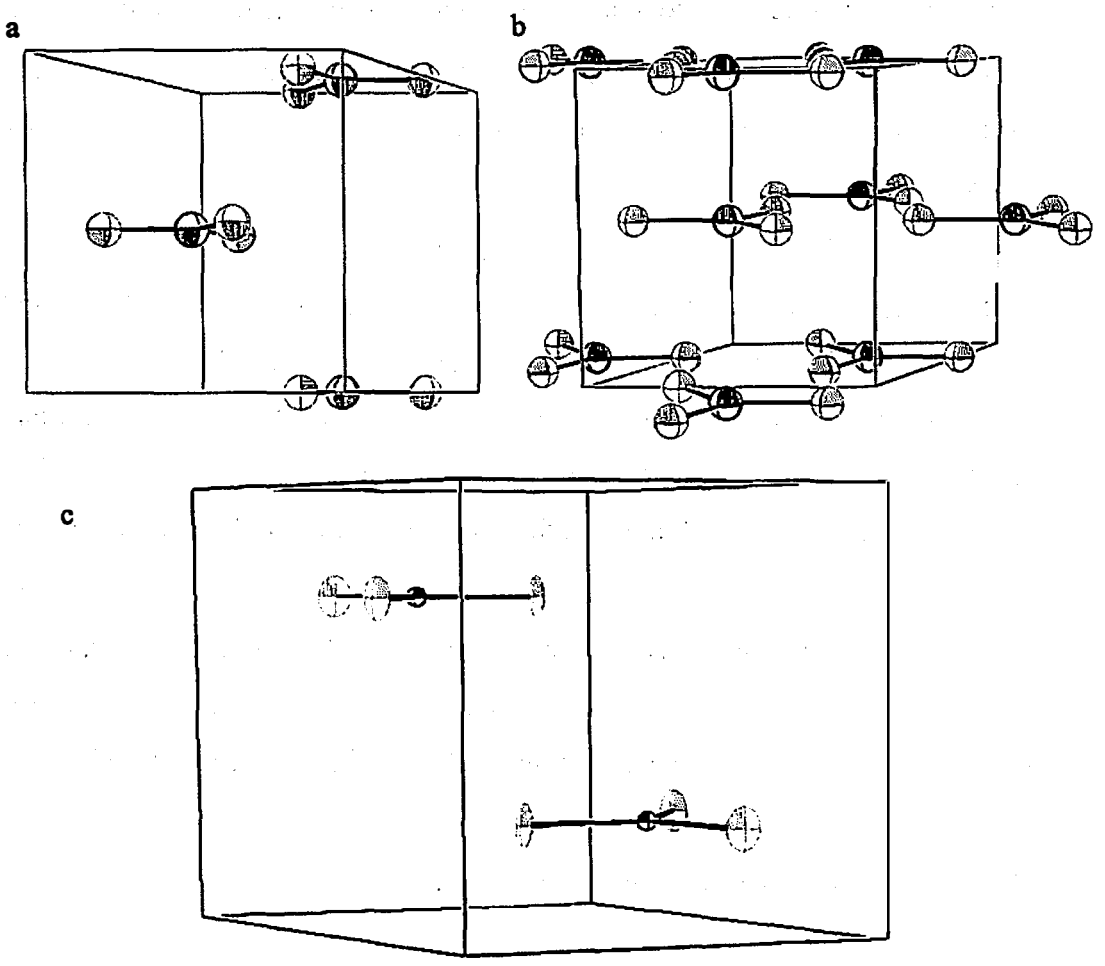

Figure 4.2 Crystalline structures of a)BCl_3, b)BBr_3 and c) BI_3.[267-270]

structures.[271,275-277] At 128 K, BF_3 crystallizes in the triclinic space group $P\bar{1}$ and contains 8 molecules in the unit cell.[275] This structure is shown in figure 4.3 and from this along with a metastable phase of BF_3 at 142 K which is in the orthorhombic space group $P2_1/c$ with 8 molecules in the unit cell.[276,277]

The structure of BF_3 in the solid state at 128 K consists of a *pseudo* trigonal bipyramidal [3+2] coordinate boron, forming a chain structure parallel to the *c* axis.[275] In other words each boron atom has 3 intramolecular contacts from the molecule itself, with an additional 2 intermolecular boron-fluorine contacts. It can also be seen that in each structure there is one fluorine on each boron atom that has no intermolecular contacts. The B-F bond length is in this structure is $r_{BF} = 1.279 - 1.300\text{Å}$ and $F\hat{B}F = 118° - 120.8°$.

4.1.2 DESCRIPTION OF THE LIQUID STATE

In the liquid state there is some evidence of intermolecular association. Infra-red spectroscopy measurements show that in liquid BF_3, the formally forbidden υ_1 breathing mode is observed. This implies that the local symmetry of the molecule is perturbed, allowing this transition to occur.[272] It has also been noted that the viscosity data for liquid BF_3 may indicate some degree of molecular association as the viscosity is reported as being "unusually high" and the $\log\eta - 1/T$ function, where η is the viscosity measured in centipoises, has been reported as being non-linear.[272,278]

Trouton's constant is an empirical measure which is defined as

$$\frac{\Delta H_{vap}}{T} \tag{4.1}$$

where ΔH_{vap} (J g^{-1}) is the enthalpy of heat of vaporization and T represents the temperature of the boiling point of the liquid in question in degrees centigrade. The Trouton's constant for BF_3 in comparison with other associated and non-associated fluids is shown in table 4.1. From this table, it is clear that BF_3 has a Trouton's constant

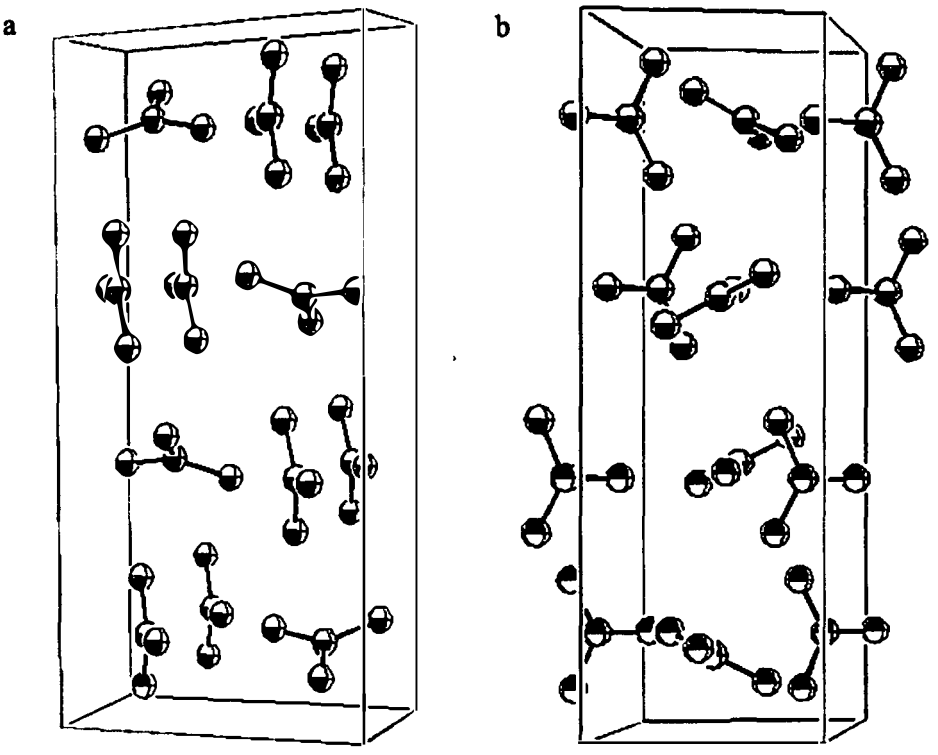

Figure4.3: Crystalline structures of boron trifluoride at a) 128 K and b) 142 K.[275-277]

Table 4.1: Trouton's constant for BF_3 compared with associated and non associated fluids.

Compound	Trouton's constant/ $Jg^{-1}C^{-1}$	Compound	Trouton's constant/ $Jg^{-1}C^{-1}$
BF_3	106.69	He	23.85
H_2O	109.20	CH_3OH	104.18
CH_4	82.84	CH_3CH_2OH	111.29

comparable to associated fluids such as water, methanol and ethanol whereas non-associated fluids such as liquid helium and methane show have much lower values.[278,279]

Later studies showed that the entropy of evaporation is not much larger than the average for a non-associated fluid and that the measured viscosity of BF_3 in the liquid phase shows a $\log\eta - 1/T$ function that is linear within experimental error.[272,280] Though there is some discrepancy in the literature concerning the degree of association by these thermodynamic measurements, bulk thermodynamic measurements provide no structural information about the liquid in question and do not discount the possibility of association on a local level.

4.1.3 LEWIS ACID BEHAVIOR OF BX_3

The strength of the Lewis acidity of the boron trihalides has often been assumed to increase with the atomic number of the halide, with BF_3 being atypically weak. The rationale for this chemical behavior is usually based on the assumed decreasing strength of $p\pi - p\pi$ "back-bonding" interactions between the ligating halide and the boron center with increasing halide atomic number. $p\pi - p\pi$ back-bonding refers to the donation of electron density associated with the *p*-orbitals from halogen atoms to an unoccupied orbital at the boron center and is shown pictorially in figure 4.4.

The back-bonding model derives mainly from a valence bond description which was first conceived by Pauling to account for the inaccuracy in the calculated covalent

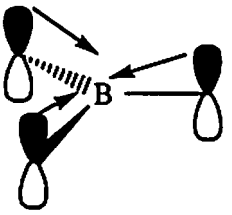

Figure 4.4: pπ- pπ back-bonding in BX_3

F-B BF_3 bond length which is much shorter than expected.[281,282] This model is still used extensively to explain bond strengths and stabilities observed in certain Lewis acid-base complexes such as the boron trihalide·ammonia series where $BF_3{\cdot}NH_3 < BCl_3{\cdot}NH_3 < BBr_3{\cdot}NH_3$,[173,283] however this explanation is not fully supported by group theoretical considerations where bonding is shown to be delocalized over all of the atoms in the molecule.[284-286] The molecular orbital diagram for any BX_3 is shown in figure 4.5. It is clear from this diagrams that the halogen ligands give rise to orbitals which do not have any symmetry equivalent from the central boron atom. This indicates that the electrons which occupy these orbitals, namely e', e" and a_2' are not involved directly in bonding but that the electron density in BX_3 is delocalized over the halogen ligands rather than bonding to the boron center. Moreover, charge calculations based on an ionic model, which is a justifiable model based on coordination arguments, show that the fluorine atoms in BF_3 carry a significant charge indicating that a large degree of back-bonding to the central boron atom is not likely.[286] The experimental evidence for the trend of acidity observed in the boron trihalide series is not uniformly supportive on close examination as the Lewis acidity is base dependent. BF_3 has shorter stronger B-X bonds the other boron trihalides, these bonds are necessarily lengthened upon complexation with a Lewis base when considering a ligand close-packing model.[287-289] In this model, the B-X bonds are more easily lengthened or distorted with the increasing atomic number of the halide ligand where the larger halides give rise to much lower bond energies. In the case of strong Lewis bases such as NH_3, the parent Lewis acid must be heavily distorted from its monomeric D_{3h} symmetry to accommodate the B-N bond, therefore the stability of the $BX_3{\cdot}NH_3$ complexes is in the order mentioned above.

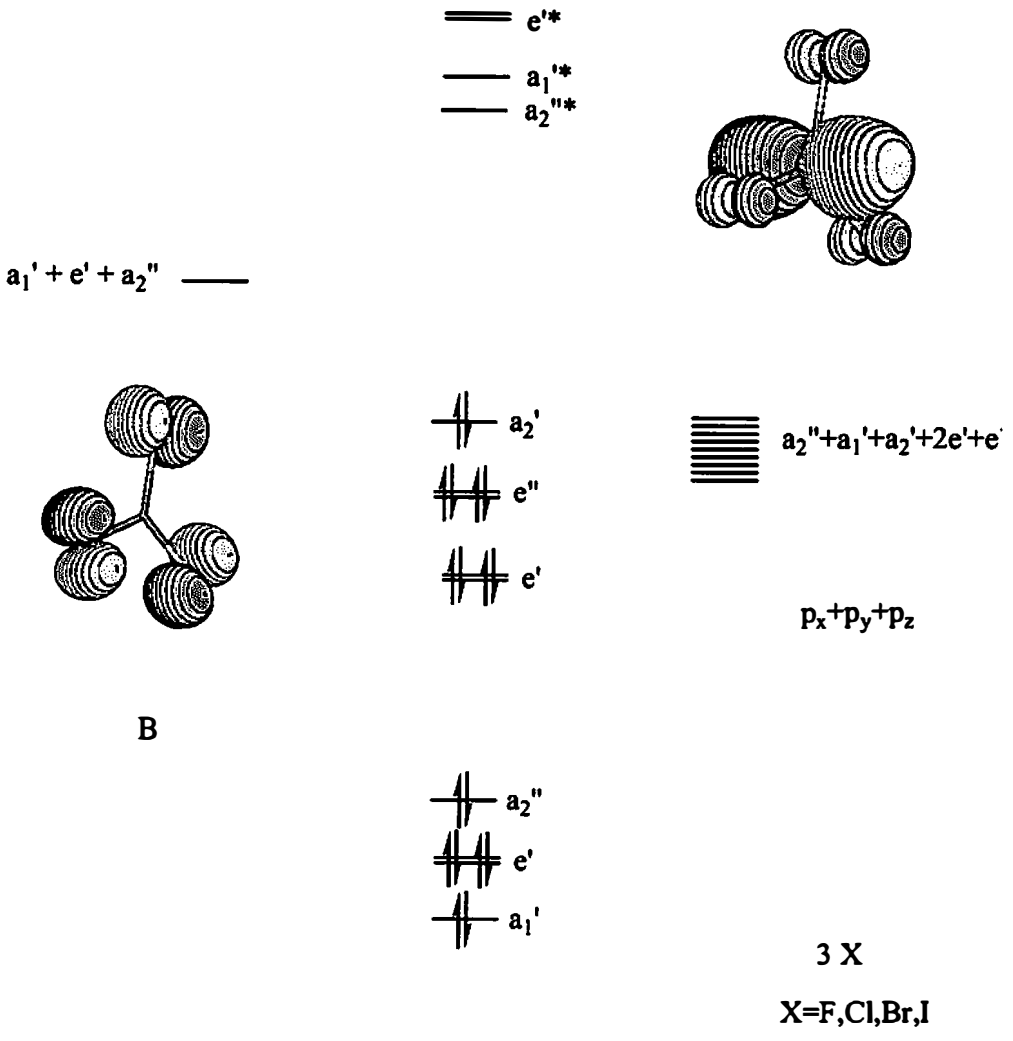

Figure 4.5: Molecular orbital diagram for BX_3 where X is a halogen. The HOMO (a_2') is shown on the left and the LUMO(a_2") is shown on the right.

However, with weak Lewis bases such as CH_3F, CO or CH_3CN the parent Lewis acid is virtually undistorted leading to an opposite trend in the strength of complexation observed, where the acidity of BF_3 is the highest.[287,290] This is shown pictorially in figure 4.6. This evidence is also corroborated by the solid state structure of the BX_3 series. The heavier congeners have fewinteractions that imply intermolecular Lewis acid-base behavior. BF_3 shows strong inter-molecular interactions in the solid state suggesting that intermolecular Lewis acid-base behavior is indeed more probable in comparison.

4.1.4 ASSESSMENT OF ASSOCIATION IN LIQUID AND SUPERCRITICAL BF_3

In the liquid state there is evidence that the molecular D_{3h} symmetry is perturbed. In order to elucidate the propensity for intermolecular Lewis acid-base interactions in a phase with no *a priori* ordering, the liquid structure of BF_3 was closely examined in the supercritical state and just above the temperature of fusion in the normal fluid using neutron diffraction. Other neutron diffraction data sets were also recorded at two temperatures at which the sample is liquid and one at an additional supercritical temperature. By structurally examining a sample where the densities are of a similar magnitude to that of the solid but where there is an absence of long-range order, the degree of association between the molecules may be assessed.

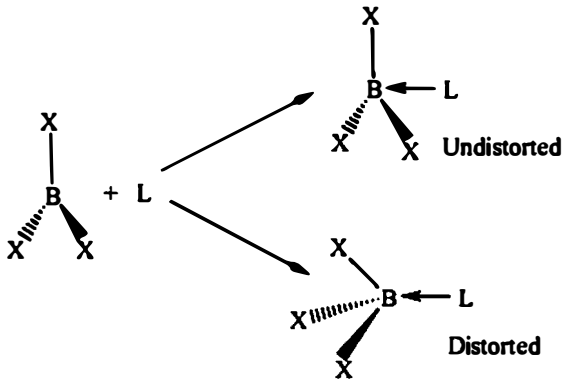

Figure 4.6: Possible Lewis acid-base adduct geometry for BX_3.

In principle, completely isotropic arrangements of molecules may occur in the absence of any intermolecular interactions. Given the observation of the [3+2] structural motif in the solid and the spectroscopic evidence,[272] there is reason to believe that these intermolecular Lewis interactions may exist in the pure liquid, implying that this motif is energetically favorable.

This interpretation is additionally supported by infrared measurements in the liquid phase, which show no indication of strong dimer formation,[272] the spectrum of the dimer having been recorded from matrix isolation experiments.[291,292] Though some of the other bulk liquid evidence supports a non-associated fluid, the infra-red spectrum recorded from the liquid phase shows the presence the forbidden υ_1 band. It is noteworthy that environmentally induced changes in transitions have been observed before, especially on changing phase from, for example, the solution phase to the solid state, where degeneracies are often raised due to a lowering of local symmetry. The appearance of forbidden bands is rarer on phase change though recently, elegant calculations have been used to determine the mechanism of the ingression of forbidden bands, admittedly in very different systems.[293-295]

4.2 EXPERIMENTAL

4.2.1 SAMPLE HANDLING AND PREPARATION

$^{11}BF_3$ was purchased from Ozark Fluorine and used without further purification. Mass spectroscopic measurements estimated the ^{10}B concentration to be approximately 0.35% and the sample also contained a small amount of hydrocarbon contamination. Using a Monel/316 SS high vacuum line described in detail in chapter 6, 2.368g (0.034 mol) of $^{11}BF_3$ were condensed into a volume-calibrated sample container constructed from titanium-zirconium alloy,[296] under high vacuum and sealed with a Swagelok® 1/8" stainless steel needle valve. The sample cell volume was found to be 3.11 cm^3 by both water calibration and gas calibration measurements. As the BF_3 pressure in the sample container was autogenous, the phase of BF_3 measured was controlled by

adjusting the temperature of the sample. Salient thermodynamic data for BF_3 are shown in table 4.2.

4.2.2 NEUTRON MEASUREMENTS

Diffraction data were collected at 300±2 K, 266±2 K, 253±2 K, 203±2 K, and at 153±2 K over a Q range of 0.3-40 $Å^{-1}$. The neutron diffraction data were corrected for container scattering, attenuation, absorption, multiple scattering, and inelastic scattering using standard analysis procedures.[14] Because there was a small amount of hydrocarbon present in the sample and a small proportion (0.35%) of highly absorbing ^{10}B which contributed to the background corrections, initially the 300 K data were constrained in the first peak of the real space data to give a coordination number of 3.00±0.10 F atoms around a single boron atom and 1.00±0.10 B atom bonded to each fluorine atom at r_{min} of the first peak in real space. In order to satisfy this coordination number constraint, the number density of the sample at 300 K was adjusted accordingly. The remaining data sets were corrected by constraining oscillations at high Q in $S_{BF_3}(Q)$ to match that of the 300 K data by adjusting the number density at each different state point. The effective number densities for each data set are reported in table 4.2. This constraint was verified by the coordination number of the B-F peak in the real space

Table 4.2: Thermodynamic values for BF_3.

T_M / K		146	T_B / K		173
$T_{critical}$ / K		260.8	$P_{critical}$ / *MPa*		26.55
$p(T)^a$ / *kPa*					
T/K	153	203	253	266	300
p	18.57	700.03	5152.90	7534.95	17113.57
$\rho(T)^b$ / *atoms*^{1} $Å^{-3}$					
T/K	153±2	203±2	253±2	266±2	300±2
ρ	0.042	0.037	0.030	0.025	0.023

[a] *calculated via* $\lg P = 4.69215 - \left(\frac{663.463}{T - 30.795}\right)$ [b] *effective density*

transformation of each data set. The coordination numbers with respect to the number of F atoms around a single B atom are 3.01 ± 0.10, 3.03 ± 0.10, 3.00 ± 0.10, and 2.95 ± 0.10 in 266 K, 253 K, 206 K and 153 K data sets, respectively. The coordination numbers with respect to the number of boron atoms covalently bound to each F atom are 1.00±0.10, 1.01±0.10, 1.00±0.10 and 0.98±0.10 in 266 K, 253 K, 206 K and 153 K data sets, respectively.

4.2.3 RMC ANALYSIS

In order to analyze the data in a more quantitative manner, RMC modeling was undertaken at 153K and at 300K using a system of 1000 boron atoms and 3000 fluorine atoms, constrained to satisfy the neutronically determined densities and the structurally determined intramolecular constraints of distance and coordination number. RMC modeling and its necessary caveats are described in more detail in chapter 3, section 3.2.6.

4.2.4 EXPERIMENTAL DATA

The corrected diffraction data at the five experimental temperatures for $^{11}BF_3$ are shown in figure 4.7 and the associated real space pair correlation functions in figure 4.8, shown as $T(r) = 4\pi\rho r G_{BF_3}(r)$ where ρ is the density (Table 4.2). RMC fits to the diffraction data are shown in figure 4.9, with the associated real space pair correlation functions in figure 4.10, again in terms of $T(r)$. In addition, the partial structure factors derived from the RMC fits are shown in figure 4.11 and the associated partial pair correlation functions in figure 4.12.

4.3 DISCUSSION

The total pair correlation function for BF_3, $G_{BF_3}(r)$, with the appropriate weighting factor for each partial pair correlation function is written as follows,

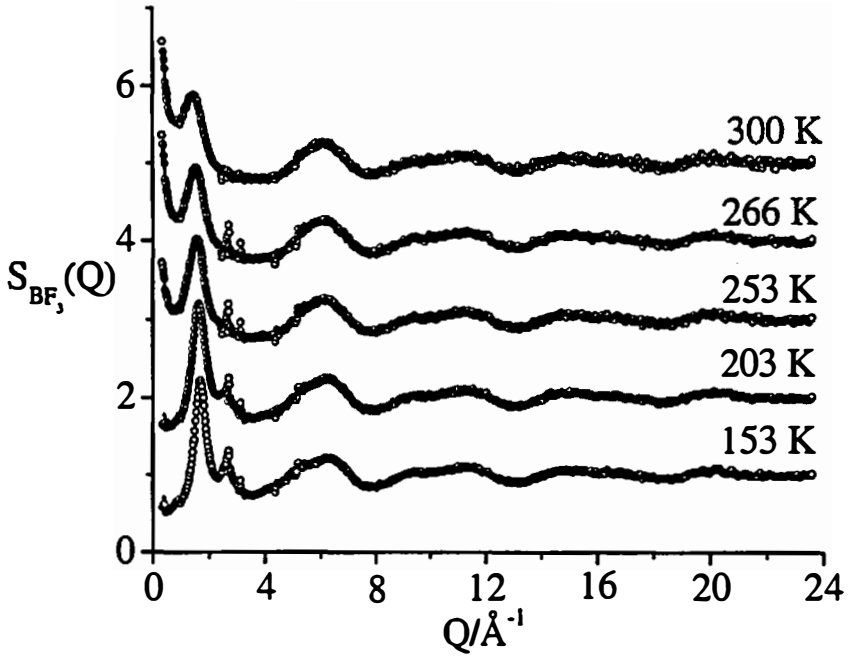

Figure 4.7: Total structure factor data for BF_3. $S_{BF_3}(Q)$ at 153 K, $S_{BF_3}(Q)$ + 1 at 203 K, $S_{BF_3}(Q)$ + 2 at 253 K, $S_{BF_3}(Q)$ + 3 at 266 K and $S_{BF_3}(Q)$ + 4 at 300 K. The circles are the data and the line is the smoothed fit to the data.

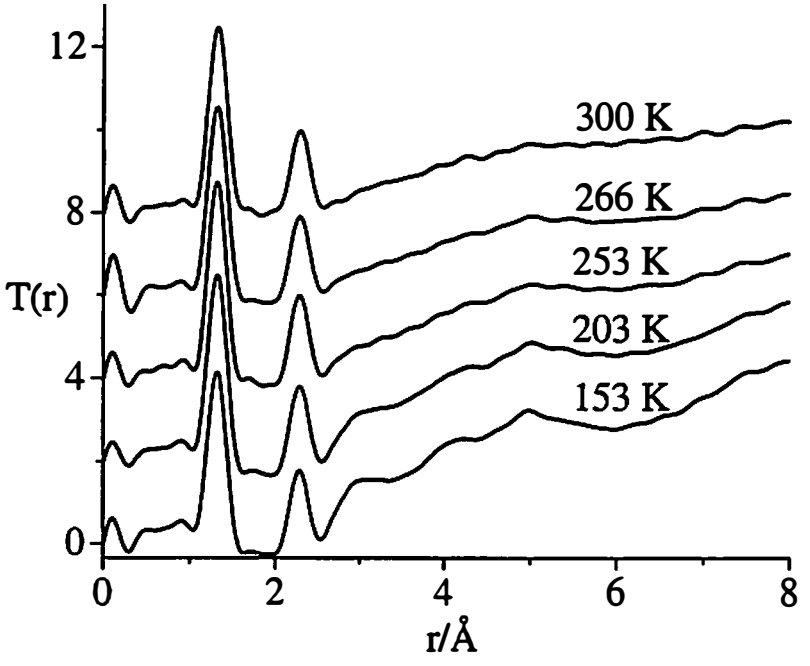

Figure 4.8: Total pair correlation function for BF_3, $T(r) = 4\pi\rho r G_{BF_3}(r)$. $T(r)$ at 153 K, $T(r)$ + 2 at 203 K, $T(r)$ + 4 at 253 K, $T(r)$ + 6 at 266 K and $T(r)$ + 8 at 300 K.

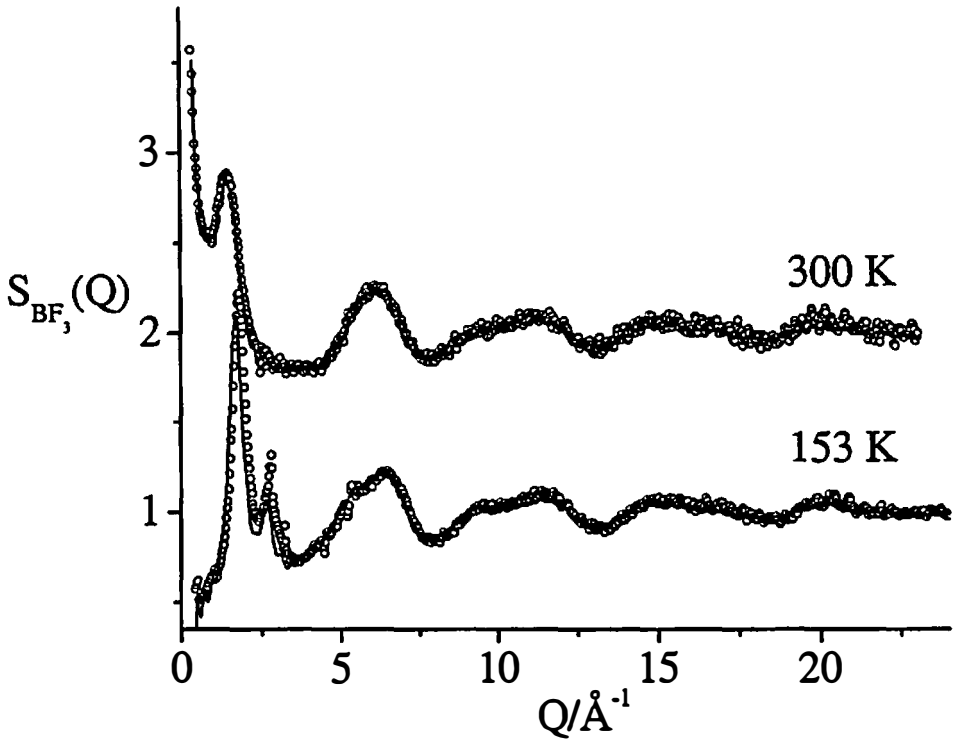

Figure 4.9: Total structure factor data for BF_3 compared with RMC fits to the data. $S_{BF_3}(Q)+1$ at 300 K and $S_{BF_3}(Q)$ 153 K. The circles represent the diffraction data and the solid line shows the RMC fit to the data.

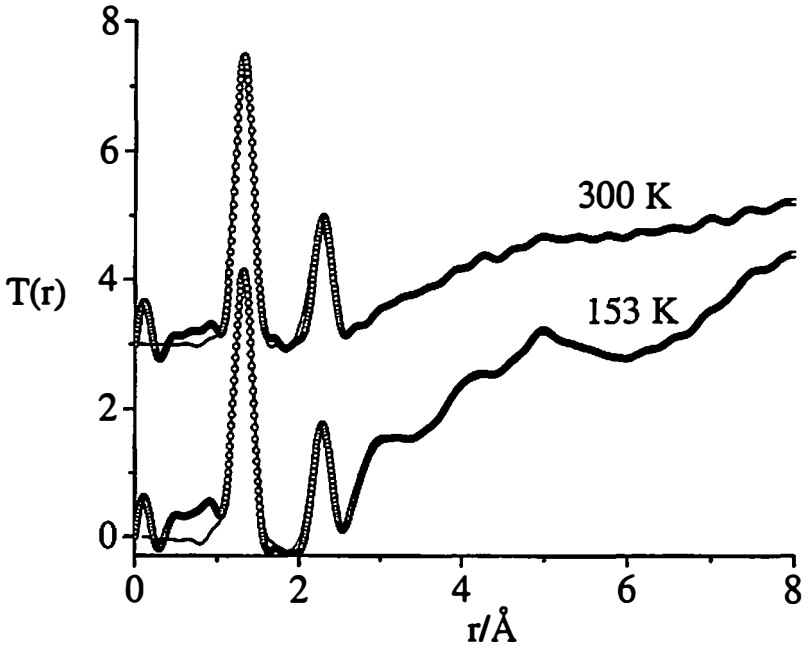

Figure 4.10: Total pair correlation function for BF_3 compared with RMC fits to the data. $T(r)$ at 153 K and $T(r)+3$ at 300 K. The circles represent the diffraction data and the solid line shows the RMC fit to the data.

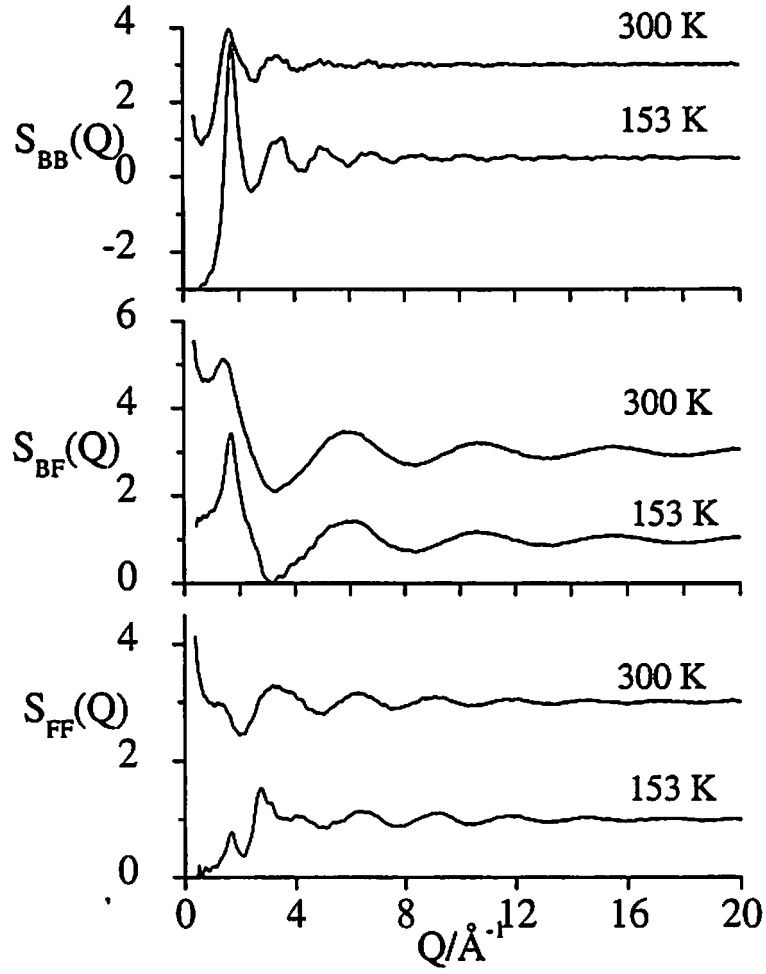

Figure 4.11: RMC generated partial structure factors for $^{11}BF_3$. $S_{\alpha\beta}(Q)$ at 153 K and $S_{\alpha\beta}(Q)+2$ at 300 K ($\alpha = B, F$ and $\beta = B, F$).

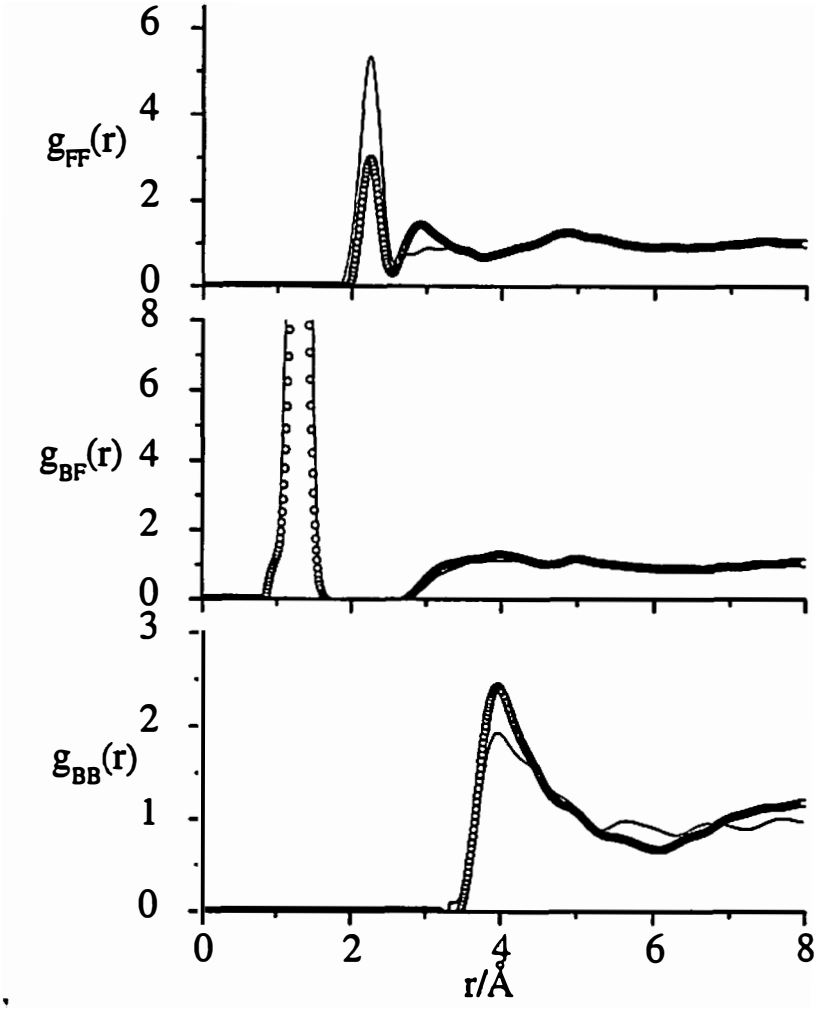

Figure 4.12: RMC generated pair correlation functions for $^{11}BF_3$. The circles represent the 153 K data and the solid line represents the 300 K data ($\alpha = B, F$ and $\beta = B, F$).

$$G_{BF_3}(r) = 0.079 g_{BB}(r) + 0.405 g_{BF}(r) + 0.517 g_{FF}(r) \quad (4.2)$$

From this equation, it is evident that the total structure factor is dominated by the fluorine-fluorine and boron-fluorine pair correlation functions, $g_{BF}(r)$ and $g_{FF}(r)$. The measurement of the total structure factor is an appropriate method to investigate the structure of the liquid, given the weighting constants for this system. This is fortunate as an isotopic substitution experiment on BF_3 is impossible as F is monoisotopic and ^{10}B has a high absorbance cross section. The neutron scattering constants for boron and fluorine are shown in table 4.3. As the diffraction patterns and their associated pair correlation functions both contain contributions from both the intra- and intermolecular structure, the discussion of the data and associated real space functions is divided into the intramolecular structure and the intermolecular structure.

4.3.1 RADIAL INTRAMOLECULAR STRUCTURE

The radial molecular structure is easily identified in figures 4.8 and 4.10, with the boron-fluorine and fluorine-fluorine intramolecular vectors apparent at $r_{BF} = 1.32 \pm 0.02$ Å and $r_{FF} = 2.29 \pm 0.02$ Å respectively. The structure is also consistent with the presence of a three-coordinate boron atom with D_{3h} symmetry. D_{3h} symmetry depends on r_{BF} and r_{FF} as well as the F$\hat{B}$F angle. The F$\hat{B}$F angle is calculated from the distances shown in figure 4.8 by the geometrical relation

$$(r_{FF})^2 = (r_{BF})^2 + (r_{BF})^2 - 2(r_{BF})(r_{BF})\cos\angle\text{FBF} \quad (4.3)$$

and was found to be 120.32^0 at all temperatures measured. In addition, at each

Table 4.3: Neutron scattering constants for boron and fluorine.

Isotope	Natural abundance	b_{coh}/fm	σ_{incoh}/barns	σ_{scatt}/barns	σ_{abs}/barns
^{10}B	0.20	-0.1-1.066*i*	3	3.1	3835
^{11}B	0.80	6.65	0.21	5.77	0.0055
^{19}F	1	5.654	0.0008	4.018	0.0096

temperature the intra-molecular bond distances are identical such that any temperature dependence on the bond length is not detectable. In each total pair correlation function there is a sharply defined minima after the appearance of the two intramolecular peaks at 2.55±0.09 Å (Figure 4.8). This distance corresponds with the radius of BF_3 calculated from the density and assuming it is spherical and that there is no isotope effect on the structure from ^{11}B ($r_{density} = 2.53Å$).

The associated contribution to the diffraction pattern from each intra-molecular partial structure factor is shown in figure 4.13 from both the data measured and the subsequent RMC fits to the data at 153 K and 300 K. In each case, these partial structure factors are multiplied by Q for clarity.

D_{3h} symmetry is known to be lowered both computationally and experimentally upon complex formation.[290,297-310] Given that the infrared spectroscopic studies on weakly bound systems show a lengthening of r_{BF} in all cases, the measurements presented here at all temperatures show a distance which is in accord with the unperturbed molecule. This can be interpreted qualitatively as indicating that any axial interaction in the liquid and the supercritical fluid is weak and if the molecule is structurally perturbed by this interaction, the perturbation to the molecule is below the sensitivity of these diffraction measurements.

4.3.2 RADIAL INTERMOLECULAR STRUCTURE

The contribution of the intermolecular structure to the diffraction pattern is shown in figure 4.14 with the real space counterpart shown in figure 4.15. From the RMC model that best fits the data, the partial structure factors and the associated pair correlation functions can be extracted, and these are shown in figure 4.16 and 4.17 respectively.

The greatest change occurs with the boron-fluorine and the fluorine-fluorine pair correlation functions, whereas the boron-boron pair correlation function remains almost unchanged with physical state. Given that the interaction between molecules will most

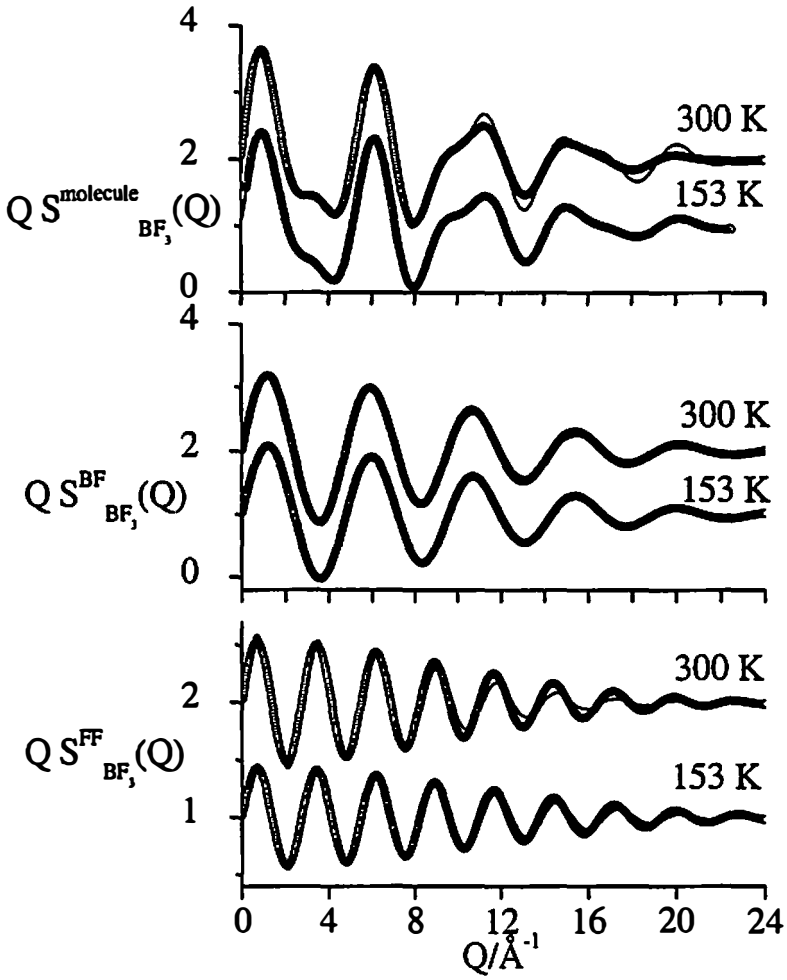

Figure 4.13: Intramolecular structure comparison, RMC (solid lines) and data (circles). $QS^{intra}_{BF_3}(Q)+1$ *at 300 K and* $QS^{intra}_{BF_3}(Q)$ *at 153 K. Intramolecular BF partial structure factor* $QS^{intra}_{BF}(Q)+1$ *at 300 K and* $QS^{intra}_{BF}(Q)$ *at 153 K. Intramolecular FF partial structure factor* $QS^{intra}_{FF}(Q)+1$ *at 300 K and* $QS^{intra}_{FF}(Q)$ *at 153 K.*

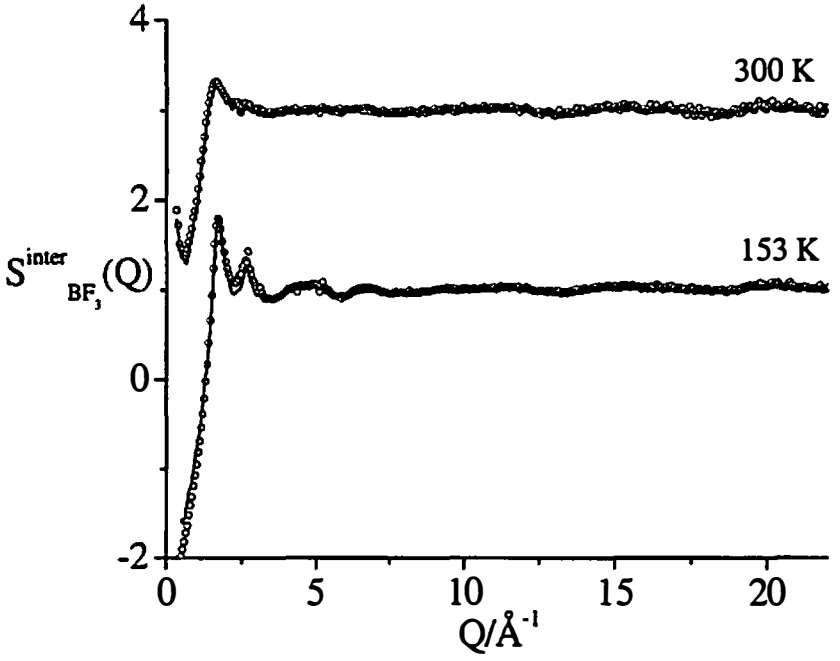

Figure 4.14: Intermolecular structure factor for BF_3, RMC (solid lines) and data (circles). $S^{inter}_{BF_3}(Q)+2$ at 300 K and $S^{inter}_{BF_3}(Q)$ at 153 K.

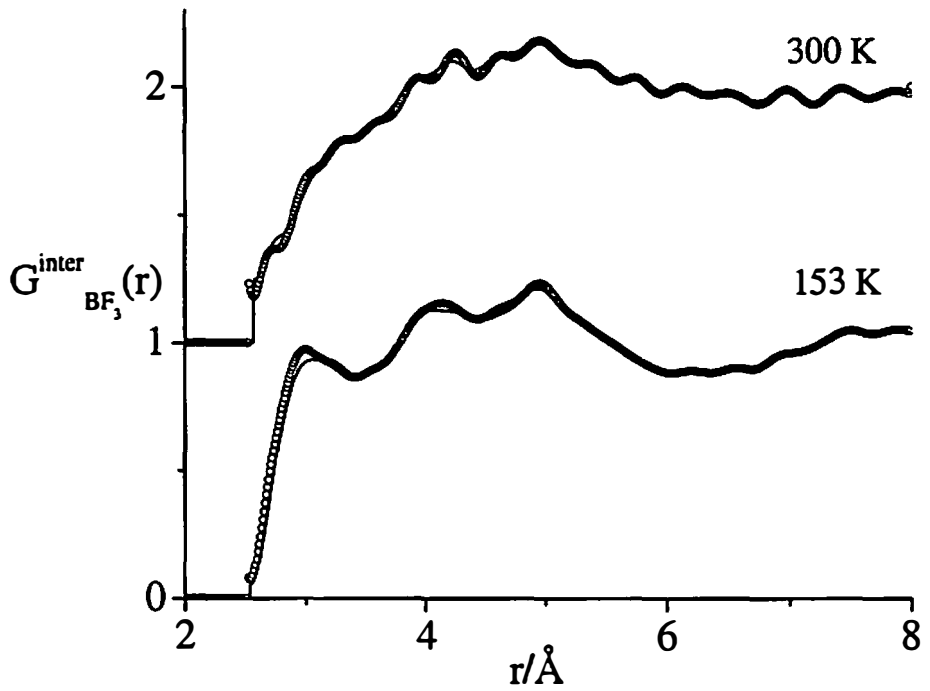

Figure 4.15: Intermolecular pair distribution function for BF_3, RMC (solid lines) and data (circles). $G^{inter}_{BF_3}(r)+1$ at 300 K and $G^{inter}_{BF_3}(r)$ at 153 K.

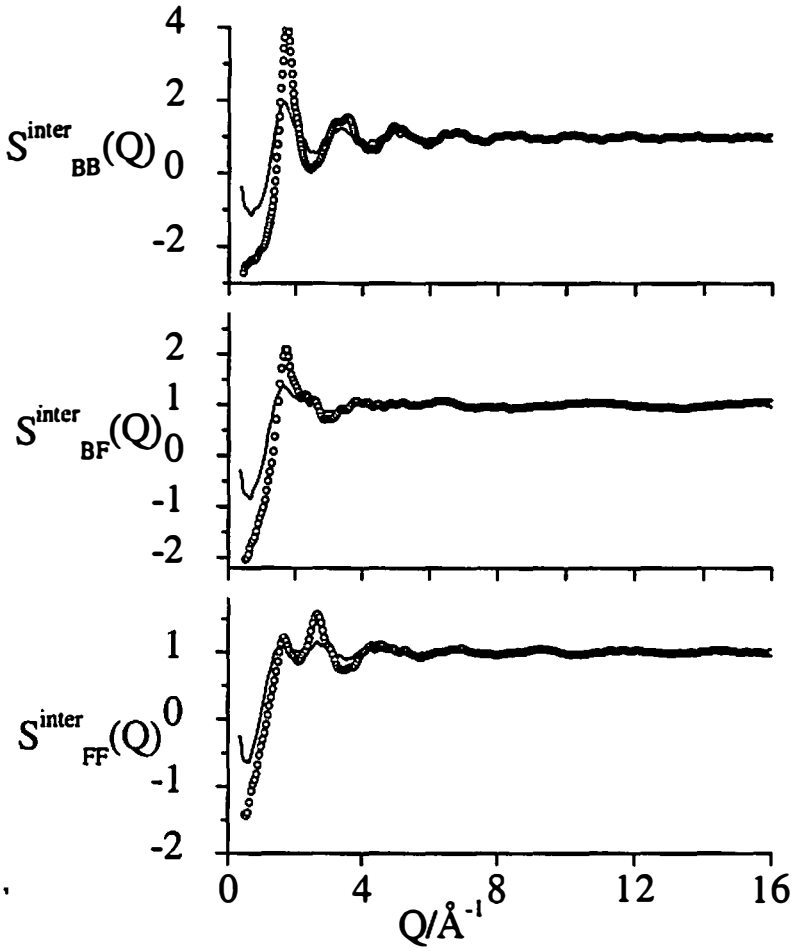

Figure 4.16: RMC generated intermolecular partial structure factors, $S_{\alpha\beta}(Q)$, for BF_3. The solid line represents the supercritical fluid at 300K and the circles represent the liquid phase at 153 K.

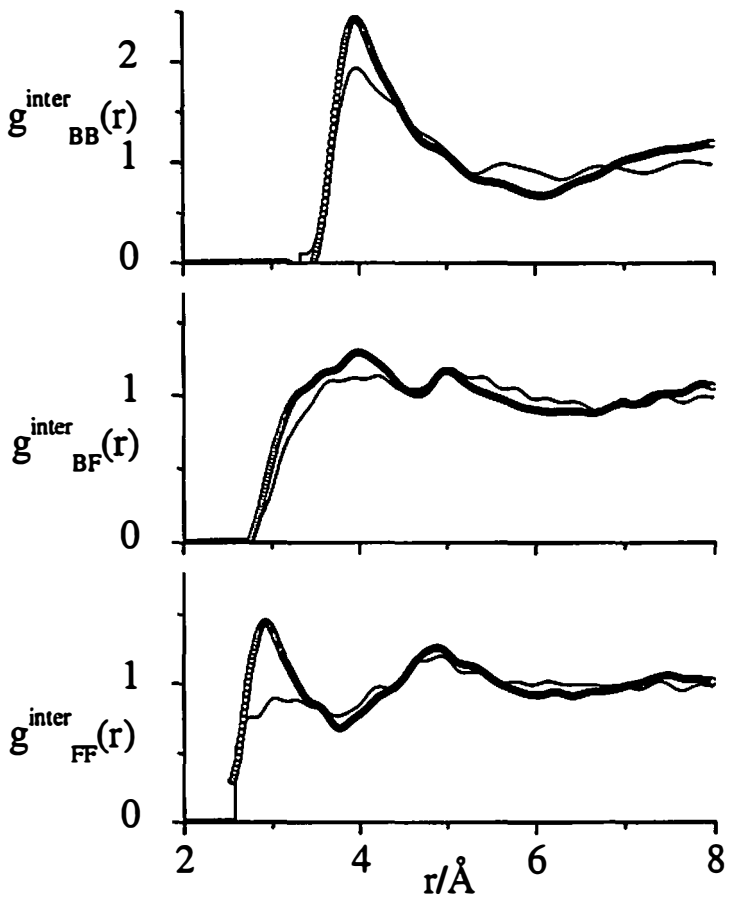

Figure 4.17: RMC generated pair correlation functions, $g_{\alpha\beta}(r)$, for BF_3. The solid line represents the supercritical fluid at 300K and the circles represent the liquid phase at 153 K.

probably involve a B-F interaction, the changes in both fluorine-dependent pair correlation functions is unsurprising.

The diffraction pattern for the two supercritical state points is also dominated by the limit behavior of $S(Q)$ and is mathematically described by

$$\lim_{Q\to 0}\left(\frac{d\sigma}{d\Omega}\right)=\left(\sum_i b_i\right)^2 k_B T\rho\chi_T \tag{4.4}$$

where k_B is Boltzmann's constant and χ_T is the isothermal compressibility at temperature T. This observation is in accord with other neutron diffraction experiments on supercritical fluids.[311-315]

It is clear from the total intermolecular pair correlation function, that the liquid is more structured than the supercritical fluid as the distribution of sites in the supercritical fluid is far broader. The population of sites is also more nearly equal, so that differences in spatial distribution of sites and the population of these sites in the supercritical fluid is smoother than in the liquid; this is in accord with the conventional picture of the structure of a gas, though the density of a supercritical fluid is greater than a normal gas. With the increase in density, there must necessarily be an increase in structure. However, the intermolecular contact remains almost identical in both phases measured, though the occupancy of this closest contact is much lower in the supercritical fluid. The liquid and supercritical phases are not simply the same structure, scaled according to the density; there are significant changes both in the occupied structural sites and the population of these sites whereas the closest intermolecular contact remains the same.

Figure 4.18(a(i)) shows the difference in structure between the liquid state and the supercritical state, where $4\pi\rho r G_{BF_3}^{153\,K}(r)-4\pi\rho r G_{BF_3}^{300\,K}(r)$ is shown. The major difference is the removal of structure in the first coordination sphere. Figure 4.18(a(ii)) is presented for comparison and shows $4\pi\rho r G_{BF_3}^{266\,K}(r)-4\pi\rho r G_{BF_3}^{300\,K}(r)$, i.e. the difference between the two supercritical states. In this case, the change in structure is far less and shows that the site distribution and site occupancy is more even in the

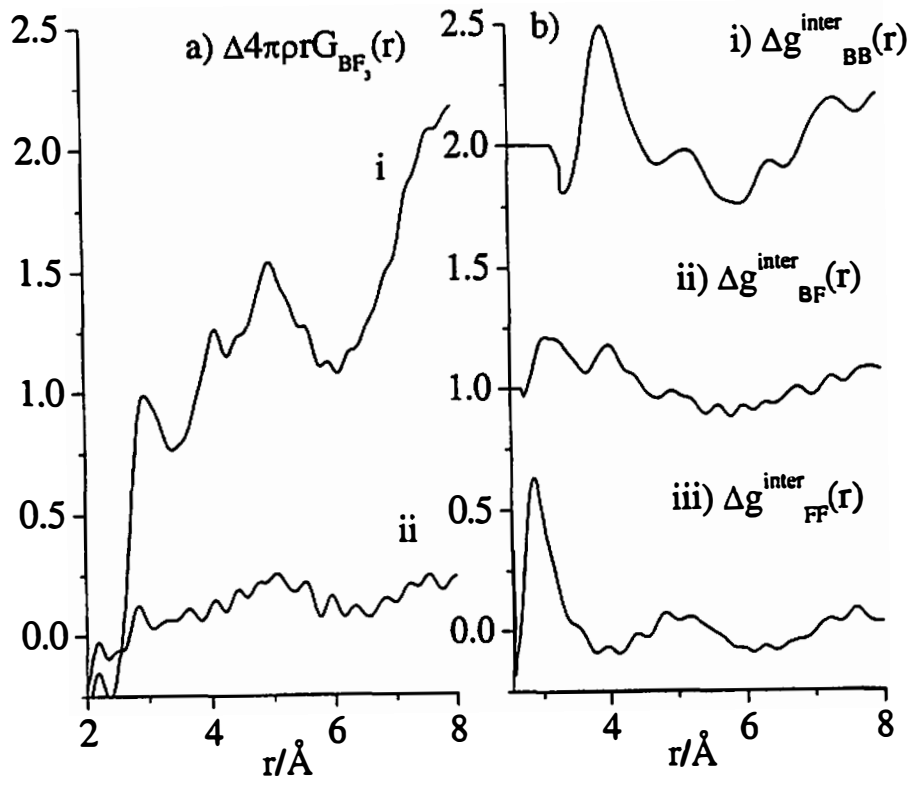

Figure 4.18: Intermolecular differences for the total pair correlation functions where $\Delta 4\pi\rho r G^{X}_{BF_3}(r) = 4\pi\rho r G^{X\,K}_{BF_3}(r) - 4\pi\rho r G^{300\,K}_{BF_3}(r)$. *i)* $\Delta 4\pi\rho r G^{153\,K}_{BF_3}(r)$ *and ii)* $\Delta 4\pi\rho r G^{153\,K}_{BF_3}(r)$ *and b) RMC extracted partials where* $\Delta g_{\alpha\beta}(r) = g^{153\,K}_{\alpha\beta}(r) - g^{300\,K}_{\alpha\beta}(r)$ *i)* $\Delta g_{BB}(r)$, *ii)* $\Delta g_{BF}(r)$, *and iii)* $\Delta g_{FF}(r)$

supercritical state, as expected. Figure 4.18(b) shows the difference in RMC partial pair distribution functions between the liquid and supercritical state, $\Delta g_{\alpha\beta}(r) = g_{\alpha\beta}^{153K}(r) - g_{\alpha\beta}^{300K}(r)$.

The diffraction pattern and in particular, the first sharp diffraction peak also shows that liquid BF_3 is not a layered liquid,[316,317] in contrast to assertions made from thermodynamic measurements of liquid mixture of Xe and BF_3 or BCl_3.[318] In this study Xe added to each of these boron trihalides is purported to result in a "breaking" of structure from a layered liquid. Though the liquid does show structure in the first coordination sphere, which is detailed below in the discussion of the angular structure extracted from the RMC model and which implies a disposition for some quasi- coplanar orientational preference of the BF_3 planes in the first coordination sphere only. There is no evidence for intermediate range order, which, for the purposes of this discussion, constitutes the definition of a layered liquid.

4.3.3 ANGULAR INTERMOLECULAR STRUCTURE

The radial structure of the fluid is directly observable from the Fourier transform of the diffraction data. As with any sample that displays macroscopic angular invariance, there are no angular data that are directly measurable. However, from the RMC model best fit to the data, it is possible to extract angular information from the model, with the same caveats as stated above for the reliability of the physical picture of a RMC model. The configuration of molecules generated by the RMC model is shown in figure 4.19 for the liquid at 153 K.

In order to visualize the angular structure from the RMC model, two sets of angular distributions were extracted. Figure 4.20 and table 4.4 shows the angles, distances and constraints that were used as parameters. θ was either fixed at $90 \pm 10^{\circ}$ or left unconstrained; α and β were then varied in 1° increments from 0° to 180°. At each angular section the number of boron or fluorine atoms at the intramolecular boron-fluorine bond distance were counted. This extraction was then performed at steps of

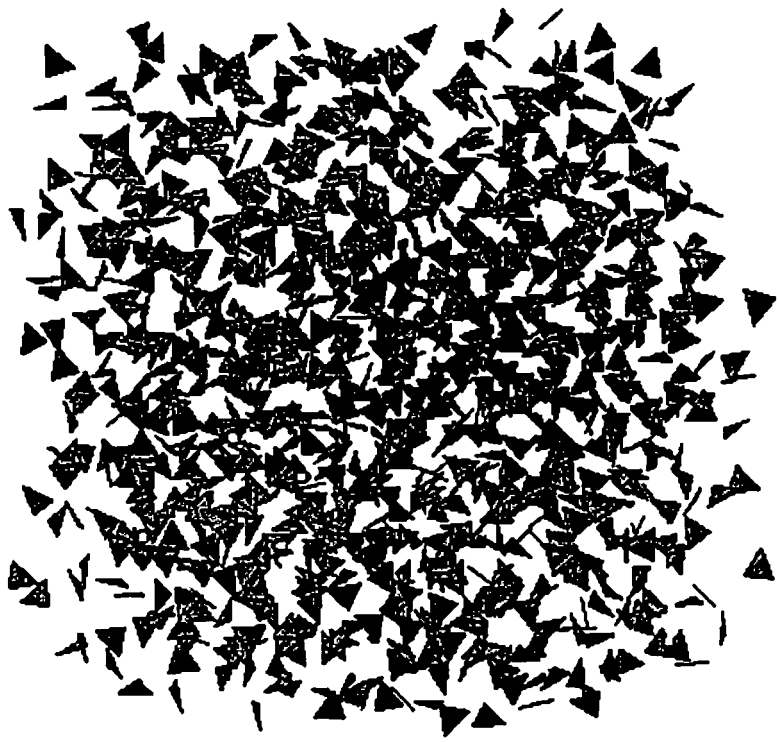

Figure 4.19: BF_3 molecules produced from the RMC model of the liquid at 153K.

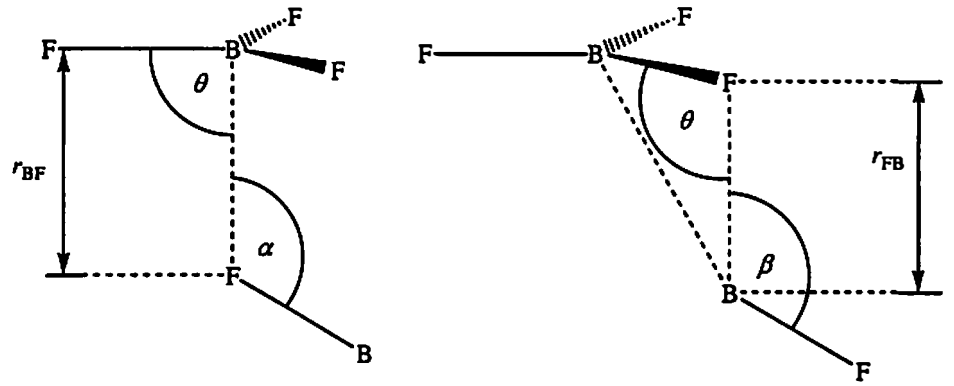

Figure 4.20: Salient angles for nearest neighbor interactions between two BF_3 molecules used as structural parameters for the extracted RMC fit to the data giving the angular distribution of (a) the BFB triplet and (b) the FBF triplet.

Table 4.4: Parameters for the angular extractions from the RMC models of BF_3.

Extraction	r_{BF}	r_{FB}	α	β	θ
BFB constrained	$2.5 \le r_{BF} \le 6.5$	-	$0 \le \alpha \le 180$	-	$90 \pm 10^{\circ}$
BFB unconstrained	$2.5 \le r_{BF} \le 6.5$				*unconstrained*
FBF constrained	-	$2.5 \le r_{FB} \le 6.5$	-	$0 \le \beta \le 180$	$90 \pm 10^{\circ}$
FBF unconstrained		$2.5 \le r_{FB} \le 6.5$			*unconstrained*

0.5 ± 0.25 Å along r_{BF} or r_{FB} (figure 4.20), giving a picture of the angular distributions in ½ Å shells around the average molecule. This type of extraction was performed on the fit to the lowest temperature data collected at 153 K and on the fit to the highest temperature data collected at 300 K. The angular extractions and the parameters are presented in table 4.4.

The results of these angular extractions are shown in figures 4.21 and 4.22. Figures 4.21(a) and (b) show the unconstrained BFB triplets for the normal fluid and supercritical fluid, respectively and figures 4.21(c) and (d) show the same for the FBF triplet. Figures 4.22(a) and (b) show the constrained BFB triplets for the normal fluid and supercritical fluid, respectively and figures 4.22(c) and (d) show the constrained FBF triplets in a similar manner.

At the longest distances examined around the average molecule, i.e. beyond the first coordination sphere, in both the supercritical and normal fluid, the angular distribution is isotropic, that is there is no net angular distribution. This shows that any ordering in the liquid and supercritical fluid is confined to the first coordination sphere of the molecule and that there is no layering or intermediate range order.

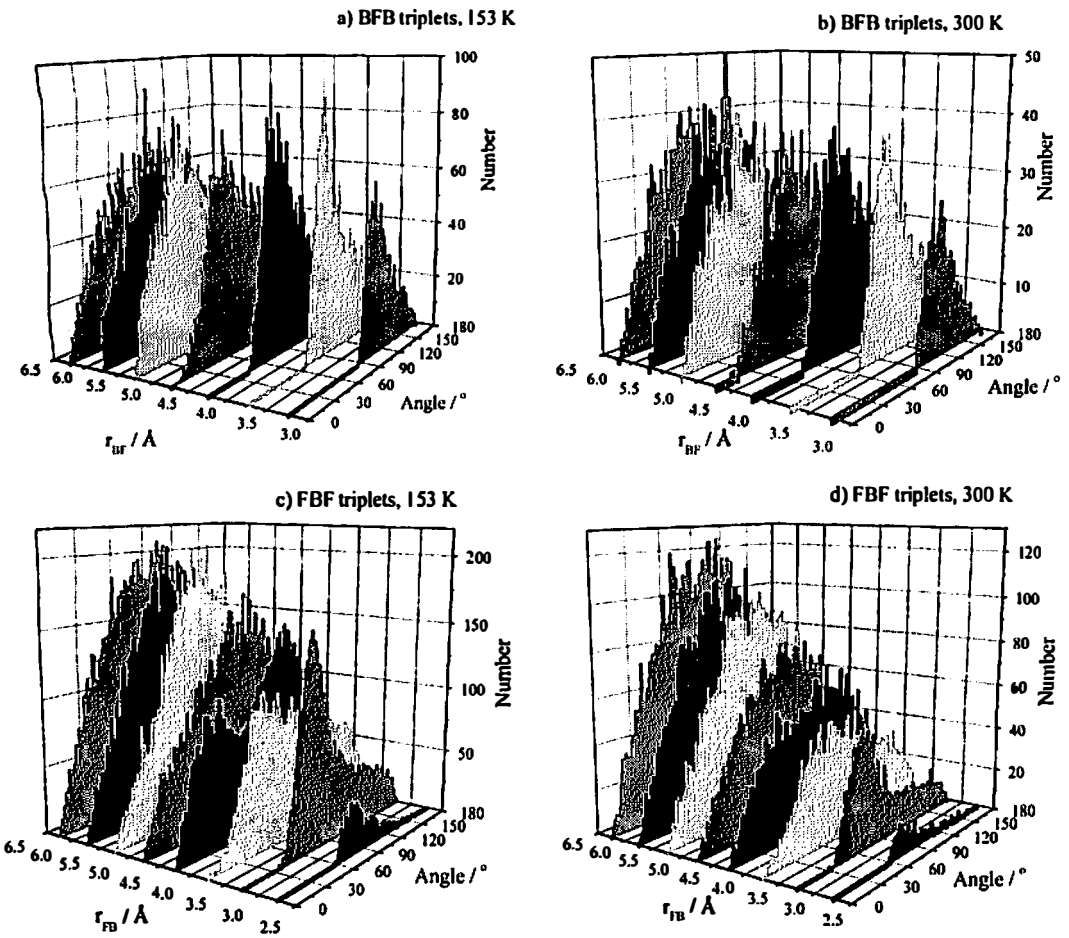

Figure 4.21: Unconstrained triplet counts for BF3 at 153 K and 300 K. The graphs show the angle between different molecules at r_{BF} and r_{FB} intermolecular distances in steps of 0.5 Å

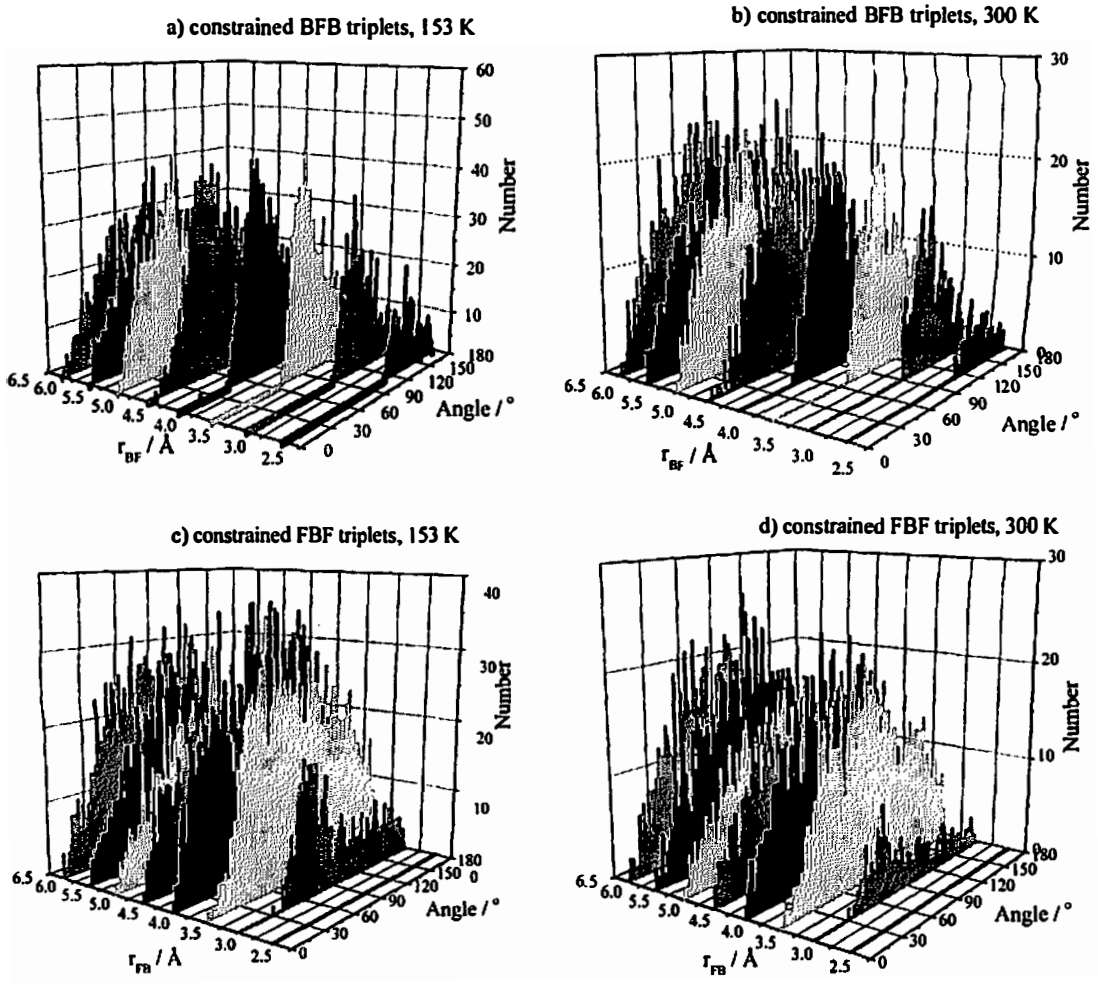

Figure 4.22: Constrained, with respect to θ in figure 4.20, triplet counts for BF_3 at 153 K and 300 K. These graphs show the angle between different molecules at r_{BF} and r_{FB} intermolecular distances in steps of 0.5 Å.

4.3.4 THE BFB TRIPLET IN THE LIQUID AND SUPERCRITICAL FLUID

The constrained BFB triplet (figures 4.22(a) and (b)) examines the axial coordination of the average BF_3 molecule with a fluorine atom in the molecular nearest neighbor. This triplet shows a distinct preference for coordination axially at both state points and this preference decreases as r_{BF} increases. Moreover, this structural preference is far more evident in the normal fluid; it is unsurprising that the structure of the supercritical fluid is less dependent on this interaction. At all temperatures there is a significant isotropic component, the limits of which are constrained by the steric imposition of the proximity of the average molecule at the particular distance. However, it is evident then that the axial [3+2] coordination in the solid is retained in the first coordination sphere, though, at both state points, there is also a significant proportion of the molecules that display no orientational preference. The distances for the axial ligation of B in the crystal structure are found at 2.78 – 2.85 Å.[277]

Once the distance between the B atom in the average molecule and the extracted FB atom pair becomes sufficient that isotropic orientation becomes sterically possible, past ~ 3.75 Å, a proportion of the molecules assume this disposition, over which an axial contribution is also added. In the supercritical fluid, this is far less apparent.

4.3.5 THE FBF TRIPLET IN THE NORMAL AND SUPERCRITICAL FLUID

At the closest distance of interaction between the average molecule and its nearest neighbor, a dual distribution is observed, reflecting the tilted nature of the molecule. The double maximum is observed due to the presence of F_{exo} and F_{endo}, as illustrated in figure 4.23.

This distribution reoccurs in the extraction at 4.25 Å, with the distribution between these two distances showing a *quasi*-isotropic distribution. Beyond this distance from the average molecule, the distribution is smooth and becomes isotropic. A diagram of the angular distribution at the maximum number density with distance is shown in figure 4.24.

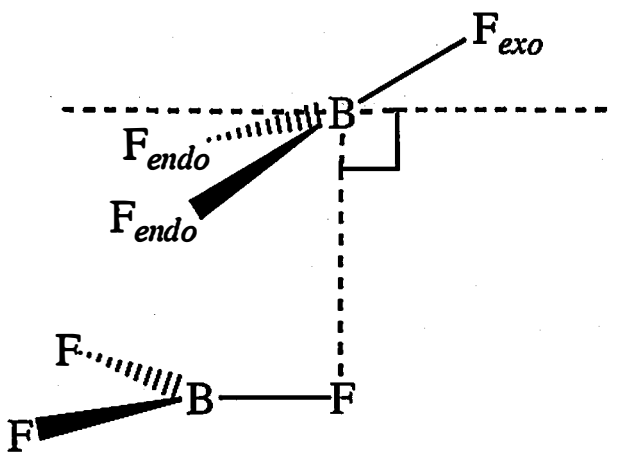

Figure 4.23: Axial BF_3 intermolecular interactions.

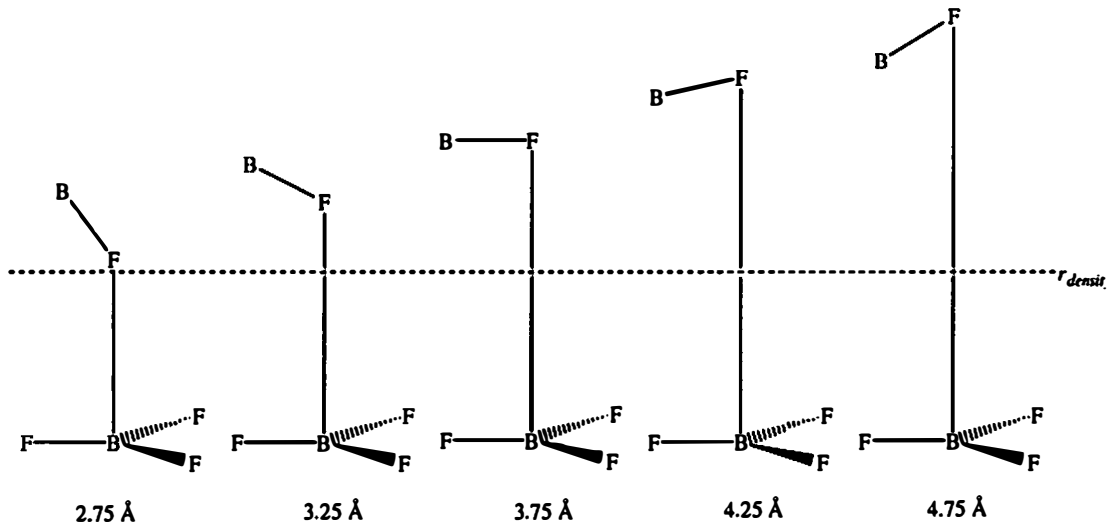

Figure 4.24: Axial interactions in liquid and supercritical BF_3, showing the density derived radius to scaled relative to the BF bond length, and the orientation of the maximum in the BFB triplet.

4.4 CONCLUSIONS

The measurements presented here are in agreement with the viscosity and entropy of vaporization data where both measurements support a non-associated fluid model in the bulk fluid.[280]

Liquid and supercritical boron trifluoride both display orientational structure within the first coordination sphere. Though there is no evidence of a layered liquid, the [3+2] structural motif, present in all phases of the solid structure, is somewhat retained in the liquid and in the supercritical fluid to a lesser extent. It is clear that there is an intermolecular Lewis acid-base interaction present in the pure liquid and that there is competition between the intramolecular F-B π back-donation and the intermolecular F···B interaction. However, given that this intermolecular interaction is structurally evident, it is clear that the intramolecular $p\pi - p\pi$ interaction is not sufficient to prevent intermolecular F···B Lewis acid-base interactions in the absence of *a priori* orientational constraints. This implies that the Lewis acidity of BF_3 is not solely a function of the valence bond intramolecular F-B $p\pi - p\pi$ back-donation. There is also no evidence of a dimeric structure in the liquid state. This lack of dimerization could be interepreted as support for valence bond description where the $p\pi - p\pi$ interactions in BF_3 dictate its strength as a Lewis acid. However, this lack of dimerization is also in agreement with the ionic model calculations of the boron trihalide complexes where the strength of acidity is base dependent.[284,286,287] In addition the intermolecular interaction between BF_3 molecules, albeit weak, is in accord with the ionic model calculations but is not consistent with a valence bond model.

The supercritical fluid also displays a slight orientational interaction between molecules in the first coordination sphere; moreover, the intramolecular contact in the supercritical phase is identical to that observed in the liquid. The supercritical phase is characterized by a wider distribution of sites in real space than the liquid and the population of these sites is also far more even than the normal fluid. Accordingly, a model of the supercritical state that is either entirely unstructured, by analogy with a

perfect gas, or is simply a liquid structure scaled by the density is not supported by these measurements.

It is therefore concluded that liquid BF_3 is partially associated on a local scale i.e. a scale that spans the first coordination sphere, in a manner reminiscent of the crystal structures. Though the fluid is isotropic beyond this distance, as far as can be determined by diffraction experiments, the interactions within the first coordination sphere clearly dominate the behavior of the liquid. Accurate thermodynamic measurements by Calado *et al.* have been interpreted on the basis that liquid BF_3 is a "layered liquid", a structural model that is refuted by these measurements if the definition of a layered liquid is that conventionally used in discussions of liquid structures and implies intermediate range order. There is some degree of ordering in the first coordination sphere. Calado's supposition, even though classical thermodynamics is formally ignorant of the structure of matter, is intuitive as, in the absence of any long range forces, the dominating interaction is that between nearest neighbors, the angular and radial disposition of which imply a preference for a *pseudo*-planar disposition of molecules not only in the first coordination sphere.

CHAPTER 5: STRUCTURAL STUDIES OF WATER IN FLUOROSULFURIC ACID

5.1 INTRODUCTION

The hydronium ion, H_3O^+, is a highly important species in aqueous solutions - the presence of H_3O^+ in aqueous media is the sole criteria for a material being defined as an acid, using Brønsted-Lowry acid-base theory.[319,320] Though the presence of the hydronium ion is solution is invoked often, the direct structural observation of H_3O^+ is limited. In solution, this is due to the fact that the protonation of water is a dynamic process leading to the formation of a hydronium ion that is short lived. Even in the solid phase the direct structural characterization of H_3O^+ is difficult. In the phase diagrams of the hydrates of the hydrogen halides the composition can be written as $HX.nH_2O$ (n =1,2,3,4,6) where X=Cl, Br and I.[159] In each of these diagrams the water molecules form clusters which are difficult to structurally distinguish. The exception to this rule the crystalline hydrates of HF, which are in the form $H_2O.mHF$ (m =1,2,4).[160,161] It should be noted that HF is a superacid and that the isolation of H_3O^+ is usually only possible in superacidic solutions or in very dilute acidic solutions.

The evidence for the H_3O^+ in solution includes NMR measurements[321-323] that have been used to characterize this species; this evidence is supported both in solution and in the solid phase by Raman and IR spectroscopy.[324,325]

5.1.1 BRØSTED-LOWRY ACID BASE THEORY

Aqueous acid-base theory was first introduced by Brønsted and Lowry and is based on the presence of hydronium ion, H_3O^+. Brønsted-Lowry acidity defines the universal pH scale[319,320] based on the autoprotolysis of water, where the equilibrium value, K_w, is a constant.

$$H_2O + H_2O \rightleftharpoons H_3O^+ + OH^- \quad K_w = [H_3O^+][OH^-] = 10^{-14} \tag{5.1}$$

The pH scale is based in the H^+ or H_3O^+ concentration, where pH=-log $[H_3O^+]$. Brønsted-Lowry acidity is essentially proton acidity that is all Brønsted-Lowry acids

contain at least one proton that can be transferred. In this theory, only the liquid phase is considered, and the strongest acid can only be the hydronium ion by definition.

5.1.2 GAS PHASE AND SOLID STATE STUDIES

The hydronium ion has been observed in the gas phase[326-330] and the existence of $H^+(H_2O)_n$ has been quantified by various types of mass spectroscopy for pure water.[331] In these studies, it was shown that H^+ does not exist as a bare proton but is instead solvated by a varying number of water molecules, even in the gas phase.

There have been several studies that have proven the existence of the hydronium ion in the solid state. Before the emergence of any structural data, infrared and Raman measurements on solid compounds indicated the existence of the hydronium ion. In 1953, Ferriso *et al.* measured solid state IR spectra for reactions between H_2O and HCl.[324] In these spectra the authors noted a contribution which resembled neither ice nor a hydrogen halide, but rather that of ammonia. They speculated not only the possible existence of H_3O^+, but also predicted a "symmetrical pyramidal" structure for the hydronium ion. This result was corroborated by Taylor, *et al.* using solid state Raman studies of the hydronium ion in hydronium perchlorate.[325]

The only direct structural studies of the hydronium ion to date have been confined to the solid phase, in which many of these compounds have been crystallized from strongly acidic or superacidic solutions. Lundgren *et al.* have characterized the solid state structure of the hydronium ion in trifluoromethanesulfonic acid or triflic acid, $[H_3O]^+[CF_3SO_3]^-$,[135-138] and Mootz has isolated the hydronium ion in fluorosulfuric acid, $[H_3O]^+[FSO_3]^-$.[133] At 223 K, $[H_3O]^+[FSO_3]^-$ crystallizes in the space group Pnma, with 4 formula per unit cell, as shown in figure 5.1.

$[H_3O]^+[FSO_3]^-$ is characterized by strong O-H···O hydrogen bonds, in which the O···O intermolecular distance between the hydronium cation and the fluorosulfate anion is 1.83±0.05 Å. Figure 5.2 shows appropriate atomic labels for molecular FSO_3H and fluorosulfate monohydrate in order to facilitate discussion. Table 5.1 shows a comparison between the heavy atom distances in crystalline FSO_3H and in the

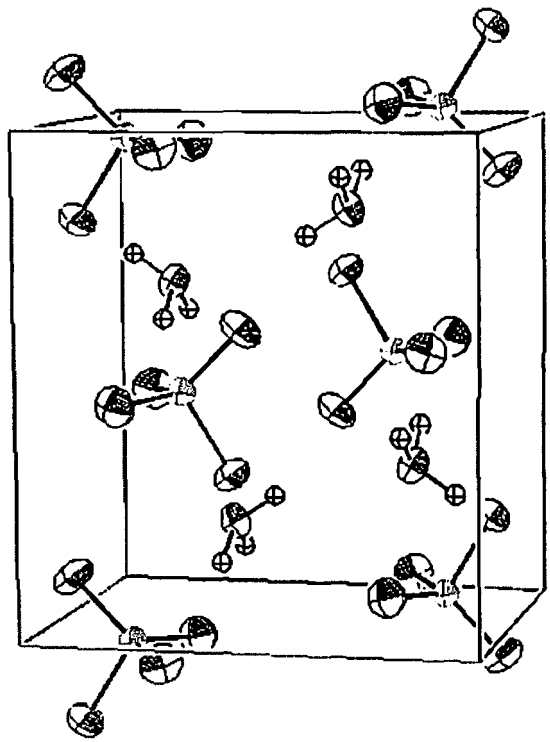

Figure 5.1: Solid state structure of $[H_3O]^+[FSO_3]^-$ at 223 K.[133]

Table 5.1: Interatomic distance and angles for fluorosulfuric acid and the fluorosulfate anion in fluorosulfate monohydrate.[132,133]

Distances/ Å		
	FSO_3H	$[FSO_3]^-$
r(S-O_1)	1.518(1)	1.438(2)
r(S-O_2)	1.412(1)	1.418(3)
r(S-O_3)	1.420(1)	
r(S-F)	1.540(1)	1.552(2)
r(O_1-H)	0.63(3)	-
r(H···O_3')	2.02(3)	-
Angles/ ^{0}		
	FSO_3H	$[SO_3F]^-$
O_1-S-O_3	107.2(1)	-
O_2-S-O_3	120.9(1)	113.3(1)
O_1-S-O_2	113.1(1)	115.9(1)
O_1-S-F	100.7(1)	103.6(1)
O_2-S-F	106.6(1)	102.8(1)
O_3-S-F	106.2(1)	-

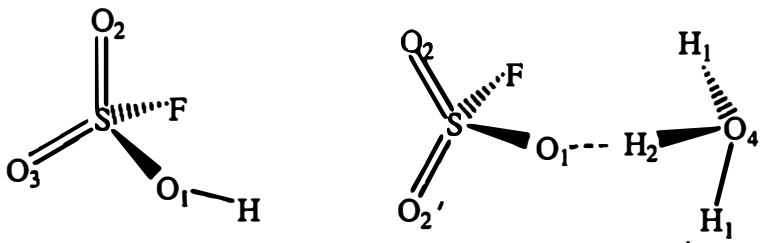

Figure 5.2: The molecular structure of FSO_3H and $[H_3O]^+[FSO_3]^-$.[133]

fluorosulfate anion in crystalline $[H_3O]^+[FSO_3]^-$.[132,133]

Both structures presented in table 5.1 have heavy ion positions that can be described as distorted tetrahedral. The only significant change in bond distances between crystalline FSO_3H and $[FSO_3]^-$ is the S-O_1 bond distances which decreases by ~0.1 Å from the pure acid to the monohydrate. The bond angles in the $[FSO_3]^-$ structure more closely resemble a tetrahedron, although the tetrahedral configuration is evident in both structures.

Table 5.2 shows all of the inter and intra-molecular distances between cation and anion for the $[FSO_3]^-[H_3O]^+$ structure with reference to figure 5.2.

Whereas the fluorosulfate anion remains pseudotetrahedral, the hydrogen bonding structure between cation and anion is pseudo linear, with very short strong hydrogen bonds of 1.86 Å and 1.56 Å. In addition the hydronium cation has very short intramolecular bonds of 0.82 Å and 1.01 Å. As was the case in the solid state structure of FSO_3H which has an intramolecular bond length of 0.63 Å, an O-H distance of 0.82 Å seems unreasonably short. Although the other hydrogen distances appear reasonable, it is useful to compare these results with a neutron diffraction study. In conventional X-ray diffraction studies, as described in chapter 2, precise hydrogen atom locations are extremely difficult to determine. This is compounded by the fact that this system, as was the case with FSO_3H, was measured in Teflon, which has a large amorphous background and is described in more detail in chapter 6.

In regard to hydrogen bonding distances the neutron diffraction study on

Table 5.2: Inter- and intramolecular distances and angles for $[FSO_3]^-[H_3O]^+$ $[FSO_3]^-$.[132,133]

Distances/ Å		
	$[SO_3F]^-$	$[H_3O]^+$
r(S-O_1)	1.438(2)	-
r(S-O_2)	1.418(3)	-
r(S-F)	1.552(2)	-
r(O_4-H_1)	-	1.01(4)
r(O_4-H_2)	-	0.82(5)
r(H_2···O_1)	1.83(5)	1.83(5)
r(H_1···O_1')*	1.56(4)	1.56(4)
Angles/ °		
	$[SO_3F]^-$	$[H_3O]^+$
O_2-S-O_2'	113.3(1)	-
O_1-S-O_2	115.9(1)	
O_1-S-F	103.6(1)	
O_2-S-F	102.8(1)	
H_1-O_4-H_1	-	114(4)
H_1-O_4-H_2	-	109(2)
O_4-H_1-O_1'	172(4)	172(4)
O_4-H_2-O_1	160(5)	160(5)
S-O_2-H_1*	129(1)	129(1)
S-O_1-H_2	172(2)	172(2)

$[H_3O]^+$ $[CF_3SO_3]^-$ provides a useful comparison.[137] Triflic acid has a Hammett acidity function of $H_o = -14.3$ and, although not as acidic as FSO_3H, it is still a superacid.[111] In the structure of $[H_3O]^+[CF_3SO_3]^-$ all of the O-H bond lengths for the hydronium ion are ~0.9 Å. In addition all of the hydrogen bonding distances, $H_3O^+\cdots O$, are all between ~1.7Å and ~1.5Å. With the exception of the $r(O_4\text{-}H_2)$ distance in $[FSO_3]^-[H_3O]^+$, all of the distances appear plausible.

In addition to $[H_3O]^+[CF_3SO_3]^-$ and $[H_3O]^+[FSO_3]^-$, Christie *et al*, have isolated hydronium ion salts of $[SbF_6]^-$ and $[AsF_6]^-$ in superacidic solutions.[127,140] In all of these structural studies, the hydronium ion retains approximate C_{3v} symmetry. All of the available experimental and theoretical data support this geometry.[110,127,133,135-139,159,324,332-335] The hydronium ion is shown in its C_{3v} geometry in figure 5.3.

5.1.3 EVIDENCE IN SOLUTION

The earliest evidence for H_3O^+ in the liquid phase came from measurements on HBr + H_2O in solutions of sulfur dioxide[332,333] where the solid state low temperature vibrational spectra of these solutions supported the existence of the hydronium ion in the liquid phase.[324] In this and similar studies, the hydronium ion was considered to be too short-lived to be seen by vibrational spectroscopy.[336,337] The primary difficulty in these studies arose from the presence of strong water bands, which overlaid any potential vibrational bands from the hydronium ion itself, as most of these studies were performed in dilute aqueous solutions. In a later study by Giguère *et al.* on HBr + H_2O of varying concentrations, they discovered a peak attributable to the υ_2 asymmetric stretch for the hydronium ion.[338] This peak, which was not present in HBr or H_2O, is

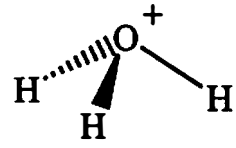

Figure 5.3: Molecular structure of H_3O^+

located at 1050 cm^{-1} for 45% mol H_2O in HBr. Moreover, the authors observed that as the molar concentration of H_2O in the acid increased, the peak shifted to higher wave numbers. The authors proposed that the increase in this stretching frequency was attributable to the formation of $H_2O\cdots H_3O^+$ contacts in the more dilute solutions.

In the solution phase H_3O^+ is stable enough to be characterized through NMR spectroscopy in the superacidic systems FSO_3H:SbF_5 and HF:SbF_5.[110,339]

Early NMR studies of H_2O in FSO_3H:SbF_5[340] and HF-BF_3[341] showed two distinct signals by ^1H NMR that were attributed in each case to the acid and the hydronium ion. In these studies, it could not be established that the water species was H_3O^+ and not $H_5O_2^+$.

In 1976, Gold *et al.* performed ^1H NMR experiments on the FSO_3H:SbF_5:H_2O:SO_2 system using combinations of isotopomers of the fluorosulfuric acid and water, namely D_2O, H_2O, FSO_3D and FSO_3H.[339] In this study they observed the hydronium ion as H_3O^+, H_2DO^+ and HD_2O^+ showing that only the hydronium ion was formed in these solutions, due to the isotopic spin couplings. In later studies on the HF/DF:SbF_5:H_2O system this result was corroborated by Olah *et al.*[335]

5.1.4 Previous Theoretical studies

The NMR results show that there is H/D exchange between the hydrogen sites on the water and the acid used as the isotopomeric species formed, eliminating the possibility of the water merely being protonated. In order to explain this phenomena, Olah noted that the only way isotopic exhange could occur in these highly acidic systems was through the formation of the intermediate H_4O^{2+},[110] and that this exchange either took place by either a "deprotonation/protionation" mechanism, given by

$$HD_2O^+ \overset{-D^+}{\rightleftharpoons} HDO \overset{+H^+}{\rightleftharpoons} H_2DO^+ \qquad (5.2)$$

or by a "protonation/deprotonation" mechanism, given by

$$HD_2O^+ \overset{+H^+}{\rightleftharpoons} H_2D_2O^{2+} \overset{-D^+}{\rightleftharpoons} H_2DO^+ \qquad (5.3)$$

In order to evaluate these two possibilities and the stability of the H_4O^{2+} dication in solution, *ab initio* and DFT calculations have been performed.[335,342,343] *Ab initio* calculations indicated that H_4O^{2+} is unstable towards deprotonation; the kinetic barrier for H_4O^{2+} to decompose to H_3O^+ is theoretically very high. This necessarily eliminates protonation/deprotonation as a possible mechanism.[335,342] However, in the subsequent DFT calculations, the deprotonation/protionation mechanism proved to be the most thermodynamically favorable.[343] Even though the calculations show that the protonation of H_3O^+ is unfavorable, Olah favors the mechanism in equation 5.3, as the calculations were performed on gas phase molecules and do not fully describe the solution phase and proposed that solvation or clustering of small dications might render H_4O^{2+} more thermodynamically accessible.[110]

5.2 Experimental

5.2.1 Sample Handling and Preparation

FSO_3H and FSO_3D were prepared as described in chapter 2. Neutron measurements, *vide infra*, revealed that the incorporation of D for H was greater than 99.8%. The purity of FSO_3H with respect to water was assayed using Raman spectroscopy and was determined to be greater than 99.9% pure with respect to H_2O, as is shown in chapter 2.

In order to prepare high purity water, deionized H_2O was prepared by distillation under an argon atmosphere from 0.05 mol % $KMnO_4$ and 0.25 mol % NaOH, with the distillation being repeated 3 times. D_2O (99.999 % D) was purchased from Aldrich Chemical company and 0.07 mol % Na metal was added. This basic mixture was then subsequently distilled under an argon atmosphere after the addition of 0.05 mol % $KMnO_4$. In order to measure accurate quantities, the FSO_3H was first cryogenically transferred into an empty, previously weighed ampoule, and the amount of H_2O (or D_2O) needed was determined and transferred into a separate ampoule using a Hamilton microliter syringe under an argon atmosphere. Both water and the corresponding acid were cryogenically transferred into quartz tubing (0.4cm ID, 0.5cm OD) for the neutron

experiments and to borosilicate tubing (0.4cm ID, 0.5cm OD) for the high energy X-ray experiments, allowed to react and then flame sealed under dynamic vacuum to give an approximate sample volume in each case of 0.5 cm^3.

Raman samples were prepared by first adding pure FSO_3D or FSO_3H to an all glass flat plate Raman tube equipped with a Kontes® Teflon-tap. After pure FSO_3H was measured, incremental amounts of H_2O were added (0.1 mol %, 0.5 mol %, 1.0 mol %, 5.0 mol % and 10 mol %) with a Hamilton gas-tight syringe and subsequently measured.

5.2.2 RAMAN MEASUREMENTS

All Raman spectra were acquired on a Dilor XY raman spectrometer (Instruments S.A., Inc, Edison, NJ) using a 514nm Rayleigh line, as described in chapter 2. Figure 5.2 shows the Raman spectra for pure FSO_3H and FSO_3H with addition of 10 mol % H_2O.

As was shown in chapter 2, the addition of water to pure fluorosulfuric acid decreases the peak intensities corresponding to the O-H bend, the S-OH stretch, the S-F stretch and the SO_2 symmeteric stretch, signifying the loss of a proton from fluorosulfuric acid. Also observable in figure 5.4 is the slight decrease in intensity from FSO_3H to FSO_3H+10% H_2O in the peak at ~1450 cm^{-1}. In pure FSO_3H, this peak corresponds to the SO_2 asymmetric stretches. In addition, a peak at 1080 cm^{-1} occurs which most likely corresponds to a fundamental vibration from the protonated water species present in the solution. As was the case with pure FSO_3H, the FSO_3H-H_2O system showed a high fluorescent background from ~1700cm^{-1} to ~3000cm^{-1} so no clear observations could be made in this region.

The most distinctive change in the FSO_3H spectra upon the addition of water, is the appearance of a peak at ~1080 cm^{-1}.[338] By analogy with previous measurements on HBr-H_2O, this peak can be attributed to the υ_2 asymmetric stretch for the hydronium ion as stated above. The location of this peak at the same approximate frequency in both the FSO_3H, H_2O and HBr, H_2O systems indicates that the same protonated water

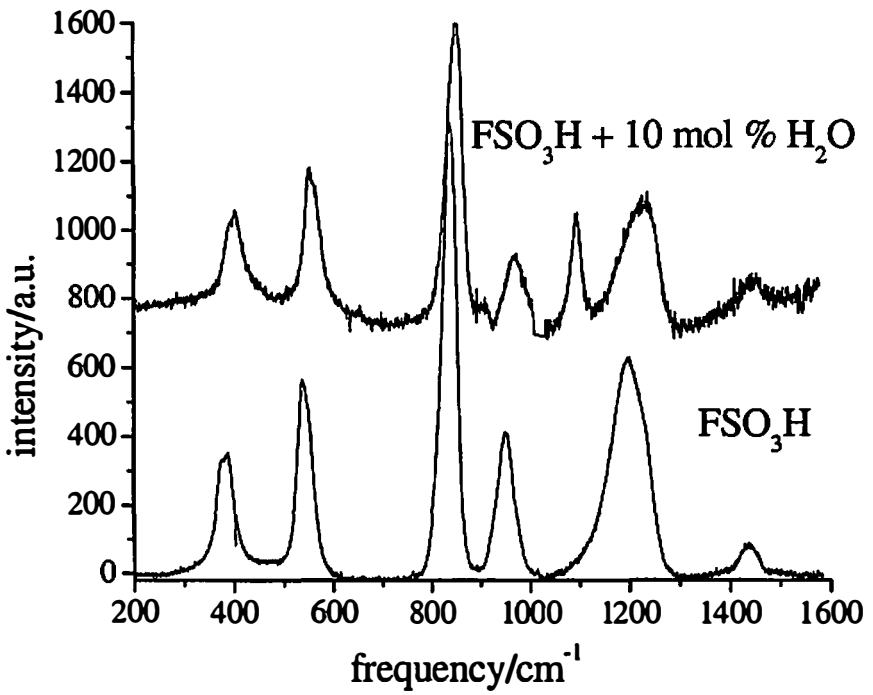

Figure 5.4: Raman spectra for FSO_3H and 90 mol % FSO_3H/10 mol % H_2O +800.

species is present in both samples. H_3O^+ is the most likely species present in the system.

5.2.3 NEUTRON MEASUREMENTS

Neutron diffraction experiments were at 300 K performed on $0.9FSO_3H:0.1H_2O$, hereafter termed FSO_3H/H_2O, and $0.9FSO_3D:0.1D_2O$, hereafter termed FSO_3D/D_2O. The neutron diffraction data were corrected for container scattering, attenuation, multiple scattering, and inelastic scattering using standard analysis procedures as described in chapter 1.[14] In addition, all of tubes were blown from the same cane of tube to ensure that their wall geometries were as similar as possible, in order to minimize systematic errors in the difference experiments. The small error between the quartz tubes was additionally checked by comparison of the calculated intramolecular scattering contribution to the measured data. Both neutron differences agreed to within 5% to the expected intramolecular nearest neighbor atoms *vide infra.* This clearly indicates that the SiO_2 container corrections and the data normalization have been performed correctly.

5.2.4 HIGH ENERGY X-RAY MEASUREMENTS

High energy X-ray experiments were performed on FSO_3H/H_2O and FSO_3D/D_2O at 300 K. These data were corrected for detector efficiency, instrumental geometrical effects, polarization, empty container scattering and subsequently normalized to the sum of the atomic form factors plus Compton scattering to yield a pseudo-nuclear structure factor, as described in chapter 1.[102]

X-ray experiments were performed on both of the isotopomers at the same state conditions and showed no significant isotopic quantum effect, within the limits of the experimental error (~1%), supporting the use of the isotopic substitution technique in neutron diffraction in this case.

5.2.5 RECORDED DIFFRACTION DATA

The total neutron structure factor $S^N_{T/D_2O}(Q)$ for FSO_3D/D_2O, compared with $S^N_T(Q)$ for FSO_3D (both measured at 300 K) is shown in figure 5.5. The pseudo-nuclear functions from the high energy X-ray data for FSO_3D/D_2O, $S^X_{T/D_2O}(Q)$ and FSO_3H/H_2O, $S^X_{T/H_2O}(Q)$ compared with FSO_3D, $S^X_T(Q)$ are shown in figure 5.6 for the 300 K data and FSO_3D/D_2O, $S^X_{T/D_2O}(Q)$ and FSO_3H/H_2O, $S^X_{T/H_2O}(Q)$ at 193 K are shown in figure 5.7. Measurements on FSO_3D are described in detail in chapter 2.

The total pair correlation function for FSO_3H/H_2O, $G^A_{T/H_2O}(r)$, where A is the radiation source used, can be written as:

$$G^A_T(r) = \sum_{\alpha,\beta} a^A_{\alpha\beta} g_T(r) = a^A_{HH} g_{HH}(r) + 2a^A_{HF} g_{HF}(r) + 2a^A_{HS} g_{HS}(r) + 2a^A_{HO} g_{HO}(r) + 2a^A_{SO} g_{SO}(r) + 2a^A_{SF} g_{SF}(r) + 2a^A_{OF} g_{OF}(r) + a^A_{OO} g_{OO}(r) + a^A_{FF} g_{FF}(r) + a^A_{SS} g_{SS}(r) \quad (5.4)$$

here $a^A_{\alpha\beta}$ is the weighting from atoms α and β for radiation source A, where N signifies a neutron measurement and X signifies a high energy X-ray measurement. Table 5.3 lists these constants for all measurements obtained.

As was the case in the FSO_3H measurements, the Fourier transformation of the high energy X-ray data and the neutron data, $G^N(r)$ and $G^X(r)$ respectively, contain all of the partial pair correlation functions, although in the case of the high energy X-rays the intensity of the scatter is mostly confined to the heavy atom positions.

The pair correlation functions for the neutron data are shown in figure 5.8 for FSO_3D/D_2O and FSO_3D. As was seen in FSO_3D, the FSO_3D/D_2O neutron total pair correlation function contains 10 partials and as such, all of the hydrogen atom positions are overlaid with the heavy atom positions.

$G^N_{T/D_2O}(r)$ can be written as

$$G^N_{T/D_2O}(r) = 0.454 g_{HX}(r) + 0.546 g_{XX}(r) \quad (5.5)$$

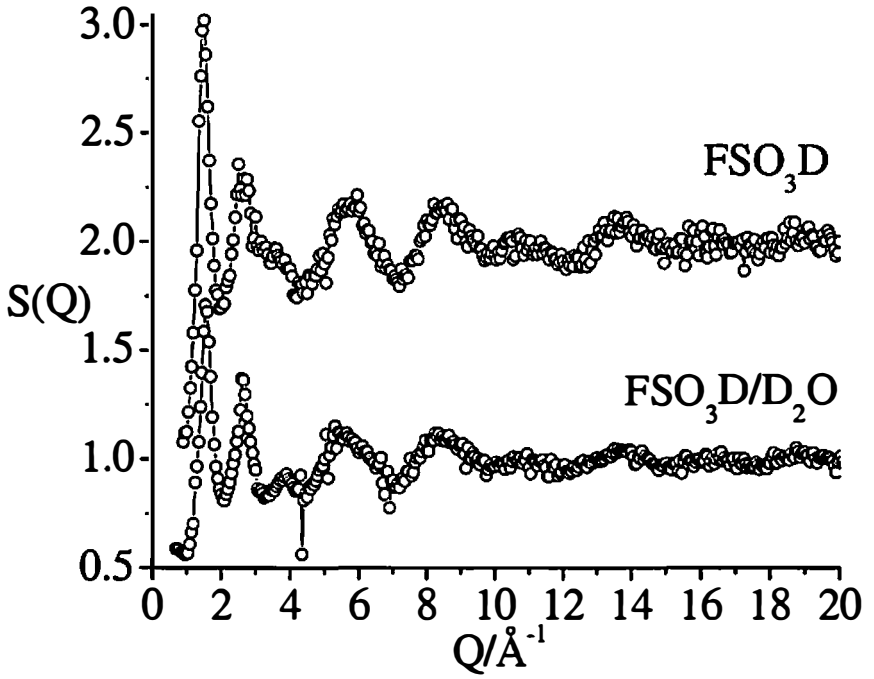

Figure 5.5: Measured total structure factor for FSO_3D and FSO_3D/D_2O using neutrons. $S_T^N(Q)+1$ at 300 K and $S_{T/D_2O}^N(Q)$ at 193 K.

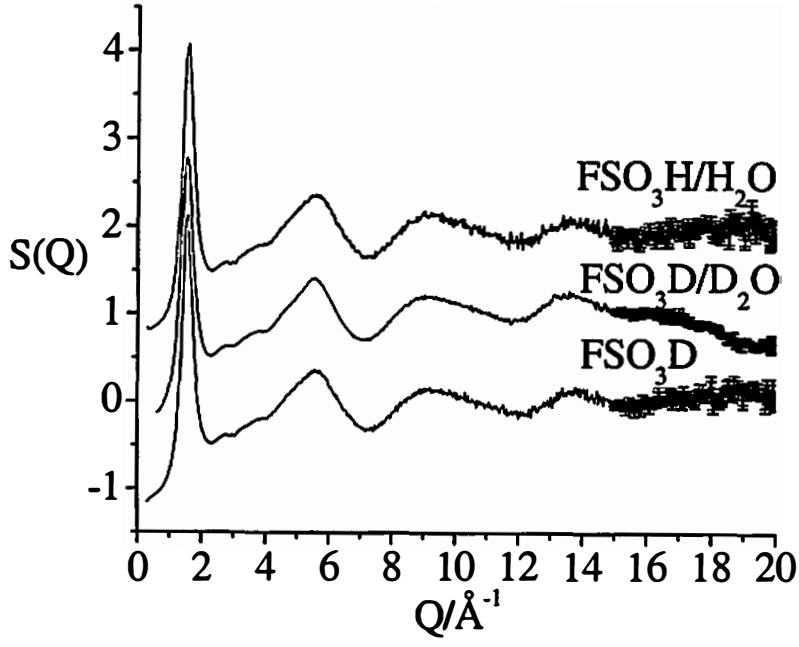

Figure 5.6: Measured total structure factor for FSO_3H/H_2O, FSO_3D/D_2O and FSO_3D, using high energy X-rays at 300 K. $S^X_{T/H_2O}(Q)+1$, $S^X_{T/D_2O}(Q)$ and $S^X_T(Q)-1$.

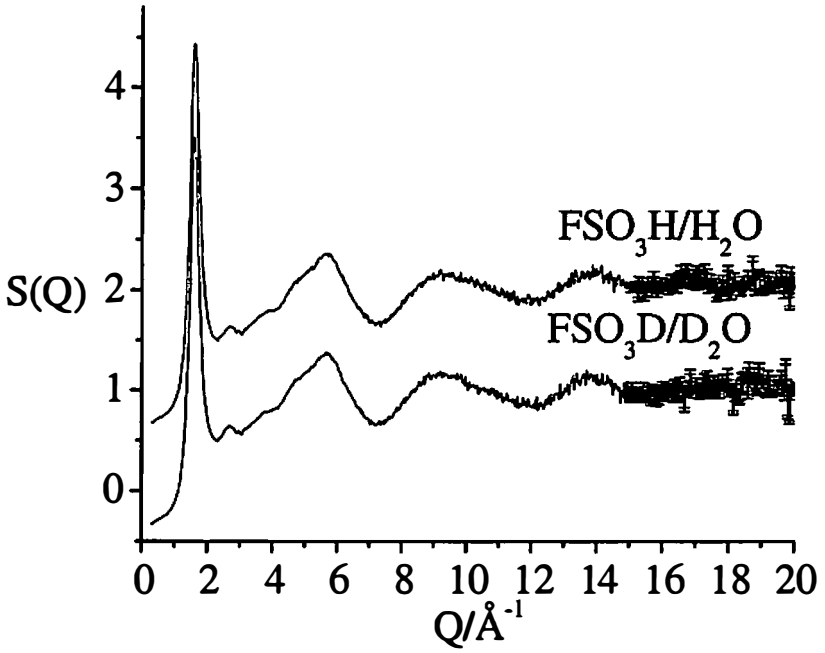

Figure 5.7: Measured total structure factor for FSO_3H/H_2O and FSO_3D/D_2O using high energy X-rays at 193 K. $S^X_{T/H_2O}(Q)+1$ and $S^X_{T/D_2O}(Q)$.

Table 5.3: Neutron and X-ray weighting factors for FSO_3H/H_2O and FSO_3D/D_2O.

	FSO_3D/D_2O neutron	FSO_3H/H_2O neutron	X-ray 0 $Å^{-1}$	X-ray 1 $Å^{-1}$	X-ray 2 $Å^{-1}$	X-ray 5 $Å^{-1}$	X-ray 10 $Å^{-1}$
a_{HH}^{A}	0.0209	0.0066	0.047	0.035	0.017	0.001	0.000
$2a_{HF}^{A}$	0.0245	-0.0137	0.500	0.486	0.294	0.033	0.002
$2a_{HS}^{A}$	0.0123	-0.0069	0.889	0.839	0.488	0.068	0.005
$2a_{HO}^{A}$	0.0811	-0.0454	1.675	1.371	0.806	0.084	0.005
$2a_{SO}^{A}$	0.0240	0.0240	18.551	16.054	11.242	3.448	1.095
$2a_{SF}^{A}$	0.0072	0.0072	6.482	5.681	4.095	1.338	0.376
$2a_{OF}^{A}$	0.0476	0.0476	10.435	9.286	6.763	1.655	0.397
a_{SS}^{A}	0.0018	0.0018	5.762	5.350	3.398	1.393	0.519
a_{FF}^{A}	0.0072	0.0072	1.824	1.643	1.235	0.321	0.068
a_{OO}^{A}	0.0786	0.0786	14.930	13.118	9.297	2.133	0.577

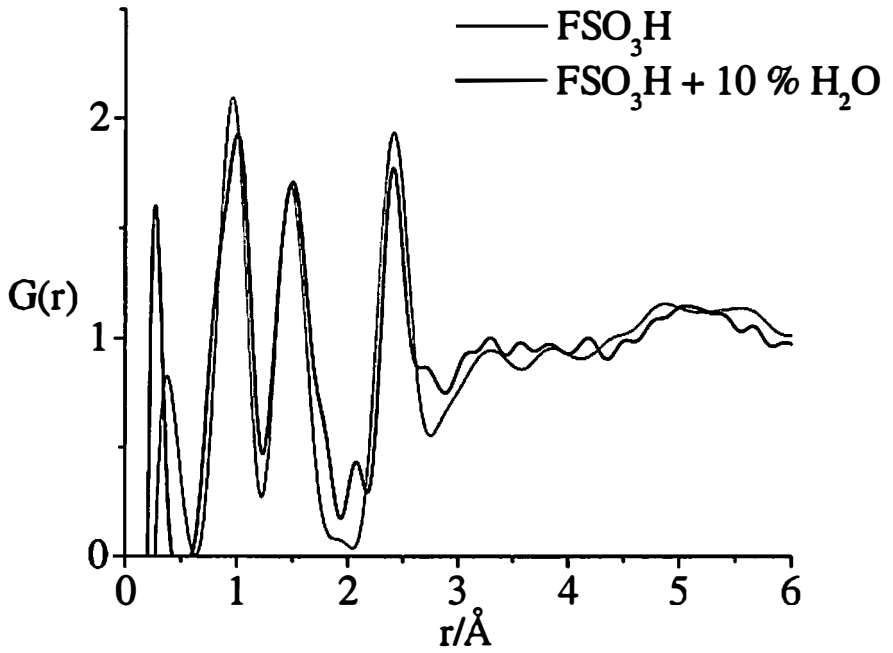

Figure 5.8: Total pair correlation functions for FSO_3H/H_2O and FSO_3D/D_2O using neutrons at 300 K. $G^N_{T/D_2O}(r)$ and $G^N_T(r)$.

where g_{XX} signifies the sum of the partial pair correlation functions that contain only the heavy atom distances and g_{HX} is the sum of the partial pair correlation functions that contain only hydrogen related distances. As a comparison, $G_T^N(r)$ can be written as

$$G_T^N(r) = 0.368 g_{HX}(r) + 0.632 g_{XX}(r) \tag{5.4}$$

Fourier transformation of the high energy x-ray total structure factor, $S_{T/D_2O}^X(Q)$ yields $G_{T/D_2O}^X(r)$ where 93.7% of the weighting in FSO_3H/H_2O and FSO_3D/D_2O can be attributed to the heavy elements present in the sample. This allows for the direct evaluation of the heavy atom positions and can be written as

$$G_{T/D_2O}^X = G_{T/H_2O}^X = 0.937 g_{XX}(r) + 0.063 g_{HX}(r) \tag{5.5}$$

As was stated in chapter 2, this formula is given for the values at Q=0 however with X-rays the form factors vary with Q which are not easily expressed in real space.

$G_{T/D_2O}^X(r)$ and $G_{T/H_2O}^X(r)$ are shown in figure 5.9, together with the total pair correlation function for FSO_3D $G_T^X(r)$ at 300 K. $G_{T/D_2O}^X(r)$and $G_{T/H_2O}^X(r)$ are shown in figure 5.10 for the 193 K data.

5.2.6 FIRST ORDER DIFFERENCE FUNCTION

In order to elucidate the structure related only to the hydrogen positions, hereafter termed the [H,D] site, independent neutron diffraction measurements for isostructural and isotopomeric samples of FSO_3H/H_2O and FSO_3D/D_2O allowed for the first order difference function to be obtained as described in chapter 1. The first order difference function, in this case, only contains the partial structure factors with respect to the [H,D] site, namely $\Delta S_{HX/H_2O}^N(Q)$.

The extracted first order difference function for FSO_3H/H_2O, $\Delta S_{HX/H_2O}^N(Q)$, compared with the extracted first order difference function for pure FSO_3H $\Delta S_{HX}^N(Q)$ function is shown in figure 5.11.

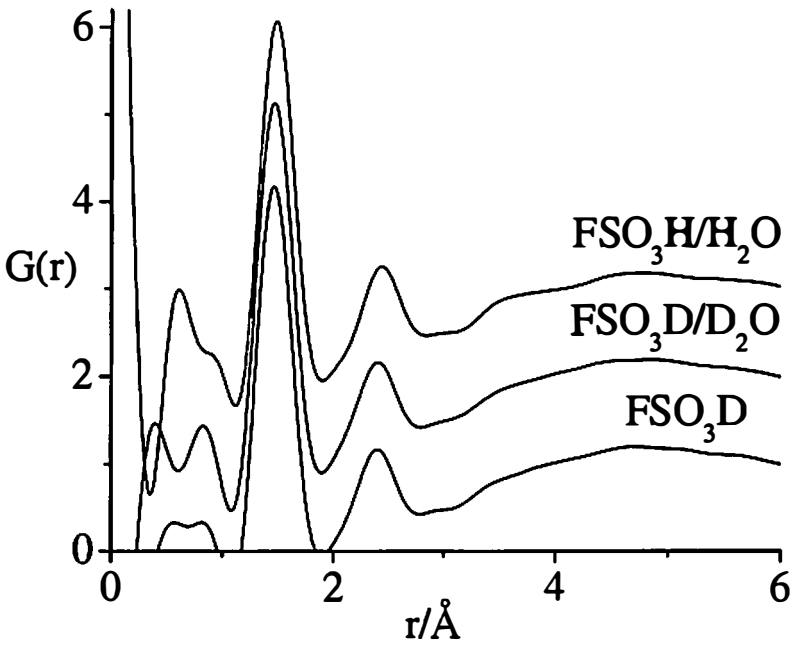

Figure 5.9: Total pair correlation function for FSO_3H/H_2O, FSO_3D/D_2O and FSO_3D, using high energy X-rays at 300 K. $G^X_{T/H_2O}(r)+2$, $G^X_{T/D_2O}(r)+1$ and $G^X_T(r)$.

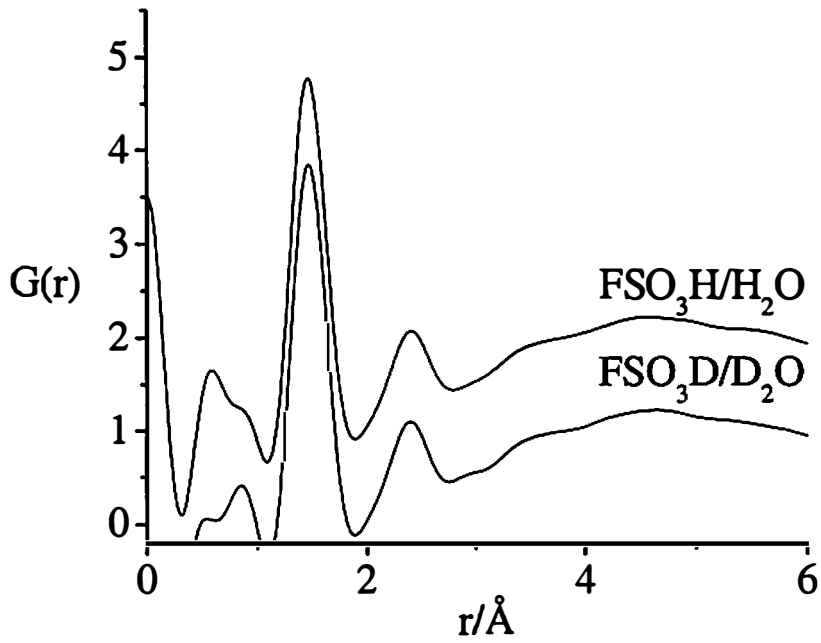

Figure 5.10: Measured total structure factor for FSO_3H/H_2O and FSO_3D/D_2O using high energy X-rays at 193 K. $G^{X}_{T/H_2O}(r)+1$ and $G^{X}_{T/D_2O}(r)$.

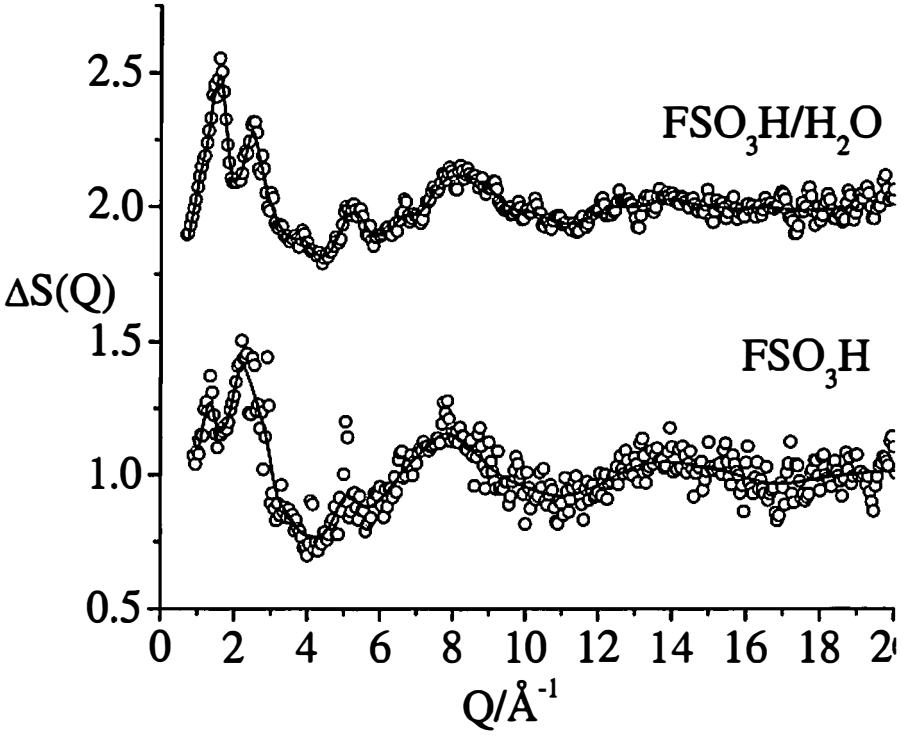

Figure 5.11: First order difference function for FSO_3H/H_2O and FSO_3H at 300 K. $\Delta S^N_{HX/H_2O}(Q)$ and $\Delta S^N_{HX}(Q)$.

The real space counterparts $\Delta G^{N}_{HX/H_2O}(r)$ and $\Delta G^{N}_{HX}(r)$ are shown in figure 5.12 and represent only the pair correlation functions associated with the [H,D] sites.

Explicitly, $\Delta G^{N}_{HX/H_2O}(r)$ is written as

$$\Delta G^{N}_{HX/H_2O}(r) = 0.638 g_{HO}(r) + 0.193 g_{HF}(r) + 0.097 g_{HS}(r) + 0.072 g_{HH}(r) \quad (5.5)$$

and $\Delta G^{N}_{HX}(r)$ is written as

$$\Delta G^{N}_{HX}(r) = 0.636 g_{HO}(r) + 0.207 g_{HF}(r) + 0.104 g_{HS}(r) + 0.054 g_{HH}(r) \quad (5.6)$$

5.3 Discussion

For all of the samples at all of the temperatures measured, the high energy X-ray diffraction patterns are extremely similar. In real space, each high energy X-ray total pair correlation function gives the same peak positions for both the FSO_3H/H_2O system at both temperature measured and pure FSO_3H at 300 K. In each case the first peak is located at 1.465±0.05 Å and the second at 2.410±0.03 Å as is seen in figure 5.8, 5.9, and 5.10. As was shown in chapter 2, the first peak corresponds to the S-O and S-F covalent bonds in the molecule, and the second peak corresponds to the O-F and O-O distances.

The angle between the heavy atoms positions in these systems can be assessed by

$$\left(r_{O(F,O)}\right)^2 = \left(r^{intra}_{S(O,F)}\right)^2 + \left(r^{inter}_{S(O,F)}\right)^2 - 2\left(r^{intra}_{S(O,F)}\right)\left(r^{intra}_{S(O,F)}\right)\cos\theta \quad (3.7)$$

where $\theta = O\hat{S}X, X = O, F$.

In each case the distances measured in the X-ray data gives an angle of $O\hat{S}X = 110.7° \pm 0.3°$. This clearly indicates that the FSO_3 positions in each case form a pseudotetrahedral structure and that the heavy atom structure of the FSO_3H molecule is unperturbed by the addition of water. More importantly, from this analysis it is also clear that the structures of FSO_3^- and FSO_3H are identical with respect to the intramolecular heavy atom positions, to within the sensitivity of this technique. This indicates that the intramolecular structure of both FSO_3H (as is seen in chapter 2) and

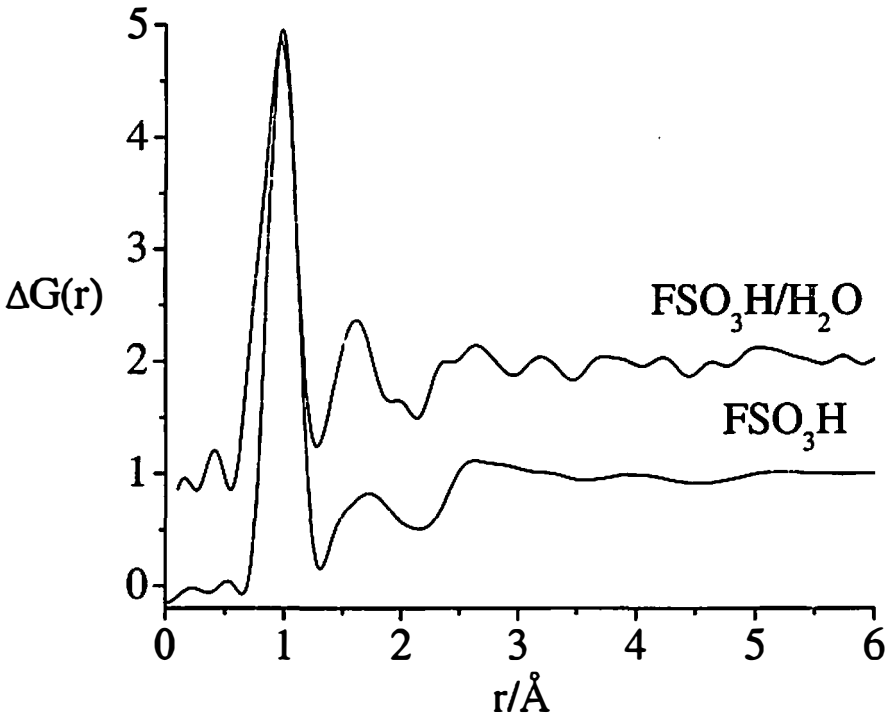

Figure 5.12: Partial pair correlation functions for the hydrogen distances in FSO_3H/H_2O and FSO_3H at 300 K. $\Delta G^{N}_{HX/H_2O}(r)$ and $\Delta G^{N}_{HX}(r)$.

the intramolecular structure of FSO_3H/H_2O are different only with respect to the position of the hydrogen atom. This is supported by inspection of the neutron total structure factor measurements and their associated pair correlation functions (figure 5.5 and 5.8). In figure 5.8, the peak positions are similar in $G^N_{T/D_2O}(r)$ and $G^N_T(r)$, though there are some clear structural differences. The supposition that most of these changes are due to the hydrogen structure is reasonable as HX correlations account for 40% of the peak intensity in $G^N_{T/D_2O}(r)$. The primary difference between $G^N_{T/D_2O}(r)$ and $G^N_T(r)$ is the addition of new intensity between the peaks that cannot be accounted for by FSO_3H, and an increase in the height of the OD intramolecular peak.

5.3.1 COORDINATION NUMBER ANALYSIS

The coordination number of the first peak in both neutron total pair correlation functions, $G^N_{T/D_2O}(r)$ and $G^N_T(r)$, was ascertained by the running coordination number method as described in chapter 1. With respect to the number of oxygen atoms around deuterium atoms (O@D) $c^{intra}_{DO} = 1.04 \pm 0.1$ in $G^N_T(r)$ and $c^{intra}_{DO} = 1.00 \pm 0.1$ in $G^N_{T/D_2O}(r)$.

The coordination number was also assessed with respect to the number of deuterium atoms around the oxygen atoms (D@O). In this case, $c^{intra}_{OD} = 0.34 \pm 0.1$ in pure FSO_3D which is expected as 1 out of 3 oxygen atoms in the FSO_3H molecule have an OD covalent bond. In FSO_3D/D_2O $c^{intra}_{OD} = 0.40 \pm 0.1$, showing that 40% of the oxygen atoms in this system are associated with an OD bond. The increase in intramolecular OD coordination is expected as D_2O has been added to the system.

Figure 5.13 shows four compositional models for species and their relative concentrations that may be present in the FSO_3H/H_2O system.

The D@O coordination number was assessed in each of the possible model systems, to determine which model is most consistent with the data presented here. In each of these models the total number of oxygen atoms in the system is 2.8, with respect

I $0.8\,FSO_3H + 0.1\,FSO_3^- + 0.1\,H_3O^+$

II $0.7\,FSO_3H + 0.1\,FSO_3^-\text{-}H^+\text{-}O_3SF + 0.1\,H_3O^+$

III $0.7\,FSO_3H + 0.2\,FSO_3^- + 0.1\,H_4O^{2+}$

IV $0.5\,FSO_3H + 0.2\,FSO_3^-\text{-}H^+\text{-}O_3SF + 0.1\,H_4O^{2+}$

Figure 5.13: Models for the composition of $0.9FSO_3H{:}H_2O$.

to D@O coordination number values. Table 5.4 shows the predicted D@O coordination numbers at the position of the first peak in the $FSO_3D{:}D_2O$ data for each model shown in figure 5.13.

It is clear from table 5.4 that it is not possible to distinguish between the four models using only the coordination number from the neutron total pair correlation functions. All of the models give results consistent with experiment within error for the D@O coordination number. However, models I and III are can be discounted by chemical arguments. An unsolvated FSO_3^- ion in a solution of FSO_3H is highly unlikely given that ions dissolved in any solution are always solvated to some extent.[173] Moveover, in superacidic systems this is even more pronounced given the electrophilicity of the hydrogen in these cases.[111]

The exclusion of models I and III leaves only models II and IV, which contain the bifluorosulfate anion, $[FSO_3]_2H$. Although the predicted D@O coordination numbers of model II is closest to experiment, within error of the measured value.

The presence of H_3O^+ is consistent with NMR data on small amounts of water dissolved in a superacid.[335,339] Furthermore, though the Raman data (figure 5.4) indicate the presence of H_3O^+ in the FSO_3H/H_2O system measured here, it should be noted that the structure of H_4O^{2+} has never been characterized, and no theoretical studies have calculated the vibrational spectrum of this ion.

Table 5.4: Calculated D@O coordination number for models of the FSO_3D/D_2O system.

	c_O^D FSO_3D	c_O^D D_3O^+	c_O^D D_4O^{2+}	c_O^D total	c_O^D / # oxygens
I	0.8	0.3	-	1.1	0.39
II	0.7	0.3	-	1.0	0.36
III	0.7	-	0.4	1.1	0.39
IV	0.5	-	0.4	0.9	0.32

5.3.2 [H/D] PAIR CORRELATION FUNCTION

In order to investigate these models further, all of the heavy ion positions for F,S, and O in the neutron total pair correlation function for FSO_3D/D_2O (figure 5.8) were fit with Gaussian functions. The Gaussian functions were subtracted from the data in real space to give a resulting pair correlation function which contains not only all of the hydrogenated distances, but any distances associated with the intermolecular structure of the FSO_3D/D_2O system. Figure 5.14 shows the total pair correlation function for FSO_3H/H_2O without the intramolecular FSO_3H (or FSO_3^-) positions. In addition, the first order difference function for this system is shown as a comparison. This graph is only shown from 0.5 to 4 Å for clarity.

From figure 5.14, it is clear that the first order difference pair correlation function is similar to the total pair correlation function without the FSO_3 heavy ion positions. This indicates that many of the changes to the structure of FSO_3H upon the addition of water occur with the position of the hydrogen atom.

There is a clear peak at ~2.1 Å in figures 5.14 and 5.8 that does not appear in the FSO_3D total structure factor measurements. This is corroborated in $\Delta G^N_{HX/H_2O}(r)$, where there is evidence of a small peak at 2 Å.

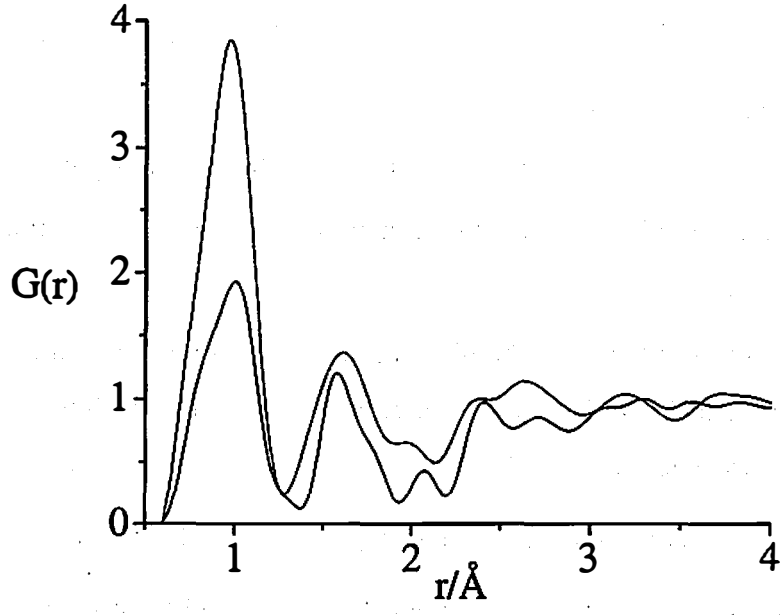

Figure 5.14: $G^{N}_{T/D_2O}(r)$- *intramolecular heavy atom positions (black line) compared with* $\Delta G^{N}_{HX/H_2O}(r)$ *(red line).*

5.3.3 ANGLE AND COORDINATION NUMBER ANALYSIS OF THE [H/D] PAIR CORRELATION FUNCTION

Assuming that model II is the most consistent with the data and that D_3O^+ retains C_{3v} symmetry, it is possible to discount the peak at ~2.1 Å in figure 5.14 as being an HH correlation associated with the hydronium ion by

$$(r_{DD})^2 = (r_{OD}^{intra})^2 + (r_{OD}^{inter})^2 - 2(r_{OD}^{intra})(r_{OD}^{intra})\cos\theta \qquad \text{for} \quad r_{OD} \approx 1 \quad \text{Å} \quad \text{and}$$

$\theta = 109.5°$ the calculated DD distance is 1.63 Å.

It is also unlikely that this feature is due to an H-S correlation, as only ~4% of the intensity in the total pair correlation function can be attributed to this correlation, as is seen in table 5.3.

It is therefore likely that the distance at ~2.1Å corresponds to a longer hydrogen bonding distance in O-D···O or O-D···F, either in the bifluorosulfate anion or between the hydronium ion and the FSO_3D solvent.

Partial pair correlation functions $\Delta G^N_{HX/H_2O}(r)$ and $\Delta G^N_{HX}(r)$ for the hydrogen distances in FSO_3H/H_2O and FSO_3H, both show an intramolecular OH peak at ~0.98 Å (figure 5.12). The second peak in both pair correlation functions is the hydrogen bonding peak. In this peak there is clearly a different peak profile in the FSO_3H/H_2O hydrogen bonding peak compared to the peak seen in pure FSO_3H. In pure FSO_3H, as is shown in chapter 2, this peak is best fit by two Gaussians, corresponding to two distinct hydrogen bonding distances in the pure fluid. These peak positions are 1.48 Å and 1.74 Å at 300 K. In the FSO_3H/H_2O system this peak has one maximum at $r_{HX} = 1.62 \pm 0.1$ Å.

The coordination number of the hydrogen bonding peak, using an integrated area from $r = 1.28$ Å to $r = 1.91$ Å (before the small feature at ~2 Å) with respect to oxygen or fluorine atoms with around the hydrogen site (O,F@H), is $c_{HX}^{inter} = 1.00 \pm 0.1, X = O, F$, and the coordination number in the small feature at ~2 Å, using an integrated area from $r = 1.91$ Å to $r = 2.13$ Å for O,F@H, is

$c_{HX}^{inter} = 0.35 \pm 0.1$. The coordination number with respect to H@O is $c_{OH}^{inter} = 0.12 \pm 0.1$. The presence of this addition peak in $\Delta G_{HX/H_2O}^{N}(r)$ suggests another hydrogen bonding peak which may be accounted for by the presence of a hydrogen bond between the H_3O^+ molecule and the FSO_3H solvent.

In comparison with FSO_3H where the total coordination number in the hydrogen bonding peak is $c_{HX}^{inter} = 0.76 \pm 0.1, X = O, F$, the FSO_3H/H_2O system is more tightly bound with respect to the hydrogen sites.

5.4 Conclusions

The data presented here are consistent with the H_3O^+ in a solution of FSO_3H. The coordination number analysis suggests that there is no appreciable concentration of H_4O^{2+}, though the error in this measure is substantial. The Raman data also suggest the presence of only H_3O^+. The presence of a longer hydrogen bond in the $\Delta G_{HX/H_2O}^{N}(r)$ function suggests hydrogen bonding from the hydronium ion to the fluorosulfuric acid solvent. This is corroborated by the $G_{T/D_2O}^{N}(r)$ function, in which there is a shoulder in the peak at ~2.5 Å that is not accounted for by the structure of the heavy atoms in pure FSO_3H. The crystal structure of $[FSO_3]^-[H_3O]^+$ gives an O···O distance, between the hydronium ion and the fluorosulfate ion of ~2.65 Å.

If there is indeed a longer O-H···X bond present in this system the most likely model for exchange is one in which a deprotonation/protionation mechanism is favored, although it is entirely plausiable that the protonation and exchange of water takes place *via* a transition state and that neither of the mechanisms proposed by Olah are valid as a description of the ground state of the fluid. Figure 5.15 shows a potential scheme by which the proton transfer may take place.

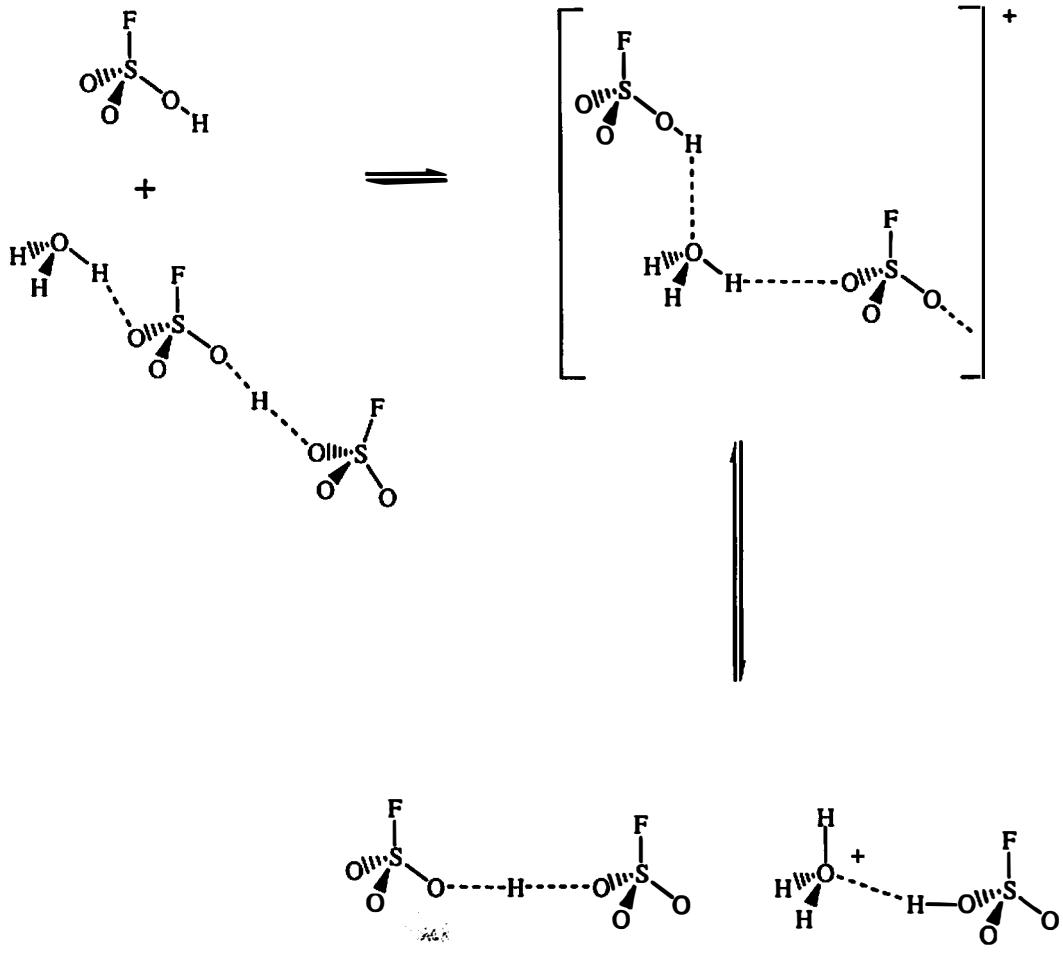

Figure 5.15: Possible scheme for proton exchange in fluorosulfuric acid and water.

CHAPTER 6: SAMPLE ENVIRONMENT FOR HYDROGEN FLUORIDE EXPERIMENTS

Part of the work reported in this chapter has been published in the *Review of Scientific Instruments*[344] and is included in its published form in the appendix.

All machine work was performed by Timothy H. Free of the University of Tennessee machine shop.

6.1 INTRODUCTION

In order to apply neutron scattering and high energy X-ray scattering to chemically ambitious samples, sample environment (SE) equipment that satisfies the chemical and experimental constraints must be designed and built. Recent advances in SE equipment have lead to the development of facilities to study chemical reactions *in situ* or in a time resolved manner.[99,345,346] These include the hydrothermal crystallization of dense phase materials and zeolites,[347-352] chemical reactions[345] and catalytic processes.[99,346]

In this chapter, the design, construction and preliminary results using sample cells are reported which allow the measurement of structural and dynamical properties of highly aggressive and reactive samples with the conservation of both chemical and isotopic integrity. Because of the toxic nature of anhydrous hydrogen fluoride, the design of the equipment must meet very severe safety constraints.

There are stringent constraints to designing SE for anhydrous HF, given the neutronic properties of hydrogen and the chemical nature of the sample. Moreover, the interplay between sample structure and the structure of the material used in cell construction is a vital consideration in order to apply X-ray and neutron scattering techniques to these chemically difficult samples.

6.2 Design Constraints

6.2.1 Neutronic Considerations

Although the interaction between the nucleus and the neutron is very strong, the low density of nuclear matter in a material of average density ensures that the net interaction of neutrons with matter is extremely weak, as is described in chapter 1. High energy X-rays yield information analogous to neutron techniques, also because of their penetration ability. This gives neutron and high energy X-ray scattering one of their major experimental advantages – that of great penetration. The range of materials out of which SE equipment can be built is wider than that for analogous experiments with X-rays of conventional energies ($\lambda \approx 1$ Å, $E_{incident} \approx 45$ meV). The penetration of neutrons is such that almost any non-absorbing material may be used, allowing the construction of high temperature and high-pressure apparatus that would be impossible at an X-ray source. An exception to this generality is the use of diamond anvil cells in X-ray diffraction experiments; such cells are only now being developed for work at neutron sources. That diamond anvil cells can be used easily in an X-ray experiment is a result of the large discrepancy in the fluences at current neutron and X-ray sources. Samples for X-ray experiments can often be much smaller than are required at a neutron source.

The range of physical variables that is accessible to investigations using neutron scattering is often wider than the analogous X-ray experiment. The caveat to this lack of proscription of construction material is that the background, which the cell material presents in the scattering experiment, must be accounted for in the data analysis and ideally considered beforehand in the design of the SE equipment.

By paying careful attention to the neutronic properties of the elements of which the apparatus is constructed, several unique approaches to sample environment design are available. Neutronically, vanadium or alloys such as $Ti_{2.08}Zr$, are common materials for construction of SE equipment for neutron scattering experiments, due to the mechanical and neutronic properties of the metals. Vanadium and $Ti_{2.08}Zr$ are chosen because of the elastic scattering cross-sections these materials possess. The former has

a very small elastic cross-section ($b_V = -0.3824$ fm)[30,31] and is predominately an incoherent scatterer, whilst the latter exploits the opposite scattering length phases of neutrons from Ti and Zr, which are $b_{Ti} = -3.438$ fm; $b_{Zr} = 7.16$ fm.[30,31] As long as the Ti and Zr atoms reside on the equivalent sites in the alloy, a cell constructed from $Ti_{2.08}Zr$ has no coherent elastic cross-section and as such, contributes no elastic background.

However, Ti, Zr, and V are chemically reactive, and being electropositive are especially susceptible to oxidation. They are suitable for conventional chemical samples but not for acidic, protic or oxidizing samples,[353-356] where the chemical stability of these elements is low and the sample may corrode or weaken the cells with potentially unpleasant results. Given the possibility of neutron activation with certain materials, the hazards are also not purely chemical. The material from which the SE equipment is constructed requires a balance between safely containing hazardous, reactive samples and minimizing the scattering background.

6.2.2 Chemical Considerations

There are several commercially available materials which can safely contain fluoride-containing samples, including polytetrafluoroethylene (PTFE)[357] and Alloy 400 ($Ni_{1.86}Cu$). Of these, PTFE has the greater general resistant to fluorides at low temperatures and pressures, especially in the presence of traces of water. Copper and nickel are also both largely resistant to attack by fluorides, and can be treated with F_2 to passivate the surface through the formation of a fluoride surface coating, which renders these materials resistant to further attack.[238] Indeed, Alloy 400 and nickel are used as the material of choice in the construction of apparatus for the synthesis and study of many high valent fluorides. Consequentially, the construction outlined below should be applicable to any fluoride that is stable in Alloy 400 or nickel. For materials that contain the hydronium ion, such as aqueous solutions of HF and FSO_3H, this containment is probably not suitable. The constraint of chemical resistance is required

in experiments such as these in order to preserve both the chemical and isotopic purity of the sample, as well as for radiological safety considerations.

6.2.3. Elastic Background Scattering Considerations

PTFE is a partially crystalline material[358-360] and the phase diagram is well known. [361,362] The diffraction pattern from this material, which forms the background, contains Bragg peaks, which arise from the periodic crystalline lattice, together with a diffuse component which arises from the local and intermediate range atomic correlations. There also exists a phase transition in PTFE that occurs at 303 K, which is an added factor in any consideration of the background signal.

Alloy 400 is a polycrystalline material, the scatter from which is predominately Bragg in nature, with low levels of diffuse scatter. Figure 6.1 shows the diffraction pattern recorded on GLAD; figure 6.2 shows the corresponding pair distribution function for both materials. The high energy X-ray data would produce a similar pattern, differing only in regard to peak intensities and is therefore not shown.

The samples for which this suite of SE equipment was designed were liquids, and as such exhibit a complete absence of Bragg scatter, due to the absence of any lattice; the diffraction intensity is confined to diffuse scatter. The choice of material is therefore crucial if the subtraction of background signal is to be successful. In the subtraction of a diffuse background from diffuse sample scatter, there is no simple *a priori* method for determining from what source the diffuse signal is recorded – sample or cell. In this respect, the material most suitable for sample containment in a liquid diffraction experiment of this type is alloy 400, even though both Cu and Ni have a large neutron scattering cross-section $\left(b_{Ni} = 10.3 \text{ fm}\right)$, $\left(b_{Cu} = 7.718 \text{ fm}\right)$[30,31] and therefore have Bragg peaks of very high intensity. However, subtraction of the prominent Bragg intensity is possible both through standard analysis proceedures[14,102] and through empirical subtraction, as is shown in chapter 3.

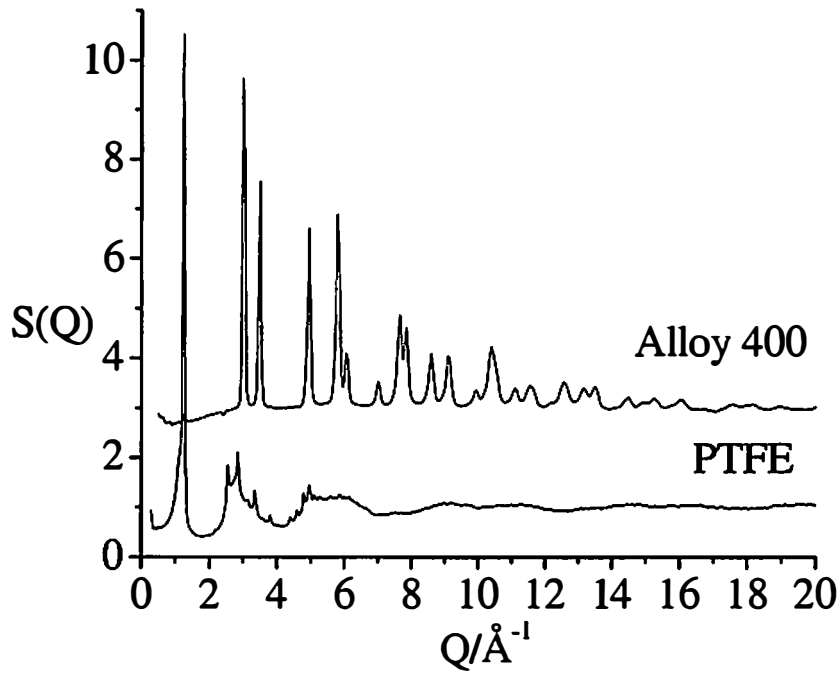

Figure 6.1: The diffraction pattern of alloy 400, $S(Q)+2$ and PTFE, $S(Q)$.

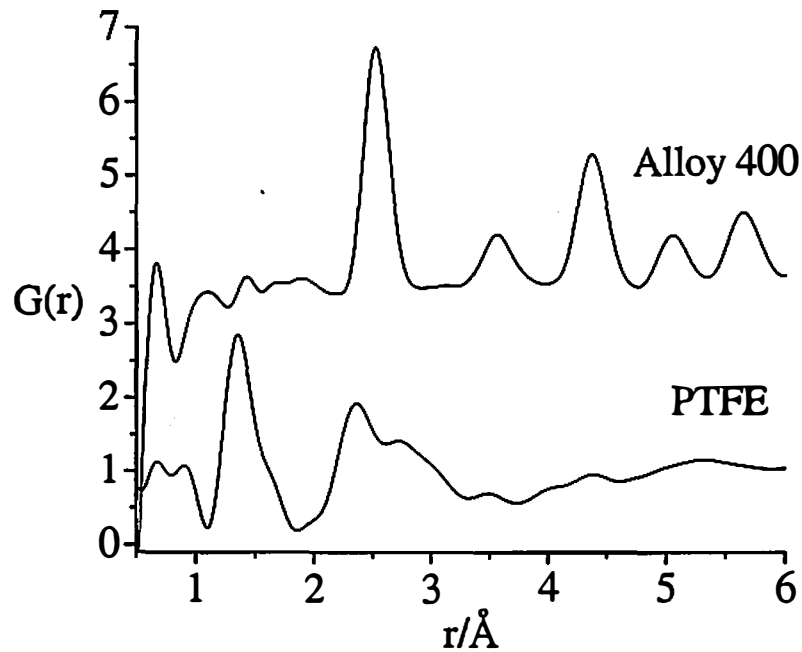

Figure 6.2: Total pair correlation function for alloy 400, $G(r)$ +3, and PTFE, $G(r)$.

6.2.3. ATTENUATION AND MULTIPLE SCATTERING CONSIDERATIONS

When running neutron diffraction experiments on samples containing a large amount of hydrogen it is necessary to reduce the thickness of the sample in the beamsince the high incoherent scattering cross section of hydrogen $(\sigma_{incoh} = 80.3 \text{ barns})$ leads to large multiple scattering effects. Even a 1 mm thick sample of HF has a significant multiple scattering contribution of ~20% and an absorption coefficient of ~5% neglecting the container at $2\theta = 20^0$ and 1.8 Å. Therefore, a flat plate geometry is optimal as it maximizes the number of atoms in the beam whilst minimizing the multiple scattering. [62] In comparison for a 6.6 mm thick flat plate DF sample the total scattering cross section is 5.82 barn/atom yielding multiple scattering contribution of ~15% and an absorption coefficient of only ~2% at $2\theta = 20^0$ and 1.8 Å. The low absorption and respectable coherent scattering cross section of DF allows relatively large samples to be placed in the beam without significant attenuation or multiple scattering effects. Considerations for the HF sample thickness in high energy x-ray experiments (~115 KeV) are also based on the minimization of multiple scattering and attenuation effects. It has been found that whilst the multiple scattering effects have a significant Q-dependence, the attenuation coefficient is usually relatively constant with momentum transfer at high energies.[61] However, it is expected that these effects will show a greater angular dependence for a flat plate geometry sample, than for a cylindrical one. For a 115 KeV incident x-ray beam the calculated attenuation coefficient (obtained using the method described by Soper, *et al.*)[63] from a 4 mm HF sample is approximately 6% and the multiple scattering contribution only ~2%. The multiple Bragg scattering and attenuation due to the heavy elements in the alloy 400 container are far greater than that from the HF sample. However, since the sample is small and is comprised of light elements, the single and multiple scattering effects from the metal container do not differ significantly with or without the presence of a sample.

In order to minimize multiple scattering in inelastic and quasielastic experiments, the total scattering strength of the sample including the sample cell is typically restricted to ensure 90% to 92% total transmission.[363] In the case of HF, the

macroscopic cross-section is approximately 2.7 cm^{-1} at the elastic energy of the spectrometer, ~4.3meV $\left(\sigma_{incoh}^{HF} \times \rho_{HF} = 90 \text{ barn} \times 0.03 \; H \; atoms / \AA^3\right)$. For a 92% transmission, this results in an ideal sample thickness along the beam direction of 0.3 mm. The sample cell will provide a relatively strong, additional signal centered at zero energy transfer.

6.3. SAMPLE CELL DESIGN FOR STRUCTURAL AND DYNAMICAL MEASUREMENTS

6.3.1. DIFFRACTION CELLS

All parts of the diffraction cells used in this work with the exception of the valves and the 'o'-rings are machined from Alloy 400. They all consist of two separable parts; a cell head which allows for transfer of hydrogen fluoride via the vacuum line described below and a sample cell body in which the sample is contained during the diffraction experiment. The two parts are joined using a 1" SwageLok® nut and a PTFE 'o'-ring seal. The sample cells constructed for the diffraction experiments are shown in figure 6.3.

The body of the sample cell head was machined from Alloy 400 bar stock. In order to load the samples into the body of the cell the top portion of the cell head was drilled with a 6.35 mm bore that turns 90^0 in approximately the middle of the head. A piece of 6.35 mm O.D. Alloy 400 seamless tubing was welded onto the outside top of the cell in order to connect the needle valve. The lower portion of the head was additionally machined with threads to fit a SwageLok® 1" nut, which allows for the connection with the body of the sample cells. At this interface, a knife-edge was machined to present a sealing surface to the 'o'-ring. Appropriately sized PTFE 'o'-rings were machined to effect the vacuum seal.

In order to minimize background container scattering, the wall thickness of each cell body was machined as thin as possible, while still maintaining the integrity of the container. The composition of the sample and the type of radiation used constrained the cell body design further. It is necessary to have a cell body of sufficient length so that

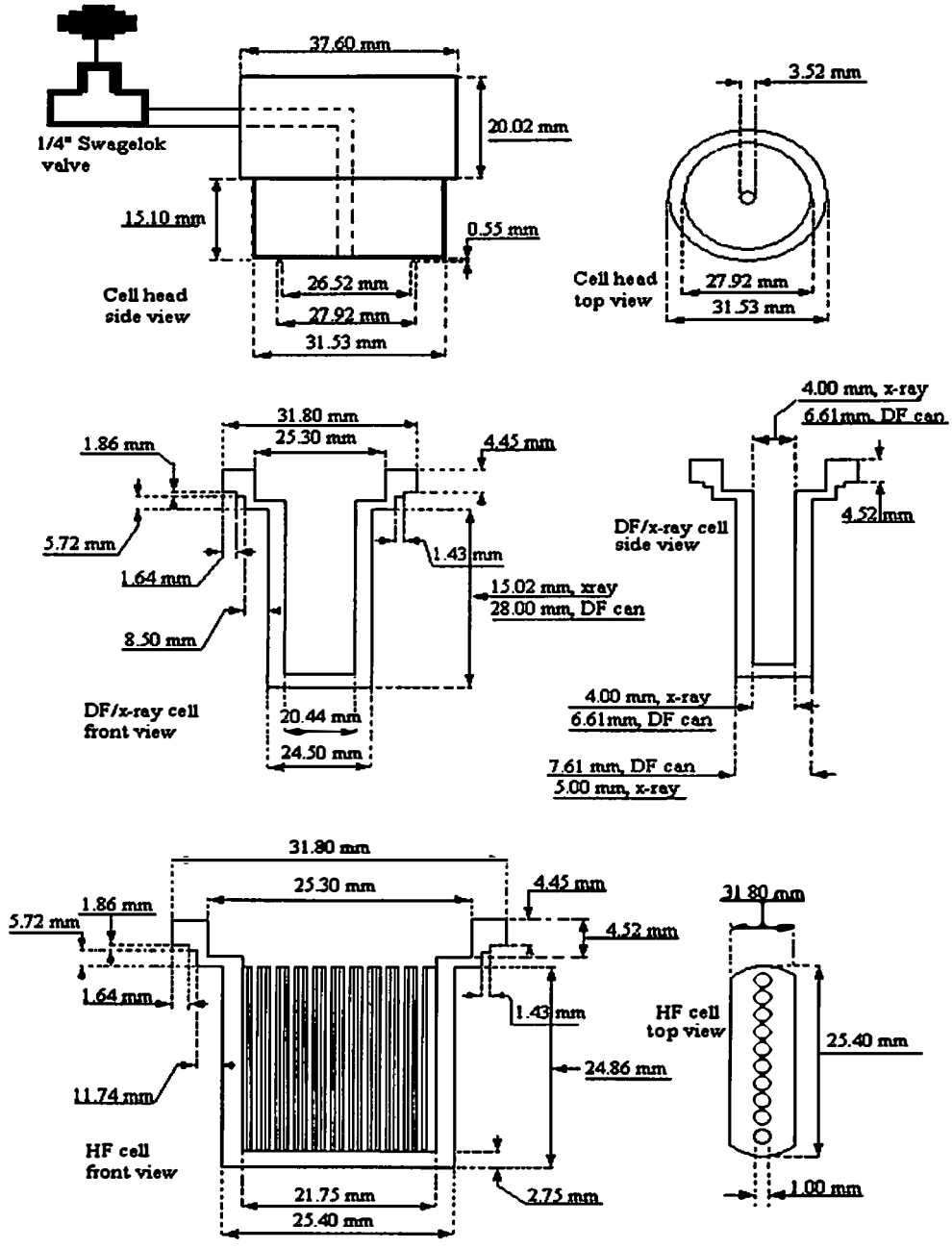

Figure 6.3: Neutron and high energy X-ray diffraction sample cells.

only sample and the thinnest part of the can encounters the radiation beam while keeping cell head from adding to further background contamination.

The design and dimensions of the X-ray and DF neutron cells are also shown in figure 6.3. In the case of all of the X-ray samples and the deuterium fluoride neutron sample, the cell bodies were machined as large as possible within the wall thickness, multiple scattering and attenuation constraints. This allowed for a 6.60 mm sample thickness in the case of the deuterium fluoride neutron measurement and a 4 mm sample in thickness in the high-energy X-ray experiments. The hydrogen fluoride neutron cell body was of a different design (figure 6.3) this cell was constructed by soldering individual pieces of alloy 400 tubing (1.5 mm O.D. 1 mm I.D.) to an alloy 400 frame using Safety-Silv® 45% silver cadmium-free silver solder in a Stay-silv® black high temperature flux.

6.3.2. QUASIELASTIC CELLS

In a quasielastic experiment, which utilizes the incoherent scatter from hydrogen, the sample cell has a limited volume to minimize the large signal from hydrogen. The cell body and cell heads, shown in figure 6.4, are of a similar construction to the diffraction cells where the two portions can be joined by a Swagelok® ½" nut. The cell head is of the same design as the diffraction cell heads (figure 6.3) but on a smaller scale, with the bore in the cell being 3.14 mm.

Because the of the small sample size thickness (~0.3 mm for HF and ~1.9 mm for H0.04D0.96F), the cell bodies were fabricated from available alloy 400 seamless tubing, to form an appropriately sized annulus. In each case a 6.41 mm O.D. x 4.93 mm ID tube was used for the outer portion of the annulus and smaller sized tubing was used to give the appropriate sample thickness. In the case of HF, the inner tube was 4.76 mm OD and in the case of H0.04D0.96F, the inner tube was 3.18 mm OD. For each set of samples the thickness was somewhat less than ideal, but the calculation ignored the scattering from the seamless alloy 400 tubing. In order to effectively vacuum transfer the samples into the cell bodies, a split Y bore was drilled into the top of the cell body

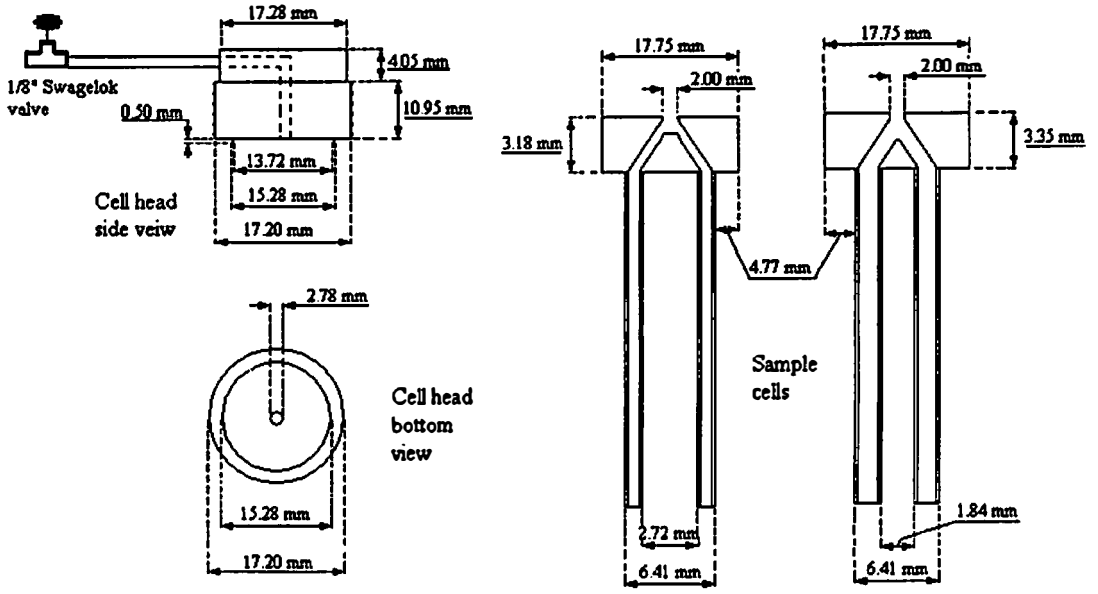

Figure 6.4: Quasielastic cells.

to allow for access to the annulus created by the tubing. The tubing was welded to the top of the cell body by the same method described above. The neutron and X-ray experiments for which these cells were designed required the preparation of isotopomers of hydrogen fluoride of known composition. Not onlymust the chemical purity of the sample be retained at all times, but also the isotopic nature of the samples needed to be similarly conserved. Given the lability in reaction of the H/D site in anhydrous hydrogen fluoride, ingress of water and other proton-containing materials had to be minimized. The basic techniques for satisfying these requirements are mature in the field of inorganic chemistry.[238] For this reason a fluorine/high vacuum line was constructed and is described in detail in section 6.4.

6.4 DESIGN OF THE SYNTHESIS AND GAS HANDLING APPARATUS

In order to prepare and handle hydrogen fluoride and deuterium fluoride in the laboratory, both synthetically and in order to prepare samples for the neutron experiments, a high vacuum line was constructed from alloy 400 and stainless steel tubing and equipped with SwageLok® fittings and needle valves. As a further precaution against contamination, and to allow the manipulation of liquids *via* Schlenk methodologies; an argon gas line was incorporated into the design. The synthetic equipment is therefore a hybrid Schlenk – high vacuum line and is hereafter termed the gas handling line. The gas handling line consists of five major components: vacuum, argon, fluorine and hydrogen fluoride circuits, connected to a central manifold.

6.4.1 MANIFOLD DESIGN

The 214.2 mm x 51 mm x 51 mm manifold is machined from alloy 400 bar stock. A 37.8 mm diameter bore is drilled into the center of the manifold and finished as closely as possible to a mirror finish so minimize any adsorption of gas and potential reactivity problems on passivation. The ports are drilled and then tapped with NPT connections; the NPT connections are sealed using Teflon tape. The manifold is shown in figure 6.5. Prior to assembly, the manifold was closely examined for burr and any

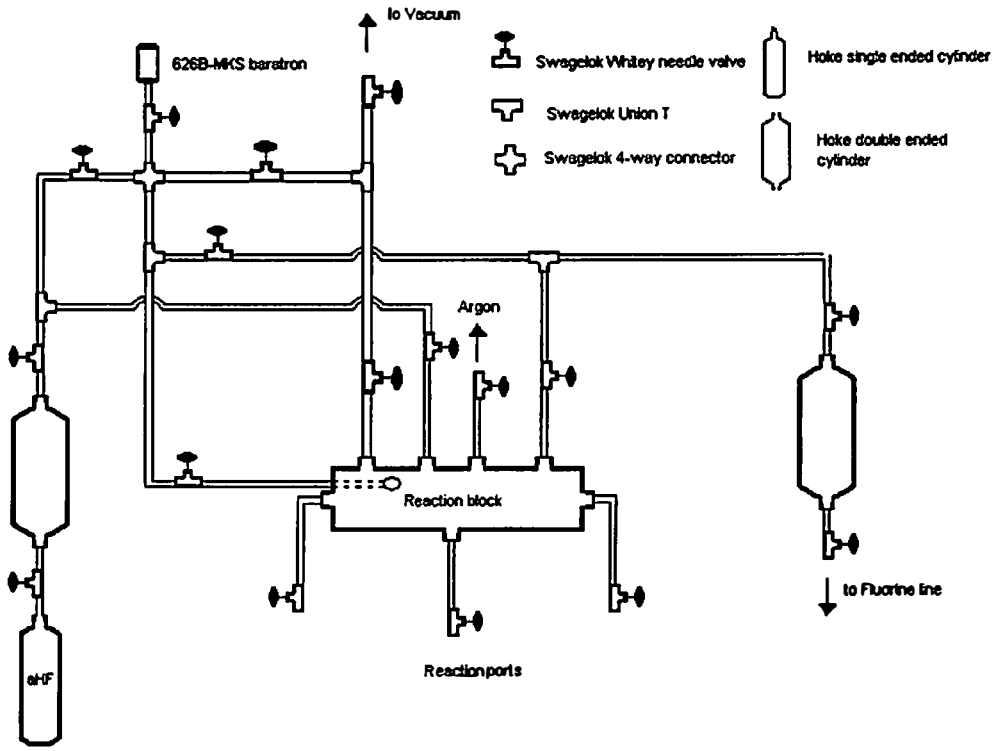

Figure 6.5: Reaction manifold for high vacuum line.

residual imperfections were removed, for the same reasons as the finishing of the interior bore. A port to the low pressure MKS 626A Baratron allows the pressure in the manifold to be measured.

6.4.2 F_2 AND HYDROGEN FLUORIDE CIRCUITS

The fluorine circuit and hydrogen fluoride circuit are constructed from 6.35 mm O.D. (4.57mm I.D.) seamless alloy 400 tubing and are equipped with Swagelok® ¼" alloy 400 or 316 stainless steel needle valves. The hydrogen fluoride circuit is shown with the reaction block in figure 6.5. The fluorine circuit is shown in figure 6.6. In order to provide a large constant volume, 2000 ml Hoke® bottles, constructed from 316 stainless steel, are introduced in the circuit. The fluorine circuit is additionally equipped with a higher pressure (1000 psi) MKS 870B baratron for measurement of higher pressures of fluorine than the manifold baratron will allow.

6.4.3 VACUUM CIRCUIT

The vacuum line, shown in figure 6.7, is constructed entirely from 12.7 mm O.D, 10.9 mm I.D 316 stainless steel seamless tubing and is equipped with SwageLok® ½" 316 stainless steel needle valves. There are two traps in place on the system. The first contains pelletized Al_2O_3, used as a scrubber trap for fluorine; the second trap is a removable glass liquid nitrogen cryogenic trap for the removal of volatiles before the pump, attached to a 316 SS trap head and sealed with Apiezon® W black wax. The scrubber can be bypassed for faster pumping and is fitted with a sintered steel 320 μm particulate filter down stream. The scrubber can also be removed and recharged without interruption of the line function.

The vacuum system is connected to the manifold (figure 6.5) and to the fluorine system (figure 6.6). The line is evacuated using a diffusion pump with Fomblin® as the working fluid, with a two-stage rotary pump as a roughing pump, the latter using conventional hydrocarbon pump oil. The diffusion pump is fitted with a by-pass valve to allow for evacuation using only the roughing pump.

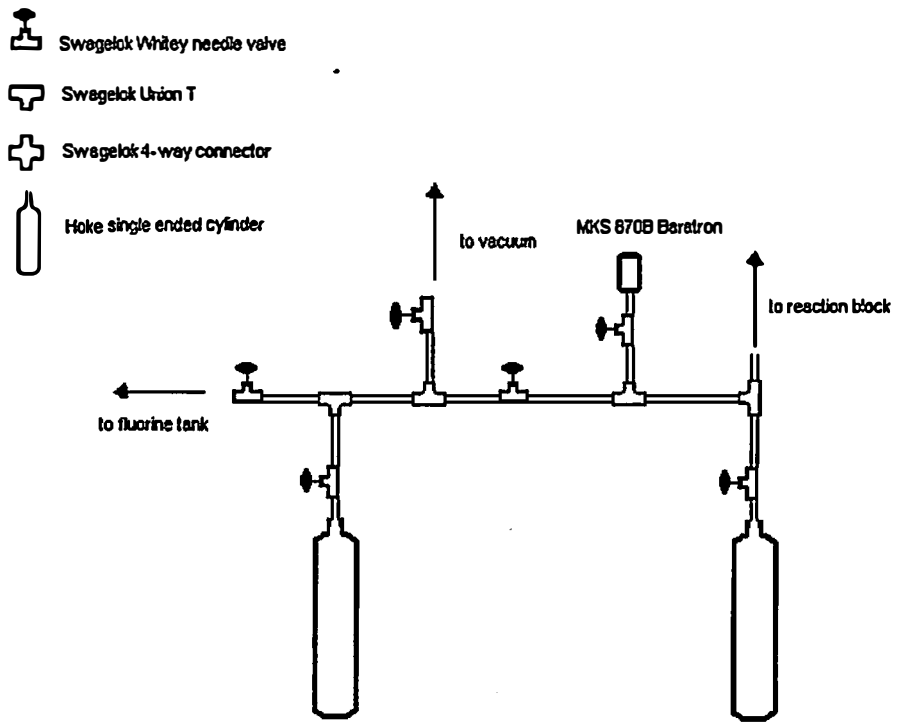

Figure 6.6: Fluorine circuit.

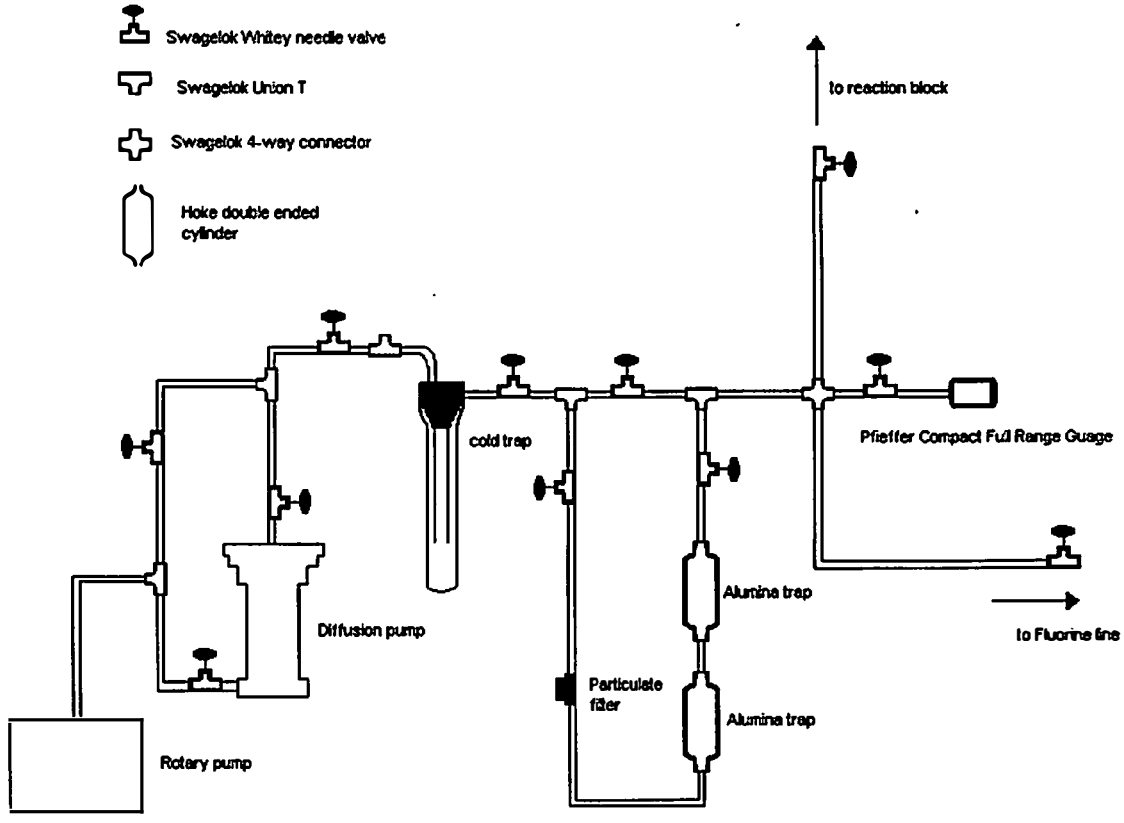

Figure 6.7: Vacuum circuit.

Pressure measurement was conducted using two electronic manometers, with ranges of 0 – 1000 Torr and 0 – 1000 psi (1 Torr = 0.001333 bar; 1 psi = 0.068948 bar) respectively. The magnitude of the vacuum was measured using a combination Pfieffer

Pirani – cold cathode ion gauge, with a range of 0 – 10^{-8} mbar. All wetted parts of the gauges were constructed from Inconel®.

6.5 CONSTRUCTION OF THE SYNTHESIS AND GAS HANDLING APPARATUS

Before commencing with assembly and use, all tubing was thoroughly degreased using 'gum solvent', a mixture by volume of 1:1:1 toluene:acetone:methanol until evaporation of the solvent left no visible residue. The tubing and other components were then freed of traces of solvent and other oxidizable volatiles by fast passage of O_2 and the line was then assembled, according to the designs described above.

The line was then both vacuum leak-tested and pressure tested with Ar. All portions of the line, except the vacuum line, were volume calibrated with Ar repeatedly, so that each segment can be used as a constant volume, allowing the barometric measurement of molar quantities of gas. It was found to maintain a static vacuum of 10^{-5} mbar over a period of weeks. After leak testing and calibration, and in order to pre-dry the line prior to drying and passivation with F_2, the line was evacuated and dried by heating the system strongly under high vacuum.

Passivation is an important aspect of the construction of any fluorine line and the portions of the gas handling line that would be wetted by F_2 or hydrogen fluoride were passivated initially by evacuation and then pressurization at ambient temperatures to sub-ambient pressures with a 5% solution of F_2 in N_2. After any pressure drop had ceased, the line was evacuated and the procedure was repeated at slightly higher initial pressure. Once atmospheric pressure had been attained and no further decrease in pressure was observed, the cycle of pressurization and evacuation was repeated with F_2 until atmospheric pressure had been reached. A pressure of 1.5 bar of F_2 was then admitted and the line left under this pressure for 24 hrs. Finally, the line was evacuated.

Reaction vessels and synthesis bombs are attached to the outlets from the manifold and volatiles are transferred by standard cryogenic techniques.[238]

6.6 DISCUSSION

Neutron diffraction experiments performed on samples of DF, HF and $[H_{1/2}D_{1/2}]F$, prepared using the above equipment and cells showed that the conservation of the isotopic nature of the samples was essentially that of the materials used to prepare the samples and that no measureable ingression of adventitious [H] occurred.[364] Given that the isotopomers of HF were dried with a pressure of F_2 prior to charging the sample can, this finding is a measure of the total [H] ingression, as H_2O is oxidized by F_2 to HF and O_2. Neutron scattering is particularly sensitive to the presence of hydrogen due to the large incoherent scattering cross-section, as discussed above.

Figures 6.8 and 6.9, show the diffraction pattern of the sample can for DF with and without the presence of the sample for both X-rays and neutrons, respectively. Whereas in figures 6.8 and 6.9 the presence of the sample is not immediately noticeable, in the Fourier transform of the diffraction pattern, the structure due to DF can be clearly seen overlayed with the local structure of alloy 400 for both diffraction patterns. This is shown in figures 6.10 and 6.11 for neutron measurements and X-ray measurements, respectively. This figure shows the advantage of using a crystalline material as the material from which the cells were constructed. The background intensity is confined to the pair correlation function expected from a cubic crystalline system and subtraction of the diffraction pattern of the cell in both high energy x-ray experiments and neutron experiments proved to be tractable, though laborious, using a combination of standard methods and empirical methods. The DF sample data after corrections for both x-ray and neutron scattering measurements are shown in chapter 3

Previous, unpublished neutron diffraction data using PTFE cells proved to be far less tractable, with structural results that are less reliable.[364] The reason for this is clear when figures 6.1 and 6.2 are considered. The determination of the source of scatter from alloy 400 is far more distinct than from PTFE, both in reciprocal and real space.

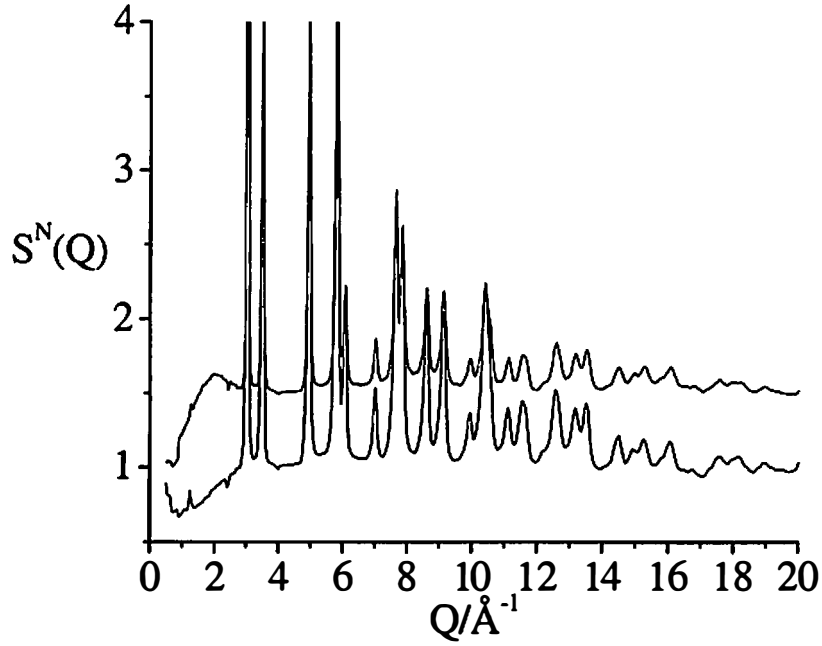

Figure 6.8: Neutron diffraction pattern for alloy 400, $S^N(Q)$ and alloy 400 plus DF, $S^N(Q)+0.5$.

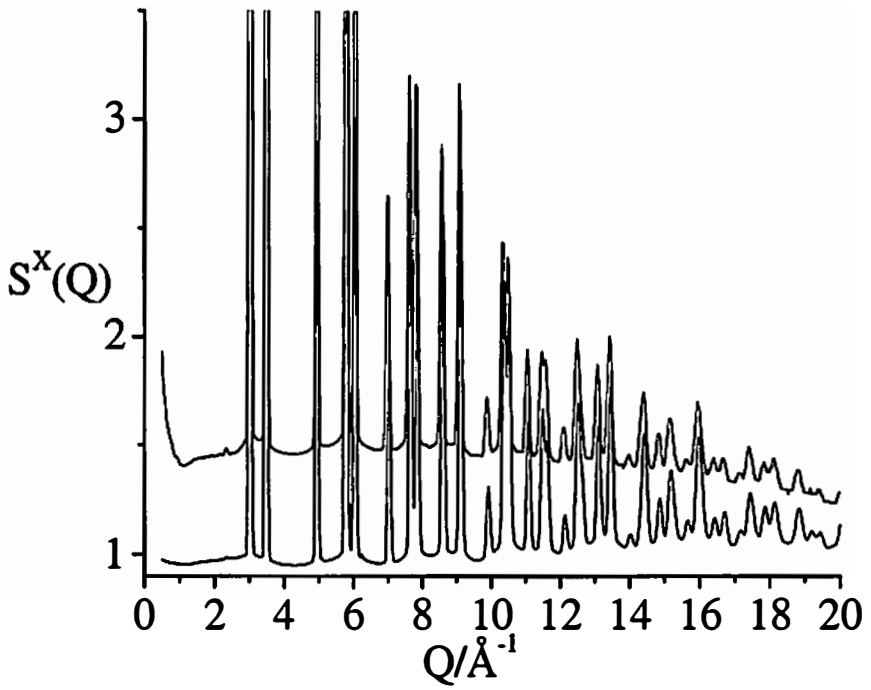

Figure 6.9: High energy x-ray diffraction pattern for alloy 400, $S^X(Q)$ and alloy 400 plus DF, $S^X(Q)$+0.5.

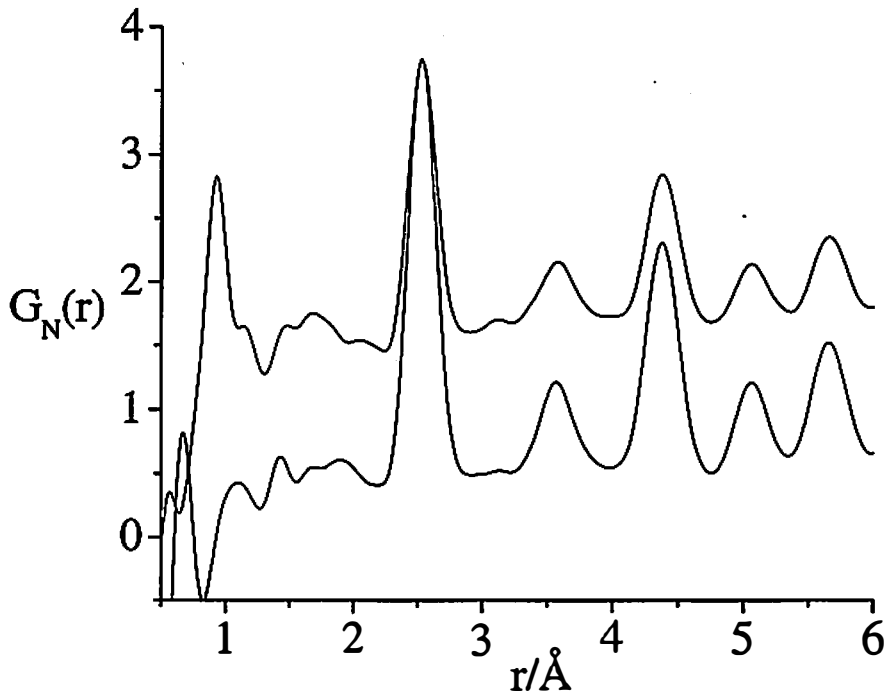

Figure 6.10: Fourier transformation of alloy 400, $G^N(r)$ and alloy 400 plus DF, $G^N(r)+1$.

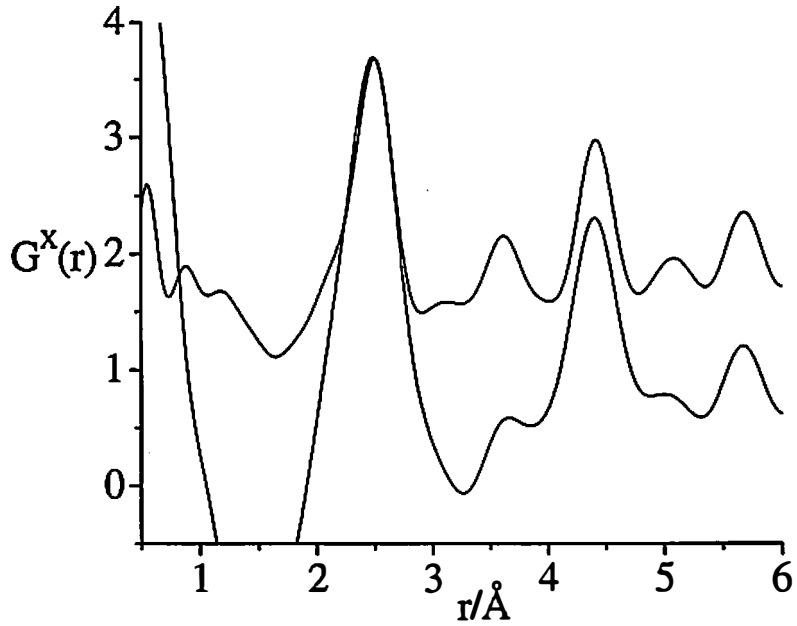

Figure 6.11: Fourier transformation of alloy 400, $G^x(r)$ and alloy 400 plus DF, $G^x(r)+1$.

Though the intensity of the background in a crystalline sample container is far more dramatic in reciprocal space than for a polymer-based cell, it is the source of the diffracted intensity that is important when considering a sample container. With a crystalline system, almost all of the background intensity, beyond that from the ubiquitous local structure, is confined to Bragg intensity, whereas for a partially or completely amorphous cell, this is not the case. The periodicity in a crystalline system, inherent due to the presence of a lattice, limits the local structure to a minimum, as in the presence of a lattice, only a small number of unique distances are required to describe the structure in real or reciprocal space.[10,56,365,366] For liquid samples, it is clear that minimization of diffuse scatter, beyond the local structure, is the most important consideration.

WORKS CITED

1 http://www.pns.anl.gov/glad/glad.html

2 http://www.pns.anl.gov/ipns.htm

3 http://www.aps.anl.gov/aps/frame_home.html

4 P. W. Atkins and R. S. Friedman, *Molecular Quantum Mechanics, 3rd Edition* (Oxford University Press, Oxford, 1997).

5 S. J. L. Billinge, *Unpublished work* (2003).

6 S. J. L. Billinge and M. F. Thorpe, Eds., *Local Structure from Diffraction* (Plenum Press, New York, 1998).

7 J. Byrne and J. M. Robson, *Neutrons, nuclei and matter : An exploration of the physics of slow neutrons* (Institute of Physics, 1996).

8 P. A. Egelstaff, *An Introduction to the Liquid State*, 2nd ed. (Oxford University Press, Oxford, 1994).

9 S. Glasstone and M. C. Edlund, *The Elements of Nuclear Reactor Theory* (D. Van Nostrand Company, Inc., New York, 1952).

10 A. Guinier, *X-ray Diffraction in Crystals, Imperfect Crystals, and Amorphous Bodies* (1963).

11 D. A. Keen, *A comparison of various commonly used correlation functions for described total scattering*, J. App.Cryst. **34,** 172-177 (2001).

12 D. J. Littler and J. F. Raffle, *An Introduction to Reactor Physics* (McGraw-Hill, New York, 1957).

13 R. Pynn, *Neutron scattering: a primer*, Neutron scattering: a primer; Los Alamos Science (1990).

14 A. K. Soper, W. S. Howells, and A. C. Hannon, *ATLAS - Analysis of Time-of-Flight Diffraction Data from Liquid and Amorphous Samples* (1989).

15 G. L. Squires, *Introduction to the Theory of Thermal Neutron Scattering* (Dover, 1997).

16 J. Chadwick, Bakerian Lecture, Proc. R. Soc. A **142,** 1 (1933).

17 J. Chadwick, *Possible Existence of a Neutron*, Nature **192,** 312 (1932).

18 W. Bothe and H. Becker, *Artificial excitation of the nuclear g-radiation*, Z. fur Phys. **66,** 289-306 (1930).

19 H. C. Webster, *The artificial production of nuclear γ-radiation.*, Proc. Roy. Soc. **129,** 428-53 (1932).

20 K. Sasaki, M. Konno, F. Hiraga, H. Iwasa, T. Kamiyama, Y. Kiyanagi, E. B. Iverson, and J. M. Carpenter, *Experimental studies on neutronics of CH_3D and HD cold neutron moderators*, JAERI-Conf **2001-002,** 873-881 (2001).

21 B. C. Boland, G. C. Stirling, and A. D. Taylor, *Reflector studies for pulsed neutron moderators*, 10 pp. (1977).

22 H. S. Camarda, *Monte-Carlo studies of deuterium oxide and water neutron moderators for time of flight experiments*, Nucl. Instrum. & Meth. **106,** 205-12 (1973).

23 J. A. Ayres and C. A. Trilling, *Heavy water and organic fluids as neutron moderator and reflector materials*, Nucl. Eng. Des. **14,** 363-89 (1970).

24 J. B. Vetrano, *Hydrides as neutron moderator and reflector materials*, Nucl. Eng. Des. **14,** 390-412 (1970).

25 J. R. Beyster, J. L. Wood, W. M. Lopez, and R. B. Walton, *Measurements of neutron spectra in water, polyethylene, and zirconium hydride*, Nucl. Sci. and Eng. **9,** 168-84 (1961).

26 M. A. Rollier, *Doctoral dissertation*, (It, 1959).

27 B. N. Brockhouse, *Neutron scattering properties of liquid moderators*, U.S. At. Energy Comm. **ORNL-2739,** 1 p. (1959).

28 E. U. Vaughan and E. R. Cohen, *Neutron moderation by chemically bound hydrogen*, U.S. At. Energy Comm. **ORNL-2739,** 16 pp. (1959).

29 J. H. Hubbell, W. J. Veigele, E. A. Briggs, R. T. Brown, D. T. Cromer, and R. J. Howerton, *Atomic form factors, incoherent scattering functions, and photon scattering cross sections*, J. Phys. Chem. Ref. Data **4,** 471-501 (1975).

30 http://www.ncnr.nist.gov/resources/n-lengths/

31 V. F. Sears, Neutron News **3,** 29-37 (1992).

32 M. von Laue, *Determination of crystal structures by means of X-rays,* Naturwissenschaften **8,** 968-71 (1920).

33 L. Bragg, *The development of X-ray analysis* (1975).

34 L. Bragg, *The diffraction of X-rays,* Brit. J. Radiol. **29,** 121-6 (1956).

35 T. Egami, *PDF analysis applied to crystalline materials,* Local Struct. Diffr., [Proc. Conf.], 1-21 (1998).

36 T. Egami, *Determining medium range order by powder diffraction,* J. Phys. Chem. Solids **56,** 1407-13 (1995).

37 V. Petkov, R. G. DiFrancesco, S. J. L. Billinge, M. Acharya, and H. C. Foley, *Local structure of nanoporous carbons,* Philos. Mag. B **79,** 1519-1530 (1999).

38 T. Proffen, R. G. DiFrancesco, S. J. L. Billinge, E. L. Brosha, and G. H. Kwei, *Measurement of the local Jahn-Teller distortion in* $LaMnO_{3.006}$, Phys. Rev. B. **60,** 9973-9977 (1999).

39 T. Proffen and S. J. L. Billinge, *PDFFIT, a program for full profile structural refinement of the atomic pair distribution function,* J. Appl. Cryst. **32,** 572-575 (1999).

40 P. F. Peterson, T. Proffen, I. K. Jeong, S. J. L. Billinge, K. S. Choi, M. G. Kanatzidis, and P. G. Radaelli, *Local atomic strain in* $ZnSe_{1-x}Te_x$ *from high real space resolution neutron pair distribution function measurements,* Los Alamos Natl. Lab., Prepr. Arch., Condens. Matter, 1-8, arXiv:cond-mat/0009364 (2000).

41 P. F. Peterson, M. Gutmann, T. Proffen, and S. J. L. Billinge, *PDFgetN: a user-friendly program to extract the total scattering structure factor and the pair distribution function from neutron powder diffraction data,* J. Appl. Cryst. **33,** 1192 (2000).

42 T. Proffen, *Analysis of occupational and displacive disorder using the atomic pair distribution function: a systematic investigation*, Z. Fur Krist. **215,** 661-668 (2000).

43 M. Gutmann, S. J. L. Billinge, E. L. Brosha, and G. H. Kwei, *Possible charge inhomogeneities in the CuO_2 planes of $YBa_2Cu_3O_{6+x}$ (x=0.25,0.45,0.65,0.94) from pulsed neutron diffraction*, Phys. Rev. B **61,** 11762-11768 (2000).

44 T. E. Faber and J. M. Ziman, *A theory of the electrical properties of liquid metals.III. The resistivity of binary alloys*, Phil. Mag. **11,** 153-173 (1965).

45 L. Van Hove, *Correlations in space and time and Born approximation scattering in systems of interacting particles*, Phys. Rev. **95,** 249-262 (1954).

46 H. Eyring and R. P. Marchi, *Significant structure theory of liquids*, J. Chem. Educ. **40,** 562-72 (1963).

47 H. Eyring and J. Hirschfelder, *The theory of the liquid state*, J. Phys. Chem. **41,** 249-57 (1937).

48 H. Eyring and T. Ree, *Significant liquid structure. VI. The vacancy theory of liquids*, Proc. Natl. Acad. Sci. U.S. **47,** 526 (1961).

49 H. Eyring, T. S. Ree, and T. Ree, *Recent developments in the significant structure theory of liquids*, Intern. J. Eng. Sci. **3,** 285-305 (1965).

50 H. Eyring and M. S. Jhon, *Significant Liquid Structures* (1969).

51 E. J. Fuller, T. Ree, and H. Eyring, *Significant structures in liquids. II*, Proc. Natl. Acad. Sci. U.S. **45,** 1594-9 (1959).

52 D. Henderson and H. Eyring, *The theory of liquids and dense gases*, Ann. Rev. Phys. Chem. **15,** 31-62 (1964).

53 J. Hirschfelder, D. Stevenson, and H. Eyring, *A theory of liquid structure*, J. Chem. Phys. **5,** 896-912 (1937).

54 M. S. Jhon and H. Eyring, *Significant structure theory of liquids*, Phys. Chem. **8A,** 335-75 (1971).

55 J. F. Kincaid and H. Eyring, *The liquid state*, J. Phys. Chem. **43,** 37-47 (1939).

56 N. H. March and M. P. Tosi, *Atomic Dynamics in Liquids* (1976).

57 W. E. Roseveare, R. E. Powell, and H. Eyring, *Structure and dynamics of liquids*, J. App. Phys. **12**, 669-79 (1941).

58 M. A. Howe, R. L. McGreevy, and E. R. Howells, *The analysis of liquid structure data from time-of-flight neutron diffractometery*, J. Phys. Condens. Mat. **89**, 3433-3451 (1989).

59 G. Placzek, *Scattering of neutrons by systems of heavy nuclei*, Phys. Rev. **86**, 377-88 (1952).

60 J. A. Johnson, A. J. G. Ellison, and D. L. Price, *The GLAD manual* (Argonne National Laborotory, 1999).

61 H. F. Poulsen, J. Neuefeind, H. B. Neumann, J. R. Schneider, and M. D. Zeidler, *Amorphous silica studied by high energy X-ray diffraction*, J. Non-Cryst. Solids **188**, 63-74 (1995).

62 A. K. Soper, *Multiple scattering from an infinite plane slab*, Nucl. Instrum. & Meth. **212**, 337-47 (1983).

63 A. K. Soper and P. A. Egelstaff, *Multiple scattering and attenuation of neutrons in concentric cylinders: I. Isotropic first scattering*, Nucl. Instrum. & Meth. **178**, 415-25 (1980).

64 P. A. Egelstaff and A. K. Soper, *The scattering of slow neutrons by diatomic molecular fluids. II. Moment expansions*, Mol. Phys. **40**, 569-84 (1980).

65 P. A. Egelstaff and A. K. Soper, *The scattering of slow neutrons by diatomic molecular fluids. I. Models*, Mol. Phys. **40**, 553-67 (1980).

66 A. K. Soper and A. Luzar, *A neutron-diffraction study of dimethyl sulfoxide-water mixtures*, J. Chem. Phys. **97**, 1320-31 (1992).

67 A. K. Soper and P. A. Egelstaff, *The structure of hydrogen chloride gas*, Mol. Phys. **39**, 1201-20 (1980).

68 A. K. Soper and P. A. Egelstaff, *The structure of liquid hydrogen chloride*, Mol. Phys. **42**, 399-410 (1981).

69 A. K. Soper, *The structure of liquid water at room temperature*, Chem. Phys. **88,** 187-97 (1984).

70 A. K. Soper and M. G. Phillips, *A new determination of the structure of water at 25.degree*, Chem. Phys. **107,** 47-60 (1986).

71 J. Turner, A. K. Soper, and J. L. Finney, *A neutron-diffraction study of tetramethylammonium chloride in aqueous solution*, Mol. Phys. **70,** 679-700 (1990).

72 C. Andreani, V. Merlo, M. A. Ricci, and A. K. Soper, *Neutron diffraction study of the partial pair correlation functions of liquid hydrogen sulfide*, Mol. Phys. **73,** 407-15 (1991).

73 J. Turner, J. L. Finney, and A. K. Soper, *Neutron diffraction studies of structure in aqueous solutions of urea and tetramethylammonium chloride and in methanol*, Z. Naturforsch., A: Phys. Sci. **46,** 73-83 (1991).

74 C. Andreani, M. Nardone, F. P. Ricci, and A. K. Soper, *Neutron diffraction study of liquid hydrogen iodide*, Phys. Rev. A **46,** 4709-16 (1992).

75 U. Buontempo, P. Postorino, M. A. Ricci, and A. K. Soper, *Neutron-diffraction study of water at high temperature*, Europhys. Lett. **19,** 385-9 (1992).

76 J. Turner, A. K. Soper, and J. L. Finney, *Water structure in aqueous solutions of tetramethylammonium chloride*, Mol. Phys. **77,** 411-29 (1992).

77 J. L. Finney, A. K. Soper, and J. Z. Tuner, *Water perturbation close to nonpolar groups in aqueous solutions*, Pure Appl. Chem. **65,** 2521-6 (1993).

78 A. K. Soper, C. Andreani, and M. Nardone, *Reconstruction of the orientational pair-correlation function from neutron-diffraction data: the case of liquid hydrogen iodide*, Phys. Rev. E **47,** 2598-605 (1993).

79 A. K. Soper and J. L. Finney, *Hydration of methanol in aqueous solution*, Phys. Rev. Lett. **71,** 4346-9 (1993).

80 A. K. Soper and J. Turner, *Impact of neutron scattering on the study of water and aqueous solutions*, Int. J. Mod. Phys. B **7,** 3049-76 (1993).

81 C. Andreani, F. Menzinger, M. A. Ricci, A. K. Soper, and J. Dreyer, *Neutron diffraction from liquid hydrogen bromide - study of the orientational correlations*, Phys. Rev. B **49,** 3811-3820 (1994).

82 J. L. Finney and A. K. Soper, *Solvent structure and perturbations in solutions of chemical and biological importance*, Chem. Soc. Rev. **23,** 1-10 (1994).

83 J. Turner and A. K. Soper, *The effect of apolar solutes on water structure: alcohols and tetraalkylammonium ions*, J. Chem. Phys. **101,** 6116-25 (1994).

84 R. H. Tromp, P. Postorino, G. W. Neilson, G. W. Ricci, M. A. Ricci, and A. K. Soper, *Neutron diffraction studies of H_2O/D_2O at supercritical temperatures. A direct determination of $g_{HH}(r)$, $g_{OH}(r)$, and $g_{OO}(r)$*, J. Chem. Phys. **101,** 6210-15 (1994).

85 M. A. Ricci, M. Nardone, F. P. Ricci, C. Andreani, and A. K. Soper, *Microscopic structure of low temperature liquid ammonia: A neutron diffraction experiment*, J. Chem. Phys. **102,** 7650-5 (1995).

86 A. Pertsemlidis, A. M. Saxena, A. K. Soper, T. Head-Gordon, and R. M. Glaeser, *Direct evidence for modified solvent structure within the hydration shell of a hydrophobic amino acid*, Proc. Natl. Acad. Sci. U. S. A. **93,** 10769-10774 (1996).

87 D. T. Bowron, J. L. Finney, and A. K. Soper, *The structure of pure tertiary butanol*, Mol. Phys. **93,** 531-543 (1998).

88 J. F. C. Turner, A. K. Soper, and C. R. A. Catlow, *Unpublished results* (1998).

89 C. Tulk, C. J. Benmore, D. D. Klug, P. A. Egelstaff, and J. Urquidi, *Structural studies of several distinct metastable forms of ice.*, Science **297,** 1320-1323 (2002).

90 J. C. Wasse, S. Hayama, N. T. Skipper, C. J. Benmore, and A. K. Soper, *The structure of saturated lithium- and potassium-ammonia solutions as studied by using neutron diffraction*, J. Chem. Phys. **112,** 7147-7151 (2000).

91 B. Tomberli, C. J. Benmore, P. A. Egelstaff, J. Neuefeind, and V. Honkimaki, *Isotopic quantum effects in water structure measured with high energy photon diffraction*, J. Phys. Condens. Mat. **12,** 2597-2612 (2000).

92 C. J. Benmore and Y. L. Loh, *The structure of liquid ethanol: A neutron diffraction and molecular dynamics study*, J. Chem. Phys. **112,** 5877-5883 (2000).

93 C. J. Benmore and P. S. Salmon, *Structure of fast-ion conducting chalcogenide glasses - the Ag- As-Se system*, J. Non-Cryst. Solids **156,** 720-724 (1993).

94 C. J. Benmore and P. S. Salmon, *The accuracy of partial structure factors for glassy materials as measured by using neutron diffraction*, Methods Determ. Partial Struct. Factors Disord. Matter Neutron Anomalous X-ray Diffr., Proc. ILL/ESRF Workshop, 30-3 (1993).

95 C. J. Benmore and P. S. Salmon, *Structure of fast-ion conducting and semiconducting glassy chalcogenide alloys*, Phys. Rev. Lett. **73,** 264-267 (1994).

96 J. Zhao, P. H. Gaskell, M. M. Cluckie, and A. K. Soper, *A neutron diffraction, isotopic substitution study of the structure of $Li_2O.2SiO_2$ glass*, J. Non-Cryst. Solids **232-234,** 721-727 (1998).

97 C. Pitteloud, D. H. Powell, A. K. Soper, and C. J. Benmore, *The structure of interlayer water in Wyoming montmorillonite studied by neutron diffraction with isotopic substitution*, Physica B **276-278,** 236-237 (2000).

98 D. H. Powell, H. E. Fischer, and N. T. Skipper, *The structure of interlayer water in Li-montmorillonite studied by neutron diffraction with isotopic substitution*, J. Phys. Chem. B. **102,** 10899-10905 (1998).

99 J. F. C. Turner, C. J. Benmore, C. M. Barker, N. Kaltsoyannis, J. M. Thomas, W. I. F. David, and C. R. A. Catlow, *Probing the nature of acetylene bound to the active site of a NiNa-Zeolite Y catalyst by in situ neutron scattering*, J. Phys. Chem. B **104,** 7570-7573 (2000).

100 A. V. De Siqueira, C. Lobban, N. T. Skipper, G. D. Williams, A. K. Soper, R. Done, J. W. Dreyer, R. J. Humphreys, and J. A. R. Bones, *The structure of pore fluids in swelling clays at elevated pressures and temperatures*, J. Phys. Condens. Mat. **11,** 9179-9188 (1999).

101 J. K. Walters, N. T. Skipper, and A. K. Soper, *The interlayer structure of a graphite-potassium-ammonia intercalation compound by neutron diffraction*, Chem. Phys. Lett. **300,** 444-450 (1999).

102 J. Urquidi, C. J. Benmore, J. Neuefeind, and B. Tomberli, *ISOMER-X: a program for the analysis of high-energy X-ray diffraction experiments*, J. App. Cryst. **36,** 368 (2003).

103 C. J. Benmore and P. A. Egelstaff, *Quantum effects in the electronic structure of liquid methanol measured by g-ray diffraction*, J. Phys. Condens. Mat. **8,** 9429-9432 (1996).

104 C. J. Benmore, B. Tomberli, P. A. Egelstaff, and J. Neuefeind, *Quantum effects in the structure of liquid benzene at room temperature*, Mol. Phys. **99,** 787-794 (2001).

105 B. Tomberli, P. A. Egelstaff, C. J. Benmore, and J. Neuefeind, *Isotopic quantum effects in the structure of liquid methanol: I. Experiments with high-energy photon diffraction*, J. Phys. Condens. Mat. **13,** 11405-11420 (2001).

106 B. Tomberli, C. J. Benmore, P. A. Egelstaff, J. Neuefeind, and V. Honkimaki, *Temperature dependence of structural quantum effects in liquid methanol*, Europhys. Lett. **55,** 341-347 (2001).

107 R. J. Gillespie, *Fluorosulfuric acid and related superacid media*, Acc. Chem. Res. **1,** 202-9 (1968).

108 R. J. Gillespie and E. A. Robinson, *Non-Aqueous Solvent Systems* (Academic Press Inc, New York, 1965).

109 G. A. Olah, *My Search for Carbocations and Their Role in Chemistry (Nobel Lecture)*, Angew. Chem., Int. Ed. **34,** 1393-1405 (1995).

110 G. A. Olah, *Superelectrophiles*, Angew. Chem., Int. Ed. **32,** 767-788 (1993).

111 T. A. O'Donnell, *Superacids and Acidic Melts as Inorganic Chemical Reaction Media* (VCH Publishing Inc, 1992).

112 N. Bartlett, R. D. Chambers, A. J. Roche, R. C. H. Spink, L. Chacon, and J. M. Whalen, *New fluorination of organic compounds using thermodynamically unstable nickel fluorides*, J. Chem. Soc., Chem. Comm., 1049-1050 (1996).

113 R. Hagiwara, F. Hollander, C. Maines, and N. Bartlett, *The crystal structure of $[Ag(XeF_2)_2]AsF_6$ formed in the oxidation of xenon by silver(II) fluoride hexafluoroarsenate*, Eur. J. Solid State Inorg. Chem. **28,** 855-66 (1991).

114 G. Lucier, J. Muenzenberg, W. J. Casteel, Jr., and N. Bartlett, *Preparation and Structural and Magnetic Properties of $AgF^+MF_6^-$ (M = Ir, Ru, Sb, Bi) and $Ag^{2+}(BiF_6^-)_2$*, Inorg. Chem. **34,** 2692-8 (1995).

115 B. Zemva, K. Lutar, L. Chacon, M. Fele-Beuermann, J. Allman, C. Shen, and N. Bartlett, *Thermodynamically unstable fluorides of nickel: NiF_4 and NiF_3 syntheses and some properties*, J. Am. Chem. Soc. **117,** 10025-34 (1995).

116 B. Zemva, L. Chacon, K. Lutar, C. Shen, J. Allman, and N. Bartlett, *Syntheses and some properties of new nickel fluorides*, J. Fluor. Chem. **71,** 195-196 (1995).

117 F. Okino and N. Bartlett, *Hexafluoroarsenates of graphite from its interaction with AsF_5, arsenic pentafluoride + fluorine and dioxygenylium hexafluoroarsenate(1-) and the structure of $C_{14}AsF_6$*, J. Chem. Soc., Dalton Trans., 2081-90 (1993).

118 G. Lucier, C. Shen, W. J. Casteel, Jr., L. Chacon, and N. Bartlett, *Some chemistry of high oxidation state transition metal fluorides in anhydrous HF*, J. Fluor. Chem. **72,** 157-63 (1995).

119 N. Bartlett, G. Lucier, C. Shen, W. J. Casteel, Jr., L. Chacon, J. Munzenberg, and B. Zemva, *The oxidizing properties of cationic high oxidation state transition-element fluoro species*, J. Fluor. Chem. **71,** 163-164 (1995).

120 G. Lucier, S. H. Elder, L. Chacon, and N. Bartlett, *The room temperature oxidation of gold, ruthenium, osmium, iridium, platinum, or palladium with fluorine in anhydrous hydrogen fluoride*, Eur. J. Solid State Inorg. Chem. **33,** 809-820 (1996).

121 S. H. Elder, G. M. Lucier, F. J. Hollander, and N. Bartlett, *Synthesis of Au(II) fluoro complexes and their structural and magnetic properties*, J. Am. Chem. Soc. **119,** 1020-1026 (1997).

122 L. C. Chacon, J. M. Whalen, and N. Bartlett, *Fluorination of organic compounds with K_2NiF_6 and R-NiF_3. Synthesis and characterization of the novel fluorinated cation: $(CHF_2)_4N^+$*, Book of Abstracts, 213th ACS National Meeting, San Francisco, April 13-17, **FLUO-010** (1997).

123 C. Shen, B. Zemva, G. M. Lucier, O. Graudejus, J. A. Allman, and N. Bartlett, *Disproportionation of Ag(II) to Ag(I) and Ag(III) in fluoride systems and syntheses and structures of $(AgF^+)_2AgF_4$-MF_6- salts (M = As, Sb, Pt, Au, Ru)*, Inorg. Chem. **38,** 4570-4577 (1999).

124 S. P. Mallela, S. Tomic, S. Lee, S. Karunanithy, H. A. Carter, J. R. Sams, and F. Aubke, *Reactions of selected methyltin(IV) and -germanium(IV) halides in anhydrous HF, HSO_3F and HSO_3CF_3*, J. Fluor. Chem. **44,** 309-28 (1989).

125 D. Zhang, S. J. Rettig, J. Trotter, and F. Aubke, *Superacid Anions: Crystal and Molecular Structures of Oxonium Undecafluorodiantimonate(V), $[H_3O][Sb_2F_{11}]$, Cesium Fluorosulfate, $CsSO_3F$, Cesium Hydrogen Bis(fluorosulfate), $Cs[H(SO_3F)_2]$, Cesium Tetrakis(fluorosulfato)aurate(III), $Cs[Au(SO_3F)_4]$, Cesium Hexakis(fluorosulfato)platinate(IV), $Cs_2[Pt(SO_3F)_6]$, and Cesium Hexakis(fluorosulfato)antimonate(V), $Cs[Sb(SO_3F)_6]$*, Inorg. Chem. **35,** 6113-6130 (1996).

126 H. Willner and F. Aubke, *Homoleptic metal carbonyl cations of the electron-rich metals: their generation in superacid media together with their spectroscopic and structural characterization*, Angew. Chem., Int. Ed. **36,** 2402-2403 (1997).

127 K. O. Christe, C. J. Schack, and R. D. Wilson, *Novel onium salts. Synthesis and characterization of oxonium hexafluoroantimonate ($OH_3^+SbF_6^-$) and oxonium hexafluoroarsenate ($OH_3^+AsF_6^-$)*, Inorg. Chem. **14,** 2224-30 (1975).

128 K. O. Christe, W. W. Wilson, D. A. Dixon, S. I. Khan, R. Bau, T. Metzenthin, and R. Lu, *The aminodiazonium cation, $H_2N_3^+$*, J. Am. Chem. Soc. **115,** 1836-42 (1993).

129 M. Atoji and W. N. Lipscomb, *The crystal structure of hydrogen fluoride*, Acta Crystallogr. **7,** 173-5 (1954).

130 M. W. Johnson, E. Sandor, and E. Arzi, *Crystal structure of deuterium fluoride*, Acta Crystallogr. B. **B31,** 1998-2003 (1975).

131 D. Mootz and K. Bartmann, *Fluorides and fluorine acids. 19. Fluoronium ions H_2F^+ and $H_3F_2^+$: crystal structure analysis*, Angew. Chem. **100,** 424-5 (1988).

132 K. Bartmann and D. Mootz, *Fluorides and fluoro acids. 25. Structures of two strong Brønsted acids: (I) fluorosulfuric acid and (II) trifluoromethanesulfonic acid*, Acta Crystallogr. C **C46,** 319-20 (1990).

133 D. Mootz and K. Bartmann, *Hydrates of fluorosulfuric acid: the melting diagram of the system fluorosulfuric acid-water and the crystal structure of the fluorosulfuric acid monohydrate*, Z. Anorg. Allg. Chem. **592,** 171-8 (1991).

134 D. Mootz and K. Bartmann, *Fluoride and fluoroacids. 29. Crystal chemistry of superacids: formation and structure of the low-melting antimony pentafluoride adducts $SbF_5.CF_3SO_3H$ and $SbF_5.7HF$*, Z. Naturforsch., B: Chem. Sci. **46,** 1659-63 (1991).

135 J. O. Lundgren, *Hydrogen bond studies. CXXX. The crystal structure of trifluoromethanesulfonic acid tetrahydrate, $H_9O_4{+}CF_3SO_3$*, Acta Crystallogr. B **B34,** 2428-31 (1978).

136 J. O. Lundgren, *Hydrogen bond studies. CXXXI. The crystal structure of trifluoromethanesulfonic acid pentahydrate, $H_3O^+CF_3SO_3^-.4H_2O$*, Acta Crystallogr. B **B34,** 2432-5 (1978).

137 J. O. Lundgren, R. Tellgren, and I. Olovsson, *Hydrogen bond studies. CXXXIV. Neutron diffraction study of oxonium trifluoromethanesulfonate*, Acta Crystallogr. B **B34,** 2945-7 (1978).

138 J. B. Spencer and J. O. Lundgren, *Hydrogen bond studies. LXXIII. Crystal structure of trifluoromethanesulfonic acid monohydrate at 298 and 83 K*, Acta Crystallogr. C **29,** 1923-8 (1973).

139 J. O. Lundgren and J. M. Williams, *Hydrated proton $H^+(H_2O)n$. I. Single crystal neutron diffraction study of the oxonium ion in p-toluenesulfonic acid monohydrate*, J. Chem. Phys. **58,** 788-96 (1973).

140 K. O. Christe, P. Charpin, E. Soulie, R. Bougon, J. Fawcett, and D. R. Russell, *Structure and vibrational spectra of oxonium hexafluoroarsenates(V) and -antimonates(V)*, Inorg. Chem. **23,** 3756-66 (1984).

141 K. O. Christe, R. D. Wilson, and A. E. Axworthy, *New synthesis of tetrafluoroammonium(+) salts and its mechanistic interpretation involving a new and exceptionally powerful oxidizing species*, Inorg. Chem. **12,** 2478-81 (1973).

142 T. Pfleiderer, I. Waldner, H. Bertagnolli, K. Tödheide, and H. E. Fischer, *The structure of liquid and supercritical deuterium fluoride from neutron scattering using high-pressure techniques*, J. Chem. Phys. **113,** 3690-3696 (2000).

143 M. Deraman, J. C. Dore, J. G. Powles, J. H. Holloway, and P. Chieux, *Structural studies of liquid hydrogen fluoride by neutron diffraction. I. Liquid deuterium fluoride at 293 K*, Mol. Phys. **55,** 1351-67 (1985).

144 S. E. McLain, C. J. Benmore, and J. F. C. Turner, *The structure of liquid fluorosulfuric acid investigated by neutron diffraction*, J. Chem. Phys. **117,** 3816-3821 (2002).

145 L. P. Hammett and A. J. Deyrup, *A series of simple basic indicators. I. The acidity functions of mixtures of sulfuric and perchloric acids with water.*, J. Am. Chem. Soc. **54,** 2721-39 (1932).

146 S. M. Chackalackal and F. E. Stafford, *Infrared Spectra of Methane-, Fluoro- and Chlorosulfonic Acids*, J. Am. Chem. Soc. **88,** 4815-4819 (1966).

147 R. Savoie and P. A. Giguere, *Etude infrarouge des acides fluo- et chloro-sulfuriques*, Can J. Chem. **42,** 277-287 (1964).

148 S. M. Chackalackal and F. E. Stafford, *Infrared Spectra of the Vapors above Sulfuric and Deuteriosulfuric Acids*, J. Am. Chem. Soc. **88,** 723-728 (1966).

149 G. A. Olah, A. Burrichter, G. Rasul, and G. K. S. Prakash, *The protiotetramethylammonium dication $(CH_3)_3NCH_4^{2+}$: hydrogen/deuterium exchange and calculational studies. Search for the parent protioammonium dication NH_5^{2+}*, J. Am. Chem. Soc. **119,** 4594-4598 (1997).

150 W. V. Cicha, F. G. Herring, and F. Aubke, *The system fluorosulfuric acid (HSO_3F) and bis(fluorosulfuryl)peroxide ($S_2O_6F_2$). A solution study*, Can. J. Chem. **68,** 102-8 (1990).

151 R. J. Gillespie and E. A. Robinson, *The Raman spectra of sulfuric, deuteriosulfuric, fluorosulfuric, chlorosulfuric, and methanesulfonic acids and their anions*, Can. J. Chem. **40,** 644-57 (1962).

152 T. Yamaguchi, K. Hidaka, and A. K. Soper, *The structure of liquid methanol revisited: a neutron diffraction experiment at -80°C and +25°C*, Mol. Phys. **97,** 603-605 (1999).

153 A. Frisch and M. Frisch, Gaussian 98, *98th Edition* (1998).

154 Y. Waseda, *The Structure of Disordered Materials* (McGraw-Hill, New York, 1980).

155 L. Bianchi, O. N. Kalugin, A. K. Adya, and C. J. Wormald, *The structure of liquid methanol: a molecular dynamics study using three-site models*, Mol. Simul. **25,** 321-338 (2000).

156 R. J. Hinde, *Personal communication with S. E. McLain* (2001).

157 F. H. Allen and W. D. S. Motherwell, *Applications of the Cambridge Structural Database in organic and crystal chemistry.*, Acta Crystallogr. B **B58,** 407-422 (2002).

158 I. J. Bruno, P. R. Eddington, M. Kessler, C. F. Macrae, P. McCabe, J. Pearson, and R. Taylor, *New software for searching the Cambridge Structural Database and visualizing crystal structures*, Acta Crystallogr. B **B58,** 389-397 (2002).

159 J. O. Lundgren, *Hydrogen bond studies. XL. Crystal structures of three hydrates of hydrogen bromide, $HBr.nH_2O$, n=1,2 and 3*, Acta Crystallogr. B **26,** 1893-9 (1970).

160 D. Mootz and W. Poll, *Fluorides and fluoro acids. V. Crystal structure of the 1:4 phase in the water-hydrogen fluoride system and a new study of one of the 1:2 phases*, Z. Anorg. Allg. Chem. **484,** 158-64 (1982).

161 D. Mootz, U. Ohms, and W. Poll, *Crystal structures of acid hydrates and oxonium salts. XVIII. Water-hydrogen fluoride melting-point diagram and structures of the 1:1 and a 1:2 phase*, Z. Anorg. Allg. Chem. **479,** 75-83 (1981).

162 J. Emsley, *Lattice energies of the alkali metal bifluorides, $U(MHF_2)$*, Polyhedron **4,** 489-90 (1985).

163 J. Emsley, O. P. A. Hoyte, and R. E. Overill, *Ab initio studies of the strongest type of hydrogen bond: carboxylic acid-fluoride systems*, J. Chem. Soc., Perkin Trans. 2, 2079-82 (1977).

164 S. E. McLain, C. J. Benmore, J. E. Siewenie, J. Urquidi, and J. F. C. Turner, *On the liquid structure of hydrogen fluoride*, Angew. Chem., Int. Ed., in press (2004).

165 R. A. D. Boisson, *The fluorochemical industry. A. The fluorochemical industry in the United States*, Organofluorine Chem., 579-93 (1994).

166 H. Fielding and B. Lee, *Blue John and family. Fluorine, hydrogen fluoride, and fluorides*, Chem. Br. **14,** 173-6, 179-80 (1978).

167 E. B. Segal, *First aid for a unique acid: HF*, Chem. Health Saf. **5,** 25-28 (1998).

168 E. B. Segal, *First aid for a unique acid, HF: a sequel*, Chem. Health Saf. **7**, 18-23 (2000).

169 J. J. Kirkpatrick, D. S. Enion, and D. A. Burd, *Hydrofluoric acid burns: a review*, Burns **21**, 483-93 (1995).

170 K. Kono, T. Watanabe, T. Dote, K. Usuda, H. Nishiura, T. Tagawa, M. Tominaga, Y. Higuchi, and M. Onnda, *Successful treatments of lung injury and skin burn due to hydrofluoric acid exposure*, Int. Arch Occ. and Enviro. Health **73**, S93-S97 (2000).

171 N. Karger, T. Vardag, and H. D. Luedemann, *p,T-dependence of self-diffusion in liquid hydrogen fluoride*, J. Chem. Phys. **100**, 8271-6 (1994).

172 G. Gore, *On Hydrofluoric Acid*, Philosophical Trans. Royal Soc. **159**, 173-200 (1869).

173 N. N. Greenwood and A. Earnshaw, *Chemistry of the Elements, 2nd Edition* (Butterworth and Heinemann, Oxford, 1997).

174 A. L. Allred, *Electronegativity values from thermochemical data*, J. Inorg. Nucl. Chem. **17**, 215-21 (1961).

175 D. E. O'Reilly, *Self-diffusion coefficients and rotational correlation times in polar liquids*, J. Chem. Phys. **49**, 5416-20 (1968).

176 D. E. O'Reilly, *Self-diffusion in liquid hydrogen fluoride. Reply to comments*, J. Chem. Phys. **52**, 5974-5 (1970).

177 R. H. Cole, *Dielectric constant and association in liquid HF*, J. Chem. Phys. **59**, 1545 (1973).

178 J. A. Barnes, T. E. Gough, and M. Stoer, *The vibrational dependence of the dipole moment of hydrogen fluoride*, Can. J. Chem. **72**, 499-505 (1994).

179 J. Besida and T. A. O'Donnell, *Stabilization of homopolyatomic cations of iodine in anhydrous hydrogen fluoride*, Inorg. Chem. **28**, 1669-73 (1989).

180 R. Gut, *The autoprotolysis constant of liquid anhydrous hydrogen fluoride*, J. Fluor. Chem. **15**, 163-7 (1980).

181 J. Janzen and L. S. Bartell, *Electron-diffraction structural study of polymeric gaseous hydrogen fluoride*, J. Chem. Phys. **50,** 3611-18 (1969).

182 A. E. Douglas and F. R. Greening, *The electronic spectra of hydrogen chloride and hydrogen fluoride*, Can. J. Phys. **57,** 1650-61 (1979).

183 D. F. Smith, *Hydrogen fluoride polymer spectrum, hexamer and tetramer*, J. Chem. Phys. **28,** 1040-1056 (1958).

184 *Gmelin Handbook of Inorganic and Organometallic chemistry* (New York, Heidelberg: Springer-Verlag, 1992).

185 P. Gunther, K. Holm, and H. Strunz, *The structure of solid hydrogen fluoride*, Z. physik. Chem. B **43,** 229 (1939).

186 W. N. Lipscomb, *Personal communication with J. F. C. Turner* (2003).

187 H. Boutin, G. J. Safford, and V. Brajovic, *Low-frequency molecular motions in HF, KHF_2, KH_2F_3, and NaH_2F_3*, J. Chem. Phys. **39,** 3135-40 (1963).

188 P. A. Giguere and N. Zengin, *Infrared spectra of hydrogen fluoride in the crystalline state*, Can. J. Chem. **36,** 1013-1019 (1958).

189 J. S. Kittelberger and D. F. Horning, *Vibrational spectrum of cyrstalline HF and DF*, J. Chem. Phys. **46,** 3099-3108 (1967).

190 S. P. Habuda and Y. V. Gagarinsky, Acta Crystallogr. B **B27,** 1677-1678 (1971).

191 R. H. Maybury, G. Sheffield, and J. J. Katz, *Infrared spectra of liquid anhydrous hydrogen fluoride, liquid sulfur dioxide, and hydrogen fluoride-sulfur dioxide solution*, J. Chem. Phys. **23,** 1277-1281 (1955).

192 J. Shamir and A. Netzer, *NMR Studies of anhydrous hydrogen fluoride solutions*, Can. J. Chem **51,** 2676-2684 (1973).

193 J. W. Ring, *Vibrational modes of hydrogen-bonded chains in liquid and solid hydrogen fluoride*, J. Chem. Phys. **68,** 2911-14 (1978).

194 J. W. Ring and P. A. Egelstaff, *Hydrogen motions in liquid hydrogen fluoride*, J. Chem. Phys. **51,** 762-70 (1969).

195 B. Desbat and H. Pham Van, *Structure of liquid hydrogen fluoride studied by infrared and Raman spectroscopy*, J. Chem. Phys. **78,** 6377-83 (1983).

196 D. P. Visco, Jr. and D. A. Kofke, *A comparison of molecular-based models to determine vapor-liquid phase coexistence in hydrogen fluoride*, Fluid Phase Equilib. **158-160,** 37-47 (1999).

197 U. Balucani, D. Bertolini, G. Sutmann, A. Tani, and R. Vallauri, *Velocity correlations in liquid hydrogen fluoride*, J. Chem. Phys. **111,** 4663-4671 (1999).

198 U. Balucani, G. Garberoglio, G. Sutmann, and R. Vallauri, *Analysis of single-molecule dynamics in liquid HF*, Chem. Phys. Lett. **315,** 109-114 (1999).

199 U. Balucani, D. Bertolini, A. Tani, and R. Vallauri, *Transport properties of liquid hydrogen fluoride*, J. Chem. Phys. **112,** 9025-9040 (2000).

200 D. Bertolini, G. Sutmann, A. Tani, and R. Vallauri, *Viscous versus elastic response of hydrogen-bonded liquids: collective dynamics in HF*, Phys. Rev. Lett. **81,** 2080-2083 (1998).

201 G. Garberoglio and R. Vallauri, *Instantaneous normal mode analysis of liquid HF*, Phys. Rev. Lett. **84,** 4878-4881 (2000).

202 G. Garberoglio, D. Pasqualini, G. Sutmann, and R. Vallauri, *Dynamical properties of hydrogen bonded liquids*, J. Mol. Liq. **96-97,** 19-29 (2002).

203 G. Garberoglio and R. Vallauri, *Instantaneous normal mode analysis of short-time dynamics in hydrogen-bonded liquids*, Physica A **314,** 492-500 (2002).

204 P. Jedlovszky and R. Vallauri, *Computer simulations of liquid HF by a newly developed polarizable potential model*, J. Chem. Phys. **107,** 10166-10176 (1997).

205 P. Jedlovszky and R. Vallauri, *Computer simulation study of liquid HF with a new effective pair potential model*, Mol. Phys. **92,** 331-336 (1997).

206 P. Jedlovszky and R. Vallauri, *Structural properties of liquid HF: a computer simulation investigation*, Mol. Phys. **93,** 15-24 (1998).

207 P. Jedlovszky, M. Mezei, and R. Vallauri, *Comparison of polarizable and nonpolarizable models of hydrogen fluoride in liquid and supercritical states: A Monte Carlo simulation study*, J. Chem. Phys. **115,** 9883-9894 (2001).

208 D. Kim and M. L. Klein, *Liquid hydrogen fluoride with an excess proton: Ab initio molecular dynamics study of a superacid*, J. Am. Chem. Soc. **121,** 11251-11252 (1999).

209 M. L. Klein, I. R. McDonald, and S. F. O'Shea, *An intermolecular force model for dimeric hydrogen fluoride*, J. Chem. Phys. **69,** 63-6 (1978).

210 M. L. Klein and I. R. McDonald, *Structure and dynamics of associated molecular systems. I. Computer simulation of liquid hydrogen fluoride*, J. Chem. Phys. **71,** 298-308 (1979).

211 I. R. McDonald and M. L. Klein, *Molecular dynamics studies of hydrogen-bonded liquids*, Faraday Discuss. Chem. Soc. **66,** 48-57 (1978).

212 C. Zhang, D. L. Freeman, and J. D. Doll, *Monte Carlo studies of hydrogen fluoride clusters: cluster size distributions in hydrogen fluoride vapor*, J. Chem. Phys. **91,** 2489-97 (1989).

213 M. E. Cournoyer and W. L. Jorgensen, *An improved intermolecular potential function for simulations of liquid hydrogen fluoride*, Mol. Phys. **51,** 119-32 (1984).

214 W. L. Jorgensen, *Quantum and statistical mechanical studies of liquids. 2. Monte-Carlo simulations of liquid hydrogen fluoride*, J. Am. Chem. Soc. **100,** 7824-31 (1978).

215 W. L. Jorgensen and M. E. Cournoyer, *Quantum and statistical studies of liquids. 1. An intermolecular potential function for the hydrogen fluoride dimer from ab initio 6-31G computations*, J. Am. Chem. Soc. **100,** 4942-5 (1978).

216 W. L. Jorgensen, *Basis set dependence of the structure and properties of liquid hydrogen fluoride*, J. Chem. Phys. **70,** 5888-97 (1979).

217 S. Wierzchowski and D. A. Kofke, *UB association bias algorithm applied to the simulation of hydrogen fluoride*, Fluid Phase Equilibria **194-197**, 249-256 (2002).

218 H. Sun, R. O. Watts, and U. Buck, *The infrared spectrum and structure of hydrogen fluoride clusters and the liquid: semiclassical and classical studies*, J. Chem. Phys. **96**, 1810-21 (1992).

219 A. Munoz-Losa, I. Fernandez-Galvan, M. E. Martin, and M. A. Aguilar, *Theoretical study of liquid hydrogen fluoride. Application of the averaged solvent electrostatic potential/Molecular Dynamics method*, J. Phys. Chem. B **107**, 5043-5047 (2003).

220 C. Martin, M. Lombardero, J. A. Anta, and E. Lomba, *Integral equation study of liquid hydrogen fluoride*, J. Chem. Phys. **114**, 355-362 (2001).

221 S. K. Nayak and R. Ramaswamy, *Solid to liquid transition in model (HF)n clusters*, Mol. Phys. **89**, 809-817 (1996).

222 D. P. Visco, Jr., D. A. Kofke, and R. R. Singh, *Thermal properties of hydrogen fluoride from EOS + association model*, AIChE J. **43**, 2381-2384 (1997).

223 D. P. Visco, Jr. and D. A. Kofke, *Vapor-liquid equilibria and heat effects of hydrogen fluoride from molecular simulation*, J. Chem. Phys. **109**, 4015-4027 (1998).

224 D. P. Visco and D. A. Kofke, *Modeling the Monte Carlo simulation of associating fluids*, J. Chem. Phys. **110**, 5493-5502 (1999).

225 D. P. Visco, Jr. and D. A. Kofke, *Improved thermodynamic equation of state for hydrogen fluoride*, Ind. Eng. Chem. Res. **38**, 4125-4129 (1999).

226 D. P. Visco, Jr. and D. A. Kofke, *Improved thermodynamic equation of state for hydrogen fluoride.. [Erratum to document cited in CA131:219419]*, Ind. Eng. Chem. Res. **39**, 242 (2000).

227 R. G. Della Valle and D. Gazzillo, *Towards an effective potential for the monomer, dimer, hexamer, solid, and liquid forms of hydrogen fluoride*, Phys. Rev. B **59**, 13699-13706 (1999).

228 U. Roethlisberger and M. Parrinello, *Ab initio molecular dynamics simulation of liquid hydrogen fluoride*, J. Chem. Phys. **106**, 4658-4664 (1997).

229 M. Kreitmeir, H. Bertagnolli, J. J. Mortensen, and M. Parrinello, *Ab initio molecular dynamics simulation of hydrogen fluoride at several thermodynamic states*, J. Chem. Phys. **118**, 3639-3645 (2003).

230 T. Yogi, *Structure and properties of diatomic liquid HF*, J. Phys. Soc. Jpn. **67**, 1643-1648 (1998).

231 P. Jedlovszky, *The local structure of various hydrogen bonded liquids: Voronoi polyhedra analysis of water, methanol, and HF*, J. Chem. Phys. **113**, 9113-9121 (2000).

232 S. J. Wierzchowski, D. A. Kofke, and J. Gao, *Hydrogen fluoride phase behavior and molecular structure: A QM/MM potential model approach*, J. Chem. Phys. **119**, 7365-7371 (2003).

233 S. J. Wierzchowski and D. A. Kofke, *Hydrogen fluoride phase behavior and molecular structure: Ab initio derived potential models*, J. Chem. Phys. **119**, 6092-6099 (2003).

234 A. Munoz Losa, I. Fernandez Galvan, M. E. Martin, and M. A. Aguilar, *An averaged solvent electrostatic potential/molecular dynamics study of the influence of the electron correlation on the properties of liquid hydrogen fluoride*, Theochem **632**, 227-234 (2003).

235 S. Y. Liem and P. L. A. Popelier, *High-rank quantum topological electrostatic potential: Molecular dynamics simulation of liquid hydrogen fluoride*, J. Chem. Phys. **119**, 4560-4566 (2003).

236 S. Raugei and M. L. Klein, *Nuclear quantum effects and hydrogen bonding in liquids*, J. Am. Chem. Soc. **125**, 8992-8993 (2003).

237 A. K. Karmakar, S. Sarkar, and R. N. Joarder, *Molecular Clusters in Liquid tert-Butyl Alcohol at Room Temperature*, J. Phys. Chem. **99,** 16501-3 (1995).

238 D. F. Shriver and M. A. Drezdzon, *The Manipulation of Air-Sensitive Compounds*, 2nd ed. (John Wiley & Sons, 1986).

239 *Handbook of Chemistry and Physics, 83rd Edition* (CRC Press, New York, 2002-2003).

240 R. L. McGreevy and A. Mellergard, *The development of RMC methods for modeling structural disorder in crystalline materials*, AIP Conference Proceedings **479,** 19-27 (1999).

241 R. L. McGreevy and M. A. Howe, *Reverse Monte Carlo (RMC): modeling disordered structures*, Annu. Rev. Mater. Sci. **22,** 217-42 (1992).

242 R. L. McGreevy, *Reverse Monte Carlo modelling*, J. Phys. Condens. Mat. **13,** R877-R913 (2001).

243 R. L. McGreevy, *Reverse Monte Carlo methods for structural modeling*, Comput. Modell. Inorg. Crystallogr. 151-184 (1997).

244 R. L. McGreevy, *RMC: progress, problems and prospects*, Nucl. Instrum. Methods Phys. Res., Sect. A **354,** 1-16 (1995).

245 R. L. McGreevy, *Reverse Monte Carlo: fact and fiction*, J. Non-Cryst. Solids **156-158,** 949-55 (1993).

246 J. Krawczyk, A. Pietraszko, R. Kubiak, and K. Lukaszewicz, *Diffuse scattering and short-range order in uranium iodine phthalocyanine* $[U_{1-x}Pc_2]I_{2-y}$ *and the X-ray structure analysis of crystals withdiffuse superstructure reflections*, Acta Crystallogr. B. **59,** 384-392 (2003).

247 J. Krawczyk, A. Pietraszko, and K. Lukaszewicz, *Diffuse x-ray scattering and reverse Monte Carlo simulation of the short-range order in ytterbium iodine phthalocyanine* $[YbPc_2]I_2$, Acta Crystallogr. B. **B58,** 622-626 (2002).

248 A. V. Belushkin, D. P. Kozlenko, R. L. McGreevy, B. N. Savenko, and P. Zetterstro, *A study of orientational disorder in ND_4Cl by the reverse Monte Carlo method*, Physica B **269,** 297-303 (1999).

249 A. Le Bail, *Reverse Monte Carlo and Rietveld modeling of the $NaPbM_2F_9$ (M = Fe, V) fluoride glass structures*, J. Non-Cryst. Solids **271,** 249-259 (2000).

250 S. Rycroft, A. Chahid, and R. L. McGreevy, *Neutron diffraction and RMC study of CN- orientations in $Na(CN)_xBr_{1-x}$*, Physica B **276-278,** 284-285 (2000).

251 A. I. Kolesnikov, O. I. Barkalov, M. Calvo-Dahlborg, U. Dahlborg, W. S. Howells, and E. G. Ponyatovsky, *Neutron diffraction and reverse Monte Carlo study of bulk amorphous $Ga_{38}Sb_{38}Ge_{24}$ alloys*, Phys. Rev. B. **62,** 9372-9377 (2000).

252 M. G. Tucker, M. P. Squires, M. T. Dove, and D. A. Keen, *Dynamic structural disorder in cristobalite: neutron total scattering measurement and reverse Monte Carlo modelling*, J. Phys. Condens. Mat. **13,** 403-423 (2001).

253 M. G. Tucker, D. A. Keen, and M. T. Dove, *A detailed structural characterization of quartz on heating through the a-b phase transition*, Mineralogical Magazine **65,** 489-507 (2001).

254 M. T. Dove, *An introduction to the use of neutron scattering methods in mineral sciences*, Euro. J. Mineral. **14,** 203-224 (2002).

255 L. Pusztai, *Reverse Monte Carlo simulations for determining disordered structures. Basics, and application for amorphous semiconductors*, NATO ASI Ser., Ser. 3 **23,** 215-224 (1997).

256 C. J. Benmore, *Personal communication with J. F. C. Turner* (2000).

257 S. E. McLain, J. E. Siewenie, C. J. Benmore, and J. F. C. Turner, *On the structure of boron trifluoride in liquid and supercritical phase investigated with neutron diffraction*, J. Chem. Phys. **119,** 6671-6679 (2003).

258 J. March, *Advanced Organic Chemistry*, 6th ed. (Wiley, New York, 1998).

259 Y. Yamamoto, *Acyclic stereocontrol via allylic organometallic compounds*, Acc. Chem. Res. **20,** 243-9 (1987).

260 A. G. Gershikov and V. P. Spiridonov, *The harmonic force fields of boron trifluoride, tin(IV) chloride and antimony(III) bromide obtained by the joint use of electron diffraction and vibrational spectroscopy data*, J. Mol. Struct. **73,** 91-8 (1981).

261 K. Kuchitsu and S. Konaka, *Boron-fluorine bond distance of boron trifluoride determined gas electron diffraction*, J. Chem. Phys. **45,** 4342-7 (1966).

262 S. Konaka, Y. Murata, K. Kuchitsu, and Y. Morino, *The molecular structure and force constants of boron trifluoride and boron trichloride*, Bull. Chem. Soc. Jpn. **39,** 1134-46 (1966).

263 C. W. Brown and J. Overend, *Rotation-vibration band contours in the infrared spectrum of boron trifluoride*, Spectrochim. Acta, A **25,** 1535-46 (1969).

264 E. Zeisberger and A. Ruoff, *High resolution Fourier transform infrared spectra of boron-10-labeled boron trifluoride*, J. Mol. Spectrosc. **136,** 295-316 (1989).

265 M. Oldani and A. Bauder, *Pure rotational spectrum of boron trifluoride-11B observed by microwave Fourier transform spectroscopy*, J. Chem. Phys. **86,** 624-8 (1987).

266 O. S. Binbrek, N. Krishnamurthy, and A. Anderson, *Lattice vibrations of boron trihalide crystals*, J. Chem. Phys. **60,** 4400-5 (1974).

267 M. Atoji and W. N. Lipscomb, *Boron-chlorine distance in boron trichloride*, J. Chem. Phys. **27,** 195 (1957).

268 C. Spencer and W. N. Lipscomb, *Boron-chlorine distance in boron trichloride*, J. Chem. Phys. **28,** 355 (1958).

269 M. A. Ring, J. D. H. Donnay, and W. S. Koski, *The crystal structure of boron triiodide*, Inorg. Chem. **1,** 109-11 (1962).

270 M. A. Rollier and A. Riva, *Determinazione roentgenografica della struttura cristallina del cloruro e del boro allo stato solido*, Gazz. Chim. Ital. **77,** 361-366 (1947).

271 O. S. Binbrek, J. K. Brandon, and A. Anderson, *Infrared and Raman spectra of crystalline boron trifluoride*, Can. J. Spectrosc. **20,** 52-6 (1975).

272 R. G. Steinhardt, Jr., G. E. S. Fetsch, and M. W. Jordan, *Infrared absorption spectrum of liquid boron trifluoride*, J. Chem. Phys. **43,** 4528-30 (1965).

273 D. A. Dows, *Infrared spectrum of crystalline boron trifluoride*, J. Chem. Phys. **31,** 1637-9 (1959).

274 R. J. H. Clarke and P. D. Mitchell, *Raman spectra and factor group analyses of crystalline boron trihalides*, J. Chem. Phys. **56,** 2225-32 (1972).

275 M. Y. Antipin, A. M. Ellern, V. F. Sukhoverkhov, Y. T. Struchkov, and Y. A. Buslaev, *Crystal structure of boron trifluoride at -145°C*, Dokl. Akad. Nauk SSSR **279,** 892-5 [Chem.] (1984).

276 D. Mootz and M. Steffen, *Fluorides and fluoro acids. IV. Crystal structures of boron trifluoride and its 1:1 compounds with water and methanol, hydroxo- and methoxotrifluoroboric acid*, Z. Anorg. Allg. Chem. **483,** 171-80 (1981).

277 D. Mootz and M. Steffen, *Boron trifluoride: crystal structure of a metastable phase*, Angew. Chem. **92,** 481 (1980).

278 T. H. S. Higgins and C. J. G. Raw, *Problem of molecular association in liquid boron trifluoride*, J. Chem. Phys. **23,** 606 (1955).

279 F. Daniels, *Outlines of Physical Chemistry* (Wiley and Sons, New York, 1948).

280 A. N. Spencer and M. C. J. Todd, *Viscosity and thermal conductivity of liquid boron trifluoride*, Brit. J. Appl. Phys. **11,** 60-4 (1960).

281 L. Pauling, *The Nature of the Chemical Bond*, 3rd ed. (Cornell University Press, Ithaca, NY, 1960).

282 V. Schomaker and D. P. Stevenson, *Some revisions of the covalent radii and the additivity rule for the lengths of partially ionic single covalent bonds*, J. Am. Chem. Soc. **63,** 37-40 (1941).

283 F. A. Cotton and A. P. Wilkinson, *Advanced Inorganic Chemistry*, 5th ed. (Wiley, New York, 1988).

284 R. J. Gillespie and E. A. Robinson, *Molecular geometry of "ionic" molecules: a ligand close-packing model*, Adv. Mol. Struct. Res. **4,** 1-41 (1998).

285 H. Hirao, K. Omoto, and H. Fujimoto, *Lewis Acidity of Boron Trihalides*, J. Phys. Chem. A **103,** 5807-5811 (1999).

286 E. A. Robinson, S. A. Johnson, T.-H. Tang, and R. J. Gillespie, *Reinterpretation of the Lengths of Bonds to Fluorine in Terms of an Almost Ionic Model*, Inorg. Chem. **36,** 3022-3030 (1997).

287 B. D. Roswell, R. J. Gillespie, and G. L. Heard, *Ligand close packing and the Lewis acidity of BF_3 and BCl_3*, Inorg. Chem. **38,** 4659-4662 (1999).

288 V. Jonas, G. Frenking, and M. T. Reetz, *Comparative Theoretical Study of Lewis Acid-Base Complexes of BH_3, BF_3, BCl_3, $AlCl_3$, and SO_2*, J. Am. Chem. Soc. **116,** 8741-53 (1994).

289 E. A. Robinson, G. L. Heard, and R. J. Gillespie, *The importance of ligand-ligand interactions in determining molecular geometry: the ligand close packing model*, J. Mol. Struct. **485-486,** 305-319 (1999).

290 B. J. van der Veken and E. J. Sluyts, *Reversed Lewis acidity of mixed boron halides: An Infrared study of the van der Waals complexes of BF_xCl_y with CH_3F in cryosolution*, J. Am. Chem. Soc. **119,** 11516-11522 (1997).

291 L. M. Nxumalo and T. A. Ford, *Infrared spectrum of the boron trifluoride dimer*, Vib. Spectrosc. **6,** 333-43 (1994).

292 F. M. M. O'Neill, G. A. Yeo, and T. A. Ford, *Matrix isolation infrared spectrum and ab initio calculations of the boron trifluoride dimer. Tentative assignments*, J. Mol. Struct. **173,** 337-48 (1988).

293 R. J. Hinde, D. T. Anderson, S. Tam, and M. E. Fajardo, *Probing quantum solvation with infrared spectroscopy: infrared activity induced in solid parahydrogen by N_2 and Ar dopants*, Chem. Phys. Lett. **356,** 355-360 (2002).

294 R. J. Hinde, *Absorption intensity of the Q1(0)+Q1(0) and Q1(0)+Q2(0) double vibrational transitions in solid parahydrogen*, Phys. Rev. B. **61,** 11451-11453 (2000).

295 D. T. Anderson, R. J. Hinde, S. Tam, and M. E. Fajardo, *High-resolution spectroscopy of HCl and DCl isolated in solid parahydrogen: Direct, induced, and cooperative infrared transitions in a molecular quantum solid*, J. Chem. Phys. **116,** 594-607 (2002).

296 C. J. Wormald, *Bristol University, Personal communication with J. F. C. Turner* (2003).

297 W. A. Herrebout, J. Lundell, and B. J. Van der Veken, *A cryospectroscopic study of the van der Waals complexes between vinyl fluoride and boron trifluoride: evidence for the existence of σ and π complexes*, J. Phys. Chem. A **102,** 10173-10181 (1998).

298 W. A. Herrebout, R. Szostak, and B. J. van der Veken, *Methylenecyclopropane-boron trifluoride van der Waals complexes; an Infrared and DFT study*, J. Phys. Chem. A **104,** 8480-8488 (2000).

299 W. A. Herrebout and B. J. Van der Veken, *Behavior of boron trifluoride in cryosolutions: A combined ab initio, Monte Carlo, and FTIR investigation*, J. Am. Chem. Soc. **120,** 9921-9929 (1998).

300 W. A. Herrebout and B. J. van der Veken, *Vibrational spectra and relative stabilities of the van der Waals complexes of boron trifluoride with cis-2-butene, trans-2-butene and 2-methyl propene*, J. Mol. Struct. **550-551,** 389-398 (2000).

301 B. J. van der Veken, E. J. Sluyts, and W. A. Herrebout, *The van der Waals molecules of carbonyl sulfide with hydrogen chloride and boron trifluoride. An infrared study in cryosolution*, J. Mol. Struct. **449,** 219-229 (1998).

302 B. J. van der Veken and E. J. Sluyts, *A FTIR study of the van der Waals complexes between boron trifluoride and carbon monoxide in liquefied argon*, J. Mol. Struct. **349,** 461-4 (1995).

303 B. J. van der Veken and E. J. Sluyts, *The van der Waals complex between boron trifluoride and methyl fluoride: An Infrared and ab initio study*, J. Phys. Chem. A **101,** 9070-9076 (1997).

304 L. M. Nxumalo, G. A. Yeo, and T. A. Ford, *The vibrational spectra of the boron halides and their molecular complexes. Part 6. An ab initio study of the structure, interaction energy, Mulliken atomic charges and infrared spectrum of the boron trifluoride-nitrous oxide complex*, S. Afr. J. Chem. **51,** 25-34 (1998).

305 L. M. Nxumalo and T. A. Ford, *The Fourier transform infrared spectrum of the boron trifluoride-nitrous oxide complex*, Spectrochim. Acta, A **53A,** 2511-2524 (1997).

306 L. M. Nxumalo and T. A. Ford, *The Fourier transform infrared spectrum of the boron trifluoride-carbon dioxide complex*, J. Mol. Struct. **436-437,** 69-80 (1997).

307 L. M. Nxumalo and T. A. Ford, *The vibrational spectra of the boron halides and their molecular complexes. Part 4. Ab initio predictions of the structures and vibrational spectra of the complexes of boron trifluoride with dimethyl ether and dimethyl sulfide*, Theochem **369,** 115-126 (1996).

308 L. M. Nxumalo, M. Andrzejak, and T. A. Ford, *The vibrational spectra of the boron halides and their molecular complexes. 3. Ab initio predictions of the structures, energetics, and Mulliken atomic charges of the complexes of boron trifluoride with some linear nitrogen donors*, J. Chem. Inf. Comput. Sci. **36,** 377-84 (1996).

309 L. M. Nxumalo, M. Andrzejak, and T. A. Ford, *The structure of the boron trifluoride-ammonia complex: a Fourier transform matrix isolation infrared spectroscopic and ab initio molecular orbital study*, Vib. Spectrosc. **12,** 221-235 (1996).

310 L. M. Nxumalo and T. A. Ford, *The boron trifluoride-carbon monoxide complex: a matrix-isolation infrared spectroscopic and ab initio molecular-orbital theoretical study*, S. Afr. J. Chem. **48,** 30-8 (1995).

311 T. Tassaing, M. I. Cabaco, Y. Danten, and M. Besnard, *The structure of liquid and supercritical benzene as studied by neutron diffraction and molecular dynamics*, J. Chem. Phys. **113,** 3757-3765 (2000).

312 Y. Danten, M. I. Cabaco, T. Tassaing, and M. Besnard, *A structural study of hexafluorobenzene from liquid to supercritical conditions using neutron diffraction and molecular dynamics*, J. Chem. Phys. **115,** 4239-4248 (2001).

313 C. J. Benmore and B. L. Tomberli, *The structure of carbon dioxide around naphthalene investigated using H/D substitution in neutron diffraction*, Ind. & Eng. Chem. Res. **39,** 4491-4495 (2000).

314 A. Botti, F. Bruni, A. Isopo, G. Modesti, C. Oliva, M. A. Ricci, R. Senesi, and A. K. Soper, *Water structure in supercritical mixtures of water and rare gases*, J. Chem. Phys. **118,** 235-241 (2003).

315 A. Botti, F. Bruni, M. A. Ricci, and A. K. Soper, *Neutron diffraction study of high density supercritical water*, J. Chem. Phys. **109,** 3180-3184 (1998).

316 M. Wilson and P. A. Madden, *Voids, layers, and the first sharp diffraction peak in $ZnCl_2$*, Phys. Rev. Lett. **80,** 532-535 (1998).

317 J. D. Martin, S. J. Goettler, N. Fosse, and L. Iton, *Designing intermediate-range order in amorphous materials*, Nature **419,** 381-384 (2002).

318 J. C. G. Calado and E. J. M. Filipe, *Thermodynamic studies of triangular molecules: liquid mixtures of xenon and the boron halides, BF_3 and BCl_3*, J. Chem. Soc., Faraday Trans. **92,** 215-18 (1996).

319 J. N. Brønsted, *Acid-basic function of molecules and its dependency on the electric charge type*, J. Phys. Chem. **30,** 777-90 (1926).

320 J. N. Brønsted, *The conception of acids and bases*, Recueil des Travaux Chimiques des Pays-Bas et de la Belgique **42,** 718-28 (1923).

321 R. E. Richards and J. A. S. Smith, *Nuclear magnetic resonance spectra of some acid hydrates*, Trans. Faraday Soc. **47,** 1261-74 (1951).

322 Y. Kakiuchi, H. Shono, H. Komatsu, and K. Kigoshi, *Proton magnetic resonance absorption in hydrogen perchlorate monohydrate and the structure of oxonium ion*, J. Chem. Phys. **19,** 1069 (1951).

323 A. Commeyras and G. A. Olah, *Chemistry in super acids. II. Nuclear magnetic resonance and laser Raman spectroscopic study of the antimony pentafluoride-fluorosulfuric acid (sulfur dioxide) solvent system (magic acid). The effect of added halides, water, alcohols, and carboxylic acids. Study of the hydronium ion*, J. Am. Chem. Soc. **91,** 2929-42 (1969).

324 C. C. Ferriso and D. F. Horning, *The infrared spectrum of the oxonium ion*, J. Am. Chem. Soc. **75,** 4113-14 (1953).

325 R. C. Taylor and G. L. Vidale, *Vibrational spectrum of the hydronium ion in hydronium perchlorate*, J. Am. Chem. Soc. **78,** 5999-6002 (1956).

326 T. G. Phillips, E. F. Van Dishoeck, and J. Keene, *Interstellar hydronium (H_3O^+) and its relation to the oxygen and water abundances*, Astrophys. J. **399,** 533-50 (1992).

327 L. I. Yeh, M. Okumura, J. D. Myers, J. M. Price, and Y. T. Lee, *Vibrational spectroscopy of the hydrated hydronium cluster ions $H_3O^+.(H_2O)_n$ (n = 1, 2, 3)*, J. Chem. Phys. **91,** 7319-30 (1989).

328 M. F. Jarrold, N. J. Kirchner, S. Liu, and M. T. Bowers, *Metastable and collision-induced dissociation studies of unimolecular and bimolecular reactions in the $C_2H_5O^+$, $C_2H_7O^+$, and $C_2H_8N^+$ systems: the role of methyl (CH_3^+) radiative association reactions in interstellar clouds*, J. Phys. Chem. **90,** 78-83 (1986).

329 L. B. D'Hendecourt, L. J. Allamandola, and J. M. Greenberg, *Time dependent chemistry in dense molecular clouds. I. Grain surface reactions, gas/grain interactions and infrared spectroscopy*, Astron. & Astrophys. **152,** 130-50 (1985).

330 N. N. Haese and T. Oka, *Observation of the n2(1- -> 0+) inversion mode band in oxonium ion by high resolution infrared spectroscopy*, J. Chem. Phys. **80,** 572-3 (1984).

331 P. Kebarle, S. K. Searles, A. Zolla, J. Scarborough, and M. Arshadi, *Solvation of the hydrogen ion by water molecules in the gas phase. Heats and entropies of solvation of individual reactions.* $H^+(H_2O)_{n-1} + H_2O \rightarrow H^+(H_2O)_n$, J. Am. Chem. Soc. **89,** 6393-9 (1967).

332 L. S. Bagster and B. D. Steele, *Electrolysis in liquefied sulfur dioxide*, Trans. Faraday Soc. **8,** 51-67 (1913).

333 L. S. Bagster and G. Cooling, *Electrolysis of hydrogen bromide in liquid sulfur dioxide*, J. Chem. Soc. **117,** 693-6 (1920).

334 I. Taesler and J. O. Lundgren, *Hydrogen bond studies. CXXIX. An x-ray determination of the crystal structure of hydrogen chloride hexahydrate,* $H_9O_4^+Cl^-.2H_2O$, Acta Crystallogr. B **B34,** 2424-8 (1978).

335 G. A. Olah, G. K. Prakash, M. Barzaghi, K. Lammertsma, P. V. R. Schlyer, and J. A. Pople, *Considered as onium ions. 31. Protonated hydronium dication,* H_4O^{2+}. *Hydrogen-deuterium exchange of* $D_2H^{17}O^+$ *in HF-*SbF_5 *and* $DH_2^{17}O^+$ *in DF-SbF5 and theoretical calculations*, J. Am. Chem. Soc. **108,** 1032-5 (1986).

336 A. Simon, H. Reuther, and G. Kratzsch, *Raman spectroscopic investigations. XIII.,The structure of perchloric acid*, Z. anorg. allg. Chem. **239,** 329-44 (1938).

337 L. Ochs, J. Gueron, and M. Magat, *Raman spectra of aqueous solutions of hydrogen chloride*, Journal de Physique et le Radium **1,** 85 (1940).

338 P. A. Giguere and J. G. Guillot, *Raman spectrum of hydronium* (H_3O^+) *ions in aqueous acids*, J. Phys. Chem. **86,** 3231-3 (1982).

339 V. Gold, J. L. Grant, and K. P. Morris, *Evidence for the existence of long lived oxonium ions in solution: NMR spectra of isotopic oxonium ions in fluorosulfonic acid-antimony pentafluoride ('Magic Acid') systems*, J. Chem. Soc., Chem. Comm., 397-8 (1976).

340 G. A. Olah, Y. Halpern, Y. Shen, and Y. K. Mo, *Electrophilic reactions at single bonds. XII. Hydrogen-deuterium exchange, protolysis (deuterolysis), and oligocondensation of alkanes with superacids*, J. Am. Chem. Soc. **95,** 4960-70 (1973).

341 C. MacLean and E. L. Mackor, *Nuclear magnetic resonance [NMR] of proton complexes of weak bases*, J. Chem. Phys. **34,** 2207-8 (1961).

342 W. Koch, N. Heinrich, H. Schwarz, F. Maquin, and D. Stahl, *Combine experimental and ab initio molecular orbital studies on gaseous OH_n^{2+} species (n=1-4)*, Int. J. Mass. Spectrom. Ion Processes **67,** 305-16 (1985).

343 N. Hartz, G. Rasul, and G. A. Olah, *Role of oxonium, sulfonium, and carboxonium dications in superacid-catalyzed reactions*, J. Am. Chem. Soc. **115,** 1277-1285 (1993).

344 J. F. C. Turner, S. E. McLain, T. H. Free, C. J. Benmore, K. W. Herwig, and J. E. Siewenie, *Sample containment for neutron and high energy X-ray scattering studies of hydrogen fluoride and related molecular species*, Rev. Sci. Instrum. **74,** 4410-4417 (2003).

345 E. Lalik, W. I. F. David, P. Barnes, and J. F. C. Turner, *Mechanisms of reduction of MoO_3 to MoO_2 reconciled?*, J. Phys. Chem. B **105,** 9153-9156 (2001).

346 J. F. C. Turner, R. Done, J. Dreyer, W. I. F. David, and C. R. A. Catlow, *On apparatus for studying catalysts and catalytic processes using neutron scattering*, Rev. Sci. Instrum. **70,** 2325-2330 (1999).

347 R. I. Walton, R. I. Smith, and D. O'Hare, *Following the hydrothermal crystallization of zeolites using time-resolved in situ powder neutron diffraction*, Microporous & Mesoporous Mater. **48,** 79-88 (2001).

348 R. I. Walton and D. O'Hare, *Watching solids crystallise using in situ powder diffraction*, J. Chem. Soc., Chem. Comm., 2283-2291 (2000).

349 R. I. Walton, A. Norquist, R. I. Smith, and D. O'Hare, *Recent results from the in situ study of hydrothermal crystallisations using time-resolved X-ray and neutron diffraction methods*, J. Chem. Soc., Faraday Discus. **122,** 331-341 (2002).

350 R. I. Walton, F. Millange, R. I. Smith, T. C. Hansen, and D. O'Hare, *Real time observation of the hydrothermal crystallization of barium titanate using in situ neutron powder diffraction*, J. Am. Chem. Soc. **123,** 12547-12555 (2001).

351 R. I. Walton, F. Millange, D. O'Hare, R. I. Smith, I. J. Clark, and D. C. Sinclair, *An in situ time-resolved neutron diffraction study of the hydrothermal crystallisation of barium titanate*, J. Chem. Soc., Chem. Comm., 1267-1268 (2000).

352 R. I. Walton, R. J. Francis, P. S. Halasyamani, D. O' Hare, R. I. Smith, R. Done, and R. J. Humphreys, *Novel apparatus for the in situ study of hydrothermal crystallizations using time-resolved neutron diffraction*, Rev. Sci. Instrum. **70,** 3391-3396 (1999).

353 M. Pourbaix, *Atlas of Electrochemical Equilibria in Aqueous Solutions* (1966).

354 M. Pourbaix, *Electrochemical equilibrium diagrams of the titanium--water system. Stability of titanium hydride*, Rapports Techniques - Centre Belge d'Etude de la Corrosion **No. 146-7-8-9-50,** 4 pp. (1968).

355 M. Maraghini, P. van Rysselberghe, E. Deltombe, N. de Zoubov, and M. Pourbaix, *Electrochemical properties of zirconium. Potential-pH equilibrium diagram of the system Zr-H_2O at 25 Deg*, Rapp. Tech. **No. 45,** 13 pp. (1957).

356 E. Deltombe, N. de Zoubov, and M. Pourbaix, *Electrochemical behavior of vanadium. Equilibrium voltage-pH diagram of the system vanadium-water at 25 Deg*, CEBELCOR (Centre Belge Etude Corrosion) Rapp. Tech. **No. 29,** 25 pp. (1956).

357 G. W. Stanton, J. C. Dore, and N. J. Hance, *A note on containers for neutron diffraction studies of chemically-reactive liquids*, Nuc. Instrum. Meth. **141,** 259-61 (1977).

358 M. Sprik, U. Roethlisberger, and M. L. Klein, *Structure of solid poly(tetrafluoroethylene): a computer simulation study of chain orientational, translational, and conformational disorder*, J. Phys. Chem. B. **101,** 2745-2749 (1997).

359 M. Sprik, U. Rothlisberger, and M. L. Klein, *Conformational and orientational order and disorder in solid polytetrafluoroethylene*, Mol. Phys. **97,** 355-373 (1999).

360 C. W. Bunn and E. R. Howells, *Structures of molecules and crystals of fluorocarbons*, Nature **174,** 549-51 (1954).

361 E. Dobnik and W. Borchard, *State diagrams of perfluorocarbon/solvent systems*, Makromolekulare Chemie, Macromolecular Symposia **39,** 249-70 (1990).

362 I. V. Sysoev and V. S. Khanarin, *Phase transitions in poly(tetrafluoroethylene) in the 0.1-800 MPa and 15-210° pressure and temperature ranges*, Zhurnal Fizicheskoi Khimii **58,** 735-7 (1984).

363 K. F. Bradley, S. H. Chen, T. O. Brun, R. Kleb, W. A. Loomis, and J. M. Newsam, *The design and performance of QENS, a medium resolution, inverted geometry, TOF quasielastic and inelastic spectrometer at IPNS*, Nuc. Instr. & Methods Phys. Res. **A270,** 78-89 (1988).

364 S. E. McLain, C. J. Benmore, J. Urquidi, and J. F. C. Turner, *HF and DF measured in PTFE*, Unpublished results (2001).

365 W. H. Zachariasen, *Theory of X-Ray Diffraction in Crystals* (Dover Publications, 1995).

366 D. L. Goodstein, *States of Matter* (Dover Publications, Mineola, New York, 2002).

APPENDIX

JOURNAL OF CHEMICAL PHYSICS VOLUME 117, NUMBER 8 22 AUGUST 2002

The structure of liquid fluorosulfuric acid investigated by neutron diffraction

S. E. McLain
Department of Chemistry, The University of Tennessee, Knoxville, Tennessee 37996-1600 and Intense Pulsed Neutron Source, Argonne National Laboratory, Argonne, Illinois 60439-4814

C. J. Benmore
Intense Pulsed Neutron Source, Argonne National Laboratory, Argonne, Illinois 60439-4814

J. F. C. Turner[a)]
Neutron Sciences Consortium and Department of Chemistry, The University of Tennessee, Knoxville, Tennessee 37996-1600

(Received 2 April 2002; accepted 30 May 2002)

The results of an investigation into the liquid structure of fluorosulfuric acid measured using neutron diffraction with isotopic substitution are reported. The first-order neutron difference function is extracted from data recorded at 300 and 193 K from isotopically labeled FSO_3H and FSO_3D. Analysis of the derived radial distribution functions shows that unique, multisite hydrogen bonding is present in the liquid. These results suggest hydrogen bonding between the hydrogen and fluorine as well as oxygen occurs in the liquid. The fraction of molecules that is hydrogen bound in each way varies with temperature, with the 193 K data showing a more tightly bound system. © *2002 American Institute of Physics*. [DOI: 10.1063/1.1495395]

I. INTRODUCTION

Superacids are a class of fluids that possess extremely high acidities, which far exceed those observed for the strongest aqueous acid systems.[1–4] NMR spectroscopy has shown that the normal range of bases can be augmented in superacidic media by species such as methane, xenon, hydronium ion, and first-row diatomic molecules.[5–10] It is the ability to protonate the C–H bond that gives these fluids their industrial and, in part, academic importance. They are used extensively for hydrocarbon management – the isomerization and cracking of petroleum products—as well as the investigation of reactive, carbocationic intermediates in organic chemistry.[10] More recently, they have become popular as solvent systems for inorganic synthesis, where high valent and extremely-electron-poor metal centers can be synthesized and studied.[2,11–13]

Superacids also differ from other hydrogen-bound systems, such as water, ammonia, and alcohols, in that they are highly-electron-poor hydrogen-bound systems. Previous systems on superacids and other acidic systems have usually relied on x-ray diffraction in the solid state to determine structure.[14–20] Studies of the structure of superacids in the liquid state have so far been confined to two total structure factor determinations of DF.[21,22] In this paper, the determination of the [HD] first-order difference function in neutron diffraction for a complex superacid are reported for the first time.

a)Author to whom correspondence should be addressed. Email address: jturner@novell.chem.utk.edu

II. NEUTRON DIFFRACTION THEORY AND EXPERIMENT

A. Theory

The lack of correlation between Z, the atomic number, and the strength of the neutron–nucleus interaction ensures that neutron scattering is the premier technique for the structural investigation of samples that are partially or fully composed of "light atoms," i.e., those with low Z. Hydrogen-bound systems have been the focus of the majority of liquid neutron diffraction studies due to, in part, this light-atom sensitivity.[21–30] Moreover, isotopes exhibit different scattering cross sections,[31,32] which allows the extraction of species-specific structure factors and their associated pair-distribution functions from data measured from isostructural but isotopomeric samples.

The quantity measured in a neutron diffraction experiment is the differential scattering cross section:

$$\frac{d\sigma}{d\Omega}=\frac{d\sigma}{d\Omega_{\text{self}}}+\frac{d\sigma}{d\Omega_{\text{distinct}}}=\sum_{\alpha} c_{\alpha}b_{\alpha}^{2}P(Q,\theta)+F_{N}(Q), \tag{1}$$

where $P(Q,\theta)$ is the inelastic contribution and $F_N(Q)$ is the total scattering structure factor arising from the "distinct scattering" contribution, c_α is the atomic concentration, and b_α the scattering length of isotope α. Information about the atomic structure of the sample is contained in the sum of the partial structure factors, $S_{\alpha\beta}(Q)$, where

0021-9606/2002/117(8)/3816/6/$19.00

TABLE I. Faber–Ziman coefficients for FSO_3D and FSO_3D-FSO_3H in units of barn.

$c_H^2 b_H^2$	0.00838	$2c_Sc_Ob_Sb_O$	0.02754
$c_S^2 b_S^2$	0.00225	$2c_Sc_Db_Sb_D$	−0.00591
$c_O^2 b_O^2$	0.08419	$2c_Fc_Db_Fb_D$	−0.03616
$c_D^2 b_D^2$	0.00388	$c^2 b_{D,H}^2$	0.00848
$2c_Hc_Sb_Hb_S$	0.00894	$2c_Hc_Db_Hb_{D,H}$	0.03270
$2c_Hc_Ob_Hb_O$	0.05457	$2c_Sc_Db_Sb_{D,H}$	0.01647
$2c_Hc_Db_Hb_D$	−0.01175	$2c_Oc_Db_Ob_{D,H}$	0.10068

$$S_M(Q)=\frac{F_M(Q)}{\left|\sum_\alpha c_\alpha b_\alpha\right|^2}$$

$$=\frac{1}{\left|\sum_\alpha c_\alpha b_\alpha\right|^2}\sum_{\alpha,\beta} c_\alpha b_\alpha c_\beta b_\beta |S_{\alpha\beta}(Q)-1|. \quad (2)$$

The first-order difference structure factor with the respect to the labeled site is calculated by subtraction of $F_M(Q)$ for isostructural and isotopomeric samples. In these experiments, the isotopomers used were FSO_3H and FSO_3D and so the corresponding structure factor is that related to the hydrogen/deuterium site, hereafter termed the |H,D| site, namely $\Delta F_{H,H}(Q)$, where X includes hydrogen as well as the other heavy atoms. In a similar manner, the structure factor derived from scattering for all nonhydrogen sites, $\Delta F_{XX}(Q)$, was extracted from the data by subtraction of $\Delta F_{H,H}(Q)$ from the measured total structure factor for FSO_3D.

The Fourier transform of any structure factor yields the associated radial distribution function $G(r)$, which is the sum of the respective atom–atom correlation functions, $g_{\alpha\beta}(r)$, each weighted by concentration and the bound coherent scattering length of the atomic species. The measured $S(Q)$ is related to the total radial distribution function $G(r)$ by the following equation:

$$S(q)=1+\frac{4\pi\rho}{Q}\int_0^\infty r\,dr|G(r)-1|\sin(Qr). \quad (3)$$

Fourier transformation of $\Delta F_{H,H}(Q)$ yields the real-space counterpart $\Delta G_{H,H}(r)$. As interference terms related only to the |H,D| site are present in $\Delta F_{H,H}(Q)$, $\Delta G_{H,H}(r)$ represents only the radial distribution functions associated with the |H,D| sites. Explicitly, $\Delta G_{H,H}(r)$ may be written as

$$\Delta G_{H,H}(r)=2c_Hc_Ob_O(b_D-b_H)g_{HO}(r)$$
$$+2c_Hc_Fb_F(b_D-b_H)g_{HF}(r)$$
$$+2c_Hc_Sb_S(b_D-b_H)g_{HS}(r)$$
$$+c_H^2(b_D^2-b_H^2)g_{HH}(r). \quad (4)$$

Fourier transformation of $\Delta F_{X,H}(Q)$ yields $\Delta G_{X,H}(r)$:

$$\Delta G_{X,H}(r)=2c_Sc_Ob_Sb_Og_{SO}(r)+2c_Sc_Fb_Sb_Fg_{SF}(r)$$
$$+2c_Fc_Ob_Fb_Og_{FO}(r)+c_O^2b_O^2g_{OO}(r)$$
$$+c_S^2b_S^2g_{SS}(r)+c_F^2b_F^2g_{FF}(r). \quad (5)$$

See Table I for a listing of the Faber–Ziman coefficients appearing in Eqs. (4) and (5). The distances that contribute to $\Delta G_{X,H}(r)$ are therefore those between the heavy atoms S, O, and F.

In general, integration of $g_{\alpha\beta}(r)$ gives the coordination number of atoms α and β atoms between two distances, r_1 and r_2:

$$n_\beta^\alpha(r)=4\pi c_\alpha\rho\int_{r_1}^{r_2} g_{\alpha\beta}(r)r^2dr, \quad (6)$$

where ρ corresponds to the atomic number density, which, in FSO_3H, is 0.0629 and 0.0683 atoms/Å^{-3} at 300 and 193 K, respectively.

B. Experiment: Sample handling and preparation

Fluorosulfuric acid is an aggressive material and must be handled with caution only in rigorously dried glassware or Teflon apparatus. All manipulations of FSO_3H and FSO_3D were carried out under an argon atmosphere or under vacuum on a Schlenk line ($p_{min}<10^{-2}$ mbar). All glassware was flame-dried under vacuum at least four times and allowed to cool under an argon atmosphere. FSO_3D was prepared according to the literature with the exchange between D_2SO_4 and FSO_3H being performed three times.[33] NMR measurements and neutron analysis *vide infra* revealed that the incorporation of D for H was greater than 99.6%. The purity of FSO_3H with respect to water was assayed using Raman spectroscopy and determined to be greater than 99.9% H_2O-free. The Raman spectra were acquired on a Dilor *XY* Raman spectrometer (Instruments S.A., Edison, NJ) using a 514-nm Rayleigh line. The density of FSO_3H was measured using a custom designed glass pycnometer, which was standardized against the density of methanol, which is well known.[34] FSO_3H and FSO_3D were distilled into quartz tubes (0.4 cm ID, 0.5 cm OD) and were flame-sealed under vacuum to give a sample volume of 0.478 cm^3.

Diffraction experiments were performed on the Glass Liquid and Amorphous Materials Diffractometer at the Intense Pulsed Neutron Source facility at Argonne National Laboratory. Data sets were collected at 300 and 193 K. The neutron diffraction data were corrected for container scattering, attenuation, multiple scattering, and inelastic scattering using standard analysis procedures.[35] The data were not corrected for isotope quantum effects, which have recently been shown to be small for hydroxyl hydrogens in other hydrogen-bonded liquids such as methanol; moreover, they are expected to be smaller in this heavier molecule.[36]

The small sample thickness minimizes multiple scattering effects due to the large amount of incoherent scattering from hydrogen. In addition, both tubes were blown from the same cane of tube to ensure that their wall geometries were as similar as possible, in order to minimize systematic errors in the difference experiments. The small error between the quartz tubes was additionally checked by comparison of the calculated intramolecular scattering contribution to the measured data. Both neutron differences agreed to within 5% to the expected intramolecular nearest-neighbor atoms [as discussed in the following sections (see Figs. 4 and 5)]. This

TABLE II. Interatomic distances and angles for fluorosulfuric acid, fluorosulfate, and bifluorosulfate.

	Crystal (FSO_3H)[a]	MP-aug-cc-pvdz[b]	$[SO_3F]^-$[c]	$[FSO_3HO_3SF]^-$[c]
		Interatomic distances/Å		
$r(S—O_1)$	1.51	1.628	1.458	1.471
$r(S—O_2)$	1.41	1.456	1.437	1.406
$r(S—O_3)$	1.42	1.465	1.436	1.399
$r(S—F)$	1.54	1.636	1.569	1.531
$r(O_1—H)$	0.63	0.977		1.21
$r(H\cdots O_3')$	2.02			
		Interbond angles (deg)		
$S—O_1—H$		106.8		
$O_1—S—O_3$	107.2	107.2	112.7	113.8
$O_2—S—O_3$	120.9	125.8	113.6	113.0
$O_1—S—O_2$	113.1	110.3	113.6	116.3
$O_1—S—F$	100.7	97.6	102.3	104.8
$O_2—S—F$	106.6	106.6	106.3	105.3
$O_3—S—F$	106.2	105.7	107.8	101.7

[a]Reference 20.
[b]Reference 37.
[c]Reference 18.

clearly indicates that the SiO_2 container corrections and the data normalization have been performed correctly.

C. Previous studies on the structure of fluorosulfuric acid

The structure of fluorosulfuric acid has been determined in the solid state by x-ray diffraction.[20] The molecular structure consists of a *pseudotetrahedral* sulfur atom ligated by oxo-, fluoro-, and hydroxyl moieties. Salient bond lengths and angles from x-ray diffractometry are shown in Table II. The molecule is shown in Fig. 1, together with atom labels used in this paper. It may be noted from Table II that the hydroxyl O–H bond length, $r(O_1—H)$, is very short, and this may be due to the inherent insensitivity of x-ray scattering to the presence of hydrogen.

III. RESULTS

In order to analyze the various radial distribution functions determined in these diffraction experiments, the structure of a single fluorosulfuric acid molecule was calculated using Moller-Plesset perturbation theory (MP2) with an augmented correlation consistent polarized valence double zeta aug-cc-pVDZ basis set with GAUSSIAN 98. The relevant calculated distances and angles are shown in Table II.

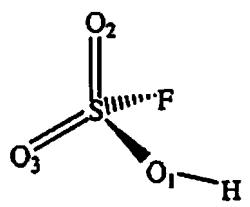

FIG. 1. Molecular structure of FSO_3H.

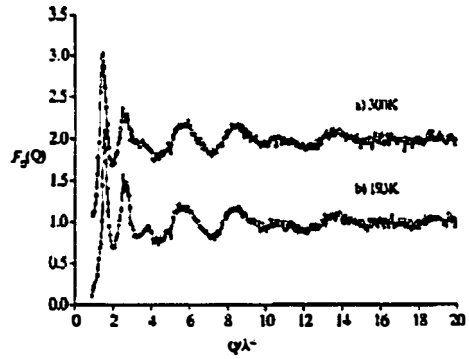

FIG. 2. Total structure factor: (a) $F_M(Q)+1$ at 300 and (b) $F_M(Q)$ at 193 K for FSO_3D.

Measurement of the density of fluorosulfuric acid in a high-vacuum pychnometer, previously calibrated with anhydrous methanol, yielded values of $\rho_{300}=1.743$ g cm^{-3} and $\rho_{193}=1.891$ g cm^{-3}. Given that isostructurality between both isotopomers is assumed for the subtraction method to be applicable, these values of the number density were used for all the data analysis procedures.

The corrected total structure factors, $F_M(Q)$, for FSO_3D for both temperatures are shown in Fig. 2. Figure 3 shows the hydrogen structure factors $\Delta F_{HX}(Q)$, extracted as described above, again for both temperatures. The radial distribution functions at 300 and at 193 K around the [H,D] site are shown in Fig. 4 and the extracted radial distribution functions for the heavy atoms, $\Delta G_{XX}(r)$, at 300 and 193 K, in Fig. 5.

Data analysis was performed by empirically fitting the derived $\Delta G_{HX}(r)$ function with Gaussian functions in order to determine the coordination number.[38] Although approximate intramolecular distances between pairs of heavy atoms were available from x-ray crystallographic studies, there was no reliable estimate in the literature for intramolecular distances between hydrogen and the heavy atoms in FSO_3H. For instance, the x-ray structure indicates the covalent O–H

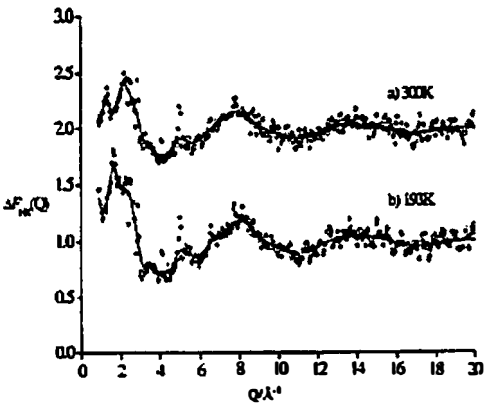

FIG. 3. Partial structure factor: (a) $\Delta F_{HX}(Q)+1$ at 300 K and (b) $\Delta F_{HX}(Q)$ at 193 K. The small sharp spurious points at 5 Å^{-1} are due to background features and do not contribute significantly to the diffuse scatter.

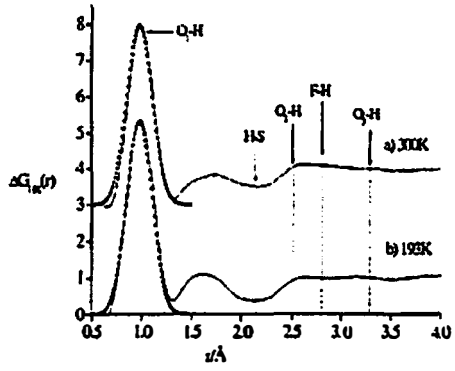

FIG. 4. (a) $\Delta G_{HX}(r)+3$ at 300 K and (b) $\Delta G_{HX}(r)$ at 193 K. The oxygen numbers correspond to the intramolecular structure shown in Fig. 1. The bond distances were calculated using density functional theory (Ref. 39).

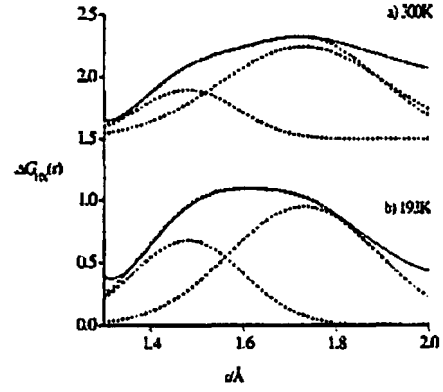

FIG. 6. $\Delta G_{HX}(r)$ hydrogen-bond peak fit with two Gaussians: (a) $\Delta G_{HX}(r)+1.5$ at 300 K and (b) $\Delta G_{HX}(r)$ at 193 K.

bond to be 0.63 Å, which is unreasonably short. Therefore, the equilibrium structure of an isolated FSO_3H molecule using Becke's 3-parameter exchange DFT and the Lee-Yang-Parr correlation function (B2LYP) with an aug-cc-pVDZ basis set and the intramolecular distances between hydrogen, and the F, S, and O atoms were taken from this structure.[39] Intramolecular contributions to $\Delta G_{XY}(r)$ were fitted using distances taken from the x-ray crystal structure data for the fluorosulfate ion, FSO_3^-, and the $[FSO_3HO_3SF]^-$ anion (Table II),[18] as well as those extracted from the density-functional calculations.[39]

The most important features in $\Delta G_{HX}(r)$ (Fig. 2) are the OH intramolecular peak at 0.98 Å and a broader peak at approximately 1.6 Å that corresponds to the intermolecular hydrogen bond. The solid-state x-ray data estimate this latter distance to be about 2.02 Å, presumably due to the exceedingly short OH intramolecular distance, and this distance is considerably longer than most common hydrogen bonds.

At 300 K in the liquid, the hydrogen-bonding peak in $\Delta G_{HX}(r)$ is asymmetric and can be more accurately fitted as the sum of two peaks centered at 1.48 and 1.74 Å, showing a 1:4 area ratio with respective coordination numbers of 0.15 ($\sigma r=\pm 0.1$) and 0.61 ($\sigma r=\pm 0.1$), with respect to oxygen or fluorine as shown in Figs. 6 and 7. It should be noted that the coherent neutron scattering lengths of oxygen and fluorine are very similar and oxygen and fluorine cannot be distinguished in this experiment. At 193 K, where the hydrogen-bond peak is sharper, the two Gaussian peaks are centered at 1.48 and 1.73 Å and have coordination numbers with respect to oxygen or fluorine of 0.31 ($\sigma r=\pm 0.1$) and 0.80 ($\sigma r=\pm 0.1$), with the areas showing a 1:2.6 ratio. The 31% increase in hydrogen coordination, calculated from the Gaussian fits and clearly illustrated in the running coordination number plot, provides evidence of a significant increase in the hydrogen-bond chain length (and/or chain branching) upon cooling the liquid. The shift to lower r upon cooling and the development of a more distinct inflection point in the running coordination number (Fig. 7) are consistent with the presence of stronger, better-defined hydrogen bonds at the lower temperature.

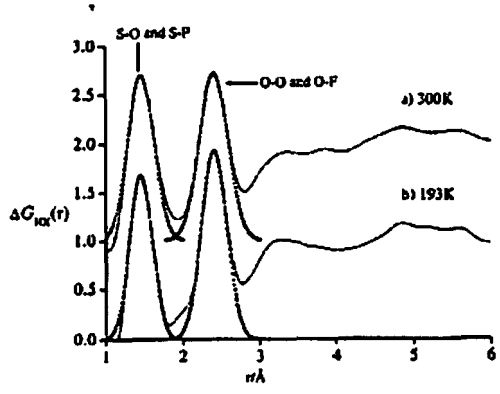

FIG. 5. (a) $\Delta G_{XY}(R)+1$ at 300 K and (b) $\Delta G_{XY}(r)$ at 193 K. The Gaussians were fitted empirically.

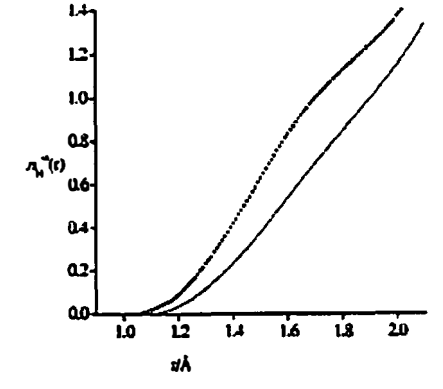

FIG. 7. Running coordination number curve for the intermolecular O–H bond, showing the average number of oxygen of fluorine atoms around a central hydrogen atom at a given distance, r. The solid line represents the 300 K data and the dotted line represents the 193 K data.

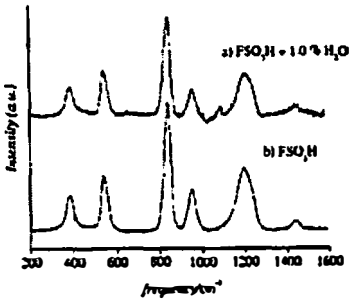

FIG. 8. Raman spectra of (a) FSO_3H and (b) FSO_3H+ 1.0 mol% H_2O.

These results imply that there are two distinct hydrogen bond distances, a phenomenon that does not occur in most other hydrogen-bound liquids such as water, methanol, or ethanol where only one hydrogen bonding atom type exists.[26,27,34] This may be evidence that there are hydrogen bonds to both fluorine and oxygen in the liquid phase.

In the reported crystal structure of FSO_3H, linear chains of molecules are bound exclusively through S—OH···O=S linkages. The other heavy-atom distances in the crystal structure includes r_{S-OH}= 1.518(1) Å, $r_{S=O}$= 1.412(1) and 1.420(1) Å, and r_{S-F}= 1.540(1) Å. These distances are not atypical, as revealed by a search of the Cambridge Crystallographic Structural Database, where the mean distances for these values were found to be 1.54±0.04 Å (S—F) and 1.54 ±0.05 Å (S—OH), and 1.42±0.04 Å (S=O).[40] It therefore appears, from this study in the liquid state, that a different hydrogen-bonding structural motif is present that is not found in the solid state.

The Raman data, shown in Fig. 8, shows that the multisite hydrogen bonding cannot be due to H_2O contamination. The Raman data taken from FSO_3H used in this experiment is consistent with former measurements[41] and with the addition of 0.1 mol% H_2O a new vibrational peak appears at 1680 cm^{-1}, and this peak continues to increase in intensity at higher water concentration. The variation of the area of this peak with concentration shows that the mol% H_2O present in FSO_3H to be virtually zero by extrapolation.

IV. DISCUSSION

Fluorosulfuric acid is a strongly hydrogen-bound fluid that is to be expected given the electronegative nature of the ligating atoms around S. Physically, it is a highly mobile liquid with a liquid range of 253.8 K (boiling point =165.5 °C; melting point = −88.3 °C), this long liquid range being due to the hydrogen-bound nature of the fluid. For comparison, the melting and boiling points of sulfuryl difluoride, O_2SF_2, are −135.8 °C and −55.4 °C, respectively - a liquid range of 80.4 K.

Because the intermolecular O···H bonding peak is best described with two Gaussians and the distant change in the profile of the intermolecular O···H bonding peak with temperature, the presence of two possible hydrogen-bonding interactions, namely O—H···F and O—H···O is a reasonable conclusion. That F···H bonding may occur in the liquid structure is not surprising as fluorine is more electronegative than oxygen. The phase diagrams of the hydrates of the hydrohalic acids are rationalized on the exceptional strength of the hydrogen bond between H and F. The crystalline hydrates of HX (X= Br,Cl) have compositions written as $HX{\cdot}nH_2O$ (n= 1,2,3,4,6),[42] whereas the crystalline hydrates of HF are in the form $H_2O{\cdot}mHF$ (m= 1,2,4).[15,19,43] Indeed, the low pK_a of aqueous HF has been attributed to the strong hydrogen-bonding interaction between H and F, which leads to the formation of HF_2^- even in the presence of a large statistical excess of water. In addition, the strongest hydrogen bond known is between hydrogen and fluorine in the bifluoride ion $[F-H-F]^-$, and the strongest calculated hydrogen is between formic acid and the fluorine ion $[HCO_2-H-F^-]$.[44,45]

However, the partial charge assigned to fluorine in isolated FSO_3H (determined from a molecular electrostatic potential analysis, CHELPG, at the B3LYP aug-cc-pVDZ level of theory)[39] is only −0.20 electrons, while the partial charges assigned to the oxygen atoms are substantially larger in magnitude, at −0.36 electrons (S—O—H) and −0.42 and −0.44 electrons (S=O). It may be noted that the distribution of the electron density may differ in a hydrogen-bound or otherwise condensed system, where the formal sharing of electron density between molecules, in a 3c-4e manner, and the presence of a dielectric may be contributing and perturbing factors.

Whereas the experimental resolution does not allow for the assignment of individual heavy-atom distances, $G_{XY}(r)$ reveals two features, an asymmetric peak with a maximum at ~1.47 Å with a coordination number of 4.16 (σ= ±0.1) fluorine or oxygens bound to sulfur and a second peak with a maximum at ~2.41 Å with a coordination number of 6.22 (σ= ±0.1) with respect to oxygen and fluorine distances. These distances are in accord with the literature values,[18] as well as those extracted from the Cambridge Crystallographic Structural Database and the other literature sources and calculations specifically cited above for the directly bonded and nonbonded distances, respectively. Given that the heavy-atom structure of fluorosulfuric acid is essentially unchanged at the two experimental temperatures within the resolution of the experiment, the largest change in the structure of the liquid is due mainly to the change in hydrogen-bond structure. Moreover, this change in hydrogen-bond structure may be due to a change in the mole fraction of molecules bound as O—H···F and O—H···O, as is shown by the change in coordination number for the double Gaussian fits to the intermolecular hydrogen-bond peak.

Preliminary density-functional theory (DFT) calculations on an isolated dimer of fluorosulfuric acid show that the dimer is stable in configurations where both O—H···F and O—H···O are present between the molecules.[39] However, given the multiple number of possible hydrogen-bonding sites in the FSO_3H molecule, the liquid structure is likely to be comprised of a three-dimensional network. Consequently, while the DFT calculations show the inherent stability of these types of linkages, calculating the relative strengths of these bonds and their temperature dependence is difficult due

to the effects of many-body intermolecular interactions in the liquid state.

Further experimental and theoretical work is needed to clarify the relative importance of O—H···O and O—H···F hydrogen bonding in liquid FSO_3H. Modeling efforts towards this end are currently in progress, utilizing molecular dynamics and (N,P,T) ensemble Monte Carlo simulations that employ periodic boundary conditions and a customized variant of the optimized potential for liquid simulations (OPLS) intermolecular potential tailored to the charge distribution in FSO_3H.

V. CONCLUSIONS

The hydrogen bond peak profile in the measured radial distribution neutron difference function for liquid fluorosulfuric acid is asymmetric and the asymmetry varies in temperature. The temperature variation of the neutron difference function, combined with the changes in the running coordination number, imply that a multi-site hydrogen-bonding motif may be present in the liquid. Although from these measurements the nature of the atoms involved in this O—H···X bond cannot be determined, due to the similarity of the scattering cross section for O and F, O—H···F and O—H···O bonding being simultaneously present cannot be excluded. Indeed, a multisite hydrogen-bonded structure involving only O would imply a frustrated hydrogen-bonded picture.

ACKNOWLEDGMENTS

We thank the Intense Pulsed Neutron Source at Argonne National Laboratory for the allocation of beam time and the Department of Energy for financial support for S.E.MeL. We thank the University of Tennessee for funding for J.E.C.T. We would also like to thank Dr. R. J. Hinde for preliminary calculations and stimulating discussion. The experiments performed at Argonne National Laboratory were supported under Contract No. W-31-109-ENG-38, U.S. DOE-BES.

[1] G. A. Olah, G. K. Surya Prakash, and J. Sommer, *Superacids* (Wiley, New York, 1985).
[2] T. A. O'Donnell, *Superacids and Acidic Melts as Inorganic Chemical Reaction Media* (VCH, New York, 1992).
[3] R. J. Gillespie, Can. Chem. News 43, 20 (1991).
[4] R. J. Gillespie, Acc. Chem. Res. 1, 202 (1968).
[5] G. A. Olah, G. Klopman, and R. H. Schlosberg, J. Am. Chem. Soc. 91, 3261 (1969).
[6] G. A. Olah, J. Shen, and R. H. Schlosberg, J. Am. Chem. Soc. 95, 4957 (1973).
[7] G. A. Olah, J. Shen, and R. H. Schlosberg, J. Am. Chem. Soc. 92, 3831 (1970).
[8] G. A. Olah and J. Shen, J. Am. Chem. Soc. 95, 3582 (1973).
[9] G. A. Olah, G. K. S. Prakash, M. Marcelli, and K. Lammertsma, J. Phys. Chem. 92, 878 (1988).
[10] G. A. Olah, Angew. Chem. Int. Ed. Engl. 34, 1393 (1995).
[11] E. Bernhardt, B. Bley, R. Wartchow, H. Willner, E. Bill, P. Kuhn, I. H. T. Sham, M. Bodenbinder, R. Broechler, and F. Aubke, J. Am. Chem. Soc. 121, 7188 (1999).
[12] E. Bernhardt, H. Willner, V. Jonas, W. Thiel, and F. Aubke, Angew. Chem. Int. Ed. Engl. 39, 1681 (2000).
[13] R. Broechler, I. H. T. Sham, M. Bodenbinder, V. Schmitz, S. J. Rettig, J. Trotter, H. Willner, and F. Aubke, Inorg. Chem. 39, 2172 (2000).
[14] D. Mootz and M. Steffen, Z. Anorg. Allg. Chem. 482, 193 (1981).
[15] D. Mootz and W. Poll, Z. Anorg. Allg. Chem. 484, 158 (1982).
[16] D. Mootz and K. Bartmann, Angew. Chem. 100, 424 (1988).
[17] K. Bartmann and D. Mootz, Acta Crystallogr., Sect. C: Cryst. Struct. Commun. 46, 319 (1990).
[18] D. Zhang, S. J. Rettig, J. Trotter, and F. Aubke, Inorg. Chem. 35, 6113 (1996).
[19] D. Mootz, U. Ohms, and W. Poll, Z. Anorg. Allg. Chem. 479, 75 (1981).
[20] K. Bartman and D. Mootz, Acta Crystallogr., Sect. C: Cryst. Struct. Commun. 46, 319 (1990).
[21] M. Deraman, J. C. Dore, J. C. Powles, J. H. Holloway, and P. Chieux, Mol. Phys. 55, 1351 (1985).
[22] T. Pfeiderer, I. Wagner, H. Bertagnolli, K. Tödheide, and H. E. Fischer, J. Chem. Phys. 113, 3690 (2000).
[23] A. K. Soper, J. Phys.: Condens. Matter 9, 2717 (1997).
[24] A. K. Soper, Chem. Phys. 258, 121 (2000).
[25] A. K. Soper and P. A. Egelstaff, Mol. Phys. 42, 399 (1981).
[26] C. J. Benmore and Y. L. Loh, J. Chem. Phys. 112, 5877 (2000).
[27] L. Bianchi, O. N. Kalugin, A. K. Adya, and C. J. Wormald, Mol. Simul. 25, 321 (2000).
[28] T. Weidkamp, J. Neuefeind, H. E. Fischer, and M. D. Zeidler, Mol. Phys. 98, 125 (2000).
[29] T. Yamaguchi, J. Mol. Liq. 78, 43 (1998).
[30] T. Yamaguchi, C. J. Benmore, and A. K. Soper, J. Chem. Phys. 112, 8976 (2000).
[31] National Institute of Science and Technology Center for Neutron Research, http://www.ncnr.nist.gov/resources/n-lengths-list.html
[32] Neutron News 3, 29 (1992).
[33] G. A. Olah, A. Burrichter, G. Rasul, and G. K. S. Prakash, J. Am. Chem. Soc. 119, 4594 (1997).
[34] T. Yamaguchi, K. Hidaka, and A. K. Soper, Mol. Phys. 97, 603 (1999).
[35] A. K. Soper, W. S. Howells, and A. C. Hannon, *Atlas Manual (1st Edition)*, ISIS Pulsed Neutron Source, Rutherford Appleton Laboratory (1989).
[36] B. Tomberli, C. J. Benmore, P. A. Egelstaff, J. Neuefeind, and V. Honkimaki, Europhys. Lett. 55, 341 (2001).
[37] A. Frisch and M. Frisch, GAUSSIAN 98 (Gaussian, Pittsburgh, 1998).
[38] Y. Waseda, *The Structure of Disordered Materials* (McGraw-Hill, New York, 1980).
[39] R. J. Hinde (unpublished).
[40] F. H. Allen and O. Kennard, Chem. Des. Auto. News 8, 1 (1993); 8, 31 (1993).
[41] R. J. Gillespie and E. A. Robinson, Can. J. Chem. 40, 644 (1962).
[42] J. O. Lundgren, Acta. Crystallogr., Sect. B: Struct. Crystallogr. Cryst. Chem. 26, 1893 (1970).
[43] N. Greenwood and A. Earnshaw, *Chemistry of the Elements*, 2nd ed. (Butterworth-Heinemann, Oxford, 1997).
[44] J. Emsley, O. P. A. Hoyte, and R. E. Overill, J. Chem. Soc., Perkin Trans. 2 2, 2079 (1977).
[45] J. Emsley, Polyhedron 4, 489 (1985).

JOURNAL OF CHEMICAL PHYSICS VOLUME 119, NUMBER 13 1 OCTOBER 2003

On the structure of boron trifluoride in liquid and supercritical phase investigated with neutron diffraction

S. E. McLain
Department of Chemistry, University of Tennessee, Knoxville, Tennessee 37996-1600 and Intense Pulsed Neutron Source, Argonne National Laboratory, Argonne, Illinois 37996

J. E. Siewenie and C. J. Benmore
Intense Pulsed Neutron Source, Argonne National Laboratory, Argonne, Illinois 37996

J. F. C. Turner[a)]
Neutron Sciences Consortium and Department of Chemistry, University of Tennessee, Knoxville, Tennessee 37996-1600

(Received 9 June 2003; accepted 7 July 2003)

The results and reverse Monte Carlo analysis of diffraction measurements of BF_3 in the liquid and supercritical state are presented. Liquid BF_3 displays order only in the first coordination sphere around the average molecule and there is no intermediate range order. Liquid BF_3 is thus not a layered liquid. Angular analysis using reverse Monte Carlo modeling shows that the dominant structural motif in the solid state, that of *pseudo* trigonal bipyramidal [3+2] coordination at B is partially retained in both the liquid and supercritical phase, though in the latter, this structural preference is greatly reduced. The structure of the supercritical phase retains the same intermolecular contact as the liquid phase, though the structural sites and population of these sites is much more widely distributed. © *2003 American Institute of Physics*.
[DOI: 10.1063/1.1604382]

I. INTRODUCTION

The boron trihalides are prototypical Lewis acids and have wide application as catalysts in industry and academic chemical research. The simplicity of the molecular structure of boron trifluoride, together with the small size of the component atoms, has ensured that BF_3 has been widely studied as an archetype for Lewis acidity.

The molecular structure of BF_3, determined by electron diffraction in the gas phase[1–3] and confirmed by spectroscopic studies[3–7] consists of a rigorously trigonal planar structure of D_{3h} symmetry with three fluorine atoms ligating the central boron atom, as shown in Fig. 1(a). The boron–fluorine distance determined in these studies is r_{BF} = 1.3133 Å, together with a fluorine–fluorine distance of r_{FF} = 2.2747 Å. In the liquid state, infrared spectroscopy shows that the formally forbidden breathing mode is observed, implying that the local symmetry of the molecule has been perturbed, allowing the transition. In addition, the viscosity data for liquid BF_3 indicates some degree of molecular association.[8,9] However, the entropy of evaporation is not much larger than the average for a nonassociated fluid.[10]

In comparison with the solid-state structures of the heavier congeners, which adopt a layered hexagonal packing motif with little intermolecular interactions that imply an intermolecular Lewis acid-base interaction,[11–13] the three published structures of boron trifluoride in the solid state are complex.[14–16] The structure of BF_3 in the solid state at 128 K consists of a *pseudo* trigonal bipyramidal [3+2] coordinate boron, forming a chain structure parallel to the c axis[14] and is shown schematically in Fig. 1(b). This [3+2] coordination at boron is found in all solid phases.

The strength of the Lewis acidity of the boron trihalides has often been assumed to increase with the atomic number of the halide, with BF_3 being atypically weak.[17] The rationale for this chemical behavior is usually based on the assumed decreasing strength of $p\pi$ $p\pi$ interaction between the ligating halide and the boron center with increasing halide atomic number. This model derives mainly from a valence bond description and is not fully supported by qualitative group theoretical considerations, where bonding is considered as delocalized over contributing atoms, or more quantitative studies.[18–20] Moreover, the experimental evidence for this trend is not uniformly supportive on close examination; the Lewis acidity is base dependent. Using the bond strength of the complex as a measure of Lewis acidic strength, with weak Lewis bases, the acidity of BF_3 is the highest, with BCl_3 being uncomplexed in certain cases.[21,22] There is debate as to the reason for the observed acidity. Arguments span from the thermodynamic, where the ground-state electronic structure and the degree of $p\pi$ $p\pi$ interaction between F and B is the defining factor for the observed order and bond strength, to the kinetic where the rearrangement of the ligating atoms at boron controls the Lewis acid strength.[18,20]

In order to elucidate the propensity for intermolecular Lewis acid-base interactions in a phase with no *a priori* ordering, the liquid structure of BF_3 is closely examined in the supercritical state and just above the temperature of fusion in

a)Electronic mail: jturner@atom.chem.utk.edu

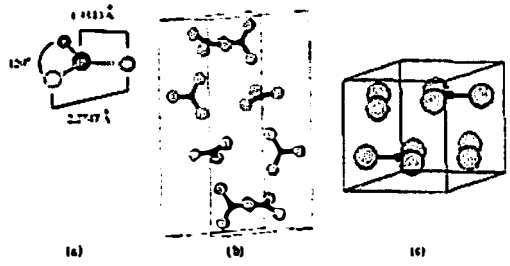

FIG. 1. The molecular structure of BF_3 in the gas phase (Refs. 1–3) (a) and in the solid state (Ref. 9) (b), together with the structure of BBr_3 in the solid state.

the normal fluid using neutron diffraction. Other diffraction data are also recorded at two temperatures at which the sample is liquid and one at a supercritical temperature. By structurally examining a sample where the densities are of a similar magnitude to that of the solid but where there is an absence of long-range order, the degree of association between the molecules may be assessed. In principle, completely isotropic arrangements of molecules may occur in the absence of any intermolecular interactions. Given the observation of the |3+2| structural motif in the solid and the spectroscopic evidence,[10] there is reason to believe that these intermolecular Lewis interactions may exist in the liquid, implying that this motif is energetically favorable. Evidence is presented from the measurement and analysis of the total structure factor that, locally, this structural motif is indeed partially retained in the liquid state within the first coordination sphere of the average molecule, but is lost or strongly decreased in the supercritical state. The analysis is undertaken using reverse Monte Carlo (RMC) modeling.[23–30]

II. NEUTRON DIFFRACTION THEORY AND EXPERIMENT

A. Theory

The lack of correlation between the atomic number, Z, and the strength of the neutron nucleus interaction ensures that neutron scattering is the premier technique for the structural investigation of samples which are partially or fully composed of "light atoms," i.e., those with low atomic number.[31–33]

The quantity measured in a neutron diffraction experiment is the differential scattering cross section, $d\sigma/d\Omega$, where

$$\frac{d\sigma}{d\Omega}=\frac{d\sigma}{d\Omega}_{self}+\frac{d\sigma}{d\Omega}_{distinct}=\sum_{\alpha} c_\alpha b_\alpha^2+P(Q,\theta)+F_N(Q), \tag{1}$$

$P(Q,\theta)$ is the inelastic contribution. $F_N(Q)$ is the total structure factor arising from the "distinct scattering" contribution, c_α is the atomic concentration and b_α the scattering length of isotope α.[34] $F_N(Q)$ is related to the Faber–Ziman partial structure factors, $S_{\alpha\beta}(Q)$ by the following equation:

$$S_{total}(Q)=\frac{F_N(Q)}{(\Sigma_\alpha c_\alpha b_\alpha)^2}=\frac{1}{(\Sigma_\alpha c_\alpha b_\alpha)^2}\sum_{\alpha\beta} c_\alpha b_\alpha c_\beta b_\beta[S_{\alpha\beta}(Q)-1]. \tag{2}$$

The Fourier transform of any structure factor yields the associated radial distribution function, $G_{total}(r)$, which is the sum of the respective atom–atom correlation functions, $g_{\alpha\beta}(r)$, each weighted by concentration and the bound coherent scattering length of the atomic species. $S_{total}(Q)$ is related to the total radial distribution function $G_{total}(r)$ by the following equation:

$$S_{total}(Q)=1+\frac{4\pi\rho}{Q}\int_0^\infty r dr(G(r)-1)\sin(Qr). \tag{3}$$

$G_{BF_3}(r)$ is shown in Eq. (4) with the appropriate weighting for each partial pair correlation function

$$G_{BF_3}(r)=0.079g_{BB}(r)+0.405g_{BF}(r)+0.517g_{FF}(r). \tag{4}$$

From Eq. (4), it is evident that the total structure factor is dominated by $g_{BF}(r)$ and $g_{FF}(r)$. The measurement of the total structure factor is, therefore, the most appropriate method to investigate the structure of the liquid, given the weighting constants for this system.

B. Experiment

1. Sample handling and preparation

$^{11}BF_3$ was purchased from Ozark Fluorine and used without further purification. Mass spectroscopic measurements estimated the ^{10}B concentration to be ~0.35% and the sample also contained a small amount of hydrocarbon contamination. Using a Monel/316 SS high vacuum line,[35] 2.36(8)g (0.034 mol) of $^{11}BF_3$ was condensed into a volume-calibrated, null-scattering sample container,[36] constructed from titanium/zirconium alloy, under high vacuum and sealed. The sample cell volume was found to be 3.11 cm^{-3}. Pressure in the sample container was autogenous and, therefore, controlled through the temperature of the sample. Salient thermodynamic data for BF_3 are shown in Table I.

2. Diffraction experiments

Diffraction experiments were performed on Glass Liquid and Amorphous Materials Diffractometer[37] at the IPNS Facility at Argonne National Laboratory. Data sets were collected at 300±2 K, 266±2 K, 253±2 K, 203±2 K, and at 153±2 K over a Q range of 0.3–40 Å. The neutron diffraction data were corrected for container scattering, attenuation, absorption, multiple scattering, and inelastic scattering using standard analysis procedures.[38] Because there was a small amount of hydrocarbon present in the sample, initially the 300 K data was constrained in the first peak of the real space data to give a coordination number of 3.00±0.10 F atoms around a single boron atom. Integration of $g_{\alpha\beta}(r)$ gives the coordination number of atoms α around β atoms between two distances, r_1 and r_2:

TABLE I. Thermodynamic values for BF_3.

T_M/K	146	T_B/K	173
$T_{critical}$/K	260.8	$P_{critical}$/MPa	26.55

	$p(T)$/kPa				
T/K	153	203	253	266	300
p	18.57	700.03	5152.90	7534.95	17113.57

	$\rho(T)$[b]/atoms Å^{-3}				
T/K	153±2	203±2	253±2	266±2	300±2
ρ	0.042	0.037	0.030	0.025	0.023

[a]Calculated *via* $\lg P = 4.692\,15 - (663.463/T - 30.795)$.
[b]Effective density.

$$n_{\alpha\beta}^{c}(r) = 4\pi c_{\alpha\beta}\rho\int_{r_1}^{r_2} g_{\alpha\beta}(r)r^2 dr. \tag{5}$$

where ρ corresponds to the atomic number density.[39]

In order to satisfy this coordination number constraint, the number density of the sample at 300 K was adjusted. The remaining data sets were corrected by constraining oscillations at high Q in $S_{BF_3}(Q)$ to match that of the 300 K data by adjusting the number density at each different state point, the effective number densities for each data set are reported in Table I. This constraint was verified by the coordination number of the B–F peak in the real space transformation of each data set. The coordination numbers are 3.01±0.10, 3.03 ±0.10, 3.00±0.10, and 2.95±0.10 in 266, 253, 203, and 153 K data sets, respectively.

III. RESULTS

The corrected diffraction data at the five experimental temperatures for $^{11}BF_3$ are shown in Fig. 2(a), with the associated real space radial distribution functions in Fig. 2(b), shown as $4\pi\rho r G_{BF_3}(r)$ where ρ is the density (Table I). In order to analyze the data in a more quantitative manner, RMC modeling was undertaken using a system of 1000 boron atoms and 3000 fluorine atoms, constrained to satisfy the

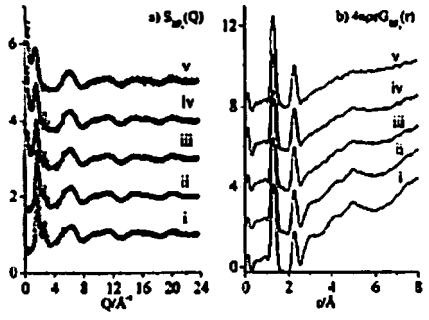

FIG. 2. (a) Total structure factor: (i) $S_{BF_3}(Q)$ at 153 K (ii) $S_{BF_3}(Q)+1$ at 203 K (iii) $S_{BF_3}(Q)+2$ at 253 K (iv) $S_{BF_3}(Q)+3$ at 266 K and (v) $S_{BF_3}(Q)+4$ at 300 K. The circles are the data and the line is the smoothed fit to the data. (b) Total distribution function: (i) $4\pi\rho r G_{BF_3}(r)$ at 153 K, (ii) $4\pi\rho r G_{BF_3}(r)+2$ at 203 K, (iii) $4\pi\rho r G_{BF_3}(r)+4$ at 253 K, (iv) $4\pi\rho r G_{BF_3}(r)+6$ at 266 K and (v) $4\pi\rho r G_{BF_3}(r)+8$ at 300 K.

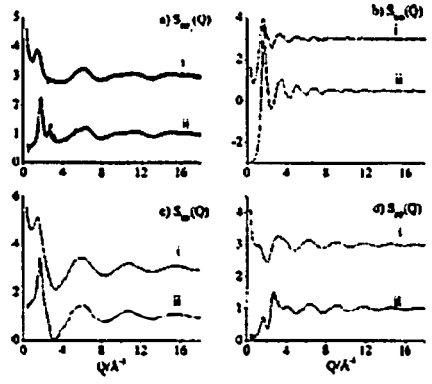

FIG. 3. (a) Total structure factor (i) $S_{BF_3}(Q)+2$ at 300 K and (ii) $S_{BF_3}(Q)$ 153 K. (b) BB partial structure factor generated from RMC (i) $S_{BB}(Q)+2$ at 300 K and (ii) $S_{BB}(Q)$ at 153 K. (c) BF partial structure factor generated from RMC (i) $S_{BF}(Q)+2$ at 300 K and (ii) $S_{BF}(Q)$ at 153 K. (d) FF partial structure factor $S_{FF}(Q)$ generated from RMC (i) $S_{FF}(Q)+1$ at 300 K and (ii) $S_{FF}(Q)$ at 153 K.

neutronically determined densities and the structurally determined intramolecular constraints of distance and coordination number.

RMC modeling has been widely used for the interpretation of disordered systems.[23,40–47] RMC generates a possible configuration that is consistent with the data,[23,24,48] and this model is often assumed to be the most disordered structure that is consistent with the data.[49] There is debate about the precise physical meaning of an RMC model, given that when such a molecular configuration is used to calculate thermodynamic properties, the energies that are calculated are often high. However, if the assertion that the structure of the RMC model is one of the most disordered consistent with the data is correct, then structure evolved in the RMC model must be required in order to fit the observed data. It should be stressed that RMC gives one possible configuration and that this configuration is not unique. RMC fits to the total structure factor at 300 and 153 K are shown in Fig. 3(a) and the RMC extracted partial structure factors, $S_{BB}(Q)$, $S_{BF}(Q)$, $S_{FF}(Q)$, are shown, respectively, in Figs. 3(b)–3(d).

IV. DISCUSSION

As the diffraction patterns and pair correlation functions contain contributions from both the intra- and intermolecular structure, the discussion of the data and associated real space functions is divided into the intramolecular structure and the intermolecular structure. Figure 4(a) shows the intramolecular portion of $G_{BF_3}(r)$, the associated contribution to the diffraction pattern from each intra-molecular partial structure factor is shown in Figs. 4(b)–4(d).

A. Radial intramolecular structure

The radial molecular structure is easily identified in Fig. 4(a), with the boron–fluorine and fluorine–fluorine intramolecular vectors apparent at 1.32±0.02 Å and 2.29±0.02 Å, respectively, and is consistent with the presence of a three-

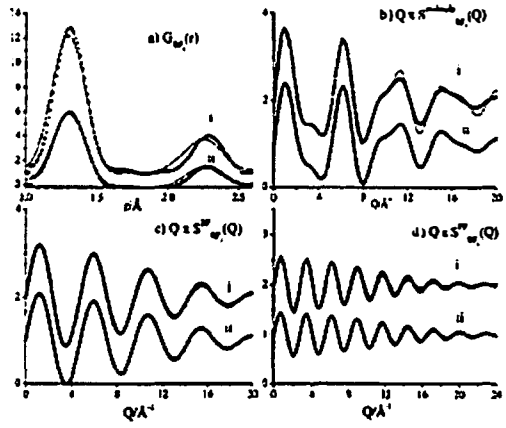

FIG. 4. Intramolecular structure comparison. RMC (solid lines) and data (circles). (a) Total pair correlation function (i) $G_{BF_3}(r)+1$ at 300 K and (ii) $G_{BF_3}(r)$ at 153 K. (b) Intramolecular structure factor multiplied by Q for clarity (i) $Q\times S^{intra}_{BF_3}(Q)+1$ at 300 K and (ii) $Q\times S^{intra}_{BF_3}(Q)$ at 153 K. (c) Intramolecular BF partial structure factor (i) $Q\times S^{intra}_{BF}(Q)+1$ at 300 K and (ii) $Q\times S^{intra}_{BF}(Q)$ at 153 K and (d) Intramolecular FF partial structure factor (i) $Q\times S^{intra}_{FF}(Q)+1$ at 300 K and (ii) $Q\times S^{intra}_{FF}(Q)$ at 153 K.

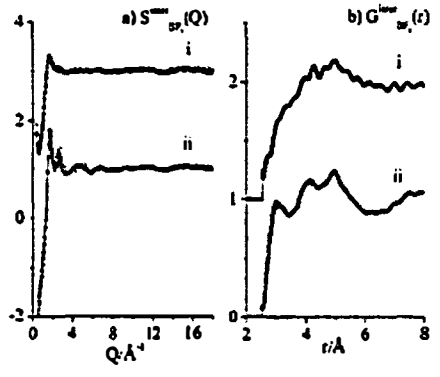

FIG. 5. Intermolecular structure comparison. RMC (solid lines) and data (circles). (a) Intermolecular structure factor (i) $S^{inter}_{BF_3}(Q)+1$ at 300 K and (ii) $S^{inter}_{BF_3}(Q)$ at 153 K and (b) Intermolecular pair distribution function (i) $G^{inter}_{BF_3}(r)+1$ at 300 K and (ii) $G^{inter}_{BF_3}(r)$ at 153 K.

coordinate boron atom with D_{3h} symmetry, when the FBF angle is calculated from the distances shown in Fig. 4. At each temperature the intra-molecular bond distances are identical, showing no temperature dependence of bond length. Also of note are the sharply defined minima in all the data at 2.55 ± 0.09 Å. This distance corresponds with the radius of BF_3 calculated from the density and assuming no isotope effect on the structure from boron-11 ($r_{density}=2.53$ Å).

D_{3h} symmetry is known to be lowered both computationally and experimentally upon complex formation.[50–62] Given that the infrared spectroscopic studies on weakly bound systems show a lengthening of r_{BF} in all cases, the measurements presented here at all temperatures show a distance which is in accord with the unperturbed molecule. This can be interpreted qualitatively as indicating that any axial interaction in the liquid and the supercritical fluid is weak and if the molecule is structurally perturbed by this interaction, then the perturbation of the molecule that is below the sensitivity of these diffraction measurements. This interpretation is additionally supported by infrared measurements in the liquid phase, which show no indication of strong dimer formation,[10] the spectrum of the dimer having been recorded from matrix isolation experiments.[63,64] The infrared spectrum of the solid shows the presence of the ν_1 breathing mode, which is forbidden for a purely D_{3h} molecule,[5,10,65] a result which allowed the prediction of B···F···B bonds in solid BF_3 prior to the x-ray structural determination.[65] The infrared spectrum recorded from the liquid phase also shows the presence of this band. Environmentally induced changes in transitions have been observed before, especially on changing phase from, for example, the solution phase to the solid state, where degeneracies are often raised due to a lowering of local symmetry; the appearance of forbidden bands is rarer on phase change though recently, elegant calculations have been used to determine the mechanism of the ingression of forbidden bands, admittedly in very different systems.[66–68]

B. Radial intermolecular structure

The contribution of the intermolecular structure to the diffraction pattern is shown in Fig. 5(a) with the real space counterpart shown in Fig. 5(b). From the RMC model that best fits the data, the partial structure factors and the associated pair correlation functions can be extracted, and these are shown in Figs. 6(a) and 6(b), respectively.

The greatest change occurs with the boron–fluorine and the fluorine–fluorine pair correlation functions, whereas the boron–boron pair correlation function remains almost unchanged with physical state; given that the interaction between molecules will most probably involve a B–F interaction, the changes in both fluorine pair correlation functions is unsurprising. The diffraction pattern for the two supercritical state points is also dominated by the limit behavior of $S(Q)$, i.e., that

$$\lim_{Q\to 0}\left(\frac{d\sigma}{d\Omega}\right)=\left|\sum_i b_i\right|^2 k_B T\rho\chi_T, \tag{6}$$

where k_B is Boltzman's constant and χ_T is the isothermal compressibility in accord with other neutron diffraction experiments on supercritical fluids.[69–72]

It is clear from the total intermolecular pair correlation function that the liquid is more structured than the supercritical fluid as the distribution of sites in the supercritical fluid is far broader. The population of sites is also more equal and so differences in spatial distribution of sites and the population of these sites in the supercritical fluid is smoother than in the liquid; this is in accord with the conventional picture of the structure of a gas, though the density of a supercritical fluid is greater than a normal gas. With the increase in density, there must necessarily be an increase in structure. However, the intermolecular contact remains almost identical in both phases, though the occupancy of this closest contact is much

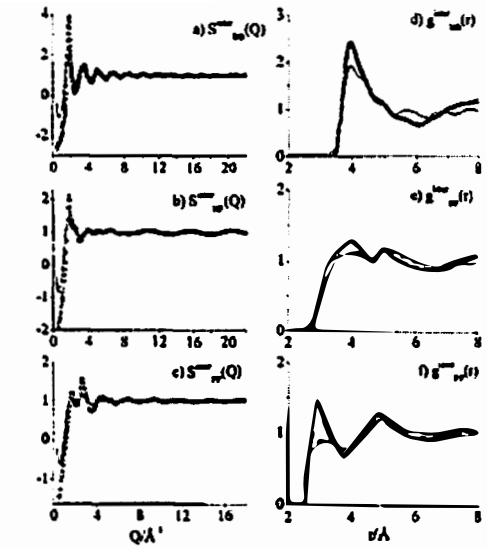

FIG. 6. RMC generated partial structure factors, $S_{\alpha\beta}(Q)$, for BF_3, with the solid line representing the supercritical fluid at 300 K and the circles representing the liquid phase at 153 K. (a) $S_{BB}(Q)$, (b) $S_{BF}(Q)$ and (c) $S_{FF}(Q)$. RMC generated pair distribution functions, $g_{\alpha\beta}(r)$, for BF_3, with the solid line representing the supercritical fluid at 300 K and the circles representing the liquid phase at 153 K. (d) $g_{BB}(r)$, (e) $g_{BF}(r)$, and (f) $g_{FF}(r)$.

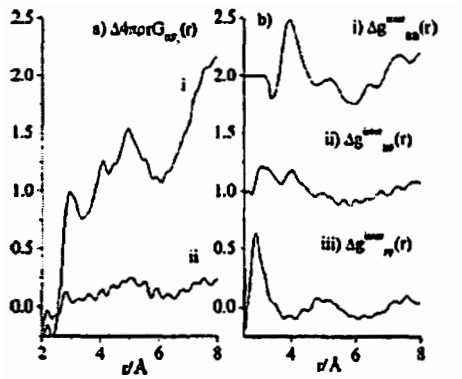

FIG. 7. Intermolecular differences for (a) total pair distribution functions where $\Delta 4\pi\rho r G^{\Delta}_{BF_3}(r) = 4\pi\rho r G^{\Delta K}_{BF_3}(r) - 4\pi\rho r G^{300\,K}_{BF_3}(r)$ (i) $\Delta 4\pi\rho r G^{153\,K}_{BF_3}(r)$ and (ii) $\Delta 4\pi\rho r G^{153\,K}_{BF_3}(r)$ and (b) RMC extracted partials where $\Delta g_{\alpha\beta}(r) = g^{153\,K}_{\alpha\beta}(r) - g^{300\,K}_{\alpha\beta}(r)$ (i) $\Delta g_{BB}(r)$, (ii) $\Delta g_{BF}(r)$, and (iii) $\Delta g_{FF}(r)$.

lower in the supercritical fluid. The liquid and supercritical phases are not simply the same structure, scaled according to the density—there are significant changes both in the occupied structural sites and the population of these sites whereas the closest intermolecular contact remains the same.

The diffraction pattern and in particular, the first sharp diffraction peak, also shows that liquid BF_3 is not a layered liquid,[73,74] in contrast to assertions made from thermodynamic measurements.[75] The liquid does show structure in the first coordination sphere, which is detailed below in the discussion of the angular structure extracted from the RMC model and which implies a disposition for some quasicoplanar orientational preference of the BF_3 planes in the first coordination sphere only. There is no evidence for intermediate range order, which, for the purposes of this discussion, constitutes the definition of a layered liquid.

Figure 7(a)(i) shows the difference in structure between the liquid state and the supercritical state, where $4\pi\rho r G^{153\,K}_{BF_3}(r) - 4\pi\rho r G^{300\,K}_{BF_3}(r)$ is shown. The major difference is the removal of structure in the first coordination sphere. Figure 7(a)(ii) is shown for comparison and shows $4\pi\rho r G^{266\,K}_{BF_3}(r) - 4\pi\rho r G^{300\,K}_{BF_3}(r)$, i.e., difference between the two supercritical states. In this case, the change is structure is far less and shows that the site distribution and site occupancy is more even in the supercritical state, as expected. Figure 7(b) shows the difference in RMC partial pair distribution functions, $\Delta g_{\alpha\beta}(r) = g^{153\,K}_{\alpha\beta}(r) - g^{300\,K}_{\alpha\beta}(r)$.

C. Angular intermolecular structure

The radial structure of the fluid is directly observable from the Fourier transform of the diffraction data. As with any sample that displays macroscopic angular invariance, there is no angular data that is directly measurable. However, from the RMC model best fit to the data, it is possible to extract angular information from the model, with the same caveats as stated above for the reliability of the physical picture of a RMC model. In order to visualize the angular structure from the RMC model, two sets of angular distributions were extracted from the model. Figure 8 shows the angles, distances and constraints that were used as parameters.

θ was either fixed at $90\pm10°$ or left unconstrained; α and β were then varied in 1° increments from 0° to 180°, and the number of boron or fluorine atoms at the intramolecular boron–fluorine bond distance were counted. This extraction was then performed at steps of 0.5 ± 0.25 Å along r_{BF} or r_{FB} (Fig. 8), giving a picture of the angular distributions in 1–2 Å shells around the average molecule. This type of extraction was performed on the lowest temperature data at 153 K, when BF_3 is liquid, and at 300 K, in the supercritical state. The angular extractions and the parameters are collected in Table II.

The results of these angular extractions are shown in Figs. 9 and 10. Figures 9(a) and 9(b) show the unconstrained

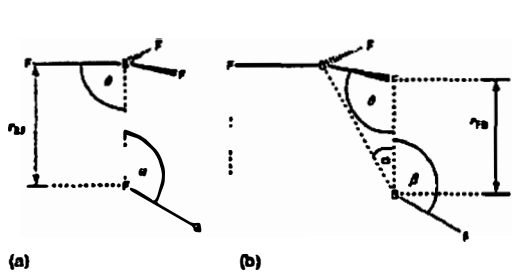

FIG. 8. Salient angles for nearest neighbor interactions between two BF_3 molecules used as structural parameters for the extracted RMC fit to the data giving the angular distribution of (a) the BFB triplet and (b) the FBF triplet.

TABLE II. Parameters for the angular extractions from the unit models of BF_3.

Extraction	r_{FB}	r_{FB}	α	β	δ
BFB constrained	$2.5<r_{FB}<6.5$	...	$0<\alpha<180$	...	$90\pm10°$
BFB unconstrained	$2.5<r_{FB}<6.5$				unconstrained
FBF constrained	...	$2.5<r_{FB}<6.5$	...	$0<\beta<180$	$90\pm10°$
FBF unconstrained		$2.5<r_{FB}<6.5$			unconstrained

BFB triplets for the normal fluid and supercritical fluid, respectively, and Figs. 9(c) and 9(d) show the same for the FBF triplet. Figures 10(a) and 10(b) show the constrained BFB triplets for the normal fluid and supercritical fluid, respectively, and Figs. 10(c) and 10(d) show the constrained FBF triplets in a similar manner.

At the longest distances examined around the average molecule, i.e., beyond the first coordination sphere, in both the supercritical and normal fluid, the angular distribution is isotropic, i.e., there is no net angular distribution. This shows that any ordering in the liquid and supercritical fluid is confined to the first coordination sphere of the molecule and that there is no layering or intermediate range order.

D. The BFB triplet in the normal and supercritical fluid

The constrained BFB triplet [Figs. 10(a) and 10(b)] examines the axial coordination of the average BF_3 molecule with a fluorine atom in the molecular nearest neighbor. This triplet shows a distinct preference for coordination axially at both state points and this preference decreases as r_{BF} increases. Moreover, this structural preference is far more evident in the normal fluid; it is unsurprising that the structure of the supercritical fluid is less dependent on this interaction. At all temperatures there is a significant isotropic component, the limits of which are constrained by the steric imposition of the proximity of the average molecule at the particular distance. However, it is evident then that the axial [3+2] coordination in the solid is retained in the first coordination sphere, though, at both state points, there is also a significant proportion of the molecules that display no orientational preference. The distances for the axial ligation of B in the crystal structure are found at 2.78–2.85 Å.[16]

Once the distance between the B atom in the average molecule and the extracted FB atom pair becomes sufficient that isotropic orientation becomes sterically possible, just ~3.75 Å, a proportion of the molecules assume this disposition, over which an axial contribution is also added. In the supercritical fluid, this is far less apparent.

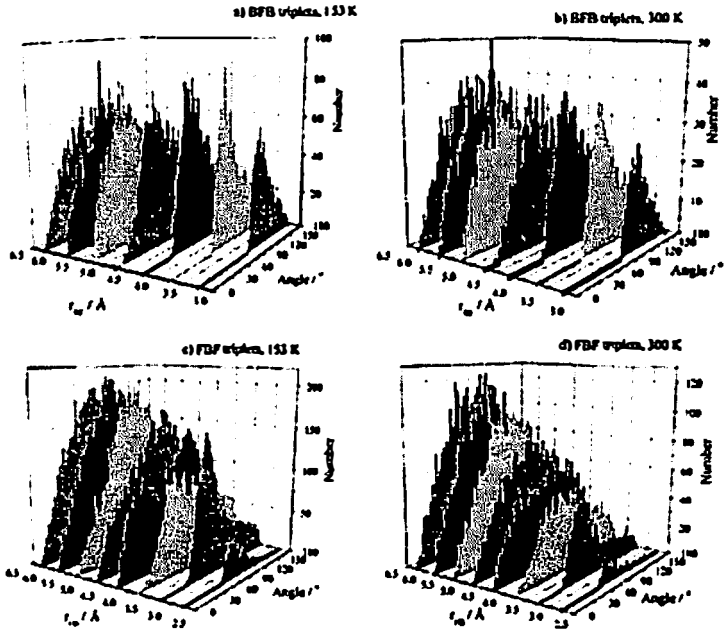

FIG. 9. Unconstrained triplet counts for BF_3 at 153 and 300 K showing the angle between different molecules at r_{FB} and r_{FB} intermolecular distances in steps of 0.5 Å.

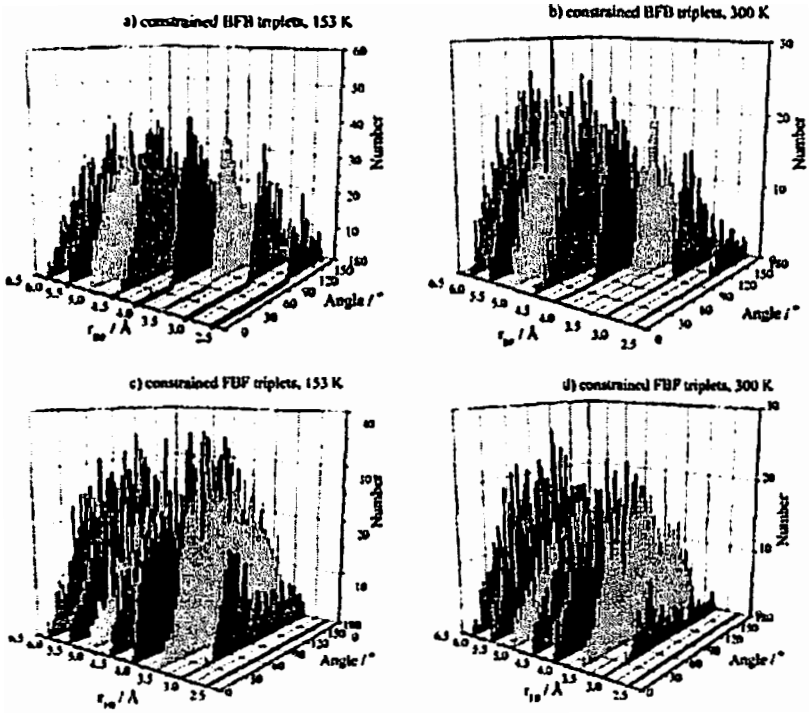

FIG. 10. Constrained with respect to θ in Fig. 8) triplet counts for BF3 at 153 and 300 K showing the angle between different molecules at rBF and rFB intermolecular distances in steps of 0.5 Å.

E. The FBF triplet in the normal and supercritical fluid

At the closest distance that the interaction between the average molecule and the nearest neighbor, a dual distribution is observed, reflecting the tilted nature of the molecule. The double maximum is observed due to the presence of F_{exo} and F_{endo}, as illustrated in Fig. 11.

This distribution reoccurs in the extraction at 4.25 Å, with the distribution between these two distances showing a *quasi*-isotropic distribution. Beyond this distance from the average molecule, the distribution is smooth and becomes isotropic. A diagram of the angular distribution at the maximum number density with distance is shown in Fig. 12.

V. CONCLUSIONS

Liquid and supercritical boron trifluoride both display orientational structure within the first coordination sphere. The structural motif, present in all phases of the solid structure, is retained in the liquid to some extent. It is clear that the intermolecular Lewis acid-base interaction is favorable in the liquid, showing that competition between the intermolecular F···B π-donation is competitive with the intramolecular F···B interaction. However, given that this is structurally evident, it is clear that the intramolecular $p\pi$–$p\pi$ interaction is not sufficient to prevent intermolecular F···B Lewis acid-base interactions in the absence of *a priori* orientational constraints, implying that the Lewis acidity of BF_3 is not solely a function of the valence bond intramolecular F–B $p\pi$–$p\pi$ donation. There is also no evidence of a dimeric structure in the liquid state.

The supercritical fluid also displays a slight orientational interaction between molecules in the first coordination sphere; moreover, the intramolecular contact in the supercritical phase is identical to that observed in the liquid. The supercritical phase is characterized by a wider distribution of sites in real space than the liquid and the population of these sites is also far more even than the normal fluid. Accordingly, a model of the supercritical state that is either entirely unstructured, by analogy with a perfect gas, or is simply a liquid structure scaled by the density is not supported by these measurements.

We, therefore, conclude that liquid BF_3 is partially associated on a local scale i.e. a scale that spans the first coordination sphere, in a manner reminiscent of the crystal structures. Though the fluid is isotropic beyond this distance, as far as can be determined by diffraction experiments, the interactions within the first coordination sphere clearly dominate the behavior of the liquid. We note that accurate and

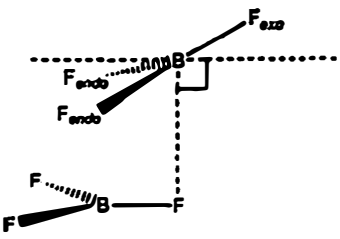

FIG. 11. Axial BF_3 intermolecular interactions.

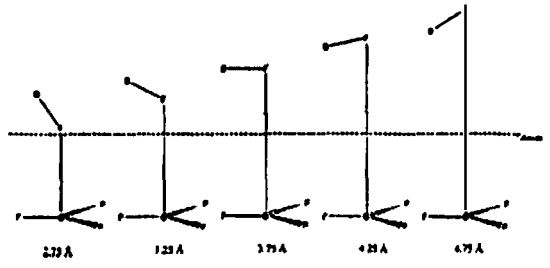

FIG. 12. Axial interactions in liquid and supercritical BF_3, showing the density derived radius, scaled relative to the BF bond length, and the orientation of the maximum in the BFB triplet.

elegant thermodynamic measurements by Calado have been interpreted on the basis that liquid BF_3 is a "layered liquid," a structural model that is refuted by these measurements if the definition of a layered liquid is that conventionally used in discussions of liquid structures and implies intermediate range order. However, there is some degree of ordering in the first coordination sphere. Calado's supposition, even though classical thermodynamics is formally ignorant of the structure of matter, is intuitive as, in the absence of any long range forces, the dominating interaction is that between nearest neighbors, the angular and radial disposition of which imply a preferment for a *pseudo*-planar disposition of molecules not only in the first coordination sphere.

ACKNOWLEDGMENTS

The authors thank the Intense Pulsed Neutron Source at Argonne National Lab for the allocation of beam time and the Department of Energy for fellowship monies for S.E.M. We also thank the University of Tennessee for funding. The experiments performed at Argonne National Laboratory were supported under contract No. W-31-109-ENG-38, US DOE-BES. This work was also funded in part by the Petroleum Research Fund (PRF-37341-G4) and the Neutron Sciences Consortium of the University of Tennessee.

[1] A. G. Gershikov and V. P. Spiridonov, J. Mol. Struct. 73, 91 (1981).
[2] K. Kuchitsu and S. Konaka, J. Chem. Phys. 45, 4342 (1966).
[3] S. Konaka, Y. Murata, K. Kuchitsu, and Y. Morino, Bull. Chem. Soc. Jpn. 39, 1134 (1966).
[4] C. W. Brown and J. Overend, Spectrochim. Acta, Part A 25, 1535 (1969).
[5] O. S. Binbrek, J. K. Brandon, and A. Anderson, Can. J. Spectrosc. 20, 52 (1975).
[6] E. Zeisberger and A. Ruoff, J. Mol. Spectrosc. 136, 295 (1989).
[7] M. Oldani and A. Bauder, J. Chem. Phys. 86, 624 (1987).
[8] T. H. S. Higgins and C. J. G. Raw, J. Chem. Phys. 23, 606 (1955).
[9] A. N. Spencer and M. C. J. Todd, Br. J. Appl. Phys. 11, 60 (1960).
[10] R. G. Steinhardt, Jr., G. E. S. Fetsch, and M. W. Jordan, J. Chem. Phys. 43, 4528 (1965).
[11] M. Atoji and W. N. Lipscomb, J. Chem. Phys. 27, 195 (1957).
[12] C. Spencer and W. N. Lipscomb, J. Chem. Phys. 28, 355 (1958).
[13] M. A. Ring, J. D. H. Donnay, and W. S. Koski, Inorg. Chem. 1, 109 (1962).
[14] M. Y. Antipin, A. M. Elkin, V. F. Sukhoverkhov, Y. T. Struchkov, and Y. A. Buslaev, Dokl. Akad. Nauk SSSR 279, 892 (1984).
[15] D. Mootz and M. Steffen, Z. Anorg. Allg. Chem. 483, 171 (1981).
[16] D. Mootz and M. Steffen, Angew. Chem. 92, 481 (1980).
[17] N. N. Greenwood and A. Earnshaw, *Chemistry of the Elements*, 2nd ed. (Butterworth and Heinemann, Oxford, UK, 1997).
[18] R. J. Gillespie and E. A. Robinson, Adv. Mol. Struct. Res. 4, 1 (1998).
[19] H. Hirao, K. Omoto, and H. Fujimoto, J. Phys. Chem. A 103, 5807 (1999).
[20] E. A. Robinson, S. A. Johnson, T.-H. Tang, and R. J. Gillespie, Inorg. Chem. 36, 3022 (1997).
[21] B. J. van der Veken and E. J. Sluyts, J. Am. Chem. Soc. 119, 11516 (1997).
[22] B. D. Rowsell, R. J. Gillespie, and G. L. Heard, Inorg. Chem. 38, 4659 (1999).
[23] R. L. McGreevy and M. A. Howe, Annu. Rev. Mater. Sci. 22, 217 (1992).
[24] R. L. McGreevy, Nucl. Instrum. Methods Phys. Res. A 354, 1 (1995).
[25] R. L. McGreevy, Comput. Modell. Inorg. Crystallogr. 1997, 151.
[26] L. Pusztai, NATO ASI Ser., Ser. 3 23, 215 (1997).
[27] F. L. B. da Silva, B. Svensson, T. Akesson, and B. Jonsson, J. Chem. Phys. 109, 2624 (1998).
[28] F. L. B. da Silva, B. Svensson, T. Aakesson, and B. Jonsson, J. Chem. Phys. 111, 5622 (1999).
[29] A. Mellergard and R. L. McGreevy, Acta Crystallogr., Sect. A: Found. Crystallogr. A55, 783 (1999).
[30] G. Toth, L. Pusztai, and A. Baranyai, J. Chem. Phys. 111, 5620 (1999).
[31] J. Byrne and J. M. Robson, *Neutrons, Nuclei and Matter: An Exploration of the Physics of Slow Neutrons* (Institute of Physics, New York, 1996).
[32] V. J. Sears, Neutron News 3, 29 (1992).
[33] http://www.ncnr.nist.gov/resources/n-lengths/list.html
[34] G. L. Squires, *Introduction to the Theory of Thermal Neutron Scattering* (Dover, New York, 1997).
[35] J. F. C. Turner, S. E. McLain, T. H. Free, C. J. Benmore, K. W. Herwig, and J. Siewenie, Rev. Sci. Inst. (in press).
[36] C. J. Wormald (personal communication).
[37] http://www.pns.anl.gov/glad/glad.html
[38] A. K. Soper, W. S. Howells, and A. C. Hannon (ISIS Pulsed Neutron Source, Rutherford Appleton Laboratory, 1989).
[39] G. W. Neilson and A. K. Adya, Annu. Rep. Prog. Chem., Sect. C: Phys. Chem. 93, 101 (1997).
[40] J. Krawczyk, A. Pietraszko, R. Kubiak, and K. Lukaszewicz, Acta Crystallogr., Sect. B: Struct. Sci. 59, 384 (2003).
[41] J. Krawczyk, A. Pietraszko, and K. Lukaszewicz, Acta Crystallogr., Sect. B: Struct. Sci. B58, 622 (2002).
[42] A. V. Belushkin, D. P. Kozlenko, R. L. McGreevy, B. N. Savenko, and P. Zetterstro, Physica B 269, 297 (1999).
[43] A. Le Bail, J. Non-Cryst. Solids 271, 249 (2000).
[44] S. Rycroft, A. Chahid, and R. L. McGreevy, Physica B 276–278, 284 (2000).
[45] A. I. Kolesnikov, O. I. Barkalov, M. Calvo-Dahlborg, U. Dahlborg, W. S. Howells, and E. G. Ponyatovsky, Phys. Rev. B 62, 9372 (2000).
[46] M. G. Tucker, D. A. Keen, and M. T. Dove, Miner. Mag. 65, 489 (2001).
[47] M. G. Tucker, M. P. Squires, M. T. Dove, and D. A. Keen, J. Phys.: Condens. Matter 13, 403 (2001).
[48] R. L. McGreevy, J. Non-Cryst. Solids 156–158, 949 (1993).
[49] M. T. Dove, M. G. Tucker, and D. A. Keen, E. J. Min. 14, 331 (2002).
[50] W. A. Herrebout and B. J. van der Veken, J. Mol. Struct. 550–551, 389 (2000).
[51] W. A. Herrebout and B. J. Van der Veken, J. Am. Chem. Soc. 120, 9021 (1998).
[52] W. A. Herrebout, R. Szostak, and B. J. van der Veken, J. Phys. Chem. A 104, 8480 (2000).
[53] W. A. Herrebout, J. Lundell, and B. J. Van der Veken, J. Phys. Chem. A 102, 10173 (1998).
[54] B. J. van der Veken, E. J. Sluyts, and W. A. Herrebout, J. Mol. Struct. 449, 219 (1998).
[55] B. J. van der Veken and E. J. Sluyts, J. Phys. Chem. A 101, 9070 (1997).
[56] B. J. van der Veken and E. J. Sluyts, J. Mol. Struct. 349, 461 (1995).
[57] L. M. Nxumalo, G. A. Yeo, and T. A. Ford, S. Afr. J. Chem. 51, 25 (1998).
[58] L. M. Nxumalo and T. A. Ford, Spectrochim. Acta, Part A 53A, 2511 (1997).
[59] L. M. Nxumalo and T. A. Ford, J. Mol. Struct. 436–437, 69 (1997).
[60] L. M. Nxumalo and T. A. Ford, THEOCHEM 369, 115 (1996).
[61] L. M. Nxumalo and T. A. Ford, S. Afr. J. Chem. 48, 30 (1995).
[62] L. M. Nxumalo, M. Amlrzejak, and T. A. Ford, Vib. Spectrosc. 12, 221 (1996).
[63] L. M. Nxumalo and T. A. Ford, Vib. Spectrosc. 6, 333 (1994).
[64] F. M. M. O'Neill, G. A. Yeo, and T. A. Ford, J. Mol. Struct. 173, 337 (1988).
[65] D. A. Dows, J. Chem. Phys. 31, 1637 (1959).
[66] R. J. Hinde, D. T. Anderson, S. Tam, and M. E. Fajardo, Chem. Phys. Lett. 356, 355 (2002).

[67]D. T. Anderson, R. J. Hinde, S. Tan, and M. E. Fajardo, J. Chem. Phys. 116, 594 (2002).
[68]R. J. Hinde, Phys. Rev. B 61, 11451 (2000).
[69]T. Tassaing, M. I. Cabaço, Y. Danten, and M. Besnard, J. Chem. Phys. 113, 3757 (2000).
[70]Y. Danten, M. I. Cabaço, T. Tassaing, and M. Besnard, J. Chem. Phys. 115, 4239 (2001).
[71]C. J. Benmore and B. L. Tomberli, Ind. Eng. Chem. Res. 39, 4491 (2000).
[72]A. Botti, F. Bruni, A. Isopo, G. Modesti, C. Oliva, M. A. Ricci, R. Scerbi, and A. K. Soper, J. Chem. Phys. 118, 235 (2003).
[73]M. Wilson and P. A. Madden, Phys. Rev. Lett. 80, 532 (1998).
[74]J. D. Mania, S. J. Gwentler, N. Fouse, and L. Ihm, Nature (London) 419, 381 (2002).
[75]J. C. G. Calado and E. J. M. Filipe, J. Chem. Soc., Faraday Trans. 92, 215 (1996).

Structure of Liquid HF

On the Structure of Liquid Hydrogen Fluoride**

*Sylvia E. McLain, Chris J. Benmore, Joan E. Siewenie, Jacob Urquidi, and John F. C. Turner**

The liquid state is the most complex phase of matter. Densities of liquids are comparable to densities of the solids, implying that the forces between particles in the liquid are of the same magnitude as those forces present in the solid. However, there is no simplification due to the presence of a lattice and no satisfactory analytic theory of the liquid state exists. However, despite this complexity, the liquid state is an outstandingly important chemical milieu in which many reactions take place.

Strongly associated fluids are particularly complex and the structure and properties of these fluids provide an exacting and stringent test of theory. Here, we report the first investigation of the structure of hydrogen fluoride at the level of the distributions of pairwise interatomic distances, the partial pair correlation functions.

Liquid HF is an important chemical and it is widely used in the petrochemical industry, as a catalyst for hydrocarbon management, and in the glass and ceramics industries.[1,2] Academically, its superior properties as a solvent have found application in both organic and inorganic chemistry, and the superacidic properties have been exploited in both disciplines, in the study of reactive intermediates and reaction mechanisms[3,4] That these highly desirable properties are not more widely applied is mainly due to the exceedingly toxic and corrosive nature of the material,[1,5] which is severe when anhydrous and only somewhat lessened in solution. Indeed, given the properties of liquid HF, it has been stated that the calculation of its properties is to be preferred over measurement.[6]

The true importance of this fluid does not solely rest with its industrial and academic applications: it is the simplest archetype for the strong hydrogen bond, and the molecular simplicity of HF makes it an attractive model for strongly hydrogen-bonded systems. That hydrogen bonding should be so important to understand need not be reiterated, once the importance of this interaction in structural biology, materials science, chemistry and physics is appreciated.[7-9] This important, directional structural interaction is responsible, inter alia, for protein conformations, the stability of the structure of DNA and the properties of water and other associated fluids.

Both the bulk properties[6,10,11] and microscopic structure[12,13] of HF have been the focus of intense theoretical investigation; there have been many calculational approaches to the structure and properties of HF using a variety of methods.[6,10-24] The overarching feature of these calculations is the complete lack of experimental data with which to compare the results of calculation at the pair correlation function level. The only structural data reported to date are two total structure factor measurements for DF at a variety of thermodynamic state points.[25,26] Given that the total structure factor is the weighted sum of the partial structure factors, it is unsurprising that there is a variance in the results of the calculated structural models of HF at the pair correlation function level.

The hydrogen bond is the dominant feature of the structural chemistry of HF in all phases; the solid is composed of unbranched, zigzag chains[27] while the vapor is composed of cyclic oligomers and clusters.[28] In the liquid, the macroscopic properties are consistent with strong hydrogen bonds, though until this report, there has been no experimental data to confirm this at the pair correlation function level.

To determine the atomic structure and therefore the hydrogen-bonded nature of HF, high-energy X-ray and neutron diffraction measurements were performed on samples of HF and DF at 296 ± 2 K and 1.2 ± 0.1 bar. Both types of radiation were used to provide complementary information on the structure.[29-31] X-rays scatter from electron density, weighting the contribution of each atom to the scattering pattern by Z the atomic number. In contrast, the interaction of neutrons with matter is dependent on the composition of the nucleus and therefore the isotopic nature of each sample defines magnitude of the scattering interaction. Assuming isostructurality between isotopomeric samples, it is possible, by taking linear combinations of diffraction patterns, to solve the structure factor equations and explicitly determine each of the individual structure factors. This technique has been widely applied to diffraction studies of liquids[32-34] as well as other disordered systems.[35] The pair correlation function is related to the scattered intensity by Fourier transformation as given in Equation (1), where ρ is the atomic number density.

$$S(Q) = 1 + \frac{4\pi\rho}{Q}\int r[G(r)-1]\sin(Qr)dr \qquad (1)$$

Extraction of the partial structure factors therefore allows the determination of the distribution of pairwise atomic distances—the pair correlation functions.

The diffraction pattern of a sample of HF, collected with radiation source A and written as $S_A^N(Q)$, is related to the

[*] Dr. J. F. C. Turner
Neutron Sciences Consortium and Department of Chemistry
University of Tennessee
Knoxville, TN, 37996-1600 (USA)
Fax: (+1) 865-974-3454
E-mail: jturner@atom.chem.utk.edu
S. E. McLain
Department of Chemistry, University of Tennessee
Knoxville, TN 37996-1600 (USA)
S. E. McLain, C. J. Benmore, J. E. Siewenie, J. Urquidi
Intense Pulsed Neutron Source, Argonne National Laboratory
South Cass Avenue, Argonne, IL 60439-4814 (USA)

[**] The authors thank Ms. B. Marzec (IPNS), Ms. J. Linton (APS), Mr. C. Kurtz (APS), and Mr. T. H. Free (University of Tennessee) for help in the facilitation of these experiments, and Dr. M. L. Klein and Dr. P. E. Egelstaff for highly interesting and stimulating discussions. This work was funded in part by the Department of Energy (No. W-31-109-ENG-38), the Petroleum Research Fund (PRF-27141-G4) and the Neutron Sciences Consortium of the University of Tennessee.

partial structure factors according to Equation (2), where $a^{\Delta}_{YY'}$

$$S^{\Delta}_{Y}(Q) = a^{\Delta}_{HH}S^{\Delta}_{HH}(Q) + a^{\Delta}_{FF}S^{\Delta}_{FF}(Q) + 2a^{\Delta}_{HF}S^{\Delta}_{HF}(Q) \quad (2)$$

(Y,Y' = H,F) is the weighting of the scattering from Y and Y' due to number density and the inherent strength of the scattering interaction.

For neutrons, this factor is written as $a^{N}_{YY'} = c_Y c_{Y'} b_Y b_{Y'}$; for X-rays it is $a^{X}_{YY'} = c_Y c_{Y'} f_Y(Q) f_{Y'}(Q)$, where c_Y is the number density of nucleus Y, b_Y is the elastic coherent scattering length,[26] and $f_Y(Q)$ corresponds to the form factor. The weighting factors for these neutron and X-ray experiments are shown in Table 1.

Our measured neutron diffraction pattern of DF is presented in Figure 1. The diffraction pattern from our experiments is in good agreement with that of Deraman et al.[28] Given that the structure of the fluid at the partial structure factor level is determined solely by $S_{HH}(Q)$, $S_{HF}(Q)$, and $S_{FF}(Q)$, the collection of X-ray and neutron diffraction data on three isotopomeric samples allows the extraction of the partial structure factors and therefore, by way of Fourier transformation, the pair correlation functions. These are shown in Figure 2a in reciprocal space and in Figure 2b in real space.

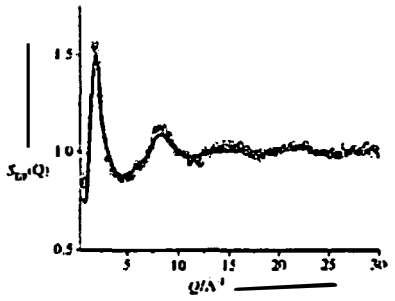

Figure 1. Total structure factor for DF measured by neutron diffraction (circles) compared with previous diffraction measurements (solid line).[28]

In the Fourier transform of the diffraction pattern of DF, the intramolecular H–F peak position in the $G^{N}_{DF}(r)$ is found at $r_{HF} = 0.93 \pm 0.02$ Å, in good agreement with the previously determined distances in liquid DF, namely 0.93 and 0.925 Å.[25,29]

The partial pair correlation functions, $g_{HH}(r)$, $g_{HF}(r)$, and $g_{FF}(r)$ (Figure 2b), define the radial structure of the fluid at the pair correlation function level. $g_{HF}(r)$ illuminates the key structural feature of the liquid, the intermolecular hydrogen bond. The intermolecular peak position in $g_{HF}(r)$, r_{HF}, was found to be 1.60 ± 0.04 Å. This relatively short distance is indicative of a very strong hydrogen bond. Moreover, the average intermolecular hydrogen–fluorine coordination number, determined from integration of $g_{HF}(r)$, where $c_{HF} = 4\pi\rho \int_1^2 r^2 g_{HF}(r)dr$ is given by $c_{HF} = 0.86 \pm 0.10$ which consistent with the presence of hydrogen-bonded chains which are short and therefore not infinite. This result is in agreement with Raman and IR spectroscopy studies which have been interpreted by using a model with chains of six or seven HF molecules.[29]

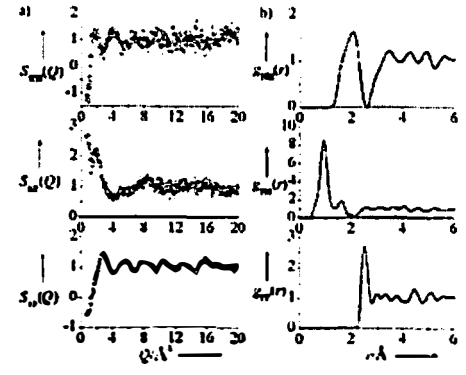

Figure 2. a) Partial structure factors, $S_{HH}(Q)$, $S_{HF}(Q)$, and $S_{FF}(Q)$. b) partial pair correlation functions, $g_{HH}(Q)$, $g_{HF}(Q)$, and $g_{FF}(Q)$.

Table 1: Weighting factors for DF and HF neutron experiments and X-ray experiments.

	DF neutron	HF neutron	X-ray 0 Å^{-1}	X-ray 1 Å^{-1}	X-ray 2 Å^{-1}	X-ray 5 Å^{-1}	X-ray 10 Å^{-1}
a^{Δ}_{HH}	0.1113	0.0350	0.250	0.191	0.093	0.004	0.000
a^{Δ}_{FF}	0.0799	0.0799	20.250	18.253	13.715	3.569	0.435
a^{Δ}_{HF}	0.1886	−0.1057	4.500	3.732	2.260	0.250	0.014

$g_{HH}(r)$ shows a large peak at $r_{HH} = 2.1 \pm 0.1$ Å with a coordination number of $c_{HH} = 1.69 \pm 0.10$. This peak extends into the region at lower r and overlaps with the intermolecular hydrogen bond in $G^{N}_{DF}(r)$. This phenomenon has also been noted in the simulation literature, though at a different thermodynamic state point of the liquid.[13] The accurate separation of the overlapping peaks in $g_{HH}(r)$ and $g_{HF}(r)$ as well as the extraction of the $g_{FF}(r)$ function, is essential in understanding the complete structure of the liquid as well as in making accurate comparisons between calculational models.

The first peak in $g_{FF}(r)$ (Figure 2b) occurs at $r_{FF} = 2.51 \pm 0.03$ Å with a coordination number $c_{FF} = 2.1 \pm 0.1$ Å. In addition, $g_{FF}(r)$ shows several peaks occurring beyond the first peak, these peaks having been predicted to some extent by several simulations,[12,16,21,24] with the ab initio molecular dynamics and QM/MM simulations showing the closest agreement.

Angular information is available from a diffraction pattern from a liquid in a limited manner and represents a statistical average of the bulk configuration of the fluid.

Taking the peak maxima from the extracted pair correlation functions as the basis for intermolecular angular

calculations is instructive. The average H-F-H angle gives an indication of the linearity of the hydrogen bonds and was found to be $\theta_{HFH} = 104 \pm 8°$, indicative of bent hydrogen bonds. The polarizable pair potential model predicts this value most accurately at $\theta_{HFH} = 107°$, although the bond lengths in this model vary from the present work.[13]

The average F-H-F angle is found to be $\theta_{FHF} = 165 \pm 10°$ and defines the degree of orientation between different molecules in the chain. The most accurate corresponding simulation value, from the ab initio MD calculations, is $\theta_{FHF} = 156°$.[14] Both non-polarizable and polarizable pair potential models predict this angle to be $\theta_{FHF} = 180°$.[13]

The degree of chain branching that occurs in the liquid also varies widely between the different models, ranging from 0%[12] to 20% branching.[15] To visualize our data and to assess the degree of branching we chose to model our data using reverse Monte Carlo (RMC) modeling.[40-42] Widely used in structural studies of disordered systems, the RMC model is thought to give the most disordered configurations that are consistent with the data[43,44] and has the advantage that no potential is prescribed in the calculations. The RMC simulation was performed simultaneously on the three measured partial structure factors using a cubic box containing 5000 HF molecules with the constraint that the average coordination number and peak positions in the simulation had to agree with the values obtained from direct the Fourier transform of the measured partial structure factor data. A comparison between the RMC partial structure factors (solid line) and the experimental partial structure factors (circles) is shown in Figure 3.

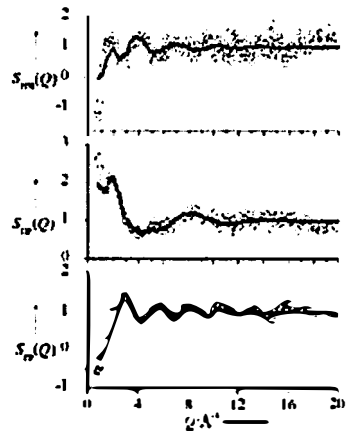

Figure 3. RMC fit (solid line) to the experimental partial structure factors (circles).

A snapshot of the RMC simulation (Figure 4) indicates that short, winding, unbranched, hydrogen-bonded chains dominate the liquid state. Integration of $g_{HF}^{RMC}(r)$ to $r_{min} = 2.15$ Å, reveals only 8% of the molecules form branched chains, this compares to values of 3.5% predicted by the ab initio simulation and 7% predicted by the polarizable potential model.[14,15]

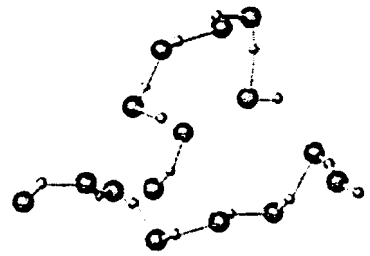

Figure 4. Two representative molecular groups taken from the RMC simulation show winding hydrogen-bonded chains dominate the liquid structure.

In summary, diffraction data from liquid hydrogen fluoride at the temperature and pressure of this measurement is consistent with the presence of short, bent, strongly hydrogen-bonded chains, with strong interchain interactions and very little branching. Despite the strength of the hydrogen bond in the liquid, the chains appear to be curtailed in length at around an average of seven molecules per chain.

As well as defining the structure of liquid HF at the partial pair correlation function level for the first time, these data provide the theoretical community with detailed experimental information required to improve simulations of HF and the methods for the calculational investigation of strongly associated fluids.

Experimental Section

Isotopic samples of HF, DF, and an $HF_{0.6}DF_{0.5}$ mixture were prepared as described elsewhere.[16] The chemical and isotopic purity of all the samples was >99.9% with <0.1% H_2O.

A series of neutron and high-energy X-ray diffraction measurements were conducted on the liquid at 296 ± 2 K and 1.2 ± 0.1 bar. Neutron diffraction data from DF and HF were recorded on the Glass, Liquid and Amorphous Diffractometer at the Intense Pulsed Neutron Source, Argonne National Laboratory (ANL), USA. High-energy X-ray diffraction data from analogous samples were measured on the 11-IDC line at BESSERC-CAT, Advanced Photon Source at ANL. The neutron data were corrected for detector efficiency, attenuation, multiple scattering, and inelastic scattering using standard methods.[45] The primary difficulties in the data correction arose from Bragg scattering from the cell and achieving correct normalization. Accordingly, each empty cell was measured separately and filled with D_2O, to correct each data set and to account for variations in the cells used. Careful empirical subtraction of the individual Bragg peaks was then performed.

High-energy X-ray data were corrected for detector efficiency, instrumental geometrical effects, polarization, and empty container scattering, and were then normalized to the sum of the form factors plus Compton scattering. X-ray experiments were performed on all of the isotopic mixtures at the same state conditions as the neutron experiments and showed no significant isotopic quantum effect, within the limits of the experimental error (~5%), supporting the use of the isotopic substitution technique in neutron diffraction in this case.

Received: November 10, 2003 [Z53289]

Keywords: fluorides · liquids · neutron diffraction · X-ray diffraction

[1] R. A. D. Boisson, *Organofluorine Chem.* 1994, 579.
[2] H. Fielding, B. Lee, *Chem. Br.* 1978, *14*, 173.
[3] G. A. Olah, *Angew. Chem.* 1995, *107*, 1519; *Angew. Chem. Int. Ed. Engl.* 1995, *34*, 1393.
[4] T. A. O'Donnell, *Superacids and Acidic Melts as Inorganic Chemical Reaction Media*, VCH Publishers, New York, 1992.
[5] E. B. Segal, *Chem. Health Saf.* 2000, *7*, 18.
[6] D. P. Visco, Jr., D. A. Kofke, *Fluid Phase Equilib.* 1999, *158–160*, 37.
[7] D. B. Northrop, *Acc. Chem. Res.* 2001, *34*, 790.
[8] T. Steiner, *Angew. Chem.* 2002, *114*, 50; *Angew. Chem. Int. Ed.* 2002, *41*, 48.
[9] C. L. Perrin, J. B. Nielson, *Annu. Rev. Phys. Chem.* 1997, *48*, 511.
[10] D. P. Visco, Jr., D. A. Kofke, *Ind. Eng. Chem. Res.* 1999, *38*, 4125.
[11] S. Wierzchowski, D. A. Kofke, *Fluid Phase Equilib.* 2002, *194–197*, 249.
[12] A. Munoz-Losa, I. Fernandez-Galvan, M. E. Martin, M. A. Aguilar, *J. Phys. Chem. B* 2003, *107*, 5043.
[13] M. Kreitmeir, H. Bertagnolli, J. J. Mortensen, M. Parrinello, *J. Chem. Phys.* 2003, *118*, 3639.
[14] U. Roethlisberger, M. Parrinello, *J. Chem. Phys.* 1997, *106*, 4658.
[15] P. Jedlovszky, R. Vallauri, *J. Chem. Phys.* 1997, *107*, 10166.
[16] C. Martin, M. Lombardero, J. A. Anta, E. Lomba, *J. Chem. Phys.* 2001, *114*, 355.
[17] P. Jedlovszky, M. Mezei, R. Vallauri, *J. Chem. Phys.* 2001, *115*, 9883.
[18] U. Balucani, G. Garberoglio, G. Sutmann, R. Vallauri, *Chem. Phys. Lett.* 1999, *315*, 109.
[19] P. Jedlovszky, R. Vallauri, *Mol. Phys.* 1998, *93*, 15.
[20] P. Jedlovszky, R. Vallauri, *Mol. Phys.* 1997, *92*, 331.
[21] M. L. Klein, I. R. McDonald, *J. Chem. Phys.* 1979, *71*, 298.
[22] I. R. McDonald, M. L. Klein, *Faraday Discuss. Chem. Soc.* 1978, *66*, 38.
[23] W. L. Jorgensen, *J. Chem. Phys.* 1979, *70*, 5888.
[24] H. Sun, R. O. Watts, U. Buck, *J. Chem. Phys.* 1992, *96*, 1810.
[25] T. Pfleiderer, I. Waldner, H. Bertagnolli, K. Todheide, H. E. Fischer, *J. Chem. Phys.* 2000, *113*, 3690.
[26] M. Deraman, J. C. Dore, J. G. Powles, J. H. Holloway, P. Chieux, *Mol. Phys.* 1985, *55*, 1351.
[27] M. W. Johnson, E. Sandor, E. Arzi, *Acta Crystallogr. Sect. B* 1975, *31*, 1998.
[28] J. Janzen, L. S. Bartell, *J. Chem. Phys.* 1969, *50*, 3611.
[29] J. Neuefeind, *J. Mol. Liq.* 2002, *98–99*, 87.
[30] J. Neuefeind, H. F. Poulsen, *Phys. Scr. T* 1995, *57*, 112.
[31] C. J. Benmore, Y. L. Luh, *J. Chem. Phys.* 2000, *112*, 5877.
[32] A. K. Soper, P. A. Egelstaff, *Mol. Phys.* 1981, *42*, 399.
[33] C. Andreani, F. Menzinger, M. A. Ricci, A. K. Soper, J. Dreyer, *Phys. Rev. B* 1994, *49*, 3811.
[34] C. Andreani, M. A. Ricci, M. Nardone, F. P. Ricci, A. K. Soper, *J. Chem. Phys.* 1997, *107*, 214.
[35] A. K. Soper, *J. Phys. Condens. Matter* 1997, *9*, 2717.
[36] S. E. McLain, C. J. Benmore, J. F. C. Turner, *J. Chem. Phys.* 2002, *117*, 3816.
[37] J. F. C. Turner, C. J. Benmore, C. M. Barker, N. Kaltsoyannis, J. M. Thomas, W. I. F. David, C. R. A. Catlow, *J. Phys. Chem. B* 2000, *104*, 7570.
[38] V. F. Sears, *Neutron News* 1992, *3*, 29.
[39] B. Deshat, H. Pham Van, *J. Chem. Phys.* 1983, *78*, 6377.
[40] R. L. McGreevy, *J. Phys. Condens. Matter* 2001, *13*, R877.
[41] R. L. McGreevy, *Nucl. Instrum. Methods Phys. Res. Sect. A* 1995, *354*, 1.
[42] R. L. McGreevy, M. A. Howe, *Annu. Rev. Mater. Sci.* 1992, *22*, 217.
[43] M. T. Dove, *Eur. J. Mineral.* 2002, *14*, 203.
[44] M. T. Dove, M. G. Tucker, D. A. Keen, *Eur. J. Mineral.* 2002, *14*, 331.
[45] J. F. C. Turner, S. E. McLain, T. H. Free, C. J. Benmore, K. W. Herwig, J. E. Siewenie, *Rev. Sci. Instrum.* 2003, *74*, 4410.
[46] A. K. Soper, W. S. Howells, A. C. Hannon, ISIS Pulsed Neutron Source, Rutherford Appleton Laboratory, 1989.

REVIEW OF SCIENTIFIC INSTRUMENTS VOLUME 74, NUMBER 10 OCTOBER 2003

Sample containment for neutron and high-energy x-ray scattering studies of hydrogen fluoride and related molecular species

John F. C. Turner[a)]
Neutron Sciences Consortium and Department of Chemistry, University of Tennessee, Knoxville, Tennessee 37996-1600

Sylvia E. McLain
Department of Chemistry, University of Tennessee, Knoxville, Tennessee 37996-1600 and Intense Pulsed Neutron Source, Argonne National Laboratory, 9700 S. Cass Avenue, Argonne, Illinois 60439

Timothy H. Free
Department of Chemistry, University of Tennessee, Knoxville, Tennessee 37996-1600

Chris J. Benmore
Intense Pulsed Neutron Source, Argonne National Laboratory, 9700 S. Cass Avenue, Argonne, Illinois 60439

Kenneth W. Herwig
Spallation Neutron Source, Oak Ridge National Laboratory, 701 Scarboro Road, Oak Ridge, Tennessee 37830

Joan E. Siewenie
Intense Pulsed Neutron Source, Argonne National Laboratory, 9700 S. Cass Avenue, Argonne, Illinois 60439

(Received 17 April 2003; accepted 28 July 2003)

The design of a suite of sample cells and sample preparation facilities to investigate the structure and dynamics of chemically reactive molecular fluorides, using high-energy x-ray and neutron scattering, is reported. A detailed discussion of both the neutronic and chemical considerations is provided, in support of the choice of the material of cell construction for both structural and dynamical experiments. The discussion of this suite of equipment also includes a detailed design of a hybrid high-vacuum Schlenk line for sample preparation. These cells were specifically designed to study hydrogen fluoride but may be used for other species that exhibit similar chemical reactivity. Background considerations for liquid diffraction experiments are also discussed and show that in designing cells for liquid samples, or samples that contain a large structurally amorphous fraction, crystalline sample containment affords far more tractable data analysis. © *2003 American Institute of Physics*. [DOI: 10.1063/1.1611999]

I. INTRODUCTION

Fluoride-based materials are among some of the most interesting systems available and display a wide range of structural, chemical, and bonding properties which lead to their application both in industry,[1–4] synthesis,[5,6] and in more fundamental, academic studies.[7,8]

Fluorine, as a ligand to both transition metals and main group elements is unique in the range of high oxidation states that it will support. The thermodynamic reason for this lies in part in the bond energy of the F–F bond,[9–11] which is low in comparison to the other halogens[11,12] [$D_0(F_2)$ = 158.78 kJ mol^{-1}; $D_0(Cl_2)$ = 242.58 kJ mol^{-1}; $D_0(Br_2)$ = 192.807 kJ mol^{-1}; $D_0(I_2)$ = 151.088 kJ mol^{-1}] and, also, in the strength of the heteroatomic bonds formed in a reaction with fluorine, which are almost always strong. The small steric encumbrance of the F atom also ensures that fluorine is a very strong π donor; in transition metal chemistry, it is a weak field ligand, consistent with strong π donation under the molecular orbital and ligand field theory of transition metal chemistry.[13] These electronic and thermodynamic properties ensure that the properties of fluoride complexes of an element are often anomalous when compared to the general trends of the chemistry of that element. The best examples of this are to be found in the chemistry of the noble gases. Indeed, it was oxidation of Xe by PtF_6 (Refs. 14 and 15) that opened up an entirely new group in the Periodic Table to chemical discovery, a chemical event not witnessed since the isolation of the alkali and alkaline earth metals by Davy. Examples of the unique structures and bonding motifs are to be found in the respective structures of O_2F_2,[16] XeF_6,[17–20] and F_2H^-.[21,22] Moreover, fluorinated inorganic fluids, such as HF, HF.SbF_5, FSO_3H, and FSO_3H.SbF_5 are the strongest acids known and are highly important fluids both academically and industrially.[5–7] Recent work into the structure of superacids and superacidic solutions[23–25] using neutron diffraction from liquid samples has required the development of appropriate sample environment (SE) equipment.

In order to apply neutron scattering and high-energy x-ray scattering to chemically ambitious samples, SE equipment that satisfies the chemical and experimental constraints must be designed and built. The work reported in this article contributes to this effort, and indeed, recent advances in SE

a)Author to whom correspondence should be addressed; electronic mail: jturner@utk.edu

equipment have lead to the development of facilities to study chemical reactions *in situ* or in a time-resolved manner.[26–28] These include the hydrothermal crystallization of dense phase materials and zeolites,[29–32] chemical reactions,[26] and catalytic processes.[27,28] In this article, the design, construction, and preliminary results using a suite of handling apparatus and sample cells are reported which allow the measurement of structural and dynamical properties of highly aggressive and reactive samples with the conservation of both chemical and isotopic integrity. Specifically, the experimental development involved in the measurement of the dynamics and structure of isotopomers of anhydrous liquid hydrogen fluoride is described. Hydrofluoric acid is an exceptionally dangerous material to handle; it has a very high chemical toxicity and causes severe and highly dangerous burns in contact with human tissue, even in aqueous solution.[33,34] Anhydrous hydrogen fluoride is even more dangerous due to the high fat solubility and volatility. In the design of the equipment, the chemical containment must, therefore, meet very severe safety constraints.

This article also demonstrates that the stringent constraints of the neutronic properties of hydrogen, of the interplay between sample structure and the structure of the material used in cell construction and those of the chemical nature of the sample can be satisfied and that neutron and high-energy x-ray scattering can be applied to chemically difficult samples.

Current fluences[35] and new instruments[36,37] recently built at neutron sources and third-generation x-ray sources[38] have significantly widened the range and complexity of chemical samples for which these types of scattering can provide detailed structural and dynamical information. The projected increase in flux at the Spallation Neutron Source,[39] presently under construction, will only amplify this trend. With respect to neutron scattering, this is a highly desirable development; neutron scattering is a particularly attractive technique chemically as the method is highly sensitivity to light atoms, defined as those with a low atomic number. This sensitivity is general for elastic neutron scattering experiments and is true for quasielastic and inelastic neutron scattering spectroscopy in a more qualified manner.

Information from elastic neutron scattering experiments is often complementary to that from the x-ray scattering analog. The complementary nature of the two techniques is due to the differing nature of the neutron-matter and x-ray-matter interaction;[40,41] elastic neutron scattering reveals the distribution of nuclear density (or magnetic spin density in certain cases) in the sample whereas the scattering density in an x-ray scattering experiment is the distribution of the electron density. Particularly well known is the sensitivity of elastic neutron scattering to hydrogen and deuterium but in general across the Periodic Table, atoms with low atomic number scatter as strongly as those with high atomic number.[42,43] in direct contrast with x rays, where the scattering power increases with the atomic number.[44] Inelastic and quasielastic experiments are extraordinarily sensitive to normal modes that involve the motion of protons in the system whether the protons are bound chemically or are translationally free. In contrast to vibrational or rotational spectroscopies, such as infrared or microwave spectroscopies, or Raman scattering, there are in general no selection rules that govern the existence of a normal mode transition.

These features of elastic, inelastic, and quasielastic neutron scattering are, in themselves, highly desirable; this desirability is only amplified by the complementary nature of the data from a neutron scattering experiment to that collected from x-ray and electromagnetic spectroscopies.

High-energy synchrotron x-ray diffraction, and its precursor γ-ray scattering, shares many of the features of neutron scattering in terms of the level of penetration possible in condensed matter.[45,46] Recently, this technique has begun to be applied to the investigation of electron density distributions[47–50] and quantum effects on the structure of liquids.[45,47–49,51–55]

II. DESIGN CONSTRAINTS

A. Neutronic considerations

Although the interaction between the nucleus and the neutron is very strong, the low density of nuclear matter in a material of average density ensures that the net interaction of neutrons with matter is extremely weak. Coupled with the lack of charge on the neutron, this gives neutron scattering one of its major experimental advantages—that of great penetration. Not only does this mean that structures and dynamics measured by neutron scattering are genuine representations of the structural and dynamical characteristics of the thermodynamic state of the sample, but also that the range of materials out of which SE equipment can be built is wider than that for analogous experiments with x rays of conventional energies. The penetration of neutrons is such that almost any nonabsorbing material may be used, allowing the construction of high-temperature and high-pressure apparatus that would be impossible at an x-ray source. An exception to this generality is the use of diamond anvil cells in x-ray diffraction experiments; such cells are only now being developed for work at neutron sources. That diamond anvil cells can be used easily in x-ray experiment is a feature of the large discrepancy in the fluences at current neutron and x-ray sources. Sample sizes for x-ray experiments need often be much smaller than at a neutron source.

The range of physical variables that is, therefore, accessible to neutron scattering investigation is often wider than the analogous x-ray experiment. The caveat to this lack of proscription of construction material is that the background, which the cell material presents in the scattering experiment, must be accounted for in the data analysis and ideally considered beforehand in the design of the SE equipment.

By paying careful attention to the neutronic properties of the elements of which the apparatus is constructed, several unique approaches to sample environment design are available. Neutronically, vanadium or alloys, such as $Ti_{2.08}Zr$, are common materials for construction of SE equipment for neutron scattering experiments, due to the mechanical and neutronic properties of the metals. Vanadium and $Ti_{2.08}Zr$ are chosen because of the elastic scattering cross sections these materials possess. The former has a very small elastic cross section ($b_V = -0.3824$ fm) (Refs. 42 and 43) and is pre-

dominately an incoherent scatterer, while the latter exploits the opposite phase of the scattered neutrons when scattered from Ti or Zr, which is denoted by a negative length for Ti ($b_{Ti} = -3.438$ fm; $b_{Zr} = 7.16$ fm).[42,43] As long as the Ti and Zr atoms reside on the same site in the alloy, a cell constructed from $Ti_{2.08}Zr$ has no coherent elastic cross section and as such, presents no elastic background.

However, Ti, Zr, and V are chemically reactive, and, being electropositive, are especially susceptible to oxidation. They are suitable for conventional chemical samples but not for acidic, protic, or oxidizing samples,[56–59] where the chemical stability of these elements is low and the sample may corrode or weaken the cells with potentially unpleasant results. Given the possibility of neutron activation with certain materials, the hazards are also not purely chemical. The material from which the SE equipment is constructed requires a balance between safely containing hazardous, reactive samples and minimizing the scattering background.

B. Chemical considerations

There are several commercially available materials which can safely contain fluoride-containing samples, among them polytetrafluoroethylene (PTFE) and alloy 400 ($Ni_{1.86}Cu$).[60] Of these, PTFE has the greater general resistant to fluorides at low temperatures and pressures, especially in the presence of traces of water. Copper and nickel are also both largely resistant to attack by fluorides and can be treated with F_2 to passivate the surface through the formation of a fluoride surface coating which renders these materials resistant to further attack.[61] Indeed, Alloy 400 and nickel are used as the material of choice in the construction of many high valent fluorides. Consequently, the construction outlined below should be applicable to any fluoride that is stable in Alloy 400 or nickel. For materials that contain hydronium ions, such as aqueous solutions of HF and FSO_3H, this containment is probably not suitable. The constraint of chemical resistance is required in experiments such as these in order to preserve both the chemical and isotopic purity of the sample, as well as for radiological considerations.

C. Elastic background scattering considerations

PTFE is a partially crystalline material[62–64] and the phase diagram is known.[65,66] The diffraction pattern from this material, which forms the background, contains Bragg peaks, which arise from the periodic crystalline lattice, together with a diffuse component which arises from the local and intermediate range atomic correlations. There also exists a phase transition in PTFE that occurs at 303 K, which is an added factor in any consideration of the background signal.

Alloy 400 is a polycrystalline material, the scatter from which is predominately Bragg in nature, with low levels of diffuse scatter. Figure 1(a) shows the diffraction pattern recorded on the glass, liquids, and amorphous materials diffractometer (GLAD) at the Intense Pulsed Neutron Source;[67] Fig. 1(b) shows the corresponding pair distribution function for both materials. The high-energy x-ray data would produce a similar pattern, differing only in regard to peak intensities and is, therefore, not shown.

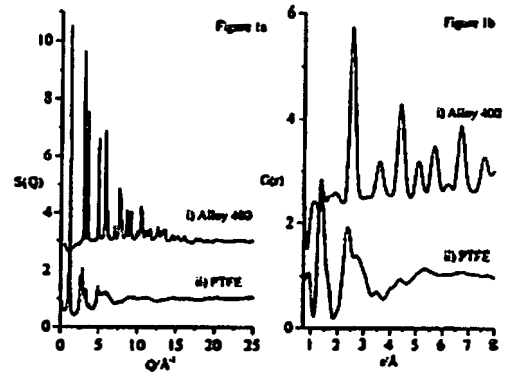

FIG. 1. (a) Diffraction pattern of (i) alloy 400 [$(S(Q)+2]$ and (ii) PTFE [$(S(Q)]$. (b) Fourier transformation of the diffraction pattern of (i) alloy 400 [$|G(r)+3|$ and (ii) PTFE [$|G(r)|$.

The samples, for which this suite of SE equipment was designed, were liquids and as such, exhibit a complete absence of Bragg scatter, due to the absence of any lattice; the diffraction intensity is confined to diffuse scatter. The choice of material is, therefore, crucial if the subtraction of background signal is to be successful. In the subtraction of a diffuse background from diffuse sample scatter, there is no simple *a priori* method for determining from what source the diffuse signal is recorded—sample or cell. In this respect, the material most suitable for sample containment in a liquid diffraction experiment of this type is alloy 400, even though Cu and Ni both have a large neutron scattering cross section ($b_{Ni} = 10.3$ fm), ($b_{Cu} = 7.718$ fm),[42,43] and therefore have Bragg peaks of very large intensity. However, subtraction of the prominent Bragg intensity is possible, both through standard analysis procedures[45,68] and through empirical subtraction.

D. Attenuation and multiple scattering considerations

When running neutron diffraction experiments on samples containing a large amount of hydrogen it is necessary to reduce the thickness of the sample in the beam since the high incoherent scattering cross section of hydrogen ($\sigma_{inch} = 80.3$ b) leads to large multiple scattering effects. Even a 1-mm-thick sample of HF has a significant multiple scattering contribution of ~20% and an absorption coefficient of ~5% neglecting the container at $2\theta = 20°$ and 1.8 Å. Therefore, a flat plate geometry is optimal as it maximizes the number of atoms in the beam while minimizing the multiple scattering.[69] In comparison for a 6.6-mm-thick flat plate DF sample the total scattering cross section is 5.82 b atom yielding multiple scattering contribution of ~15% and an absorption coefficient of only ~2% at $2\theta = 20°$ and 1.8 Å. The low absorption and respectable coherent scattering cross section of DF allows relatively large samples to be placed in the beam without significant attenuation or multiple scattering effects. Considerations for the HF sample thickness in high-energy x-ray experiments ($\epsilon \sim 115$ keV) are also based on the minimization of multiple scattering and attenuation ef-

fects. It has been found that while the multiple scattering effects have a significant Q dependence, the attenuation coefficient is usually relatively constant with momentum transfer at high energies.[70] However, it is expected that these effects will show a greater angular dependence for a flat plate geometry sample, than for a cylindrical one. For a 115 keV incident x-ray beam the calculated attenuation coefficient (obtained using the method described by Soper *et al.*[71] from a 4 mm HF sample is approximately 6% and the multiple scattering contribution only ~2%. The multiple Bragg scattering and attenuation due to the heavy elements in the alloy 400 container are far greater than that from the HF sample. However, since the sample is small and is comprised of light elements, the single and multiple scattering effects from the metal container do not differ significantly with or without the presence of a sample.

In order to minimize multiple scattering in inelastic and quasielastic experiments, the total scattering strength of the sample including the sample cell is typically restricted to ensure 90%–92% total transmission.[72] In the case of HF, the macroscopic cross-section is approximately 2.7 cm^{-1} at the elastic energy of the spectrometer, ~4.3 meV ($\sigma^{HF}_{incoh} \times \rho_{HF}$ = 90 b×0.03 H atoms/A^3). For a 92% transmission, this results in an ideal sample thickness along the beam direction of 0.3 mm. The sample cell will provide a relatively strong, additional signal centered at zero energy transfer.

III. SAMPLE CELL DESIGN FOR STRUCTURAL AND DYNAMICAL MEASUREMENTS OF HYDROGEN FLUORIDE

A. Diffraction cells

All parts of the diffraction cells with the exception of the valves and the "o" rings are machined from alloy 400. They all consist of two separable parts; a cell head which allows for transfer of hydrogen fluoride via the vacuum line described below and a sample cell body in which the sample is contained during the diffraction experiment. The two parts are joined using a 1 in. Swagelok® nut and a PTFE o-ring seal. The sample cells constructed for the diffraction experiments are shown in Fig. 2.

The body of the sample cell head was machined from alloy 400 bar stock. In order to load the samples into the body of the cell the top portion of the cell head was drilled with a 6.35 mm bore that turns 90° in approximately the middle of the head. A piece of 6.35 mm OD alloy 400 seamless tubing was welded onto the outside top of the cell in order to connect the needle valve. The lower portion of the head was additionally machined with threads to fit a Swagelok® 1 in. nut, which allows for the connection with the body of the sample cells. At this interface, a knife edge was machined to present a sealing surface to the o-ring. Appropriately sized PTFE o-rings were machined to effect the vacuum seal.

In order to minimize background container scattering, the wall thickness of each cell body was machined as thin as possible, while still maintaining the integrity of the container. The composition of the sample and the type of radiation used constrained the cell body design further. It is necessary to have a cell body of sufficient length so that only sample and the thinnest part of the can encounter the radiation beam while keeping cell head from adding to further background contamination.

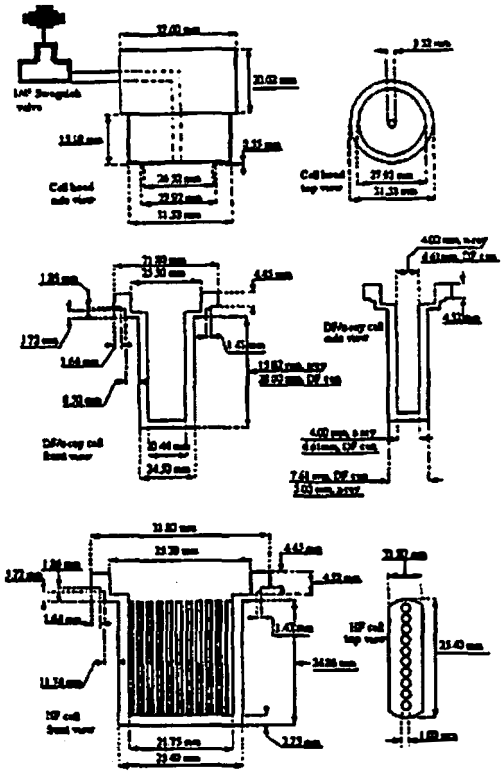

FIG. 2. Neutron and high energy x-ray diffraction sample cells.

The design and dimensions of the x-ray and DF neutron cells are shown in Fig. 2. In the case of all of the x-ray samples and the deuterium fluoride neutron sample, the cell bodies were machined as large as possible within the wall thickness, multiple scattering, and attenuation constraints. This allowed for a 0.60 mm sample thickness in the case of the deuterium fluoride neutron measurement and a 4 mm sample in thickness in the high-energy x-ray experiments. The hydrogen fluoride neutron cell body was of a different design (Fig. 2) this cell was constructed by soldering individual pieces of alloy 400 tubing (1.5 mm OD, 1 mm ID) to an alloy 400 frame using Safety-Silv® 45% silver cadmium free silver solder in a Stay-silv® black high temperature flux.

B. Quasielastic cells

In a quasielastic experiment, which utilizes the incoherent scatter from hydrogen, the sample cell has a limited volume to minimize the large signal from hydrogen. The cell body and cell heads (Fig. 3) are of a similar construction to the diffraction cells where the two portions can be joined by a Swagelok® $\frac{1}{2}$ in. nut. The cell head is of the same design as

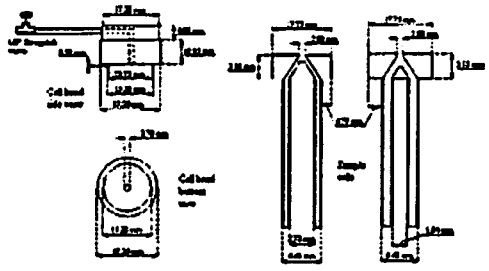

FIG. 3. Quasidasic cells.

the diffraction cell heads (Fig. 2) but on a smaller scale, with the bore in the cell being 3.14 mm.

Because the of the small sample size thickness (~0.3 mm for HF and ~1.9 mm for $H_{0.04}D_{0.96}F$), the cell bodies were fabricated from available alloy 400 seamless tubing, to form an appropriately sized annulus. In each case a 6.41 mm OD×4.93 mm ID tube was used for the outer portion of the annulus and smaller sized tubing was used to give the appropriate sample thickness. In the case of HF, the inner tube was 4.76 mm OD and in the case of $H_{0.04}D_{0.96}F$, the inner tube was 3.18 mm OD. For each set of samples the thickness was somewhat less than ideal, but the calculation ignored the scattering from the seamless alloy 400 tubing. In order to effectively vacuum transfer the samples into the cell bodies, a split Y bore was drilled into the top of the cell body to allow for access to the annulus created by the tubing. The tubing was welded to the top of the cell body by the same method described above.

IV. DESIGN OF THE SYNTHESIS AND GAS HANDLING APPARATUS

The neutron and x-ray experiments for which these cells were designed required the preparation of isotopomers of hydrogen fluoride of known composition. Not only must the chemical purity of the sample be retained at all times, but also the isotopic nature of the samples needed to be similarly conserved. Given the lability in reaction of the H/D site in anhydrous hydrogen fluoride, ingress of water and other proton-containing materials had to be minimized. The basic techniques for satisfying these requirements are mature in the field of inorganic chemistry.[6]

In order to prepare and handle hydrogen fluoride and deuterium fluoride in the laboratory, both synthetically and in order to prepare samples for the neutron experiments, a high vacuum line was constructed from alloy 400 and stainless steel tubing and equipped with Swagelok[a] fittings and needle valves. As a further precaution against contamination, and to allow the manipulation of liquids via Schlenk methodologies, an argon gas line was incorporated into the design. The synthetic equipment is therefore a hybrid Schlenk high-vacuum line and is hereafter termed the gas handling line.

The gas handling line consists of five major components: vacuum, argon, fluorine, and hydrogen fluoride circuits, connected to a central manifold.

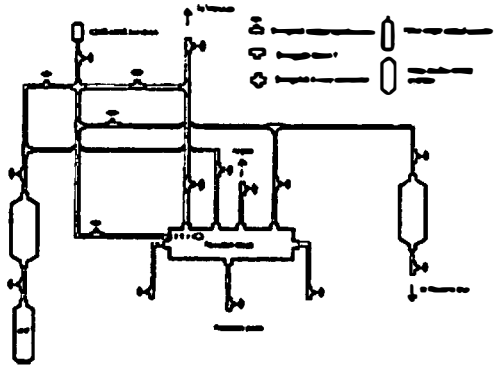

FIG. 4. Reaction manifold for the high-vacuum line.

A. Manifold design

The 214.2 mm×51 mm×51 mm manifold is machined from alloy 400 bar stock. A 37.8 mm diameter bore is drilled into the center of the manifold and finished as closely as possible to a mirror finish to minimize any adsorption of gas and potential reactivity problems on passivation. The ports are drilled and then tapped with NPT connections; the NPT connections are sealed using Teflon tape. The manifold is shown in Fig. 4. Prior to assembly, the manifold was closely examined for burr and any residual imperfections were removed, for the same reasons as the finishing of the interior bore. A port to the low pressure MKS 626A Baratron allows the pressure in the manifold to be measured.

B. F_2 and hydrogen fluoride circuits

The fluorine circuit (Fig. 5) and hydrogen fluoride circuit (Fig. 4) are constructed from 6.35 mm OD (4.57 mm ID) seamless alloy 400 tubing and are equipped with Swagelok[a] ¼ in. alloy 400 or 316 stainless steel needle valves. In order to provide a large constant volume, 2000 ml Hoke[b] bottles, constructed from 316 stainless steel, are introduced in the circuit. The fluorine circuit is additionally equipped with a

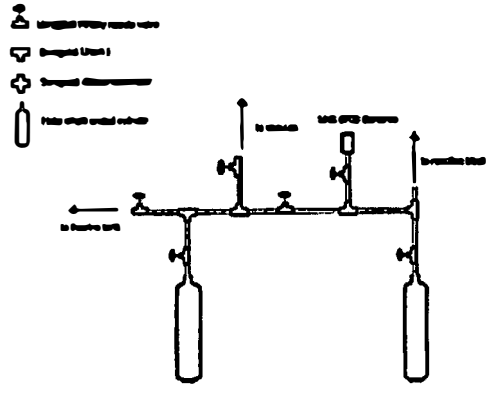

FIG. 5. Fluorine circuit.

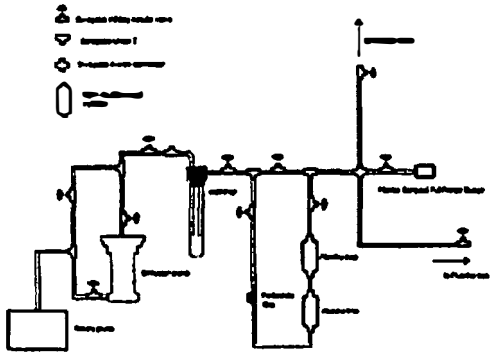

FIG. 6. Vacuum circuit.

higher pressure (1000 psi) MKS 870B baratron for measurement of higher pressures of fluorine than the manifold baratron will allow.

C. Vacuum circuit

The vacuum line (Fig. 6) is constructed entirely from 12.7 mm OD, 10.9 mm ID 316 stainless steel seamless (SS) tubing and is equipped with Swagelok[a] ¼ in. 316 stainless steel needle valves. There are two traps in place on the system. The first contains pelletized Al_2O_3, used as a scrubber trap for fluorine; the second trap is a removable glass liquid nitrogen cryogenic trap for the removal of volatiles before the pump, attached to a 316 SS trap head and sealed with Apiezon[b] W black wax. The scrubber can be bypassed for faster pumping and is fitted with a sintered steel 320 μm particulate filter down stream. The scrubber can also be removed and recharged without interruption of the line function.

The vacuum system is connected to the manifold (Fig. 4) and to the fluorine system (Fig. 5). The line is evacuated using a diffusion pump with Fomblin[c] as the working fluid, with a two-stage rotary pump as a roughing pump, the latter using conventional hydrocarbon pump oil. The diffusion pump is fitted with a bypass valve to allow for evacuation using only the roughing pump.

Pressure measurement was conducted using two electronic manometers, with ranges of 0–1000 Torr and 0–1000 psi (1 Torr=0.001 333 bar; 1 psi=0.068 948 bar), respectively. The magnitude of the vacuum was measured using a combination Pfieffer Pirani cold cathode ion gauge, with a range of $0-10^{-8}$ mbar. All wetted parts of the gauges were constructed from Inconel[c].

V. CONSTRUCTION OF THE SYNTHESIS AND GAS HANDLING APPARATUS

Before commencing with assembly and use, all tubing was thoroughly degreased using "gum solvent," a mixture by volume of 1:1:1 toluene:acetone:methanol until evaporation of the solvent left no visible residue. The tubing and other components were then freed of traces of solvent and other oxidizable volatiles by fast passage of O_2 and the line was then assembled, according to the designs described above.

The line was then both vacuum leak-tested and pressure tested with Ar. All portions of the line, except the vacuum line, were volume calibrated with Ar repeatedly, so that each segment can be used as a constant volume, allowing the barometric measurement of molar quantities of gas. It was found to maintain a static vacuum of 10^{-5} mbar over a period of weeks. After leak testing and calibration, and in order to pre-dry the line prior to drying and passivation with F_2, the line was evacuated and dried by heating the system strongly under high vacuum.

Passivation is an important aspect of the construction of any fluorine line and the portions of the gas handling line that would be wetted by F_2 or hydrogen fluoride were passivated initially by evacuation and then pressurization at ambient temperatures to sub-ambient pressures with a 5% solution of F_2 in N_2. After any pressure drop had ceased, the line was evacuated and the procedure was repeated at slightly higher initial pressure. Once atmospheric pressure had been attained and no further decrease in pressure was observed, the cycle of pressurization and evacuation was repeated with F_2 until atmospheric pressure had been reached. A pressure of 1.5 bar of F_2 was then admitted and the line left under this pressure for 24 h. Finally, the line was evacuated.

Reaction vessels and synthesis bombs are attached to the outlets from the manifold and volatiles are transferred by standard cryogenic techniques.

VI. DISCUSSION

Neutron diffraction experiments performed on samples of DF, HF, and $H_{0.5}D_{0.5}F$, prepared using the above equipment and cells showed that the conservation of the isotopic nature of the samples was essentially that of the materials used to prepare the samples and that no measurable ingression of adventitious [H] occurred.[24,25] Given that the isotopomers of HF were dried with a pressure of F_2 prior to charging the sample can, this finding is a measure of the total [H] ingression, as H_2O is oxidized by F_2 to HF and O_2. Neutron scattering is particularly sensitive to the presence of hydrogen due to the large incoherent scattering cross-section, as discussed above.

Figure 7 shows the diffraction pattern of the sample can for DF with and without the presence of the sample for both x rays and neutrons. Whereas in Figs. 7(a) and 7(c), the presence of the sample is not immediately noticeable, in the Fourier transform of the diffraction pattern, the structure due to DF can be clearly seen overlayed with the local structure of alloy 400 [Figs. 7(b) and 7(d)]. Figure 7 shows the advantage of using a crystalline material as the material from which the cells were constructed. The background intensity is confined to the pair correlation function expected from a cubic crystalline system and subtraction of the diffraction pattern of the cell in both high energy x-ray experiments and neutron experiments proved to be tractable, though laborious, using a combination of standard methods[46,68,73] and empirical methods. The DF sample data after corrections for

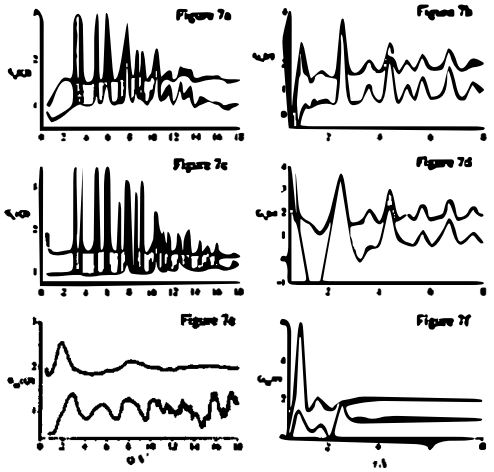

FIG. 7. (a) Neutron diffraction pattern for alloy 400, $S_N(Q)$ and for alloy 400 plus DF, $S_N(Q)+0.5$. (b) Fourier transformation of alloy 400, $G_N(r)$ and alloy 400 plus DF, $G_N(r)+1$. (c) High energy x-ray diffraction pattern for alloy 400, $S_X(Q)$ and for alloy 400 plus DF, $S_X(Q)+0.5$. (d) Fourier transformation of alloy 400, $G_X(r)$ and alloy 400 plus DF $G_X(r)+1$. (e) Corrected DF diffraction pattern using x rays, $S_{DF}(Q)$ and using neutrons $S_{DF}(Q)+1$. (f) Corrected DF Fourier transformation using x rays, $G_{DF}(r)$ and using neutrons $G_{DF}(r)+1$.

both x-ray and neutron scattering measurements are shown in Figs. 7(e) and 7(f). Previous, unpublished neutron diffraction data using PTFE cells proved to be far less tractable, with structural results that are less reliable.[74] The reason for this is clear when Fig. 1 is considered. The determination of the source of scatter from alloy 400 is far more distinct than from PTFE, both in reciprocal and real space.

Though the intensity of the background in a crystalline sample container is far more dramatic in reciprocal space than for a polymer-based cell, it is the source of the diffracted intensity that is important when considering a sample container. With a crystalline system, almost all of the background intensity, beyond that from the ubiquitous local structure, is confined to Bragg intensity, whereas for a partially or completely amorphous cell, this is not the case. The periodicity in a crystalline system, inherent due to the presence of a lattice, limits the local structure to a minimum, as in the presence of a lattice, only a small number of unique distances are required to describe the structure in real or reciprocal space.[75–78] For liquid samples, it is clear that minimization of diffuse scatter, beyond the local structure, is the most important consideration.

ACKNOWLEDGMENTS

The authors wish to extend their thanks for the provision of funding for this work to the University of Tennessee through start-up funds, the Petroleum Research Fund, administered by the American Chemical Society (PRF-37341-G6), and the Neutron Sciences Consortium of the University of Tennessee. The experiments performed at Argonne National Laboratory were supported under U.S. DOE Contract No. W-31-109-ENG-38. The authors would also like to thank Dr. J. L. Adcock (University of Tennessee) for advice and the loan of F_2 N_2 gas; B. Marzec, Dr. A. Schultz, K. Volin, M. Heimg (all of IPNS), and J. Linton and C. Kurtz (APS) for essential and material help in the facilitation of these experiments. In addition, the authors thank Dr. M. L. Klein (University of Pennsylvania) for highly stimulating discussions.

[1] D. T. Meshri, Adv. Inorg. Fluorides, 661 (2000).
[2] R. A. D. Boisson, Organofluorine Chem., 579 (1994).
[3] H. Fielding and B. Lee, Chem. Br. 14, 173 (1978).
[4] J. Sommer, Stable Carbocation Chem., Loker Hydrocarbon Res. Inst. Symp. Carbocation Chem., 497 (1997).
[5] G. A. Olah, G. K. Surya Prakash, and J. Sommer, *Superacids* (Wiley, New York, 1985).
[6] T. A. O'Donnell, *Superacids and Acidic Melts as Inorganic Chemical Reaction Media* (VCH, New York, 1992).
[7] G. A. Olah, Angew. Chem., Int. Ed. Engl. 34, 1393 (1995).
[8] R. J. Gillespie and J. Liang, J. Am. Chem. Soc. 110, 6053 (1988).
[9] J. J. DeCorpo, R. P. Steiger, J. L. Franklin, and J. L. Margrave, J. Chem. Phys. 53, 936 (1970).
[10] R. J. Le Roy and R. B. Bernstein, Chem. Phys. Lett. 5, 42 (1970).
[11] K. P. Huber and G. Herzberg, *Molecular Spectra and Molecular Structure, 4: Constants of Diatomic Molecules* (Dover, New York, 1979).
[12] J. W. Tromp and R. J. Le Roy, J. Mol. Spectrosc. 109, 352 (1985).
[13] B. N. Figgis and M. A. Hitchman, *Ligand Field Theory and Its Applications* (Wiley, New York, 2000).
[14] L. Graham, O. Graudejus, N. K. Jha, and N. Bartlett, Coord. Chem. Rev. 197, 321 (2000).
[15] N. Bartlett, Proc. Chem. Soc., 218 (1962).
[16] L. Hedberg, K. Hedberg, P. G. Eller, and R. R. Ryan, Inorg. Chem. 27, 232 (1988).
[17] R. D. Burbank and G. R. Jones, J. Am. Chem. Soc. 96, 43 (1974).
[18] R. D. Burbank and G. R. Jones, Science 171, 485 (1971).
[19] G. R. Jones, R. D. Burbank, and W. E. Falconer, J. Chem. Phys. 53, 1605 (1970).
[20] R. M. Gavin, Jr. (unpublished).
[21] J. A. Ibers, J. Chem. Phys. 40, 402 (1964).
[22] A. Pierrard, P. Gredin, and A. de Kozak, Powder Diffr. 11, 121 (1996).
[23] S. E. McLain, C. J. Benmore, and J. F. C. Turner, J. Chem. Phys. 117, 3816 (2002).
[24] S. E. McLain, J. J. Molaison, K. H. Herwig *et al.* (unpublished).
[25] S. E. McLain, C. J. Benmore, J. E. Siewenie, *et al.* (unpublished).
[26] E. Lalik, W. I. F. David, P. Barnes, and J. F. C. Turner, J. Phys. Chem. B 105, 9153 (2001).
[27] J. F. C. Turner, R. Done, J. Dreyer, W. I. F. David, and C. R. A. Catlow, Rev. Sci. Instrum. 70, 2325 (1999).
[28] J. F. C. Turner, C. J. Benmore, C. M. Barker, N. Kaltsoyannis, J. M. Thomas, W. I. F. David, and C. R. A. Catlow, J. Phys. Chem. B 104, 7570 (2000).
[29] R. I. Walton, A. Norquist, R. I. Smith, and D. O'Hare, Faraday Discuss. 122, 331 (2002).
[30] R. I. Walton, R. I. Smith, and D. O'Hare, Micro. and Meso. Mat. 48, 79 (2001).
[31] R. I. Walton and D. O'Hare, Chem. Commun. (Cambridge) 23, 2283 (2000).
[32] R. I. Walton, R. J. Francis, P. S. Halasyamani, D. O'Hare, R. I. Smith, R. Done, and R. J. Humphreys, Rev. Sci. Instrum. 70, 3391 (1999).
[33] K. Kono *et al.*, Int. J. Occup. Environ. Health 73, S03 (2000).
[34] J. J. Kirkpatrick, D. S. Enion, and D. A. Burd, Burns 21, 483 (1995).
[35] ISIS Pulsed Neutron and Muon Source, Rutherford Appelton Laboratory, Chilton, Oxon, U.K., http://www.isis.rl.ac.uk
[36] W. G. Williams, R. M. Ibberson, P. Day, and E. Enderby, Physica B 241-243, 234 (1998).
[37] General Materials Diffractometer, ISIS Pulsed Neutron and Muon Source, http://www.isis.rl.ac.uk/disordered/gem/gem_home.htm
[38] Advanced Photon Source, Argonne National Laboratory, Argonne, IL, http://www.aps.anl.gov/aps/aps_frame_home.htm
[39] Spallation Neutron Source, Oak Ridge National Laboratory, Oak Ridge, TN, http://www.sns.gov/
[40] G. L. Squires, *Introduction to the Theory of Thermal Neutron Scattering* (Dover, New York, 1997).

[44]J. Byrne and J. M. Robson, *Neutrons, Nuclei and Matter: An Exploration of the Physics of Slow Neutrons* (Institute of Physics, University of Reading, Berkshire, 1996).
[45]Neutron News 3, 29 (1992).
[46]NIST neutron scattering data, http://www.ncnr.nist.gov/resources/n-lengths/
[47]R. W. James, *The Optical Principles of the Diffraction of X Rays* (Ox Bow, Woodbridge, CN, 1948).
[48]J. Neuefeind, J. Mol. Liq. 98-99, 87 (2002).
[49]J. Neuefeind and H. F. Poulsen, Phys. Scr., T T57, 112 (1995).
[50]J. Neuefeind, C. J. Benmore, B. Tomberli, and P. A. Egelstaff, J. Phys.: Condens. Matter 14, L429 (2002).
[51]T. Weitkamp, J. Neuefeind, H. E. Fischer, and M. D. Zeidler, Mol. Phys. 98, 125 (2000).
[52]J. Neuefeind, M. D. Zeidler, and H. F. Poulsen, Mol. Phys. 87, 189 (1996).
[53]Y. S. Badyal, M. L. Saboungi, D. L. Price, S. D. Shastri, D. Haeffne, and A. K. Soper, J. Chem. Phys. 112, 9206 (2000).
[54]C. J. Benmore and P. A. Egelstaff, J. Phys.: Condens. Matter 8, 9429 (1996).
[55]B. Tomberli, C. J. Benmore, P. A. Egelstaff, J. Neuefeind, and V. Honkimaki, J. Phys.: Condens. Matter 12, 2597 (2000).
[56]B. Tomberli, C. J. Benmore, P. A. Egelstaff, J. Neuefeind, and V. Honkimaki, Europhys. Lett. 55, 341 (2001).
[57]B. Tomberli, P. A. Egelstaff, C. J. Benmore, P. A. Egelstaff, J. Neuefeind, and V. Honkimaki, J. Phys.: Condens. Matter 13, 11405 (2001).
[58]B. Tomberli, P. A. Egelstaff, C. J. Benmore, and J. Neuefeind, J. Phys.: Condens. Matter 13, 11421 (2001).
[59]M. Pourbaix, *Atlas of Electrochemical Equilibria in Aqueous Solutions* (NACE International, 1966).
[60]E. Deltombe, N. de Zoubov, and M. Pourbaix, Centre Belge Etude Corrosion Technical Report No. 29 (1956), 25 pp.
[61]M. Pourbaix, Centre Belge d'Etude de la Corrosion Technical Report No. 146-7-8-9-50 (1968), 4 pp.
[62]M. Maraghini, P. van Rysselberghe, E. Deltombe, W. de Zoubov, and M. Pourbaix, Centre Belge Etude Corrosion Technical Report No. Rapp. Tech. 45 (1957), 13 pp.
[63]G. W. Stanton, J. C. Dore, and N. J. Hance, Nucl. Instrum. Methods 141, 259 (1977).
[64]D. F. Shriver and M. A. Drezdzon, *The Manipulation of Air-Sensitive Compounds* (Wiley, New York, 1986).
[65]C. W. Bunn and E. R. Howells, Nature (London) 174, 549 (1954).
[66]M. Sprik, U. Rothlisberger, and M. L. Klein, J. Phys. Chem. B 101, 2745 (1997).
[67]M. Sprik, U. Rothlisberger, and M. L. Klein, Mol. Phys. 97, 355 (1999).
[68]E. Dobruk and W. Bonthuis, Makromol. Chem., Macromol. Symp. 39, 249 (1990).
[69]I. V. Sysoev and V. S. Khusnitin, Zh. Fiz. Khim. 58, 735 (1984).
[70]GLAD homepage, http://www.pns.anl.gov/glad/glad.htm
[71]A. K. Soper, W. S. Howells, and A. C. Hannon, *ATLAS Manual* (ISIS Pulsed Neutron Source, Rutherford Appleton Laboratory, 1989).
[72]A. K. Soper, Nucl. Instrum. Methods Phys. Res. 212, 337 (1983).
[73]H. F. Poulsen, J. Neuefeind, H. B. Neumann, J. R. Schneider, and M. D. Zeidler, J. Non-Cryst. Solids 188, 63 (1995).
[74]A. K. Soper and P. A. Egelstaff, Nucl. Instrum. Methods 178, 415 (1980).
[75]K. F. Bradley, S. H. Chen, T. O. Brun, R. Kleb, W. A. Loomis, and J. M. Newsam, Nucl. Instrum. Methods Phys. Res. A 270, 78 (1988).
[76]J. Urquidi, C. J. Benmore, J. Neuefeind, and B. Tomberli, J. Appl. Crystallogr. 36, 368 (2003).
[77]S. E. McLain, C. J. Benmore, J. Urquidi, and J. F. C. Turner (unpublished results).
[78]D. L. Goodstein, *States of Matter* (Dover, Mineola, NY, 2002).
[79]W. H. Zachariasen, *Theory of X-Ray Diffraction in Crystals* (Dover, New York, 1995).
[80]A. Guinier, *X-Ray Diffraction in Crystals, Imperfect Crystals, and Amorphous Bodies* (Dover, New York, 1963).
[81]N. H. March and M. P. Tosi, *Atomic Dynamics in Liquids* (1976).

VITA

Sylvia McLain was born in Knoxville, Tennessee in 1967. She graduated from William Blount High School in 1986, and was employed at Wendy's and Domino's Pizza until 1987 when she enrolled at the University of Tennessee in the College of Liberal Arts.

Taking a break from college, she worked for the Department of Fisheries in the Great Smoky Mountains National Park from 1989-1991 and then moved to South Carolina and was a river guide and kayak instructor for Wildwater, Ltd and the Nanatahala Outdoor Center on the Chattooga River. She taught English in Wuhan, Hubei, People's Republic of China in 1993 at the Hubei Teacher's College. Returning to the U.S., Ms. McLain again attended the University of Tennessee and in 1994 received her B. S. in Zoology.

From 1994 to 1998, she worked for Dr. G. M. McCracken in the Department of Ecology and Evolutionary Biology as a laboratory technician. Ms. McLain returned to graduate school at the University of Tennessee in 1998, and received her M.S. in Science Education in 1999.